OPTIMIZED DESIGN OF COLLECTOR SYSTEM FOR OFFSHORE WIND FARMS AND DEVELOPMENT OF A HYBRID CONTROLLER FOR SINGLE VSC-HVDC AND MULTI-TERMINAL VSC-HVDC SYSTEM

Thesis

Submitted in partial fulfillment of the requirements for the degree of

DOCTOR OF PHILOSOPHY

by

RAMU SRIKAKULAPU

DEPARTMENT OF ELECTRICAL AND ELECTRONICS ENGINEERING,

NATIONAL INSTITUTE OF TECHNOLOGY KARNATAKA,

SURATHKAL, MANGALORE -575025

January 2020

DECLARATION

by the Ph.D. Research Scholar

I hereby *declare* that the Research Thesis entitled **"Optimized Design of Collector System for Offshore Wind Farms and Development of A Hybrid Controller for Single VSC-HVDC and Multi-Terminal VSC-HVDC System"** which is being submitted to the **National Institute of Technology Karnataka, Surathkal** in partial fulfillment of the requirement for the award of the Degree of **Doctor of Philosophy in Electrical and Electronics Engineering** is a *bonafide report of the research work carried out by me*. The material contained in this Research Thesis has not been submitted to any University or Institution for the award of any degree.

....
Ramu Srikakulapu, 138012EE13F04
Department of Electrical and Electronics Engineering

Place: NITK-Surathkal
Date:

CERTIFICATE

This is to *certify* that the Research Thesis entitled **"Optimized Design of Collector System for Offshore Wind Farms and Development of A Hybrid Controller for Single VSC-HVDC and Multi-Terminal VSC-HVDC System"** submitted by **Ramu Srikakulapu** (Register Number: EE13F04) as the record of the research work carried out by him, is *accepted as the Research Thesis submission* in partial fulfillment of the requirements for the award of degree of **Doctor of Philosophy**.

Dr. Vinatha U
(Research Guide)

Prof. K N Shubhanga
(Chairman-DRPC, EEE dept.)

Acknowledgements

Abstract

This thesis deals with the optimal design of the electrical collector system of offshore wind farms (OSWFs) and the design of a robust controller for the grid-integrated OSWF with voltage source converter (VSC)- high voltage direct current (HVDC) transmission system. The worldwide installation of offshore wind farms consists of hundreds of higher rated wind turbines, which have been significantly increased in number due to their economic benefits. First part of the work in this report describes an efficient approach for improving the wind farm power production by appropriate placement of wind turbines in OSWF using the larsen and jensen wake models. A new optimization approach based on (a) elitist ant colony optimization for travelling salesman problem and multiple travelling salesmen problem and (b) firefly algorithm for travelling salesman problem and multiple travelling salesmen problem are applied to design an optimal electrical collector system for OSWF with the objective of minimizing inter-array cable length and there by reducing the cost of power production. The objective function of the electrical collector system design is expressed based on the levelized production cost and aims to minimize the levelized production cost, minimize the length of the inter-array cable between the wind turbines, achieve wake loss reduction, and optimize the power production of OSWF. The proposed approach is tested using North Hoyle and Horns Rev OSWFs with 30 and 80 wind turbines, respectively and the results obtained is observed as a valid optimal electrical collector system design.

The thesis further proposes a new hybrid controller for AC grid integrated offshore wind farm with VSC-HVDC transmission system and AC grid integrated offshore wind farms with multi-terminal VSC-HVDC transmission system. It is combination of proportional–integral (PI) based inner and sliding mode control based outer controller. With the hybrid controller, the VSCs of the HVDC transmission system are connected for control of the AC voltage, DC-link voltage, reactive power and effective power transfer between the OSWFs and an onshore AC grid. An evolutionary algorithm and proportional–integral–derivative (PID) tool are

utilized to realize the tuned gain parameters for hybrid and conventional controllers. The FRT capability, small signal analysis, and controller stability of the VSC-HVDC systems are analyzed. To check the stability of the system, small signal stability analysis is carried out with the hybrid controller and performance is compared with conventional PI controller. To examine the fault ride through (FRT) capability, a symmetrical fault and unsymmetrical fault are applied at an onshore AC grid side and the performances of the system based on the hybrid and PI controllers are analyzed. Dynamic model and linerized state-space model of the VSC-HVDC systems with hybrid and conventional controllers are developed. The analysis of the VSC-HVDC systems with hybrid and conventional controllers is conducted in the software environment of the MATLAB/Simulink. The simulation results show that the proposed control scheme provides effective active power transmission, AC voltage control, minimum reactive power transfer among the VSCs, and DC-link voltage regulation in the presence of system uncertainties and faulty condition. The controller stability is observed with the help of the Nyquist plot and eigenvalue analysis. The effect of parameter uncertainty on total system stability is examined with the help of eigenmatrix of the VSC-HVDC system.

Contents

List of Figures

List of Tables

List of Abbrevations

3L-NPC	Three-level neutral point clamped
2DOF-PID	Two-degree of freedom Proportional-integral-derivative
AC	Alternating current
ACO	Ant colony optimization
APSO	Adaptive particle swram optimization
CSC	Current source converter
DC	Direct current
DMST	Dynamic minimum spanning tree
FA	Firefly algorithm
FCM	Fuzzy c-mean
FRT	Fault ride through
GA	Genetic algorithm
GVSC	Grid side voltage source converter
HR	Horns Rev
HVAC	High voltage alternating current
HVDC	High voltage direct current
IGBT	Insulated-gate bipolar transistor
LCC	Line commutated converter
LG	Phase to ground
LLLG	Three phase to ground
MPPT	Maximum power point tracking
MST	Minimum spanning tree
MTSP	Multiple travelling salesmen problem
MT-HVDC	Multi-terminal HVDC
MVAC	Medium voltage alternating current
NH	North Hoyle
OSWF	Offshore wind farm
PI	Proportional-integral
PID	Proportional-integral-derivative
PSO	Particle swram optimization
PWM	Pulse width modulation
SLPC-VF	single large power converter-variable frequency

SMC	Sliding mode control
TSP	Travelling salesman problem
VSC	Voltage source converter
WT	Wind turbine
WVSC	Wind farm side voltage source converter
XLPE	Cross-linked polyethylene

Chapter 1

INTRODUCTION

A brief overview of the thesis and the reasons behind its motivation are presented in this chapter, followed by the research objectives, and a concise description of the flow in which the thesis is organized.

1.1 Overview

Sustainable power sources are alternative solutions for a significant amount of carbon-free electricity. Among the different sustainable power sources, wind energy has proven to be useful for large-scale energy production. The estimated installed global wind energy till 2017 is 540 GW and it is targeted to reach 4,403 GW by 2050 (, 2017, GWEC). Worldwide wind energy has decreased 637 million tons of ozone-depleting substance outflows by 2015 and the aim is to decrease three billion tons by 2030 (, 2017, GWEC). According to the current installations in various locations, wind farms are of two types: onshore wind farm and offshore wind farm (OSWF). The OSWFs are designed in clusters, where each cluster consisting of tens to hundreds of wind turbines (WTs). The estimated installed global offshore wind farm capacity till 2017 is 18 GW and it is estimated to reach 120 GW by 2030 (, 2017, GWEC). Recently, the Indian government has started 1 GW offshore wind farm project at the Gulf of Khambhat off the Gujarat coast and it plans to achieve 5 GW by 2022 and 30 GW by 2030. OSWFs have some benefits such as no land requirement, higher installation capacity, availability of better wind sources, and a lower environmental impact in comparison with onshore wind farms (Hou et al., 2017a). In OSWF, the generated power of WTs is transferred to offshore substation through inter-array cables and

connected to onshore substation through export cables, which is referred to as the electrical collector system. Figure 1.1 shows WTs arranged in radial topology, where the WTs are connected to the collector hub then to offshore platform through MV/HV transformer. Rating of the OSWF can be increased by increasing the number of WTs which consequently increase the length of submarine cables required between WTs and the collector hub. It also necessitates an electrical collector system of larger size and transformer of higher rating.
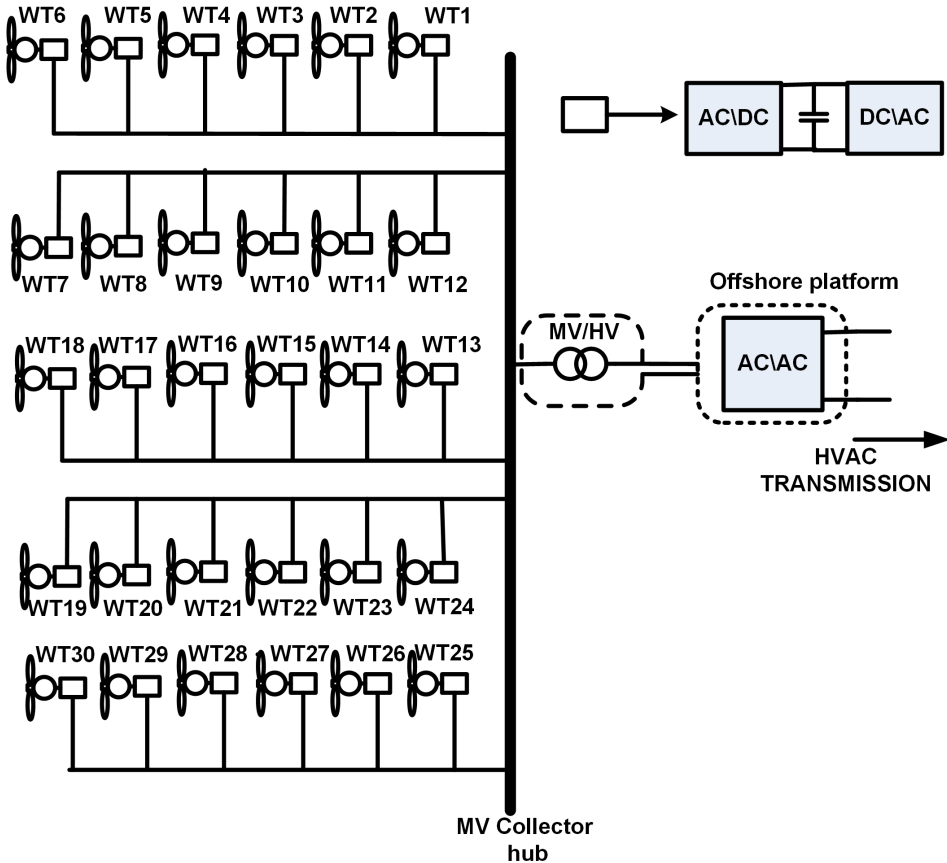
Figure 1.1: Radial topology of OSWF

Due to the reasons stated above, the capital cost of OSWF will inevitably be higher. In addition, OSWF is known to have higher maintenance and outage cost due to a critical operational environment and low accessibility. The optimized design of OSWF can achieve reduction in cost related to electrical collector system and cable layout. In large-scale OSWF, power production of WT can decline due to wake

intrusion among the WTs. Wakes formed by the upstream WTs affect the wind speed behind the rotors and decrease the power production of the downstream WTs because of reduced wind speed and increased level of turbulence. To minimize the wake effect, WTs should be separated with large dominant spaces. The standard wake models which maybe used as seen in the literature to obtain the optimal spacing between the WTs are Larsen wake, Jensen wake, Frandsen wake, and Ainslie wake model (Renkema, 2007). The Jensen and Larsen wake models are an excellent choice to solve the OSWF design problem because of its high degree of accuracy and simplicity (Shakoor et al., 2016).

The OSWFs are located far away from the shore and they require a transmission system to transmit the huge amount of power to onshore platform. High voltage direct current (HVDC) transmission system is a better choice compared to a high voltage alternative current (HVAC) transmission system. Advantages of HVDC transmission system over HVAC transmission systems are (Du, 2007): a) It can transmit the high rated power at low cost; b) It does not have limits for transmission line distance. It is effective for underground, overhead, and submarine cables; c) It has accurate and fast control of power flow; d) It does not increase the short-circuit power in the connecting system. Therefore, no need to change the circuit breakers in the transmission system; e) It can carry more power for a given size of conductor; f) It interconnects the asynchronous systems and it can transmit the power between the two AC systems operating at different nominal frequencies or the same frequency; and g) It has lower losses for same power capacity.

Among the options available for HVDC transmission system, (a) the voltage source converter (VSC) based HVDC transmission system developed using the IGBT device and (b) the line commutated converter (LCC) or current source converter based HVDC developed using thyristor device. The benefits of VSC-HVDC system are stated as follows (Du, 2007): a) It provides independent control of active and reactive power without adding the additional compensating equipment; b) In this system, the communication failure because of the disturbances can be avoided; c) It can be connected to a weak and isolated AC system or to a system where no generation source is available; d) It has black start capability, which means that the VSC is used to create a balanced set of three-phase voltages as a virtual synchronous generator; e) Size of filter required is smaller because of the high frequency switching devices; f) It suitable for OSWF applications because of a compact footprint and standardized

construction; the VSC can be easily and quickly commissioned at the preferred location; and g) The VSCs does not have any reactive power demand and also, they can control their reactive power to regulate the AC system voltage like a generator.

1.2 Research motivation

Research on the LCC based point-to-point and multi-terminal HVDC transmission has been conducted in the past. However, recently, VSC based HVDC and multi-terminal VSC-HVDC (MT VSC-HVDC) systems have become a new topic of research. The first VSC-HVDC transmission system is made by ABB and its called as HVDC Light. Its first commercial use being the connection of the 40 MW wind farm at Nas to city of Visby. The connection has a power rating of 50 MW and has a pair of extruded DC cables of 70 km length. However, the largest HVDC Light connections currently in service have a rating of 3000 MW $/\pm$ 640 kV. Siemens has completed its first ever HVDC PLUS 400 MW $/\pm$ 200 kV project in 2010. The first LCC based MT VSC-HVDC system is installed by ABB between Quebec and New England in Canada in 1986. A third terminal in Massachusetts, USA, is added in 1992, became the first three terminal HVDC system. The second LCC based three-terminal HVDC grid is deployed at Italy-Corsica-Sardinia in 2012.

The VSC-HVDC and MT VSC-HVDC technologies need to mature before being used in practical and commercial applications. Despite encouraging works in the literature on (a) electrical collector system design of the OSWF and (b) operation and control of VSC-HVDC and MT VSC-HVDC, there remains several gaps in this system which need further investigation and understanding such as:

1. Enhancement of the power production of the OSWFs by designing the optimal electrical collector system for the OSWFs. Power production enhancement can be achieved by proper placement of WTs and it needs to be studied. Wake modelling and optimal design approaches are needed to obtain the placement of wind turbines in OSWF and cable routing among the WTs in order to reduce the cost.

2. VSC-HVDC and multi-terminal VSC-HVDC transmission systems can be used to integrate the OSWFs to the onshore grid. A new controller approach based on advanced control techniques is needed to achieve effective power transfer

between the OSWFs and onshore grid. In addition it is desired to enhance the stability and performance of the system. It is also intended to give better performance in case of abnormal operating conditions such as parametric uncertainty and disturbances. It should also provide FRT capability with improved system power and voltage dynamics.

1.3   Thesis objectives

The main objectives of the thesis are as follows and Figure 1.2 illustrates an thesis objectives.

1. Design an optimal electrical collector system for the offshore wind farms to get optimal cable layout and to reduce the cost of power production of the OSWF.

2. Design of hybrid controller based on proportional–integral (PI) and sliding mode control (SMC) for the voltage source converters in a grid-integrated offshore wind farm using HVDC transmission system to get effective power transfer between the grid and OSWF and to achieve enhanced performance in terms of system performance under normal as well as abnormal conditions, system stability and FRT capability.

3. Design of hybrid controller based PI-SMC for the voltage source converters in grid-integrated multiple offshore wind farms using multi-terminal-HVDC transmission system to get effective power transfer between the grid and OSWFs and to achieve enhanced performance mentioned above.

1.4   Thesis organization

The thesis is documented with six chapters and appendix. Figure 1.3 illustrates an outline of the thesis.

Chapter 1: Presents an introduction which consists of a brief overview of the thesis and the reasons for its motivation followed by the research objectives and a concise description of the flow in which the thesis is organized.
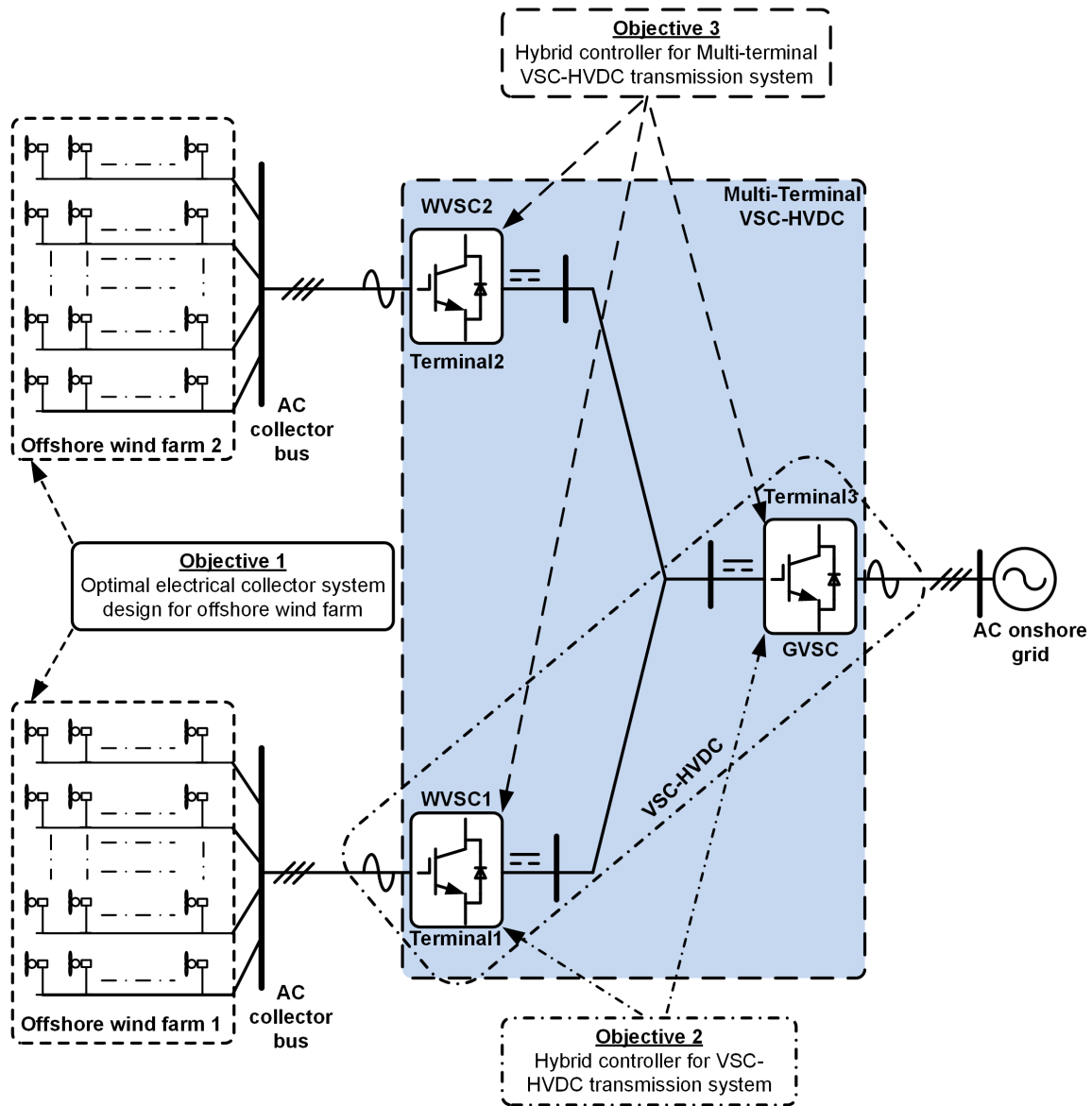
Figure 1.2: Thesis objectives

Objective 3
Hybrid controller for Multi-terminal
VSC-HVDC transmission system

Multi-Terminal
VSC-HVDC

WVSC2

Terminal2

Offshore wind farm 2

AC
collector
bus

Objective 1
Optimal electrical collector system
design for offshore wind farm

Terminal3

GVSC

AC onshore
grid

WVSC1

VSC-HVDC

Terminal1

Offshore wind farm 1

AC
collector
bus

Objective 2
Hybrid controller for VSC-
HVDC transmission system

Chapter 2: Presents the literature survey which briefly describes the different electrical collector system topology designs for offshore wind farms. A comparative review on different DC and AC collector system topologies of the OSWF is detailed. Following a review on different optimization approaches to design the optimal electrical collector system for OSWF, various control schemes adopted to develop the controller of grid-integrated OSWF with VSC-HVDC transmission system and multi-terminal VSC-HVDC transmission system are explained.

Chapter 3: Proposes a new approach to design the optimal electrical collector system for OSWFs which is based on (a) Ant colony optimization (ACO) for travelling salesman problem (TSP) and multiple travelling salesman problem (MTSP) and (b) Firefly algorithm (FA) for TSP and MTSP. The larsen and jensen wake models are used to obtain the optimal location of wind turbines. The ACO-TSP, ACO-MTSP, FA-TSP, and FA-MTSP are proposed to optimize the cable layout between the WTs and substation. The objective of the optimization is to minimize levelized production cost, minimize the length of inter-array cable, reduce wake loss, and hence maximize the OSWF power production and reduce the overall cost.

Chapter 4: This chapter deals with the new controller approach for grid integration of the OSWF with VSC-HVDC transmission system. The controller must be designed to regulate the DC-link voltage, AC voltage, active power, and reactive power. The proposed hybrid controller approach is developed by adopting the sliding mode control and conventional PI control techniques. Dynamic modelling, linearized state-space modelling and small signal stability analysis for the VSC-HVDC system are developed. The proposed hybrid controller approach enhances the system performance with regard to small-signal analysis and FRT capability at the various disturbances in the system.

Chapter 5: This chapter deals with the PI-SMC based hybrid controller approach for grid integration of the OSWFs with multi-terminal VSC-HVDC transmission system. The controller must be designed to regulate the DC-link

voltage, AC voltage, active power, and reactive power. Dynamic modelling, linearized state-space modelling and small signal stability analysis for the VSC-HVDC system are developed. The proposed hybrid controller approach enhances the system performance with regard to small-signal analysis and FRT capability at the various disturbances in the system.

Chapter 6: Summarizes the major contributions of this thesis and includes some discussions on possible future research.
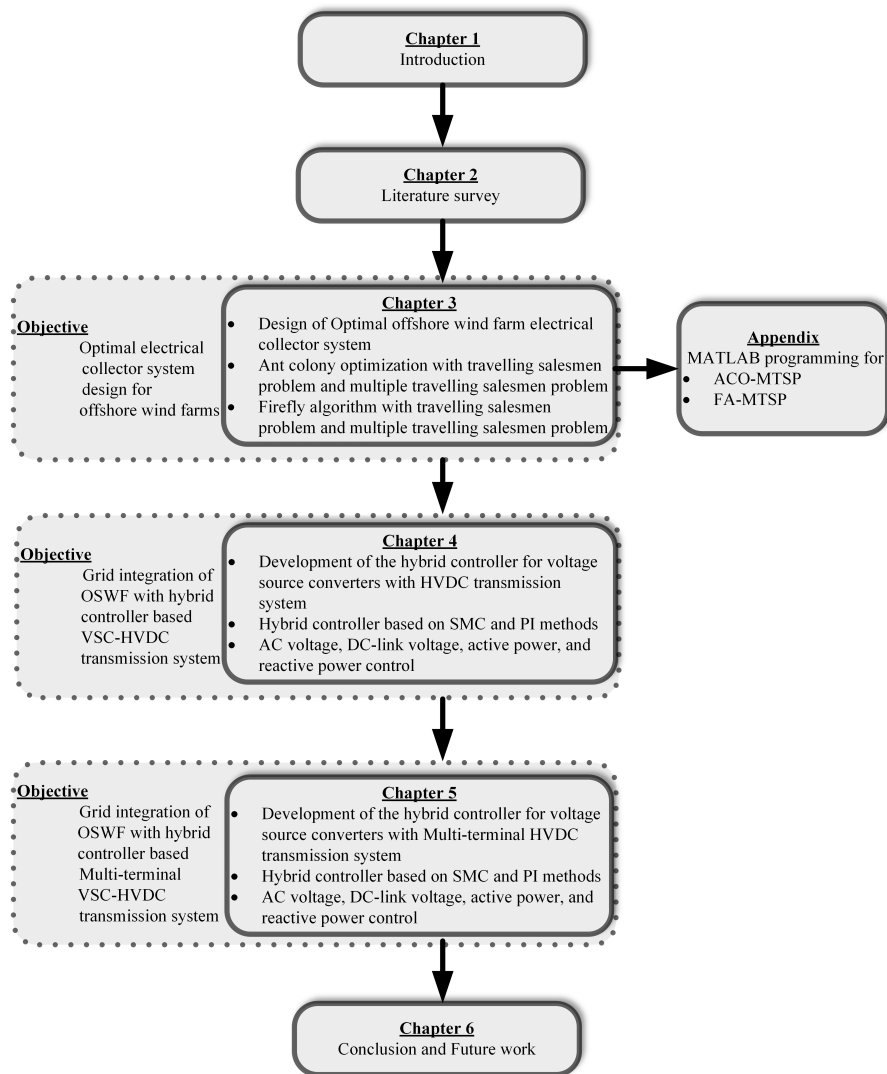
Figure 1.3: The outline of the thesis

Chapter 2

LITERATURE SURVEY

2.1 Introduction

This chapter presents the literature survey of the thesis and it explains the various electrical collector topology schemes for offshore wind farms. A comparative analysis of different DC and AC collector topologies for an offshore wind farm (OSWF) is presented. The advantages and disadvantages of different types of electrical collector topologies are discussed. Following a critical review on different optimization approaches to design the optimal electrical collector system for OSWF, various control schemes adopted to develop the controller for grid-integrated OSWF with voltage source converter (VSC)- high voltage direct current (HVDC) transmission system and multi-terminal VSC-HVDC transmission system are explained.

This chapter is organized as follows: Firstly, the OSWF electrical collector topologies are discussed and followed by the summary of various methods applied to design optimal electrical collector systems for OSWF. Secondly, the outline of the control methods used to design the controller for grid-integrated OSWF through the VSC-HVDC transmission system is explained. Lastly, the control methods applied to design the controller for grid-integrated multiple OSWFs through the multi-terminal VSC-HVDC transmission system are discussed followed by summary is detailed.

2.2 Electrical collector topologies for offshore Wind farms

The electrical collector topology is a structure, which interconnects the wind turbines (WTs) with inter-array cable and connects then to offshore substation through the collector hub. The collector hub aims to collect the generated power from the wind turbines and transmit the power to the onshore grid through the high voltage alternative current (HVAC) or HVDC transmission system. Based on the type of the collector hub, the electrical collector topologies for OSWFs are categorized as AC collector topology and DC collector topology. These are explained in detail the following sections. Figure 2.1 shows the classification of the electrical collector topologies.

2.2.1 AC collector topology

In AC collector topology, each wind turbine contains the AC-DC-AC converter and it connected to medium voltage (MV) collector hub. Further, the MV collector hub is interconnected to high voltage (HV) collector hub through the MV/HV transformer. The generated power of the AC collector topology based OSWFs is collected at MV collector hub. The salient features of the AC collector topology are: (a) it can be used for both HVAC and HVDC transmission system based OSWF; (b) it is suitable for low rating OSWFs based HVAC transmission system where additional AC/DC converter is not needed; and (c) various types of the collector topologies are available for the different ratings of OSWFs. The AC collector topology is categorized as radial topology, single-sided ring, double-sided ring, star (Quinonez-Varela et al., 2007), bifurcated radial (Bala and Sandeberg, 2014), central collector system (Ali et al., 2012), conventional AC-DC OSWF topology (De Prada et al., 2015), single large power converter-variable frequency (SLPC-VF) topology (De Prada et al., 2015), and hybrid AC-DC OSWF topology (De Prada et al., 2015). The advantages and drawbacks of AC above mentioned collector topologies are given in the Table 2.1.

```
                    ┌─────────────────────────┐
                    │   Electrical collector  │
                    │       topologies        │
                    └─────────────────────────┘
                       ╱                    ╲
        ┌──────────────────────┐      ┌──────────────────────┐
        │ AC collector topology│      │ DC collector topology│
        └──────────────────────┘      └──────────────────────┘
```

AC collector topology	DC collector topology
Radial topology	**Series topology**
Single-sided ring topology	**Parallel topology**
Double-sided ring topology	**Hybrid topology**
Star topology	**Matrix interconnection topology**
Bifurcated radial topology	**Positive and negative WT cluster with neutral topology**
Central collector topology	**DC architecture with AC aggregation topology**
Four-sided ring topology	**DC architecture with DC aggregation topology**
Conventional AC-DC OSWF topology	**Different parallel topology**
Single large power converter-variable frequency topology	**DC OSWF topology 1, 2, 3 & 4**
Hybrid AC-DC OSWF topology	

Figure 2.1: Electrical collector topology chart

Table 2.1: AC collector topologies

Topology	Figure	Advantages and Drawbacks
Radial		The advantages are low cost, simple control, less design complexity and less switchgear requirement. The drawbacks of radial topology are poor voltage regulation; poor reliability, the rating of the inter-array cable increases with the number of WTs connected in a string, and if there is any fault in the inter-array cable or near the collector hub, then the whole OSWF shuts down.
Single-sided ring		The drawback of the topology is that longer inter-array cable is required to interconnect the WTs. The advantage is improved reliability when compared to radial topology. When a fault occurs at the hub end of the connected inter-array cable, the total power flow through the redundant path is decreased and the power loss is reduced by 45% when compared to radial topology (Quinonez-Varela et al., 2007).
Double-sided ring		The advantage is that power flow occurs through other strings without loss of good units, in case any WT is affected by an internal fault. Power loss is 18% lesser than the typical radial topology (Quinonez-Varela et al., 2007). The drawbacks are that (a) the capacity of the inter-array cable must withstand the total generated power and hence it requires high rated inter-array cables and (b) the reliability of the topology is low when the fault occurs at WTs of the both sided strings (WT1 and WT12) in the same time. Compared to radial and single-sided ring topologies, the cost of double-sided ring topology is higher because it requires high rating of the inter-array cable.
Star		The advantages are (a) the inter-array cable rating reduces comparatively with respect to the topologies explained above and hence it reduces the cost of the topology, (b) the reliability and voltage regulation are improved, and (c) when a fault occurs in any WT, it will not affect the power flow of other WTs. Drawbacks are that a complex switchgear arrangement is required at the center of the collecting point and a high rating inter-array cable requires to interconnect the center of the collecting point and the collector hub. The power loss of star topology is 4% lesser than radial topology (Quinonez-Varela et al., 2007).

Topology	Figure	Advantages and Drawbacks
Bifurcated radial		The advantages are that it required small rating inter-array cable compared to double-sided ring topology and it affects to the reduction in inter-array cable cost hence, cost of topology is less compared to a double-sided ring topology. The drawbacks are that when the failure of circuit breaker or fault occurs in the inter-array cable at near to circuit breaker; it will be resulted in a complete shutdown and low reliability compared to a double-sided ring topology.
Central collector		The advantages are improved reliability compared to bifurcated radial topology and power losses are lower than that of the typical radial topology. The drawbacks are requirement of higher capacity inter-array cable between the central point and collector hub, which increases the cost and when the failure of circuit breaker or fault occurs in the inter-array cable between the collector hub and central point, it results in a loss of total generated power.
Four-sided ring		The advantages are high reliability compared to other ring topologies, lesser requirement of switchgear, improved voltage regulation and 18% lesser power loss when compared to typical radial topology (Quinonez-Varela et al., 2007). The drawback is that it requires a higher rating of inter-array cable for the redundant path.
SLPC-VF		Advantage is the capital and maintenance cost is less compared to conventional AC-DC topology. The main drawbacks are (a) complexity in control of all WTs by a single power converter, (b) it requires a high rating power converter at the collector hub because of single power converter operation which results in higher conduction losses and lower reliability, and (c) when a fault occurs in the power converter, it affects the entire system and causes a loss of total generated power (De Prada et al., 2015).

2.2.2 DC Collector topology

In DC collector topology, each wind turbine contains the AC-DC converter and it connected to DC collector hub. The generated power of the DC collector topology based OSWFs is collected at DC collector hub. The salient features of the DC collector topology are: suitable for HVDC transmission system based OSWF; Additional AC-DC-AC converter is not needed; and reduces complexity and components required are lesser as compared to AC collector topology. The DC collector topology is classified as series topology (Gil et al., 2015), parallel topology (Gil et al., 2015), hybrid topology (Chuangpishit et al., 2014), different parallel topologies (DC OSWF topology 1, 2 ,3 and 4)(Gil et al., 2015), matrix interconnection topology (Chuangpishit et al., 2014), DC architecture with AC aggregation topology (Bala and Sandeberg, 2014), and DC architecture with DC aggregation topology. The advantages and drawbacks of above mentioned DC collector topologies are given in the Table 2.2.
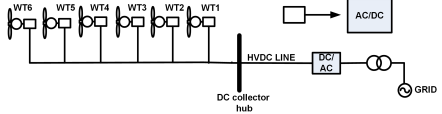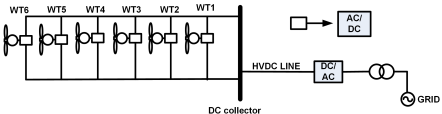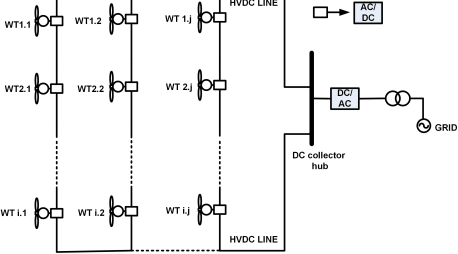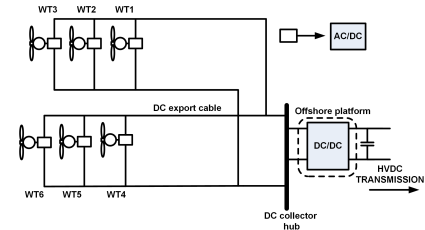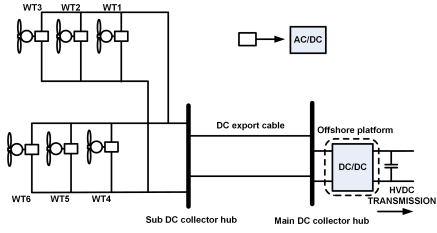
In section 2.2, the various electrical collector topologies are explained. The design of OSWF electrical collector system is an important aspect and various optimization approaches are applied to achieve an optimal design. The detailed literature survey on the optimal design of OSWF electrical collector system is explained in the following section.

2.3 Approaches for optimal design of offshore wind farm electrical collector system

Optimized design of OSWF electrical collector system refers to the placement of WTs on the sea waters at location of the OSWF and then the design of cable routing so as to improve the power production and reduce the cost of production.

In the available literature on the subject, the design of OSWF electrical collector system has been studied and researchers have applied a few optimization techniques for design of inter-array cable routing and minimization of cable cost. In large-scale OSWF, power production of WT can decline due to wake intrusion among the WTs. Wakes formed by the upstream WTs affect the wind speed behind the rotors and decrease the power production of the downstream WTs because of reduced wind speed and increased level of turbulence. To minimize the wake effect, WTs should be separated with large dominant spaces. The standard wake models which maybe used

Table 2.2: DC collector topologies

Topology	Figure	Advantages and Drawbacks
Series topology		The advantages are that it is the simplest collector topology and cost-effective. Series DC topology is best suited for local DC grids of limited size (Jovcic et al., 2015). Drawbacks are lower reliability, overvoltage, and when a fault occurs near to the collector hub WT (WT1) results in loss of power in the entire system.
Parallel topology		It is best suited for large rated WTs because of higher voltage rating. It requires the DC-DC converter to boost the DC voltage for the HVDC transmission. Parallel topology is more reliable than series topology. The drawback is an overcurrent problem.
Hybrid topology		The hybrid topology is the combination of series and parallel topology.
DC OSWF topology 1		The advantages are the minimum number of collector platforms required hence, it results in cost reduction. Drawbacks are it requires a large cross-section of inter-array cable, it needs high rating DC-DC converter and draws more power losses.
DC OSWF topology 2		The advantage is topology cost reduction due to (a) DC-DC converter is not required at the sub-DC collector hub and (b) lower rating inter-array cables. The Drawback is the requirement of high rating DC export cables to withstand the higher voltage.

Topology	Figure	Advantages and Drawbacks
DC OSWF topology 3		The advantage is a low power loss in export cables due to high voltage. The drawbacks are lower reliability and loss of total generated power if the DC-DC converter fails.
DC OSWF topology 4		Advantages are the less power loss in the DC export cable, requires lower rating inter-array cables, improves efficiency, and high reliability compared other parallel topologies. The drawback is an increased cost due to more number of DC-DC converter setups and DC collector hubs.
Matrix inter-connection topology		It is a modified series-parallel topology. It overcomes the overvoltage problem of series-parallel topology.
DC architecture with AC aggregation topology		The advantage is that individual DC-AC converter is not needed for WTs and single high rated DC-AC converter used to interconnect the WT string and AC collector hub.

Topology	Figure	Advantages and Drawbacks
DC architecture with DC aggregation topology		The advantage is that individual DC-AC converter is not needed for WTs and single high rated DC-AC converter used to interconnect the DC collector hub and onshore grid.

as seen in the literature to obtain the optimal spacing between the WTs are Larsen wake, Jensen wake, Frandsen wake, and Ainslie wake model (Renkema, 2007). The improved genetic algorithm (GA) for multiple travelling salesmen problem (MTSP) is adopted to design an optimal OSWF (Gonzalez-Longatt et al., 2012) and various cable cross sections are considered in order to design a radial topology. Bender's decomposition and Progressive contingency incorporation algorithm are applied to design an optimal electrical system a reduction in investment and a curtailed production cost (Lumbreras and Ramos, 2013). A binary integer programming with fuzzy c-means (FCM) an approach is applied to minimize the cable cost and transmission losses of OSWF, where the position of WTs is close to a substation (Chen et al., 2013). In (Chowdhury et al., 2013), the unrestricted wind farm design optimization is achieved by advanced mixed-discrete particle swarm optimization (PSO) and cost of energy is evaluated. In (Prabhu et al., 2013), authors have applied GA with harmony search algorithm to achieve the finest placement of WT, where the wake effect is taken into account. The improved GA is applied to optimal placement of the WTs in OSWF and an economic model is proposed to maximize the profitability of the project (González et al., 2013). An optimal electrical network for OSWF is designed by GA with Prim's algorithm and the objective involved the total investment cost and feasibility of crossing cables (Dahmani et al., 2015).

A hybrid AC-DC OSWF topology is optimized to minimize the total cost of OSWF

using mixed integer nonlinear programming (De Prada et al., 2015). In (Park and Law, 2015), the optimal OSWF is modeled for improving the power production of the wind farm by sequential convex programming method. A firefly algorithm (Wagan et al., 2015) and random search algorithm (Feng and Shen, 2015) are applied to achieve optimal placement of WTs in OSWF. In (Hou et al., 2015a), Prim's algorithm is employed for optimal installation of the offshore substation. The GA with geometric programming is employed to design the optimal model of OSWF (Dahmani et al., 2015). Authors have adopted the PSO for optimal allocation of the WTs with the aim of maximizing the power production while diminishing the total OSWF expenditure (Hou et al., 2015b), (Hou et al., 2017b). Clarke and Wright savings heuristic (CWH) method with vehicle routing (Bauer and Lysgaard, 2015), and capacitated minimum spanning tree (MST) (Pillai et al., 2015) are implemented for the optimization of inter-array cable routing between WTs in OSWFs. A self-adaptive allocation method is based on combination of PSO and FCM clustering algorithm proposed to place the substations and WTs in OSWF. A new electrical collector system design optimization is proposed and it is solved by Bender's decomposition algorithm, where multiple substations and cable types are considered (Chen et al., 2016). In (Hou et al., 2016c), the mixture of adaptive PSO (APSO) and MST is applied to optimize the OSWF and the optimized design by MST, dynamic MST (DMST) and APSO-MST are compared. Hou et al.(Hou et al., 2016d) have extended the work by applying an optimized power dispatch method for minimizing the levelized production cost, where PSO is applied for the optimal design of regular shaped OSWF. The optimal OSWF is achieved by using various methods such as mixed integer linear programming (Wdzik et al., 2016), binary PSO (Pookpunt and Ongsakul, 2016), GA and PSO (González et al., 2017), (Amaral and Castro, 2017), (Pillai et al., 2017), hyper-heuristics (Li et al., 2017), biogeography-based optimization (Bansal and Farswan, 2017), GA based local search (Abdelsalam and El-Shorbagy, 2018) and binary artificial algae algorithm (Beşkirli et al., 2018). In (Hou et al., 2016a), authors have applied dynamic MST method to achieve an optimal design for irregular shaped OSWF. The combination of PSO and multiple adaptive methods is applied for the optimal design of irregular shaped OSWF with restricted zones (Hou et al., 2016b). The fuzzy clustering algorithm, single parent GA, and MTSP are used to solve the hierarchical optimization model based on double-sided ring structure of OSWF (Wei et al., 2017).

In section 2.3, the various approaches to design an optimal model of the OSWF

electrical collector system is explained. The generated power is collected at collector hub and it is transmitted to grid through the VSC-HVDC transmission system. To get effective power transmission from the OSWF to grid, the VSC should be controlled using effective control approaches. The detailed literature survey on control schemes for grid-integrated OSWF through the VSC-HVDC transmission system is explained in the following section.

2.4 Control schemes for grid-integrated offshore wind farm through the VSC-HVDC transmission system

Several studies have been carried out on conventional control techniques for the grid integrated OSWFs through the VSC-HVDC transmission. An improved fault ride-through (FRT) method based on the controlled demagnetization approach is used to control the voltage reduction to avoid the overvoltage of DC link and to achieve the effective power transfer (Feltes et al., 2009). Authors Erlich et.al have extended the above work by using an improved voltage drop control approach (Erlich et al., 2014). In (Blasco-Gimenez et al., 2010), authors have proposed distributed voltage and frequency control to connect the AC grid to synchronous generator based OSWF through the HVDC link, where the link rectifier and inverter are designed based on the 12-pulse diode and thyristor bridge, respectively. An aggregation scheme based on the 3-level neutral point clamped (3L-NPC) converter is used as a rectifier for HVDC collector system to interconnect the OSWF and onshore HVDC substation. It adopted the single-phase switching strategy with minimized switching losses (Chaudhuri and Yazdani, 2011). In (Giddani et al., 2013), authors have implemented a multi-task controller based on proportional-integral (PI) control for designing a VSC-HVDC link between the two AC systems and they studied the FRT capability and transient system stability for various fault conditions. The controller dealt with the effective power transfer, independent reactive power control and regulation of system frequency. A power synchronization control is used to connect the OSWF to the grid through the VSC-HVDC link and the FRT schemes are investigated by considering the offshore and onshore faults with and without chopper (Mitra et al., 2014). Authors have proposed a communication-based FRT scheme which is the combination of PI and

de-loading control methods to interconnect the OSWFs and grid by VSC-HVDC link. It works on grid code conditions such as active voltage support, power flow balancing and FRT capability. Hence, the linearized small-signal model is obtained to examine the communication system impact on FRT scheme and DC chopper resistor rating (Nanou and Papathanassiou, 2015). Further, authors have used a coordinated control method which is the mixture of the voltage-dependent current modulation approach between the VSC-HVDC converters and the WTs (Nanou et al., 2015). The OSWF may not react to the fluctuations of grid frequency because of the delinking of VSC-HVDC and signal transmission delay. Hence, the OSWF stability will be at risk in case of high wind flow. A coordinated control method is used to regulate the system frequency by controlling the DC-link voltage of VSC-HVDC, where the coordination is operated between the DC-link capacitor energy and grid frequency (Liu and Chen, 2015). In (Egea-Àlvarez et al., 2017), the authors have applied power coordination technique to achieve the DC voltage regulation for integrating OSWF to the grid with less communication among the VSCs. The power coordination is realized by the two droop controllers such as grid side dynamic braking resistor and OSWF side controllers. A new control approach is employed to control the dc voltage, an active and reactive power of the OSWF with VSC-HVDC. It is a mixture of the multi-variable PI and single-input single-output PI controllers acting as inner and outer controllers, respectively (Pradhan et al., 2017). The new configuration based on the reduced switch count-nine switch converter is applied to achieve the uninterrupted power flow and DC voltage regulation in faulty condition for grid-connected OSWF by VSC-HVDC. To fulfill the above context and improve the FRT capability, the configuration is designed with series and shunt network interface among the grid and OSWF (Kirakosyan et al., 2017). The hybrid VSC-HVDC is designed by PI control (Nguyen and Lee, 2012) and proportional resonant control (Nguyen et al., 2015) for power transfer among the OSWF and grid. It consisted of a 12-pulse diode rectifier and VSC, which are employed on the OSWF and grid side, respectively (Nguyen and Lee, 2012).

The conventional control techniques may not give a desired response to the non-linear systems due to limitations of the parameter tuning (Ramadan et al., 2012). From the mathematical and operation viewpoint, the grid-connected OSWFs are highly non-linear systems. Accordingly, the VSC controller must be a robust and non-linear type which can enhance the stability and performance of the system (Colbia-

Vega et al., 2008). The adaptive or advanced control technique-based controllers can give better performance in case of an abnormal operating condition such as parametric uncertainties and disturbances (Ramadan et al., 2012). Some authors have adopted the non-linear and advanced control techniques to design system controllers. A fuzzy logic controller is implemented to develop the 3L-NPC converter for the grid-integrated OSWF through VSC-HVDC transmission (Muyeen et al., 2010). In (Benadja and Chandra, 2015), authors have adopted extended Kalman filter to design an adaptive sensor-less control to regulates the DC link voltage for 3L-NPC converter based VSC-HVDC link to connect the OSWF and onshore grid. To improve the VSC-HVDC system performance, two non-linear control techniques are utilized to design controllers such as sliding mode control (SMC) and two-degree of freedom PI-derivative (2DOF-PID). The active and reactive power are controlled by the SMC controller and DC voltage is regulated by 2DOF-PID controller (Ramadan et al., 2012). The combination of genetic algorithm (GA) and SMC is used to design a controller for VSC-HVDC system and it improved the dynamic stability of the system in various operating conditions (Ahmed et al., 2015). In (Yang et al., 2016), authors have applied perturbation observed-SMC method to design a controller for VSC-HVDC system and multiple studies are carried out such as AC fault analysis, parameter ambiguity, integration to weak AC grid, active, and reactive power control. The adaptive SMC based on feedback linearization (Mallick, 2011) and inertia emulation-SMC (Mahapatra and Dash, 2015) control techniques are employed to design a non-linear controller for VSC-HVDC system and the responses are observed at different conditions such as short-circuit ratio changes, faults, power oscillations. In (Zhao and Li, 2013), authors have designed a robust controller based on the adaptive backstepping for VSC-HVDC system. The controller aims to achieve stable power transmission by maintaining a stable DC voltage. The power system stability analysis is carried out on a large scale, where the OSWF is interconnected to the New England ten-machine 39-bus test system (Edrah et al., 2015). In (Kunjumuhammed et al., 2017), authors have worked on stability analysis of infinite grid integrated to OSWF with VSC-HVDC by using oscillatory modes of the system, where the system closed-loop stability is influenced by the critical modes sensitivity and OSWF parameters. The voltage stability and control of the OSWF with VSC-HVDC is discussed in (Liu and Sun, 2014). AC bus voltage instability and resonance among the OSWF and HVDC rectifier are investigated by the system impedance-stability condition, where

the harmonic linearization method is used to design the system impedance models. A new control technique is applied to reduce the power fluctuations and enhance the system damping for grid-integrated OSWF with LCC-HVDC link, where the control technique consisted of rectifier and inverter current regulators which are designed based on modal control theory. Improvement of stability is examined by the system eigenvalue analysis (Wang and Thi, 2013b).

The various control schemes for grid-integrated OSWF through the VSC-HVDC transmission system is explained in section 2.4. At present multiple OSWF sites are developed and they are separated with long distances. The multi-terminal VSC-HVDC transmission system is required to integrate the multiple OSWFs and grid. To get effective power transmission between the multiple OSWFs and grid, the VSC should be controlled using effective control approaches. The detailed literature survey on control schemes for grid-integrated OSWFs through the multi-terminal VSC-HVDC transmission system is explained in the following section.

2.5 Control schemes for grid-integrated offshore wind farms through the multi-terminal VSC-HVDC transmission system

Several studies have been carried out on control of multi-terminal HVDC (MT-HVDC) for grid integration of the OSWFs in the literature. In (Xu and Yao, 2011), authors have used PI and DC droop-based DC voltage controls to get proper power dispatch in the 4-terminal HVDC system. The methodology for droop control of MT-HVDC is discussed and it controlled the DC voltage in grid-integrated OSWFs (Prieto-Araujo et al., 2011). Authors have used optimal voltage control to minimize the loss in MT-HVDC system for OSWFs (Aragüés-Peñalba et al., 2012). In (Dierckxsens et al., 2012), a distributed DC voltage control scheme is discussed for MT-HVDC system. The small signal stability for MT-HVDC system is described and the effect of the current, DC voltage, and AC voltage controller are discussed (Kalcon et al., 2012). In (Wang and Thi, 2013a), authors have worked on stability analysis of grid-integrated OSWFs, where MT-HVDC, VSC-HVDC, and HVAC transmission systems are analyzed for a case study. The sizing of droop control with the output capacitors is simplified for primary control in MT-HVDC grids (Gavriluta et al., 2015). The power

reduction control in MT-HVDC system is demonstrated to avoid the DC overvoltage (Adeuyi et al., 2015). In (Zhao and Li, 2015), an adaptive backstepping droop controller is used to control the DC voltage for the 4-terminal HVDC system. The independent local control is proposed to regulate the current and the voltage behind the capacitor in a voltage source terminal and the inductor in a current source terminal (Sun, 2015). An SMC based active power variation control is applied to control the MT-HVDC system in (Tang et al., 2016). In (Raza et al., 2016), authors have used the DC voltage droop control for VSCs of both sides in the 4-terminal HVDC system to regulate the DC voltage between the VSCs. A communication-less DC voltage control method is proposed to get sufficient power dispatch in MT-HVDC system, where improved master/slave control method is discussed (Sandano et al., 2017). In (Khenar et al., 2017), authors have presented a control method based on a multi-loop current and voltage control to reach effective power transfer in 3-terminal HVDC system in which wind farm side DC voltage control and grid side active power control are applied.

2.6 Summary

In this chapter, different electrical collector topologies for OSWF are explained with salient features and drawbacks. Collector topologies are categorized as AC collector and DC collector topologies. Among those, AC collector topologies are widely used in design of the OSWF. In view of the practical implementation, most of OSWF collector designs are made using the radial collector topology.

In section 2.3, the literature survey on the approaches for optimal design of OSWF electrical collector system is explained. Various approaches are used for different aspects to get the optimal design of the OSWF collector system. Those are specified as follows: an improved GA-MTSP, APSO-MST, binary PSO and GA-PSO are applied for design optimal OSWF; binary integer programming with FCM for cable cost minimization; mixed-discrete PSO for unrestricted OSWF; improved GA, firefly algorithm, random search algorithm, PSO and GA with harmonic search algorithm are applied for optimal placement of WTs; Prim algorithm and PSO-FCM are used for offshore substation placement; and CWH method with vehicle routing, ACO-GA, MST are implemented for inter-array cable routing.

In section 2.4, the literature survey on control schemes for grid-integrated OSWF

through the VSC-HVDC transmission system is explained. Conventional and advanced control schemes are applied for control the performance of VSC-HVDC transmission system. Those are mentioned as follows: FRT based controlled demagnetization approach, improved voltage drop control and proportional resonant control are used for effective power transfer; PI based multi-task controller is applied for effective power transfer, reactive power control, and frequency regulation; PI based de-loading control method is used for AC voltage support and power flow balancing; coordinated control method, droop control based power coordination technique and extended Kalman filter based an adaptive sensor-less control are applied for DC voltage regulation and mixed- variable PI with single-input single-output PI controllers, SMC with 2DOF-PID, perturbation observed-SMC, and adaptive backstepping method are used for control the DC voltage, active and reactive power.

In section 2.5, the literature survey on control schemes for grid-integrated OSWFs through the multi-terminal VSC-HVDC transmission system is explained. Conventional and advanced control schemes are applied for control the multi-terminal VSC-HVDC transmission system.These are PI, DC droop based DC voltage controller, SMC based active power variation controller, communcation-less DC voltage controller and multi loop current and voltage controller are applied for effective power transfer; and Droop controller, a distributed DC voltage controller, power reduction controller, adaptive backstepping droop controller, and DC voltage droop controller are used for control the DC voltage.

In Chapter 3, a new approach is proposed to design the optimal electrical collector system for OSWFs which is based on (a) ACO for TSP and MTSP and (b) FA for TSP and MTSP. The larsen and jensen wake models are used to obtain the optimal location of wind turbines. The ACO-TSP, ACO-MTSP, FA-TSP, and FA-MTSP are applied to optimize the cable layout between the WTs and substation. The mathmatical expersions of larsen model, jensen model,power production, cable power loss, annual energy yields, levelized production cost index, and inter-array cable cost are explained. The reliazation of ACO-MTSP, FA-MTSP, and GA-MTSP approches are discussed.

Chapter 3

OPTIMAL ELECTRICAL COLLECTOR SYSTEM DESIGN FOR OFFSHORE WIND FARM

3.1 Introduction

In last two decades, the utilization of wind energy is elevated to an appreciable level. Wind energy is an alternative energy source for significant amount of carbon free electricity. Based on the placement of wind turbine (WT) the wind farms are classified into two types. They are offshore wind farm and onshore wind farm. The offshore wind farms (OSWFs) are gaining importance over onshore wind farms because of (a) no land requirement and space restrictions, (b) higher installation capacity, (c) availability of strong wind flow, and (d) no limitation for higher rated wind turbine installations. The OSWFs are designed in clusters and each culster consists of tens to hundreds of wind turbines. The OSWF contains wind turbines, transformers, offshore platforms, and submarine cables. Collector topology plays an important role in connecting these turbines to the hub. As the rating of OSWFs increase, collector systems required will be larger in size, raising losses in longer submarine AC cables (Chuangpishet and Tabesh, 2011). The capital cost of OSWF is higher than the onshore wind farms. In addition OSWFs have higher outage and maintenance cost due to critical operational environment and low accessibility. Reduction in cost can be achieved by optimal design of collector topology, cable layout and reduced number

of AC-DC converters. A novel hybrid AC-DC topology based on a mixed integer nonlinear programming has been proposed by the researchers in order to obtain a optimal design of collector topology(De Prada et al., 2015). Optimal cable layout design of collector system is obtained by graph theoretic minimum spanning tree algorithm with the objective of minimization of total trenching length is discussed in (Dutta and Overbye, 2012). The multiple travelling salesman problem and genetic algorithm (GA) are used to design optimal OSWF collector systems in(Gonzalez-Longatt, 2013).

This chapter deals with the methodology for optimal design for OSWF electrical collector system. This is achieved in two stages, first stage deals with the optimal placement of wind turbines. This is accomplished using larsen and jensen wake models. With this the wake loss is minimized and hence power production is increased. Second stage is to obtain an optimal cable length connecting the wind turbines and then to the offshore substation. For the second stage, the methodology is based on the (a) ant colony optimization (ACO) for travelling salesman problem (TSP) and multiple travelling salesman problem (MTSP) and (b) Firefly algorithm (FA) for TSP and MTSP. The work aims to minimize levelized production cost index, minimize the length of inter-array cable, minimize wake loss, and hence optimize the power production of OSWF. The proposed approach is tested with North Hoyle (NH) and Horns Rev (HR) OSWFs with 30 wind turbines and 80 wind turbines, respectively and observed as a valid optimal collector system design. The ACO-TSP, ACO-MTSP, FA-TSP, and FA-MTSP are proposed to optimize the cable layout between the wind turbines and substation. Among the ACO and FA based optimal designs, the FA based designs have given better outcomes with regards of inter-array cable length, cable cost and levelized production cost index.

This chapter is organized as follows: Firstly, the wake models and specifications of OSWF are explained, followed by the details of the ACO-MTSP and FA-MTSP approaches with a flowchart. Secondly, problem formulation is illustrated. Lastly, the results of the optimal designs pertaining to both approaches are provided with a detailed comparative assessment followed by summary is detailed.

3.2 Offshore wind farm model

Wake effect on wind turbines, plays an important role in the modelling of an offshore wind farm. The power extraction from wind farm are strongly linked with wake effect with regard to placement of WTs. The wake model takes into account the wake effect in wind farms and thereby provides the required optimal spacing between the wind turbines in order to increase the power production to an optimal value. The wake effect is the aggregated effect on the power production of the wind farm, which results from the changes in wind velocity due to the influence of the wind turbines on each other. The disrupted wind velocity value will vary with the distance between the wind turbines.

3.2.1 Wake model

Wakes in wind farms are of two types which are classified based on their distance from the wind turbine. They are near wake and far wake. The distance varies from one to several times of the wind turbine rotor diameter. The far wake models can either be kinematic wake models or field models. In this study, a kinematic far wake model is taken for analysis of wake effect. The wake effect is classified as full, partial, and non-wake effect as shown in Figure 3.1. Wake models based on Larsen and Jensen wake theory are explained in the following sections.

3.2.1.1 Larsen wake model

The Larsen model is proposed by G.C. Larsen. It is a kinematic model and is formulated using the Prandtl turbulent boundary layer equations. This wake model can give solutions for the mean velocity profile in the wake and the width of the wake. In this model the wind flow is assumed to be stationary and wind shear is neglected (Renkema, 2007). For Larsen model first order equations and solutions are given below. The wake radius r_w is expressed in (3.1).

$$r_w = 1.7563(c_1^{\frac{2}{5}})(x_{ij})^{\frac{1}{3}} \tag{3.1}$$

Where $x_{ij} = C_T \frac{A_{ol}}{A_r}(b + b_0)$, C_T is the thrust coefficient($C_T < 1$), A_{ol} is the area of overlap, A_r is the rotor area, and c_1 is a function of Prandtl mixing length and the rotor position with respect to the applied coordinate system.The wake boundary as
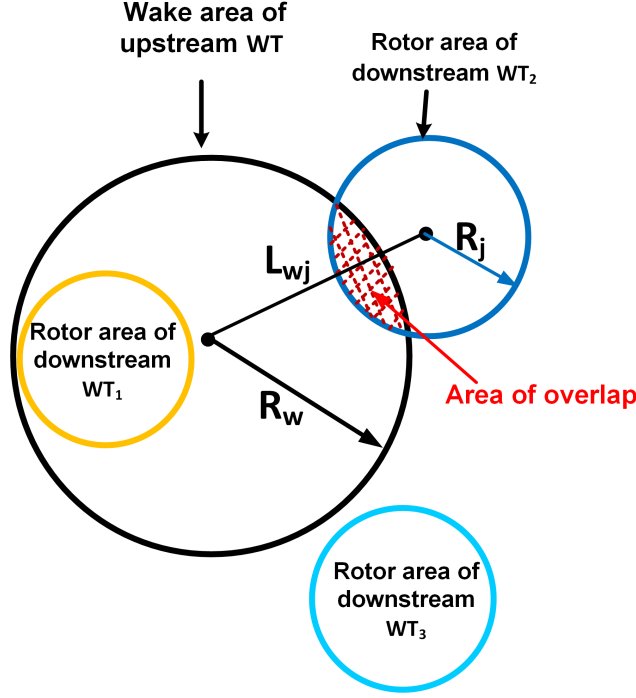
Figure 3.1: Wake effect: full wake (WT_1), partial wake (WT_2), and non-wake (WT_3)

per (3.1) is shown in Figure 3.2 by a black line. The velocity deficit in the wake $V_{d_{ij}}$ is given as,

$$V_{d_{ij}} = -\frac{V_\infty}{9} \frac{x_{ij}^{\frac{1}{3}}}{(b+b_0)} + [\frac{r^{\frac{3}{2}}}{\sqrt{3c_1^2 x_{ij}}} + 1.344 c_1^{\frac{-1}{5}}]^2 \tag{3.2}$$

where b is the distance between the WTs in downstream side $b = y * D$, value of the y is varies from 0 to 15, r is the rotor radius, and V_∞ is the undisturbed wind speed.

$$c_1 = \frac{4.3}{100} [\frac{D_{eff}}{2}]^{\frac{5}{2}} (C_T \frac{A_{ol}}{A_r} b_0)^{\frac{-5}{6}} \tag{3.3}$$

The value of b_0 depends on D, D_{eff}, and $r_{9.5}$. It is indicated in (3.4).

$$b_0 = \frac{9.5D}{(\frac{2r_{9.5}}{D_{eff}})^3 - 1} \tag{3.4}$$

28

Where D is wind turbine's rotor diameter. The effective rotor diameter D_{eff} is expressed as,

$$D_{eff} = D\sqrt{\frac{1 + \sqrt{1 - C_T}}{2\sqrt{1 - C_T}}} \qquad (3.5)$$

The value of $r_{9.5}$ is the wake radius at a distance of 9.5 times of the rotor diameter and it is given as,

$$r_{9.5} = 0.5[r_{nb} + min(H, r_{nb})] \qquad (3.6)$$

where H is the hub height and r_{nb} is described in (3.7). r_{nb} is function of the D and ambient turbulence intensity T_a.

$$r_{nb} = max(1.08D, (21.7T_a - 0.005)D) \qquad (3.7)$$

The wake formation behind the wind turbine for V_∞ of 10 m/s and T_a of 0.1 by using Larsen model is shown in Figure 3.2.
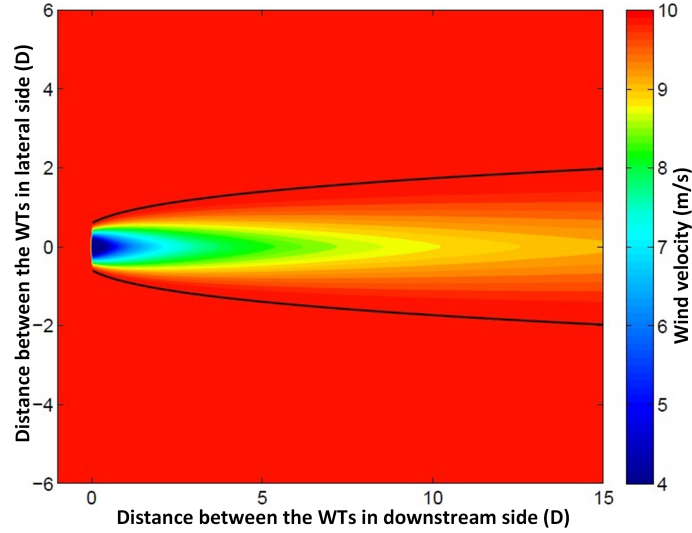
Figure 3.2: Larsen model wake formation (Renkema, 2007)

3.2.1.2 Jensen wake model

N.O.Jensen proposed the Jensen wake model which is a kinematic model (Renkema, 2007). It is a simple wake model in which the wake formation is linearly expanding. Figure 3.3 shows the Jensen wake formation diagram. The wake diameter D_w
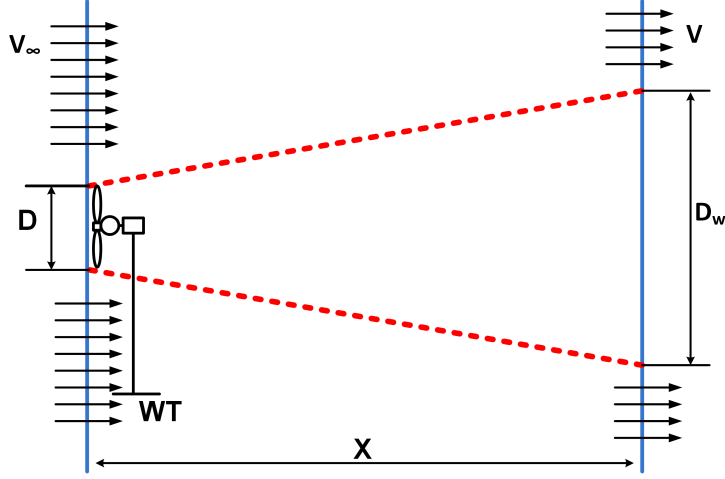
Figure 3.3: Jensen wake formation diagram

(Renkema, 2007) is shown in (3.8).

$$D_w = D(1 + 2kX) \tag{3.8}$$

Where k is the wake decay constant (k is 0.04 for offshore), and X is the relative distance behind the rotor. The velocity deficit $V_{d_{ij}}$ (Renkema, 2007) is given in (3.9).

$$V_{d_{ij}} = \left[\frac{(1 - \sqrt{1 - C_T})}{(1 + 2kX)^2)} \right] \left(\frac{A_{ol}}{A_r} \right) \tag{3.9}$$

In OSWF, the wind velocity experience by downstream wind turbines would be affected by upstream wind turbines. So, the downstream wind turbines will experience lesser wind velocity. The Katic et al. proposed a formulation to calculate the wake effect on downstream wind turbine. The total velocity deficit $V_d(j)$ at a jth location wind turbine is affected by a group of upstream wind turbines $G(j)$ is given by 3.10 (Samorani, 2013).

$$V_d(j) = \sqrt{\sum^{i \epsilon G(j)} V_{d_{ij}}^2} \tag{3.10}$$

The wind velocity at j^{th} WT V_j is shown in (3.11).

$$V_j = V_\infty(1 - V_d(j)) \tag{3.11}$$

30

In OSWF, wind turbine may experience the wind from various directions. The position of wind turbine nacelle will shift according to the direction of wind. So, the variations in wind velocity and it direction will affect the wind velocity deficit. Figure 3.4 explains the above context. The analytical equations of wake model considering the
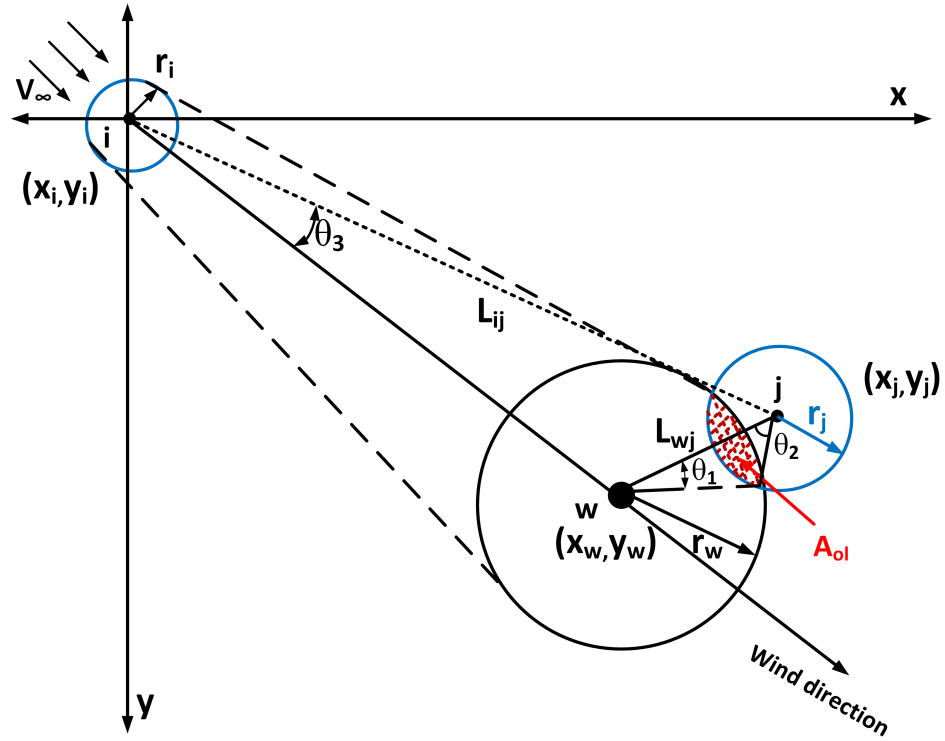
Figure 3.4: Wake model for different wind velocity and wind direction

above effect are given in (3.12)-(3.14) (Feng and Shen, 2015). i is the center of upstream wind turbine at point (x_i, y_i), j is the center of downstream wind turbine at point (x_j, y_j), w is the wake center of the upstream wind turbine at point (x_w, y_w).

$$L_{wj} = L_{ij} \sin \theta_3 \tag{3.12}$$

In (3.12), L_{wj} is the distance between wth and j^{th} points, L_{ij} is the distance between i^{th} and j^{th} points, and θ_3 is the wind deviation angle between $i - w$ and $i - j$. The chord angles θ_1 and θ_2 corresponding to w and j are shown in (3.13) and (3.14) respectively.

$$\theta_1 = arccos(\frac{r_w^2 + L_{wj}^2 - r_j^2}{2r_w L_{wj}}) \tag{3.13}$$

$$\theta_2 = arccos(\frac{r_j^2 + L_{wj}^2 - r_w^2}{2r_j L_{wj}}) \tag{3.14}$$

Where r_i, r_j, and r_w are the radius of upstream wind turbine, downstream wind turbine, and wake of upstream wind turbine, respectively. The area of overlap A_{ol} is expressed in (3.15).

$$A_{ol} = \begin{cases} \pi r_j^2 & d_{wj} \leq r_w - r_j \\ 2\theta_1 r_w^2 + 2\theta_2 r_j^2 - 2A_c & r_w - r_j \leq d_{wj} \leq r_w + r_j \\ 0 & d_{wj} \geq r_w + r_j \end{cases} \tag{3.15}$$

Where A_c and c are given in (3.16) and (3.17), respectively.

$$A_c = \sqrt{c(c - r_w)(c - L_{wj})(c - r_j)} \tag{3.16}$$

$$c = \frac{(r_w + L_{wj} + r_j)}{2} \tag{3.17}$$

The Jensen and Larsen wake models give the clear idea of the wake effect on downstream wind turbines due to upstream wind turbines. By using the wake models the placement of wind turbines and the spacing between the wind turbines in row/column wise are obtained. For these placement of wind turbines, cable routing between wind turbines and the substations has to be designed optimally taking into consideration of the following parameters. Those parameters are power production, cable power loss, annual energy yields, levelized production cost index, and inter-array cable cost. The mathematical expressions of the parameters mentioned earlier are explained in the following sections.

3.2.2 Power production

The power production of wind turbine P_i can be calculated (Hou et al., 2017a) as,

$$P_i = \begin{cases} 0 & 0 \leq V_i \leq V_{cut-in} \\ 0.5\rho C_p(\beta, \lambda)\pi r^2 V_i^3/10^6 & V_{cut-in} < V_i \leq V_{rated} \\ P_{rated} & V_{rated} < V_i \leq V_{cut-out} \\ 0 & V_{cut-out} < V_i \end{cases} \tag{3.18}$$

In (3.18), ρ is the air density (kg/m^3), C_p is the power coefficient, r is the radius of wind turbine rotor (m), P_{rated} is the rated power of wind turbine, β is the pitch angle (^{o}), and λ is the optimal tip speed ratio. V_i, V_{cut-in}, $V_{cut-out}$, and V_{rated} are the wind turbine, cut-in, cut-out, and rated wind speed (m/s), respectively. The total power production of OSWF P_T is a sum of the individual power production of wind turbines within OSWF and it can be expressed as shown in (3.19). It is proportional to V_i^3 where other parameters are constant.

$$P_T = \sum_{i=1}^{N_{wt}} P_i \tag{3.19}$$

$$P_T \propto \sum_{i=1}^{N_{wt}} V_i^3 \tag{3.20}$$

Where N_{wt} is the number of wind turbines in OSWF. The power production of a wind turbine is proportional to the cube root of the wind speed experienced by the wind turbine where the wind speed is between the cut-in and rated wind speeds.

3.2.3 Cable power losses

The power losses of AC cable $P_{L,i}$ can be described as shown in (3.21).

$$P_{L,i} = 3I_i^2 R_i \tag{3.21}$$

Where R_i is the resistance of cable (Ω/km) and I_i is the value of current flowing through the cable (A). As the number of wind turbines increases the length of the cable will increase and it results in higher power losses. The total power losses of AC cable P_{TL} should be expressed as shown in (3.22).

$$P_{TL} = \sum_{i=1}^{N_{wt}} P_{L,i} \tag{3.22}$$

3.2.4 Annual energy yields

The energy yields of the OSWF depend on total wind farm power production, cable power losses and time duration of power generation. Longer spacing between the wind turbines improves the energy yields due to higher wind velocity experienced by

the wind turbines. The annual energy yields E_A of OSWF can be formulated as (Hou et al., 2015b),

$$E_A = \sum_{i=1}^{365}(P_T - P_{TL})T_i \qquad (3.23)$$

Where T_i is the time duration when the wind turbine generates power in hours

3.2.5 Levelized production cost

Levelized production cost can be defined as the present value of price of the produced electrical energy which includes the capital investment, operating, and maintenance costs during the economic lifetime. The levelized production cost index C_{LP} is expressed (Hou et al., 2015b) in (3.24), which considers the capital cost C_{CA}, operation and maintenance cost C_{OM}, economic lifetime M, discount ratio r, and annual energy yields.

$$C_{LP} = \left[\frac{C\ r(1+r)^M}{(1+r)^M - 1} + C_{OM}\right]\frac{1}{E_A} \qquad (3.24)$$

Where C is given in (3.25).

$$C = \sum_{t=1}^{M}C_{CA}(1+r)^{-t} \qquad (3.25)$$

The capital cost C_{CA} is shown in (3.26).

$$C_{CA} = \sum_{i=1}^{N_{wt}}C_cL_cQ_c \qquad (3.26)$$

Where C_c, L_c, and Q_c are the cost, length, and quantity of the cable, respectively.

$$C_c = X_t + Y_t\ exp(\frac{Z_tS_n}{10^8})^2 \qquad (3.27)$$

In (3.27), X_t, Y_t, and Z_t are the coefficients of cost model of cable. S_n is the rated cable power as given in (3.28).

$$S_n = \sqrt{3}V_{ra}I_{ra} \qquad (3.28)$$

Where V_{ra} and I_{ra} are rated voltage and current of the cable, respectively.

The levelized production cost index of the wind farm is used as an objective function in the optimization of OSWF collector system design. It mainly depends on the cost of cable, length of the cable and annual energy yields. Levelized production cost index is directly proportional to cable length and inversely proportional to annual energy yields. Hence, optimal placement of wind turbines is the one that reduces the cable length, increase the annual energy yields and there by results in minimization of levelized production cost index.

3.2.6 Cable cost

The cost of total cable C_{ct} is the sum of the interconnecting inter-array cable cost as given in (3.29).

$$C_{ct} = \sum_{z=1}^{m} C(L_{k(z)}) = (\sum_{z=1}^{m} L_{k(z)})C_c \qquad (3.29)$$

Where $L_{k(z)} = (L_{k(1)}, L_{k(2)}, L_{k(3)}, ..., L_{k(m)})$ is the length of $'m'$ number of inter-array cables. Each inter-array cable can connect a set of wind turbines to the substation. The number of wind turbines N_c that can be interconnected through a cable depends on the cable current carrying capacity and rating of the wind turbine.

$$N_c = \frac{I_c}{I} \qquad (3.30)$$

In (3.30), I_c is the current carrying capacity of the cable and I is the value of current flow through the cable. The cable cost depends on the length of cable and number of the cables used.

Optimal design of OSWF involves firstly, suitable placement of wind turbine taking into consideration of the wake effect and then minimizing the levelized production cost index by optimally designing the cable connecting between the wind turbines to substation. For optimal solution of cable routing, different optimization techniques can be applied. In this work, two techniques ACO and FA for TSP and MTSP are applied. These techniques are explained in the following sections.

3.3 Ant Colony Optimization

Ant colony optimization is a biological motivation of ants to locate the shortest path between their nest and food. ACO is proposed by Marco Dorigo in 1992 and it is a population-based search technique. In the process of searching for food, ants release a chemical (pheromone) in their path, on the ground. Ants choose multiple random paths from their nest and in the process, decide the shortest path based on the strength of pheromones. The strength of pheromone decays fast with time; hence lesser the length of the path, the more is the resilience of the pheromone in a particular path. Optimal path is decided by the probability of optimal strength of the pheromone and the remaining ants will follow the path blindly. The advantages of the ACO are strong searching ability, can give rapid discovery of good solutions, can adapt to changes such as new distances, and guarantee convergence.

The mathematical explanation of ACO is described as follows (Dorigo and Thomas, 2004): At the starting of the food search process, the strength of pheromone $\tau_{ij}(0)$ is equal to 1.

$$\tau_{ij}(0) = 1, \forall (i, j) \in O \tag{3.31}$$

Where O is the set of travel points of ant. The probability rule to choose the next point j of ant k is given in (3.32).

$$p_{ij}{}^k = \frac{[\tau_{ij}]^\alpha}{\sum_{l \in N_i^k} [\tau_{ij}]^\alpha} \tag{3.32}$$

Where $\sum_{l \in N_i^k}$ is the neighborhood of ant k when in point i and α is the pheromone trail constant. The pheromone value is updated using the equation (3.33).

$$\tau_{ij} = (1 - \rho)\tau_{ij} + \Delta \tau^k \tag{3.33}$$

Where $\Delta \tau^k$ is the updated pheromone value of kth ant and it is specified in (3.34). It is function of the length of path L_k of ant k.

$$\Delta \tau^k = \frac{1}{L_k} \tag{3.34}$$

3.3.1 Multiple Travelling Salesmen Problem

In multiple travelling salesmen problem, a number of cities n are allotted to a number of salesmen m. The main aim of the method is that multiple salesmen have to travel to the specified cities. First, the salesmen start the tour from any one of the cities and travel to a set of other cities without arriving at the starting point in between. The conditions are (a) each salesman has to take a different route, (b) they have to touch every specified city without fail, (c) if a salesman has covered a particular city, then other salesmen should not travel to that city, and (d) In each route, salesmen have to move through a city only once during their tour (Dorigo and Thomas, 2004). In case of TSP, the number of salesmen m is 1.

3.3.2 Elitist ACO for MTSP

In combined elitist ACO and MTSP, the ants act as salesmen. Every ant randomly chooses the city and makes the individual tour from a first city. Depending on the probability rule, ants will select the next city to go to. Probability rule is a function of the distance between the cities and strength of pheromone on the route that connects the cities. The elitist strategy for ACO for MTSP is explained as follows:
An initial value of pheromone is constant and it is $\tau_{ij}(0) = 1$.
Visibility η_{ij} is routing the desirable nearest city and it is stated in (3.35).

$$\eta_{ij} = \frac{1}{d_{ij}} \tag{3.35}$$

Where d_{ij} is the distance between the city i to j; and (x_i, y_i) and (x_j, y_j) are the location of the city i and j respectively.

$$d_{ij} = \sqrt{(x_i - x_j)^2 + (y_i - y_j)^2} \tag{3.36}$$

Probability rule (Maniezzo, 1992) is given as below,

$$p_{ij} = \frac{[\tau_{ij}]^\alpha [\eta_{ij}]^\beta}{\sum_{x \in allowed} [\tau_{ij}]^\alpha [\eta_{ij}]^\beta} \tag{3.37}$$

Where p_{ij} is the probability value to select the next city, α is the pheromone trail constant, β is the guide investigation constant, and τ_{ij} is the pheromone strength of

path between the cities i to j. In (3.37), $\sum_{x \in allowed}$ is the sum of untouched cities in a tour. Update the pheromone trails using (3.38).

$$\tau_{ij} = (1 - \rho)\tau_{ij} + \sum_{k=1}^{m} \Delta\tau_{ij}^{k} + e.\Delta\tau_{ij}^{bs} \tag{3.38}$$

Where ρ is evaporation rate of pheromone (0 to 1), e is the weight parameter of the best-so-for tour, and m is the number of ants. The updated pheromone value of kth ant $\Delta\tau_{ij}^{k}$ and the pheromone value of the best-so-far $\Delta\tau_{ij}^{bs}$ are given in (3.39) and (3.40), respectively.

$$\Delta\tau_{ij}^{k} = \begin{cases} \frac{Q}{L_k} & if \ k^{th} \ ant \ tour \ in \ (i,j) \\ 0 & otherwise \end{cases} \tag{3.39}$$

$$\Delta\tau_{ij}^{bs} = \begin{cases} \frac{Q}{L_{bs}} & if \ k^{th} \ ant \ tour \ best-so-far \ in \ (i,j) \\ 0 & otherwise \end{cases} \tag{3.40}$$

Where L_{bs} is the length of tour best-so-far, L_k is the tour length of kth ant, L_0 is the initial tour length, and Q is the amount of raised pheromone coefficient.

3.3.3 Elitist ACO for MTSP realization

In ACO-MTSP approach, the optimal distance travelled by ants or salesman is the optimal length of the cable and it starts from the initial wind turbine. The travel covers the group of wind turbines and finds a route to the offshore substation. The elitist ACO for MTSP algorithm is explained by a flowchart as shown in Figure 3.5. The process of elitist ACO for MTSP is enlightened by the following steps:

(a) Initialize the basic parameters: it includes $\alpha, \beta, n, m, L_0, \tau_{ij}(0)$, and Q. The total number of cities represented in MTSP is equal to a sum of the number of wind turbines N_{wt} and number of offshore substations N_{ss}. The number of salesmen is equal to the number of inter-array cables required in a wind farm and the number of inter-array cables is decided based on the rating of wind turbine and current carrying capacity of the cable.

(b) The number of wind turbines and substation covered by each cable is equal to the $N = (N_{wt}/N_c) + N_{ss}$. Select the random wind turbines for salesman to start the tour.

(c) Initialize the location points of wind turbines (A_{wt} and B_{wt}) based on wake models and calculate the distance matrix d_{ij} of wind turbines using the equation (3.36).

(d) Calculate the visibility matrix η_{ij} of the wind turbines from the distance matrix d_{ij} of wind turbines using the equation (3.35).

(e) Create a random tour matrix T of the wind turbines using the function $randperm(N)$. Then, first tour is selected for travel from tour matrix.

(f) The probability rule equation (3.37) decides for the cable routing between the ith wind turbine to next wind turbine on a tour.

(g) After the completion of the tour, calculate the length of each tour that corresponds to the length of cable.

(h) Update the cable route parameter by equation (3.38).

(i) Check whether the number of the specified tours are completed or not. If not select the next random tour in tour matrix and repeat the steps (e) to (h).

(j) Find the minimum length of the tour L_k from the length matrix.

(k) Calculate the error value $err = L_o - L_k$. If $err > 0.001$ then go to step (d).

(l) Check the condition $err < 0.001$, then finalize the optimum tour and length of the tour.

The ACO-MTSP optimization approach is adopted to get an optimal design of the electrical collector system of OSWF.

3.4   Firefly Algorithm

Firefly algorithm is a nature-inspired metaheuristic algorithm developed from the natural behavior of fireflies. Firefly algorithm is proposed by Xin-She Yang in 2007 (Yang and Press, 2010). The flashing light generation process of firefly is called bioluminescence. It helps the fireflies to communicate with other fireflies, helps to attract copulate partners and also to provide an alert signal to warn the opponent. The advantages of Firefly algorithm are an excellent convergence rate, strong searching

Start

Initialize of number of WTs, substations, α, β, n, m, $\tau_{ij}(0)$, Lo, Q, A_{wt} and B_{wt}

Selection of random WTs

Find the d_{ij} and η_{ij}

Initialization of random tours T

Select random tour from T

Start tour from random WT i

Select next random tour

Find the p_{ij}

Update the temporary tours

Select next WT by probability rule

Tour completes

No

Yes

Calculate the L_k, $\Delta\tau_{ij}^{k}$ & $\Delta\tau_{ij}^{bs}$

Update pheromone trails

No of tours in T is complete

No

Yes

err > 0.001

No

Yes

Finalize best tour

Stop

Figure 3.5: Flow chart of elitist ACO-MTSP algorithm

ability, improvement of solution precision, and avoidance of the local optima (Zhang et al., 2016). The rules of Firefly algorithm are given below:

1. All fireflies are considered as unisex to avoid the attraction between the anti-sex fireflies.

2. The flash brightness of fireflies usually declines as distance increases. In the case of two fireflies, the firefly which emanates lesser brightness will travel in the direction of the more brightly glowing firefly. In the absence of a brighter one, it will travel randomly.

The formulation of Firefly algorithm is described as follows (Yang and Press, 2010): The brightness or light intensity $I(d)$ at the disatance d is the function of the brightness at the source I_s and distance d between the fireflies in (3.41).

$$I(d) = \frac{I_s}{d^2} \tag{3.41}$$

The d_{ij} is the distance between the firefly i and j : where (x_i, y_i) and (x_j, y_j) are the location of the firefly i and j respectively.

$$d_{ij} = \sqrt{(x_i - x_j)^2 + (y_i - y_j)^2} \tag{3.42}$$

For fixed light absorption coefficient l and the initial light intensity I_0, intensity of light $I(d)$ is given by

$$I(d) = I_0 e^{-l \ d^2} \tag{3.43}$$

Firefly's attractiveness a is proportional to the light intensity seen by adjacent fireflies, hence firefly's attractiveness can be defined as given in (3.44).

$$a = a_0 e^{-l \ d^2} \tag{3.44}$$

In (3.44), a_0 is the value of attractiveness at $d = 0$. Relative attractiveness can be expressed in terms of the a_0, l, d, and given in equation (3.45).

$$a = \frac{a_0}{1 + l \ d^2} \tag{3.45}$$

The fixed distance d_f is formed from equation (3.45).

$$d_f = \frac{1}{\sqrt{l}} \tag{3.46}$$

When $d = d_f$, the a is $a_0 e^{-1}$ for (3.44) or $a_0/2$ for (3.45). The revised location of firefly i is attracted to other brighter fireflies j as specified in (3.47).

$$x_i{}^* = x_i + a_0 e^{-l d_{ij}{}^2}(x_j - x_i) + \alpha_r \epsilon_i \tag{3.47}$$

In (3.47), the randomization parameter α_r is in the bounds of [0,1] and $\epsilon_i = rand - 1/2$, where $rand$ is a random number produced uniformly spread between the 0 and 1. For regular case, $a_0 = 1$. If $a_0 = 0$, it becomes a simple random move.

3.4.1 FA-MTSP realization

In FA-MTSP approach, the optimal distance travelled by firefly or salesman is the optimal length of the cable and it starts from the initial wind turbine. The travel covers the group of wind turbines and finds a route to the offshore substation. The FA-MTSP algorithm is explained by a flowchart as shown in Figure 3.6. The following steps explain the process of FA-MTSP:

(a) Initialize the basic parameters: it includes α_r, l, n, L_0, and a_0. The total number of cities represented in MTSP is equal to a sum of the number of wind turbines and number of offshore substations. The number of salesmen is equal to the number of inter-array cables required in a wind farm and the number of inter-array cables is decided based on the rating of wind turbine and current carrying capacity of cable.

(b) The number of wind turbines and substation covered by each cable is equal to the $N = (N_{wt}/N_c) + N_{ss}$.

(c) Initialize the location points of wind turbines (A_{wt} and B_{wt}) based on wake models and calculate the distance matrix $[d_{ij}]$ of wind turbines using the equation (3.42).

(d) Calculate matrix I from distance matrix d_{ij} of wind turbines as given in equation (3.41).

(e) Create a random tour matrix T of the wind turbines using the function $randperm(N)$. Then, first tour is selected from tour matrix for travel.

(f) Calculate the matrix $[a]$ using the equation (3.44) and check the ith wind turbine attractiveness a_i is greater than the jth wind turbine attractiveness a_j. Check the $a_i > a_j$, then travel from ith wind turbine to random wind turbine.

(g) Check the $a_i < a_j$, then travel from i^{th} wind turbine to j^{th} wind turbine. Update the position by equation (3.47).

(h) Complete the tour and calculate the optimal tour length L_k.

(i) Check the number of tours in tour matrix is completed or not. Calculate the error value $err = |L_o - L_k|$. If condition satisfies, then go to step (j). Else select the next random tour and repeat the step (e) to (h).

(j) Check the $err < 0.001$, then update the optimal L_k as L_o and repeat the step (d) to (h).

(k) Check the $err > 0.001$, then finalize the optimum tour and length of the tour.

The FA-MTSP optimization approach is implemented to get an optimal design of the electrical collector system of OSWF.

3.5   Genetic Algorithm

The genetic algorithm was developed by John Holland in 1975. genetic algorithm is an optimization and search technique based on the principles of genetics and natural selection. genetic algorithm allows a population composed of many individuals to evolve under specified selection rules to a state that maximizes the fitness. The various stages of the genetic algorithm approach are given as follows (Haupt and Haupt, 2004): define the objective function; selecting the variables and GA parameters; variable encoding and decoding; initial population; natural selection; pairing; mating; mutations; next generation; and convergence. The following steps explain the process of basic genetic algorithm:

(a) In genetic algorithm, a population of $2n$ to $4n$ trail solutions is used. Where n is the number of variables.
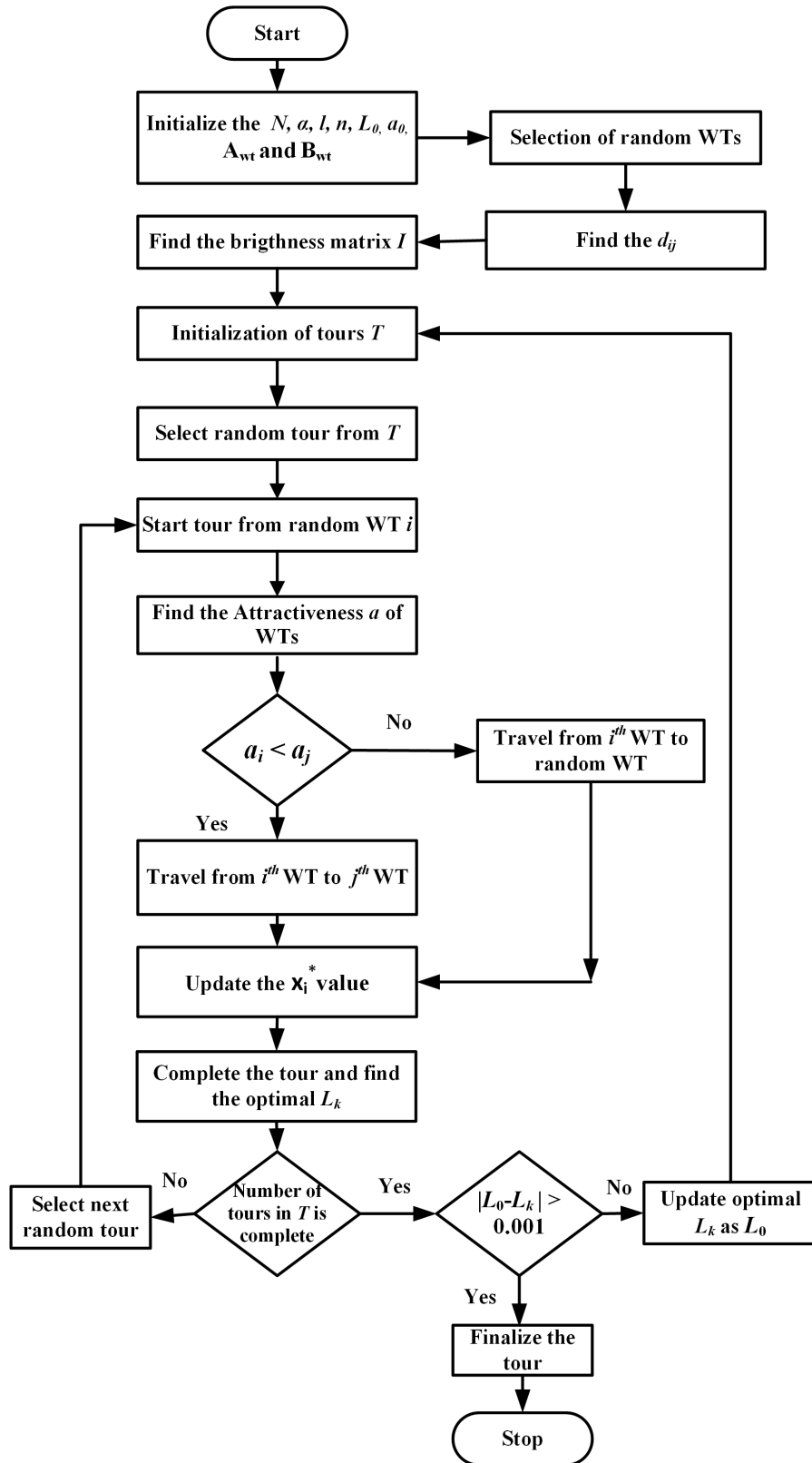
Figure 3.6: FA-MTSP approach flowchart

44

(b) Each solution is represented by a string of binary variables, related to the chromosomes in genetics.

(c) The string length can be made sufficient to accomplish any desired fitness of approximation and hence any desired accuracy can be achieved.

(d) The numerical value of the objective function corresponds to the concept of fitness in genetics

(e) After trail solution are selected, a new generation is produced by selecting, using stochastic rules, and the fittest parents produce children from among the trial solutions.

(f) New strings are created by crossover or exchanging the information among the strings of the mating pool.

(g) Some random alternation of binary digits in a string reproduces the effects of mutations.

(h) After getting the better solution, then again exchanges the bits and produce results. In some cases, the better solution or better chromosome may loose the quality. To overcome disadvantage, elitist strategy is used.

(i) In elitist strategy, better solution left untouched and remaining $n-1$ goes to the next generation. For remaining $n - 1$, permutation, combinations, mutations and crossover will be done.

(j) The better solution of present stage will be compared to the better solutions of the next stages and finalize the best solution.

3.5.1 GA-MTSP realization

In GA-MTSP approach, the optimal distance travelled by salesman is the optimal length of the cable and it starts from the initial wind turbine. The travel covers the group of wind turbines and finds a route to the offshore substation. The following steps explain the process of GA-MTSP:

(a) Initialize the basic parameters: it includes size of population p, number of generation g, and size of children population p_c. The total number of cities

represented in MTSP is equal to a sum of the number of wind turbines N_{wt} and number of offshore substations N_{ss}. The number of salesmen is equal to the number of inter-array cables required in a wind farm and the number of inter-array cables is decided based on the rating of wind turbine and current carrying capacity of cable.

(b) The number of wind turbines and substation covered by each cable is equal to the $N = (N_{wt}/N_c) + N_{ss}$.

(c) Initialize the population matrix P_m using the function $randperm(N)$.

(d) Initialize the location points of wind turbines (A_{wt} and B_{wt}) based on wake models and calculate the distance matrix d of wind turbines using the equation (3.42).

(e) Calculate the fitness for parents by the $\sum_{j=1}^{p}[P_m(j, N+1) = d(P_m(j, N), P_m(j, 1)) + \sum_{i=1}^{N-1} d(P_m(j, 1), P_m(j, i+1))]$. Update the $[P_m]$ by the function $sortrows$. The fittest parents produce children from among the trial solutions.

(f) New strings are created by crossover or exchanging the information among the strings of the mating pool.

(g) Calculate the fitness for parents and children by the $\sum_{j=1}^{p+p_c}[P_m(j, N+1) = d(P_m(j, N), P_m(j, 1)) + \sum_{i=1}^{N-1} d(P_m(j, 1), P_m(j, i+1))]$. Update the P_m by the function $sortrows$.

(h) Finalize the optimum tour and length of the tour from the bunch of best P_m.

3.6 Problem formulation

The problem formulation aims to optimize the collector system design of Offshore wind farm in terms of production cost. It includes minimizing the length of inter-array cable, minimizing the Levelized production cost index, maximizing the power production, and reducing the wake loss. It can be achieved by placing the wind turbines in the optimum position and this position is obtained from the wake models explained in section 3.2.1. The optimal placement of wind turbines can reduce the wake loss. Hence, it improves the power production and annual energy yields. In

order to minimize the Levelized production cost index, the length of connecting cable has to be minimized. In (3.24), the Levelized production cost index depends on the length of inter-array cable and the energy yield with other parameters remaining the same. Energy yield in turn is dependent on the placement of wind turbines in OSWF.

The objective function is stated below for minimize the Levelized production cost index.

$$min\left\{C_{LP}(x,y)\right\} = min\left\{\left[\frac{C(x,y)r(1+r)^M}{(1+r)^M - 1} + C_{OM}\right]\frac{1}{E_A(x,y)}\right\} \tag{3.48}$$

Subject to,

$$4D \leq x \leq 10D; 4D \leq y \leq 10D \tag{3.49}$$

Where x and y are the spacing between the wind turbines, column wise and row wise respectively. The cable length minimization reduces the cable losses and results in reduced cable cost. By placing the wind turbine optimally, the power production is improved.

The assumptions for optimization are: a) all wind turbines have the same rating, (b) yaw-misalignment influences the power production which is neglected (when wind direction varies, the nacelle will adjust its position), but yaw speed cannot follow the speed of the wind variation in a particular direction. This is called yaw-misalignment (Choi and Shan, 2013).), (c) the values of x and y should be greater than or equal to 4D. (If the spacing between wind turbines is less than 4D, the turbulence effect reduces the lifetime of wind turbine (Pérez et al., 2013).), (d) Every time, wind turbines in the OSWF work under MPPT control strategy, and (e) The wind turbines and substation are considered to be placed at a fixed position for simplifying the problem.

3.7   Case Study and Results

In this section, North Hoyle OSWF (NH OSWF) and Horns Rev OSWF (HR OSWF) are taken as reference for the case study. The optimal collector design for NH and HR OSWFs are done by using elitist ACO-TSP, ACO-MTSP, FA-TSP, and FA-MTSP and wake loss is addressed using larsen and jensen models. The wake effect calculations are discussed in subsections. The North Hoyle OSWF is located at Prestatyn in the

47

Irish Sea, United Kingdom. It consists of 30 wind turbines in 6 rows and each row has 5 wind turbines and its area is 10 km^2. The distance between the wind turbines in a row is 800 m whereas in a column is 350 m. The rated power of each wind turbine is 2 MW and a rotor diameter D is 80 m. The transmission type is MVAC/HVAC with an operating voltage level of 33 kV /132 kV. The inter-array cables interconnect the wind turbines by two radial cables with 15 wind turbines. The inter-array cable is 33 kV XLPE type AC submarine cable with a cross-section of 185 mm^2 and the total length of cable is 18 km. Two export cables are used to interconnect the collector hub and substation. It has a length of 10.781 km/13.176 km and each cable has 33 kV XLPE type with cross-sectional area of 630 mm^2. The Horns Rev OSWF is located at Blavandshuk in the North Sea, Denmark. The specifications of OSWFs are given in Table 3.1 (Hoyle, 2004) and (Rev, 2002). The parameters of AC inter-array submarine cable are provided in Table 3.2 (Wei et al., 2017).

Table 3.1: Specifications of OSWFs

Parameters	North Hoyle OSWF	Horns Rev OSWF
Total capacity	60 MW	160 MW
Number of wind turbines	30	80
Annual estimated production	197.4 GWh/year	600 GWh/year
Number of Rows/wind turbines	6/5 wind turbines	8/10 wind turbines
Distance between wind turbines in Rows / Columns	$10D$ / $4.375D$	$7D$ / $7D$
Inter-array cable length	18 km	63 km
Cut-in wind speed	3 m/s	4 m/s
Rated wind speed	13 m/s	13 m/s
Cut-out wind speed	25 m/s	25 m/s
Average wind speed	8.7 m/s	9.7 m/s

Table 3.2: AC submarine cable parameters

Cross-sectional area (mm^2)	Conductor resistance (Ω/ km)	Cable capacitance (μF/km)	Current carrying capacity (A)	Cable cost (k\$/km)
70	0.3420	0.1263	215	169.23
120	0.1966	0.1460	300	207.69
185	0.1271	0.1665	375	258.46
240	0.0971	0.1805	430	272.31

3.7.1 Computation of wake effect

The wind sharing at wind turbines on account of the wake effect is calculated based on Jensen wake model for North Hoyle and Horns Rev OSWFs are shown in Figures 3.7 and Fig 3.8, respectively. It is assumed that the primary column upstream wind turbines experience constant wind speed (1 pu). The wind experienced by subsequent wind turbines is registered with taking into effect of the wake. The separation between wind turbines in the row is 10 times of the D and 7 times of the D for North Hoyle and Horns Rev OSWFs, respectively. The wake loss value in reference OSWFs is calculated by using equation (3.10). It is found that, the value of wake loss for (a) North Hoyle OSWF is 6.35% at the $10D$ spacing between wind turbines and (b) Horns Rev OSWF is 12.04% at the $7D$ spacing between wind turbines. The wind rose of North Hoyle (npower Renewables Limited, 2007) and Horns Rev OSWFs (Hansen et al., 2012) are shown in Figures 3.9 and 3.10, respectively.
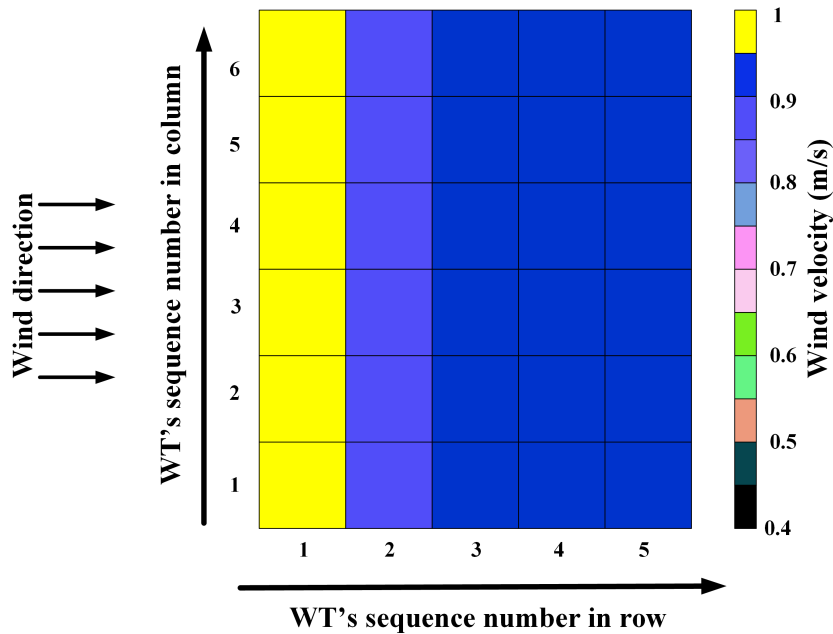
Figure 3.7: Wind speed sharing in North Hoyle OSWF at $10D$
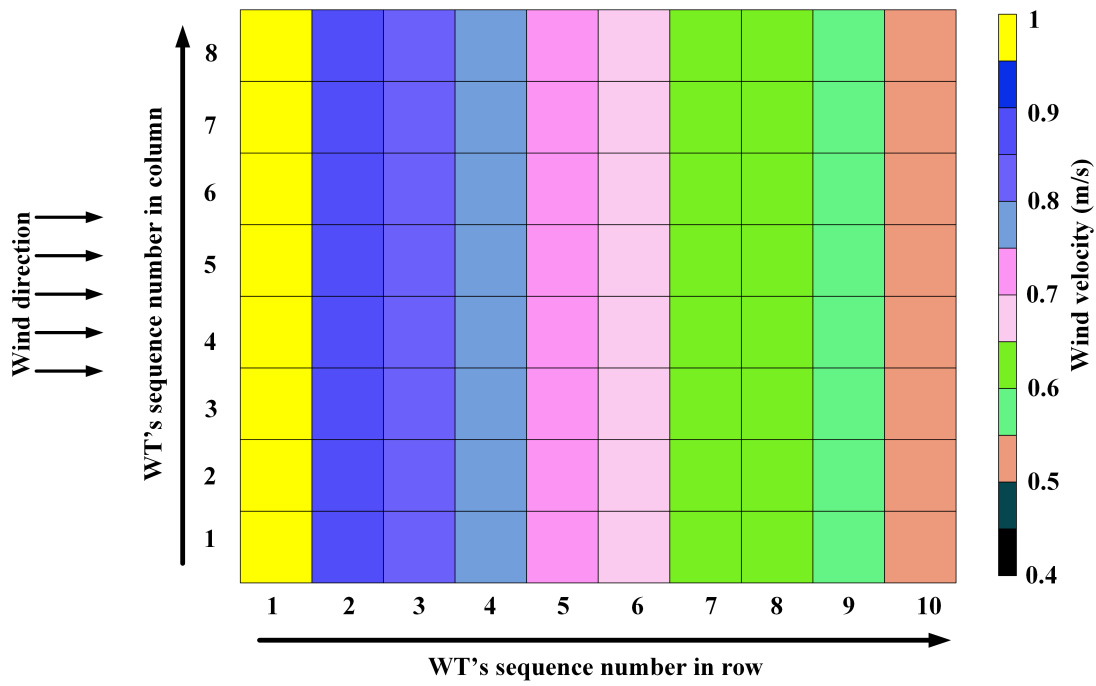
Figure 3.8: Wind speed sharing in Horns Rev OSWF at $7D$
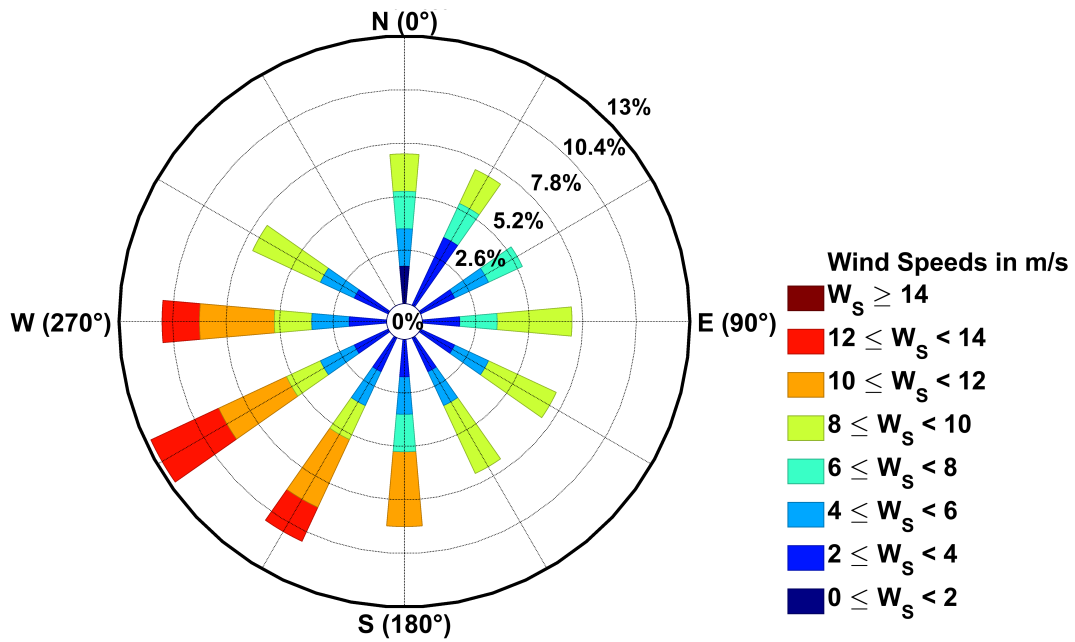
Figure 3.9: Wind rose of the North Hoyle OSWF

Figure 3.10: Wind rose of the Horns Rev OSWF

3.7.2 Case1: Without consideration of wake effect

In this case, the wake effect is not taken into consideration and minimum length of inter-array cable is found for the two reference wind farms. Figures 3.11 and 3.12 show the design of OSWF without wake effect for North Hoyle and Horns Rev OSWFs respectively based on ACO with MTSP approach.

Table 3.3: Result summary of North Hoyle and Horns Rev OSWF designs with out consideration of wake effect

OSWF	Type of collector system	Inter-array cable length (km)
Reference North Hoyle	Radial	18.000
NH based on ACO-MTSP with out consideration of wake effect	Radial	10.765
Reference Horns Rev	Radial	63.000
HR based on ACO-MTSP with out consideration of wake effect	Radial	35.706

Table 3.3 gives summary of results obtained in terms of inter-array cable length for NH and HR OSWF designs with out considering the wake effect. From the Table 3.3, it is observed that (a) for a radial collector system with ACO-MTSP the inter-array

Figure 3.11: Design of North Hoyle OSWF without consideration of wake effect
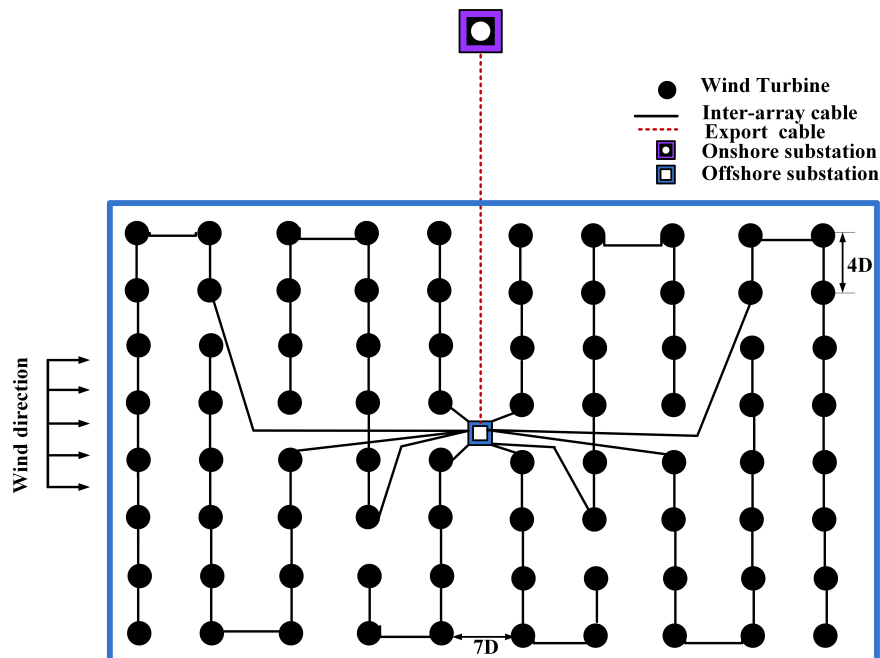
Figure 3.12: Design of Horns Rev OSWF without consideration of wake effect

cable length is 59.81% of reference NH OSWF and (b) for a radial collector system with ACO-MTSP the inter-array cable length is 56.68% of reference HR OSWF.

3.7.3 Case2: Optimized electrical collector system design of OSWF with consideration of wake effect

In this case, the wake effect is considered for the optimal model of OSWFs. The ACO-TSP, ACO-MTSP, FA-TSP, and FA-MTSP approaches are applied to achieve the optimal designs of North Hoyle OSWF and Horns Rev OSWF. The optimal design aims to minimize the inter-array cable length and wake loss. The distance between the wind turbines in row/column is taken as $7D/4D$ as evaluated from wake models. Larsen and Jensen wake model references are considered to design optimal OSWFs based on ACO-TSP, FA-TSP, ACO-MTSP and FA-MTSP approaches.

3.7.3.1 Optimal design for North Hoyle OSWF using ACO-TSP and FA-TSP

Optimal design for North Hoyle OSWF based on the (a) ACO-TSP for radial and ring collector systems are shown in Figures 3.13 and 3.14, respectively and (b) FA-TSP for radial and ring collector systems are shown in Figures 3.13 and 3.15, respectively. The distance between the wind turbines is calculated based on the Jensen wake model to get the optimal design for North Hoyle OSWF with ACO-TSP and FA-TSP methods. Table 3.4 gives summary of results obtained in terms of inter-array cable length, approximate power production and average wind velocity for (a) optimal design of NH OSWF for radial collector system based on ACO-TSP and FA-TSP, (b) optimal design of NH OSWF for ring collector system based on ACO-TSP and FA-TSP, and the results are compared with the reference wind farm of North Hoyle.

From Table 3.4, it is observed that for a ring collector system, FA-TSP results in a lower length of inter-array cable compared to the ACO-TSP. From the wake model adopted, wind velocity experienced by the wind turbine increases from 0.937 pu to 0.976 pu and accordingly the approximate power production increases from 49.280 MW to 55.714 MW.
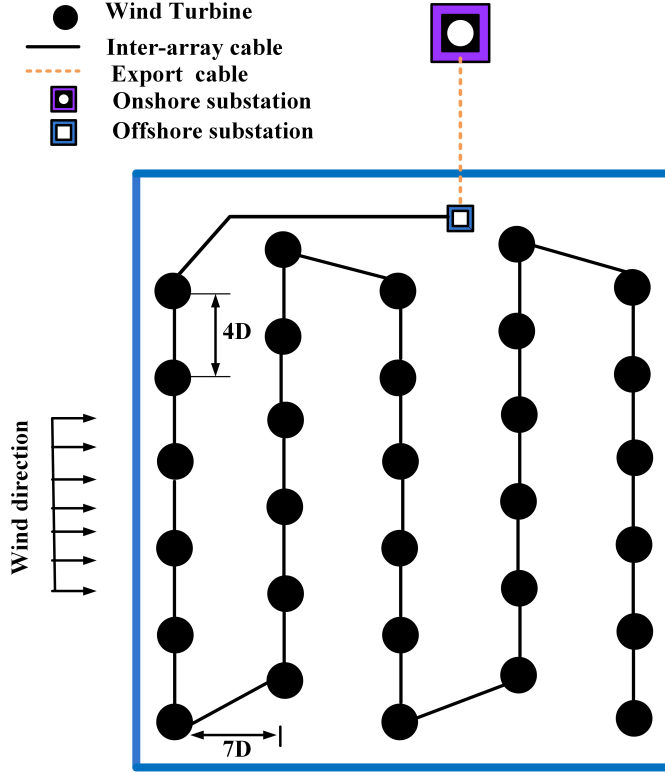
Figure 3.13: ACO-TSP and FA-TSP based optimal design of North Hoyle OSWF for radial collector system

Table 3.4: Result summary of North Hoyle OSWF designs based on ACO-TSP and FA-TSP with Jensen model

OSWF	Type of collector system	Inter-array cable length (km)	$V_{avg}(pu)$	$P_{apr}(MW)$
Reference North Hoyle	Radial	18.000	0.937	49.280
Optimal design for NH based on ACO-TSP	Radial	10.330		
Optimal design for NH based on FA-TSP	Radial	10.330	0.976	55.714
Optimal design for NH based on ACO-TSP	Ring	12.249		
Optimal design for NH based on FA-TSP	Ring	12.010		
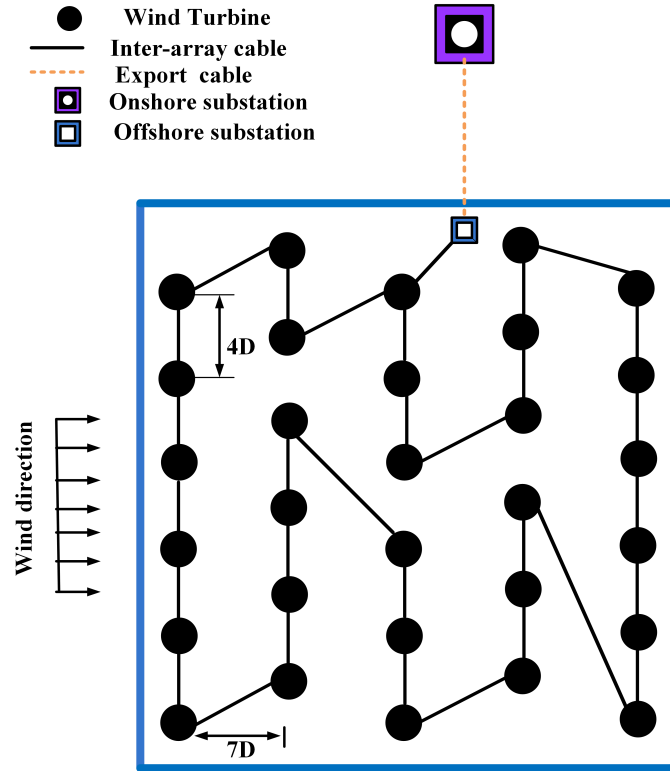
Figure 3.14: ACO-TSP based optimal design of North Hoyle OSWF for ring collector system

3.7.3.2 Optimal design for North Hoyle OSWF using ACO-MTSP and FA-MTSP

Optimal designs for North Hoyle OSWF based on the ACO-MTSP and FA-MTSP with Larsen and Jensen wake models are shown in Figures 3.16 and 3.17, respectively. The power production value depends on the availability of wind velocity in OSWF. If the amount of wake loss is low, the wind turbines can experience more wind and it leads to generation of more power in OSWF. As seen in Figure 3.18, the wake formation in optimal design of NH OSWF for radial collector system is illustrated with different colour lines. The upstream wind turbines wake is shown in red lines, indicating that the wind turbines experience full wind speed (1pu). The downstream wind turbines wake effect are shown in black and blue lines, indicating they experience different wind speeds. Table 3.5 gives summary of results obtained in terms of inter-array cable length, cable cost, V_{avg}, P_{apr}, E_A, and C_{LP} values for optimal design of
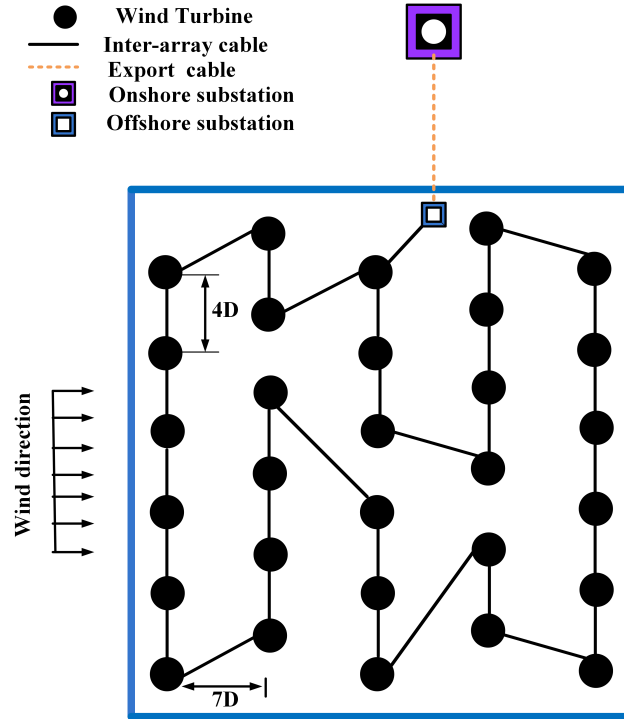
Figure 3.15: FA-TSP based optimal design of North Hoyle OSWF for ring collector system

North Hoyle OSWF for radial collector system based on ACO-MTSP, FA-MTSP, and GA-MTSP.

Table 3.5: Result summary of North Hoyle OSWF optimal designs

OSWF	Cable length (km)	Cable cost (k$)	Levelized production cost index ($/MWh)	Average wind velocity (pu)	Approximate power production (MW)	Annual energy yields (GWh)	Area (km^2)
Reference North Hoyle	18.000	4652.300	109.69	0.937	49.280	254.720	5.600
Optimal design for NH based on ACO-MTSP	10.895	2815.900	96.91	0.976	55.714	288.300	3.942
Optimal design for NH based on FA-MTSP	10.895	2815.900					
Optimal design for NH based on GA-MTSP	11.877	3069.700					
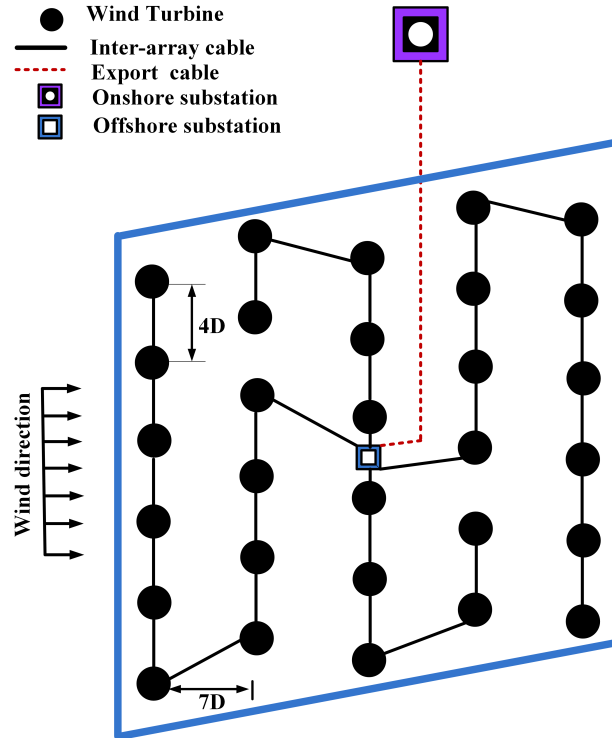
Figure 3.16: ACO-MTSP and FA-MTSP based optimal design for North Hoyle OSWF with Larsen wake model

From the Table 3.5, it can be observed that (a) the inter-array cable length is 60.53% with ACO-MTSP and FA-MTSP for a radial collector system compared to reference NH OSWF and (b) the inter-array cable length is 65.98% with GA-MTSP for a radial collector system compared to reference NH OSWF. Hence, the ACO and FA-based optimal models are better than the GA-based models with regard to the length of the inter-array cable. The Levelized production cost index of optimal design of NH OSWF for radial collector system is reduced by 11.65%. The annual energy yield is improved by 13.18%. The average wind velocity value of the optimal design of NH OSWF for radial collector system is improved by 4.16%. The wake loss value of NH OSWF is reduced by 2.40% using the Jensen wake model. The proposed approaches used in the design of the optimal OSWFs, improves the approximate power production of optimal design of NH OSWF for radial collector system by 13.06% and saves 29.61% area occupation compared to reference NH. Hence, it results in lesser installation cost.

Comparing results from Table 3.4 and 3.5, it observed that FA-TSP and ACO-TSP
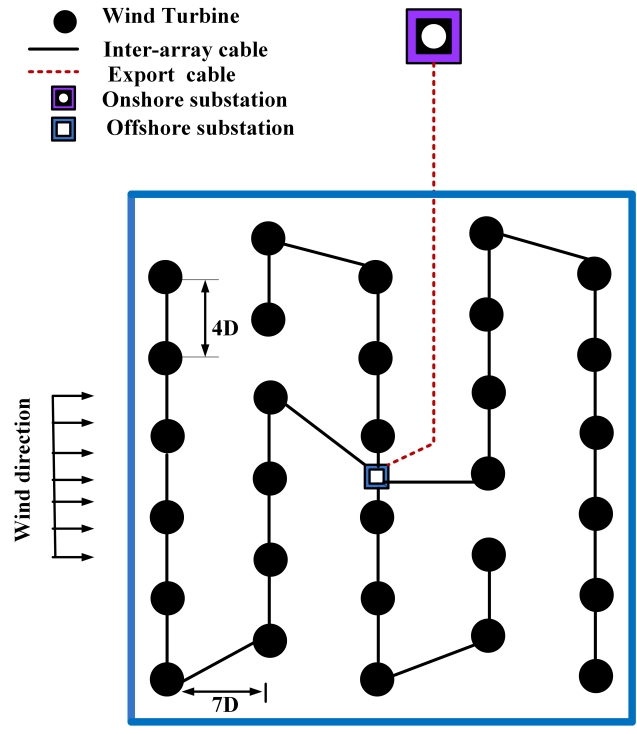
Figure 3.17: ACO-MTSP and FA-MTSP based optimal design for North Hoyle OSWF with Jensen wake model
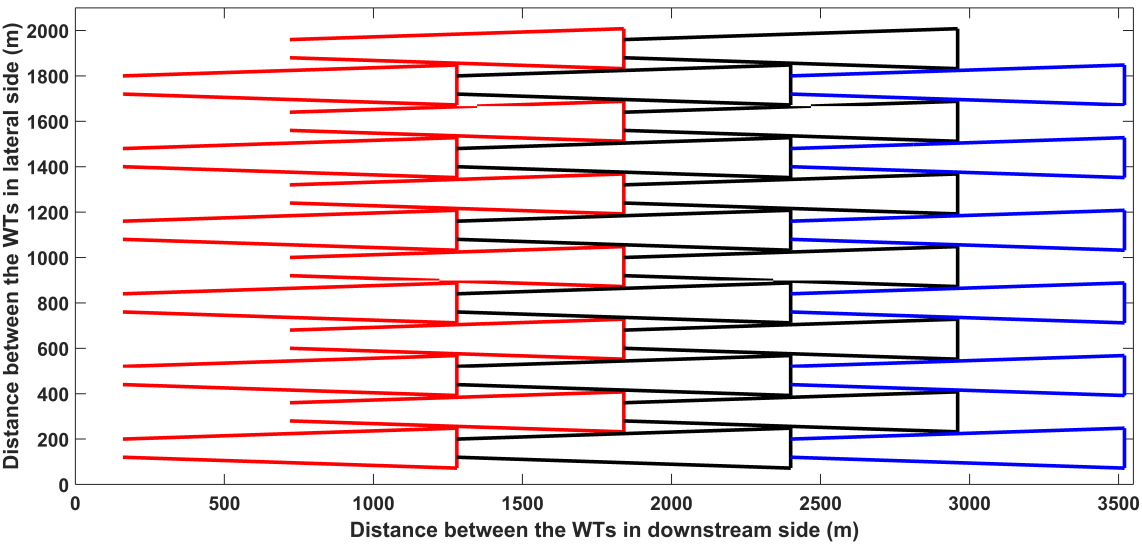
Figure 3.18: Wake formation in optimal design for North Hoyle OSWF

give lower values for inter-array cable length than the ACO-MTSP and FA-MTSP. But TSP based design needs the single inter-array cable with higher cross-section area to interconnect the wind turbines and it results in more power losses in cable. Additionally, the cost of cable will be higher. In case MTSP based design, multiple inter-array cables are used with lower cross-section area. The power connection reliability of MTSP based design is higher compared to TSP based designs. The number of wind turbines N_c that can be connected to the inter-array cable is calculated based on the current carrying capacity of the cable and rating of a wind turbine and it is tabulated in Table 3.6. In order to evaluate the N_c value, different cross-sections of inter-array cables are considered. It includes cable with cross-section of 120 mm^2, 185 mm^2, and 240 mm^2. The inter-array cable length and cable cost reduction of optimal design for NH with Larsen and Jensen wake models for different cross-section area of cable with using ACO-MTSP and FA-MTSP are compared in Table 3.7 where the cable cost reduction is specified in percentage with respect to refernce NH cable cost. From Table 3.7, it observed that (a) the 185 mm^2 cross-section cable is best regarding cable length and (b) the 120 mm^2 cross-section cable is best in terms of cable cost.

Table 3.6: N_c values for various Cross-section area of inter-array cable

Cross-section area of Inter-array cable	Approximate value of N_c	Number of wind turbines are taken into account
120 mm^2	8	8
185 mm^2	11	10
240 mm^2	13	12

Table 3.7: Results summary of North Hoyle OSWF designs with different cable cross-section area

OSWF	Wake model	Cable cross-section area (mm^2)	Inter-array cable length (km)	Inter-array cable cost reduction in %
		120	11.630	48.08
	Larsen	185	10.832	39.82
Optimal design		240	11.328	33.70
for North Hoyle		120	11.542	48.47
	Jensen	185	10.895	39.47
		240	11.338	33.63

3.7.3.3 Optimal design for Horns Rev OSWF using ACO-MTSP and FA-MTSP

Optimal designs for Horns Rev OSWF based on the ACO-MTSP and FA-MTSP with Larsen and Jensen wake models are shown in Figures 3.19 and 3.20, respectively. Table 3.8 gives summary of results obtained in terms of inter-array cable length, cable cost, V_{avg}, P_{apr}, E_A, and C_{LP} values for optimal design of Horns Rev OSWF for radial collector system based on ACO-MTSP , FA-MTSP, and GA-MTSP.
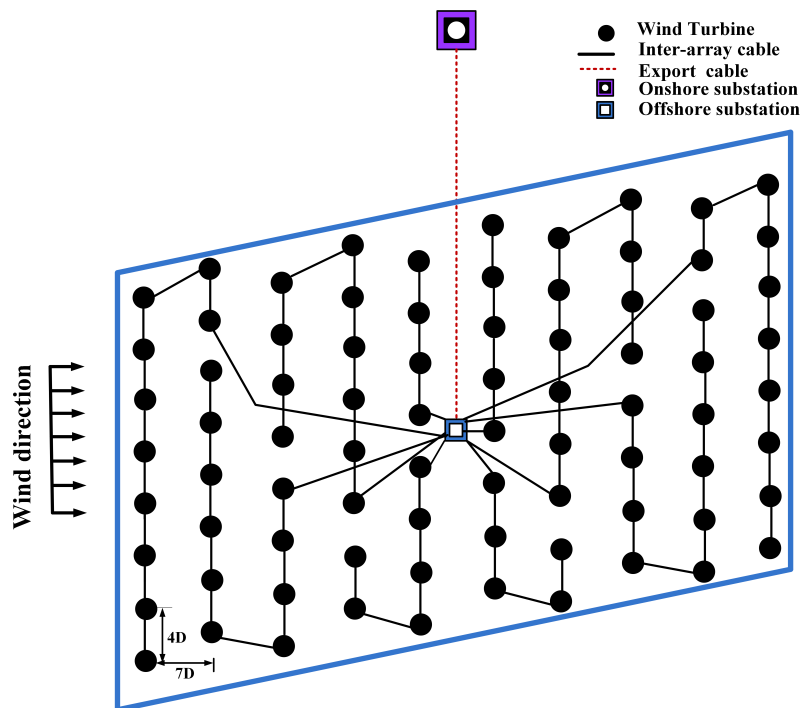
Figure 3.19: ACO-MTSP and FA-MTSP based optimal design for Horns Rev OSWF with Larsen wake model

From the Table 3.8, it is observed that (a) the inter-array cable length is 55.28% with ACO-MTSP and FA-MTSP for a radial collector system compared to reference HR OSWF and (b) the inter-array cable length is 63.11% with GA-MTSP for a radial collector system compared to reference HR OSWF. Hence, the ACO and FA-based optimal models are better than the GA-based models about length of the inter-array cable. The Levelized production cost index of optimal design of HR OSWF for radial collector system is reduced by 20.03%. The annual energy yield is improved by 25.05%. The average wind velocity value of optimal design of HR OSWF for radial
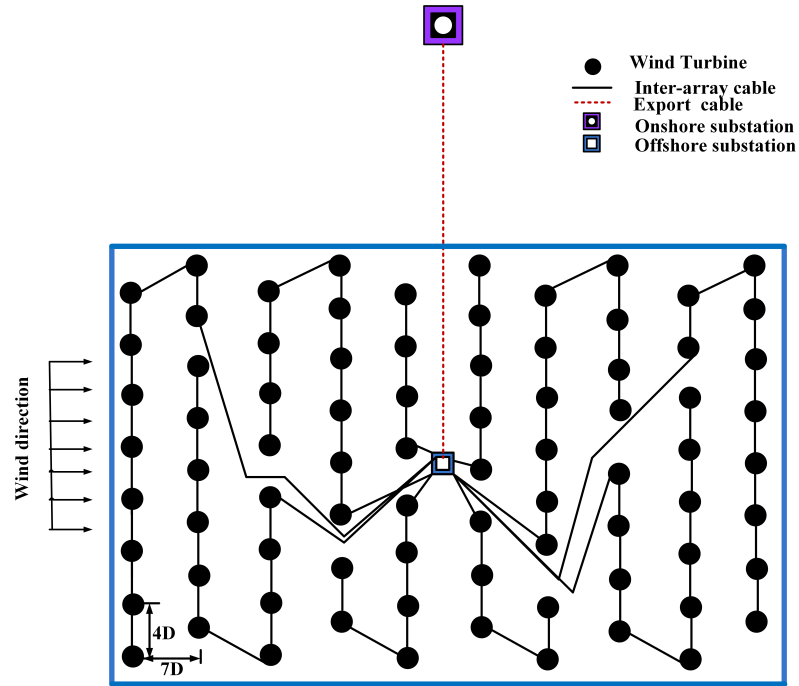
Figure 3.20: ACO-MTSP and FA-MTSP based optimal design for Horns Rev OSWF with Jensen wake model

Table 3.8: Result summary of Horns Rev OSWF optimal designs

| OSWF	Cable length (km)	Cable cost (k$)	Levelized production cost index ($/MWh)	Average wind velocity (pu)	Approximate power production (MW)	Annual energy yields (GWh)	Area (km^2)
Reference Horns Rev	63.000	16283.000	119.83	0.880	108.887	621.760	19.756
Optimal design for HR based on ACO-MTSP	34.824	9000.600	95.83	0.947	135.842	777.500	12.096
Optimal design for HR based on FA-MTSP	34.824	9000.600					
Optimal design for HR based on GA-MTSP	39.779	10281.000					

61

collector system is improved to 7.61%. The wake loss value of HR OSWF is reduced by 5.30% using the Jensen wake model. The proposed approaches used in the design of the optimal OSWFs, improves the approximate power production of optimal design of HR OSWF for radial collector system to 24.75% and saves 38.77% area occupation compared to reference HR. Hence, it results in lesser installation cost. The inter-array cable length and cable cost reduction of optimal design for HR with Larsen and Jensen wake models for different cross-section area of cable with using ACO-MTSP and FA-MTSP are compared in Table 3.9 where the cable cost reduction is specified in percentage with respect to refernce HR cable cost.

Table 3.9: Results summary of Horns Rev OSWF designs with different cable cross-section area

OSWF	Wake model	Cable cross-section area (mm^2)	Inter-array cable length (km)	Inter-array cable cost reduction in %
		120	39.538	49.57
	Larsen	185	35.287	43.99
Optimal design		240	34.607	42.12
for Horns Rev		120	38.864	50.43
	Jensen	185	34.824	44.72
		240	34.677	42.01

Table 3.10: Computation time taken by the optimization methods

Method	Computation time (s)	
	North Hoyle OSWF	Horns Rev OSWF
FA-MTSP	10.764	27.958
ACO-MTSP	6.968	26.204
GA-MTSP	33.553	75.976

From Table 3.9, it may be concluded that (a) the 240 mm^2 cross-section cable is good with reference to cable length and (b) the 120 mm^2 cross-section cable is better in terms of cable cost. The computation time of the different optimization methods used in the study is tabulated in Table 3.10. From Table 3.10, it is observed that the computation time of the GA-MTSP is high when compared to FA-MTSP and ACO-MTSP methods. Among the methods, the ACO-MTSP takes much less convergence time. Hence, ACO-based optimal designs are better designs with respect to cable

length, cable cost, computation time, and levelized production cost index.

3.8 Summary

In this chapter, new optimization approaches to design optimal electrical collector system in terms of inter-array cable length and levelized production cost for the offshore wind farm are proposed which are based on (a) ACO for TSP and MTSP and (b) FA for TSP and MTSP. The optimization approaches are applied to the reference OSWFs namely, North Hoyle OSWF and Horns Rev OSWF. The placement of wind turbines and wake effect on wind turbines are taken into consideration using Larsen and Jensen wake models while designing the electrical collector system of the OSWF. Specification of the optimal designs in terms of cable routing, inter-array cable length, cable cost, Levelized production cost index, average wind velocity, approximate power production, and area of the OSWF are evaluated. With respect to reference North Hoyle OSWF, the inter-array cable length of (a) ACO-TSP and FA-TSP based optimal design for NH OSWF is reduced by 42.61%, (b) ACO-MTSP and FA-MTSP based optimal design for NH OSWF is reduced by 39.47%, (c) GA-MTSP based optimal design for NH OSWF is reduced by 34.02%, (d) Levelized production cost index of the optimal design for NH OSWF is reduced by 11.65%, and (e) Annual energy yield of the optimal design is raised by 13.18%. With respect to reference Horns Rev OSWF, the inter-array cable length of (a) ACO-MTSP and FA-MTSP based optimal design for HR OSWF is reduced by 44.72% (b) GA-MTSP based optimal design for HR OSWF is reduced by 36.86%, (c) Levelized production cost index of the optimal design for NH OSWF is reduced by 20.03%, and (d) Annual energy yield of the optimal design is raised by 25.05%. Hence, the ACO and FA based optimal designs have given better results compared to GA based optimal designs with regards of inter-array cable length. The comparative results of ACO-based optimal designs are quite impressive about computation time and various OSWF outcomes. Thus, the proposed approaches for optimal designs show promising attributes in comparison with reference OSWF designs.

Chapter 4 deals with the new controller approach for grid integration of the OSWF with VSC-HVDC transmission system. The controller is designed to regulate the DC-link voltage, AC voltage, active, and reactive power. The proposed hybrid controller approach is developed by adopting the sliding mode control and conventional PI con-

trol techniques. The mathematical modelling of the VSC-HVDC system is explained. The dynamic modelling and linearized state space modelling of the conventional controller based VSC-HVDC system and hybrid controller based VSC-HVDC system are discussed.

Chapter 4

CONTROLLER DESIGN FOR GRID-INTEGRATED OFFSHORE WIND FARM WITH VSC-HVDC SYSTEM

4.1 Introduction

The OSWFs are located far away from the shore and need a transmission system to transmit the enormous power in MW. High voltage direct current (HVDC) transmission system is a better choice compared to a high voltage alternative current transmission system. Advantages of HVDC transmission system as compared to HVAC transmission systems are given in section 1.1. The HVDC transmission system is divided as voltage source converter (VSC) based HVDC transmission system and line commutated converter (LCC) based HVDC transmission system. The benefits of VSC-HVDC transmission system are: independent active and reactive power control; voltage support and frequency response capability; quick response to disturbances; flexible to decoupling the weak and isolated AC system; black start capability; smaller filter size due to high switching frequency devices; suitable to OSWF applications because of compact footprint; and no necessity of communication devices.(Korompili et al., 2016).

The conventional control techniques such as PI and droop control techniques may

not give a desired response in a non-linear systems due to the limitations in tuning of gain values for PI control technique (Ahmed et al., 2015) and selection of droop coefficients for droop control technique. From the mathematical and operation view point, the grid-integrated OSWFs are highly non-linear systems. Accordingly, the VSC controller must be a robust and non-linear type which can enhance the transient stability and performance of the system (Colbia-Vega et al., 2008). The sliding mode control based controllers can give better performance in case of an abnormal operating condition such as parametric uncertainties and disturbances (Ahmed et al., 2015). To overcome the limitations of conventional control techniques, in this chapter authors propose a hybrid controller which is a combination of sliding mode control (SMC) and PI control techniques for AC grid integrated OSWF VSC-HVDC system. The OSWF is integrated to grid using a high voltage direct current transmission system. In this context, the controller must be capable of controlling AC voltage, DC-link voltage, reactive power and effective power transfer. The designed controller should provide the control for the above mentioned parameters. Also, the controller is designed should have the fault ride through (FRT) capability. Small signal stability analysis is done for testing the system stability for different test cases.

This chapter is documented as follows: Firstly, the configuration and analytical model of the VSC-HVDC system is explained, Conventional controller design and proposed controller design for a wind farm side VSC and grid side VSC are discussed. Secondly, dynamic modelling of the VSC-HVDC system and an elaboration of the sliding mode control technique with mathematical equations are discussed. Detailed explanation on Linearized state-space model of the VSC-HVDC system is discussed in next section, followed by stability study on the controllers and small signal analysis on the VSC-HVDC system. Lastly, the simulation results and analysis of the VSC-HVDC system followed by summary is detailed.

4.2   Configuration of the VSC-HVDC system

The configuration of the grid integrated OSWF through VSC-HVDC transmission system is shown in Figure 4.1. The wind turbines in the 400 MW OSWF are inter-connected to 33 kV AC collector bus and it is coupled to wind farm side VSC (WVSC) through the step-up transformer-1 which is rated as 33/150 kV. Further, the WVSC and grid side VSC (GVSC) are linked by the 100 km length DC cable. The AC filters

66

are placed next to the transformer 1 and preceding the transformer 2. The GVSC and 400 kV onshore AC grid are connected through the step-up transformer 2 which is rated as 150/400 kV. The GVSC and WVSC are operated based on the proposed hybrid controller with PWM technique. The VSC-HVDC system specifications are tabulated in Table 4.1.
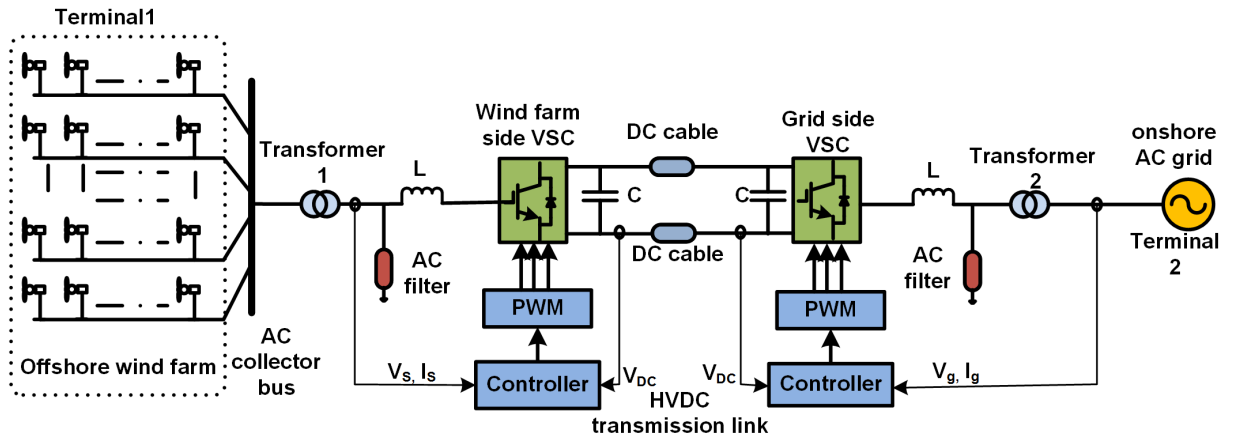
Figure 4.1: Single line diagram of the grid-integrated OSWF with VSC-HVDC transmission system

Table 4.1: Specifications of VSC-HVDC system

System	Specifications	Values
OSWF side	Rated power of OSWF	400 MW (1 pu)
	Transformer 1	33/150 $kV_{ph-ph,rms}$
DC link	Length	100 km
	Capacitor	225 μ F
Grid side	Transformer 2	150/400 $kV_{ph-ph,rms}$
	Grid voltage	400 $kV_{ph-ph,rms}$
AC filter	Inductance	16.700 μ H
	Capacitance	50.368 μ F
	Resistance	0.579 ohms

4.3 Conventional controller design for VSC-HVDC system

The design of the conventional controller is based on the PI control technique. The grid-integrated OSWF with VSC-HVDC link involves the WVSC and GVSC, where each VSC controller consists of an inner controller and outer controller. The inner and outer controllers are designed by adopting the PI technique. The inner controller has to control the AC current tracking the reference output currents provided by the outer controller. The outer controller of WVSC produces the output signals as dq component currents $i^*_{ws,d}$ and $i^*_{ws,q}$. The inner controller of WVSC produces the output signals as dq component voltages $V^*_{cs,d}$ and $V^*_{cs,q}$. The outputs of the inner controller is as reference voltage given to PWM generator through the dq to abc converter. The AC voltage controller performs as an outer controller of WVSC and it regulates the AC voltage. The conventional controller design of the WVSC is shown in Figure 4.2.

Figure 4.2: Conventional controller design for wind farm side VSC

The outer controller of GVSC produces the output signals as dq component cur-

rents $i^*_{wg,d}$, and $i^*_{wg,q}$. The inner controller of GVSC produces the output signals as dq component voltages $V^*_{cg,d}$ and $V^*_{cg,q}$. The output of the inner controller is as reference voltage given to PWM generator through the dq to abc converter. The DC voltage and reactive power controllers act as an outer controller of the GVSC and it governs the DC-link voltage and grid reactive power. The conventional controller design of the GVSC is shown in Figure 4.3.
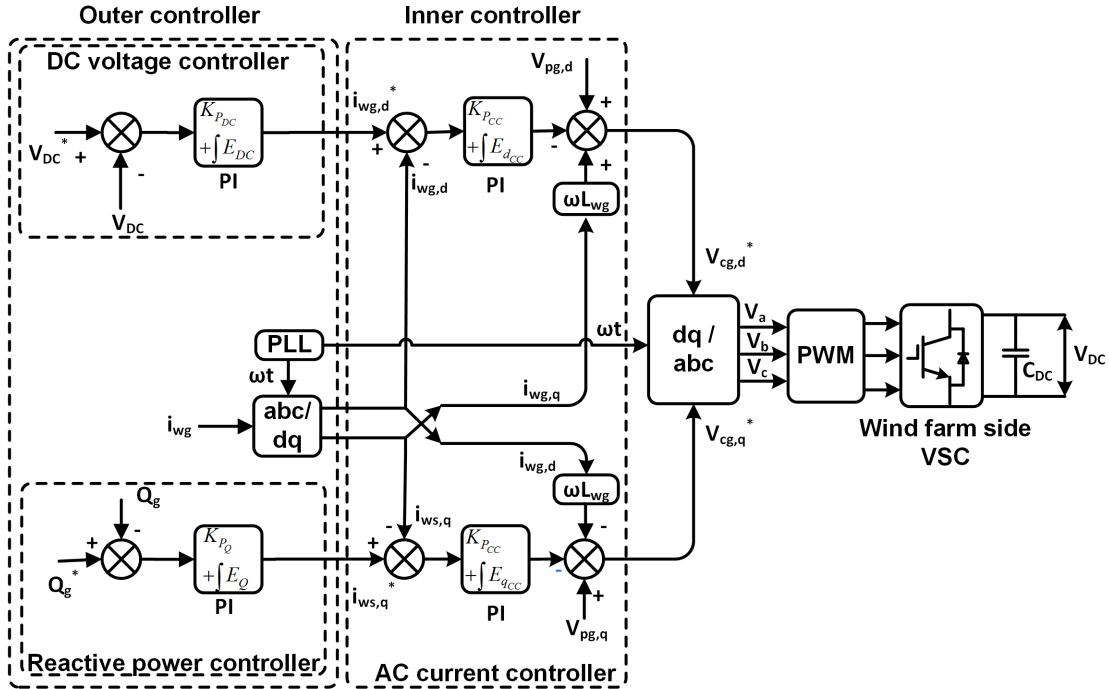
Figure 4.3: Conventional controller design for grid side VSC

4.4 Hybrid controller design for VSC-HVDC system

The design of the hybrid controller is based on the combination of the conventional PI and SMC control techniques. It can give effective control to the system by controlling the parameters such as active power, reactive power, DC-link voltage, AC current, and AC voltage. The grid-integrated OSWF with VSC-HVDC link involves the WVSC and GVSC, where each VSC controller consists of an inner and outer controller. The

inner and outer controllers are designed by adopting the PI and SMC techniques, respectively. The inner controller has to control the AC current tracking the reference output currents provided by the outer controller. The outer controller of WVSC produces the output signals as dq component currents $i^*_{ws,d}$ and $i^*_{ws,q}$. The inner controller of WVSC produces the output signals as dq component voltages $V^*_{cs,d}$ and $V^*_{cs,q}$. The outputs of the inner controller is as reference voltage given to PWM generator through the dq to abc converter. The AC voltage controller performs as an outer controller of WVSC and it regulates the AC voltage. The hybrid controller design of the WVSC is shown in Figure 4.4.

Figure 4.4: Hybrid controller design for wind farm side VSC

The outer controller of GVSC produces the output signals as dq component currents $i^*_{wg,d}$, and $i^*_{wg,q}$. The inner controller of GVSC produces the output signals as dq component voltages $V^*_{cg,d}$ and $V^*_{cg,q}$. The output of the inner controller is as reference voltage given to PWM generator through the dq to abc converter. The DC voltage and reactive power controllers act as an outer controller of the GVSC and it regulates the DC-link voltage and grid reactive power. The hybrid controller design of the GVSC is shown in Figure 4.5.
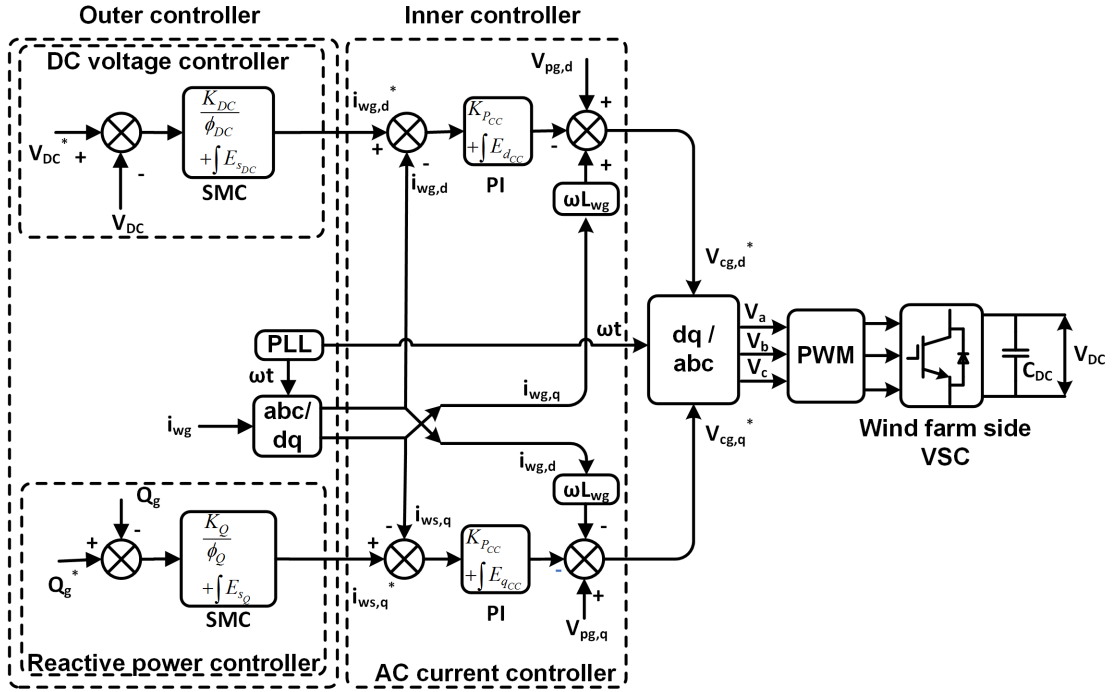
Figure 4.5: Hybrid controller design for grid side VSC

The VSC-HVDC system modelling is explained in following section. It elaborates the equations of the VSC, AC fliter, AC source, AC grid, and DC-link system with circuit diagram.

4.5 VSC-HVDC system modelling

A single line diagram and equivalent diagram of the VSC are shown in Figure 4.6. The voltage equation across points p and c using KVL is given in (4.1).

(a) Single line diagram   (b) Equivalent diagram
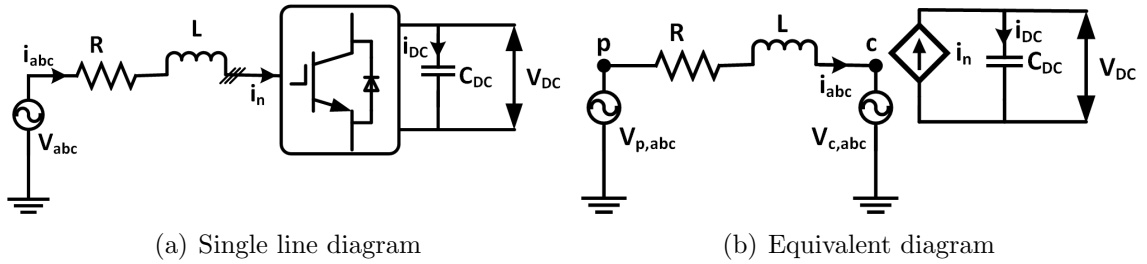
Figure 4.6: Single line and equivalent diagram of the VSC

$$V_{p,abc} - V_{c,abc} = R\ i_{abc} + L\frac{di_{abc}}{dt} \tag{4.1}$$

Where $V_{p,abc}$ and $V_{c,abc}$ are the voltages at point p and c, respectively; i_{abc} is the current flowing between the points p and c; R is phase resistance; and L is phase inductance.

The Clarke and park transformation convert the three-phase ac quantities to two-phase dq quantities. The system control with two-phase quantities is easier than the three-phase ac quantities. So, the dq frame equations reduce the complexity of system control. The phase transformation from abc frame to $\alpha\beta$ frame of reference is by Clarke transformation. Apply the Clarke transformation to convert abc to $\alpha\beta$ frame and it is given in (4.2).

$$V_{p,\alpha\beta} - V_{c,\alpha\beta} = R\ i_{\alpha\beta} + L\frac{di_{\alpha\beta}}{dt} \tag{4.2}$$

Where $V_{p,\alpha\beta}$, $V_{c,\alpha\beta}$, and $i_{\alpha\beta}$ are the $\alpha\beta$ components of the $V_{p,abc}$, $V_{c,abc}$, and i_{abc}, respectively. The Park transformation is applied to convert $\alpha\beta$ to dq frame equations and those are specified in (4.3).

$$\begin{aligned} V_{p,\alpha\beta} &= V_{p,dq}\ e^{j\omega t} \\ V_{c,\alpha\beta} &= V_{c,dq}\ e^{j\omega t} \\ i_{\alpha\beta} &= i_{dq}e^{j\omega t} \end{aligned} \tag{4.3}$$

Where $V_{p,dq}$, $V_{c,dq}$ and i_{dq} are the dq components of the $V_{p,abc}$, $V_{c,abc}$, and i_{abc} respectively; and ω is the operating frequency of the AC network. The resultant equation (4.4) is formed by substituting the (4.3) in (4.2).

$$\begin{aligned} V_{p,dq}\ e^{j\omega t} - V_{c,dq}\ e^{j\omega t} &= R\ i_{dq}\ e^{j\omega t} + L\frac{di_{dq}}{dt}e^{j\omega t} \\ &= R\ i_{dq}\ e^{j\omega t} + j\omega Li_{dq}\ e^{j\omega t} + e^{j\omega t}\ L\frac{di_{dq}}{dt} \end{aligned} \tag{4.4}$$

Divide the equation (4.4) with $e^{j\omega t}$ and the resultant equation is given in (4.5).

$$V_{p,dq} - V_{c,dq} = R\ i_{dq} + j\omega Li_{dq} + L\frac{di_{dq}}{dt} \tag{4.5}$$

The equation (4.5) is rearranged as equation (4.6).

$$L\frac{\mathrm{d}i_{dq}}{\mathrm{d}t} = V_{p,dq} - V_{c,dq} - R\ i_{dq} - j\omega L i_{dq} \tag{4.6}$$

The individual dq frame equations are given in (4.7)

$$L\frac{\mathrm{d}i_d}{\mathrm{d}t} = V_{p,d} - V_{c,d} - R\ i_d + \omega L i_q$$
$$L\frac{\mathrm{d}i_q}{\mathrm{d}t} = V_{p,q} - V_{c,q} - R\ i_q - \omega L i_d \tag{4.7}$$

In (4.7), $V_{p,d}$ and $V_{p,q}$ are the dq components of the voltage V_p at point p; $V_{c,d}$ and $V_{c,q}$ are the dq components of the voltage V_c at point c; and i_d and i_q are the dq components of the current i_{abc}.

The DC side equation is formulated by the DC-link voltage V_{DC}, a current flowing in the DC-link i_{DC} and DC-link capacitance C_{DC}. It is given in (4.8).

$$C_{DC}\frac{\mathrm{d}V_{DC}}{\mathrm{d}t} = i_{DC} \tag{4.8}$$

The apparent power exchange S, observed from reference point c in dq reference frame is stated as (4.9)

$$S = 1.5V_{c,dq}i_{dq}^* = 1.5(V_{c,d} + jV_{c,q})(i_d - ji_q)$$
$$= 1.5((V_{c,d}i_d + V_{c,q}i_q) + j(V_{c,q}i_d - V_{c,d}i_q)) \tag{4.9}$$

For steady state operation, AC side active power P_{AC} will be equal to the DC side power P_{DC} as given in (4.10) assuming converter switches are lossless.

$$P_{DC} = P_{AC}$$
$$V_{DC}i_{DC} = 1.5(V_{c,d}i_d + V_{c,q}i_q)$$
$$i_{DC} = \frac{1.5(V_{c,d}i_d + V_{c,q}i_q)}{V_{DC}} \tag{4.10}$$

The dq frame equation of (4.8) can be formed using (4.10) and it is stated in (4.11).

$$C_{DC}\frac{\mathrm{d}V_{DC}}{\mathrm{d}t} = \frac{1.5(V_{c,d}i_d + V_{c,q}i_q)}{V_{DC}} \tag{4.11}$$

The circuit diagram AC filter placed at point ps is shown in Figure 4.7. The AC filter equation is given in (4.12).
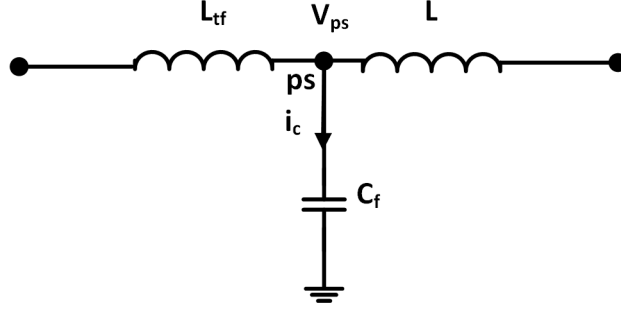
Figure 4.7: Circuit diagram of AC filter

$$C_f \frac{\mathrm{d}V_{ps}}{\mathrm{dt}} = i_c \tag{4.12}$$

The dq frame equations of AC filter are formulated using Clarke and Park transformation and those are stated in (4.13).

$$
\begin{aligned}
C_f \frac{\mathrm{d}V_{ps,d}}{\mathrm{dt}} &= \omega C_f V_{ps,q} + i_{c,d} \\
C_f \frac{\mathrm{d}V_{ps,q}}{\mathrm{dt}} &= -\omega C_f V_{ps,d} + i_{c,q}
\end{aligned}
\tag{4.13}
$$

Where C_f is the AC filter capacitance; L_{tf} is the transformer inductance; V_{ps} is the volatge at the source side point of common coupling ps; $V_{ps,d}$ and $V_{ps,q}$ are the dq components of the voltage V_{ps}; i_c is the current flowing through the AC filter capacitor; and $i_{c,d}$ and $i_{c,q}$ are the dq components of the current i_c.

The wind farm is considered as the AC source. The equivalent AC source circuit voltage equations are expressed using source voltage V_s, current flow in source circuit i_s, source resistance R_s, source reactance L_s, and voltage V_{ps} is given as (4.14).The equivalent circuit diagram AC source with AC filter is shown in Figure 4.8.

$$
\begin{aligned}
V_s &= R_s i_s + (L_s + L_{tf}) \frac{di_s}{dt} + V_{ps} \\
(L_s + L_{tf}) \frac{di_s}{dt} &= V_s - V_{ps} - R_s i_s
\end{aligned}
\tag{4.14}
$$

The dq frame equation of (4.14) is formulated using Clarke and Park transformation
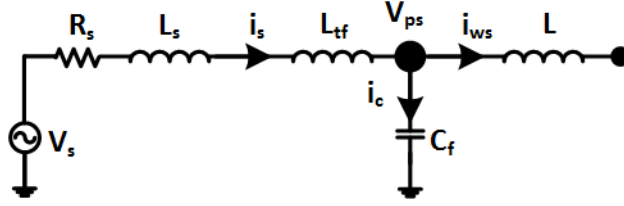
Figure 4.8: Equivalent circuit diagram of AC source with AC filter

and it is given in (4.15).

$$(L_s + L_{tf})\frac{di_{s,dq}}{dt} = V_{s,dq} - V_{ps,dq} - R_s i_{s,dq} - j\omega(L_s + L_{tf})i_{s,dq} \tag{4.15}$$

The individual dq frame equations of (4.15) are given in (4.16).

$$(L_s + L_{tf})\frac{di_{s,d}}{dt} = V_{s,d} - V_{ps,d} - R_s\ i_{s,d} + \omega(L_s + L_{tf})i_{s,q}$$
$$(L_s + L_{tf})\frac{di_{s,q}}{dt} = V_{s,q} - V_{ps,q} - R_s\ i_{s,q} - \omega(L_s + L_{tf})i_{s,d} \tag{4.16}$$

Where $i_{s,d}$ and $i_{s,q}$ are the dq components of the current i_s. The voltage equation with respect to AC filter is given in (4.17).

$$C_f\frac{dV_{ps}}{dt} = i_c = i_s - i_{ws} \tag{4.17}$$

The individual dq frame equations of (4.17) are given in (4.18).

$$C_f\frac{dV_{ps,d}}{dt} = \omega C_f V_{ps,q} + i_{s,d} - i_{ws,d}$$
$$C_f\frac{dV_{ps,q}}{dt} = -\omega C_f V_{ps,d} + i_{s,q} - i_{ws,q} \tag{4.18}$$

The equivalent grid equations can be designed based on Thevenin's circuit and it is expressed using grid voltage V_g, current flow in grid circuit i_g, grid resistance R_g, grid reactance L_g, and voltage V_{pg} at the grid side point of common coupling is given as (4.19).The equivalent circuit diagram AC grid with AC filter is shown in Figure 4.9
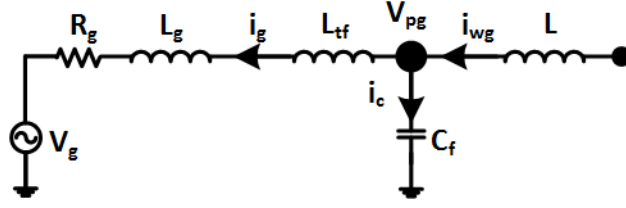
Figure 4.9: Equivalent circuit diagram of AC grid with AC filter

$$V_{pg} - V_g = R_g i_g + (L_g + L_{tf})\frac{di_g}{dt}$$

$$(L_g + L_{tf})\frac{di_g}{dt} = V_{pg} - V_g - R_g i_g \tag{4.19}$$

The dq frame equation of (4.19) is formulated using Clarke and Park transformation and it is given in (4.20).

$$(L_g + L_{tf})\frac{di_{g,dq}}{dt} = V_{pg,dq} - V_{g,dq} - R_g i_{g,dq} - j\omega(L_g + L_{tf})i_{g,dq} \tag{4.20}$$

The individual dq frame equations of (4.20) are given in (4.21).

$$(L_g + L_{tf})\frac{di_{g,d}}{dt} = V_{pg,d} - V_{g,d} - R_g\, i_{g,d} + \omega(L_g + L_{tf})i_{g,q}$$

$$(L_g + L_{tf})\frac{di_{g,q}}{dt} = V_{pg,q} - V_{g,q} - R_g\, i_{g,q} - \omega(L_g + L_{tf})i_{g,d} \tag{4.21}$$

Where $V_{pg,d}$ and $V_{pg,q}$ are the dq components of the voltage V_{pg}; and $i_{g,d}$ and $i_{g,q}$ are the dq components of the current i_g. The voltage equation with respect to AC filter is given in (4.22).

$$C_f\frac{dV_{pg}}{dt} = i_c = i_{wg} - i_g \tag{4.22}$$

The individual dq frame equations of (4.22) are given in (4.23).

$$C_f\frac{dV_{pg,d}}{dt} = \omega C_f V_{pg,q} + i_{wg,d} - i_{g,d}$$

$$C_f\frac{dV_{pg,q}}{dt} = -\omega C_f V_{pg,d} + i_{wg,q} - i_{g,q} \tag{4.23}$$

The circuit diagram of the DC-link is shown in Figure 4.10 and the general equations of the DC-link model are given in (4.24).

76
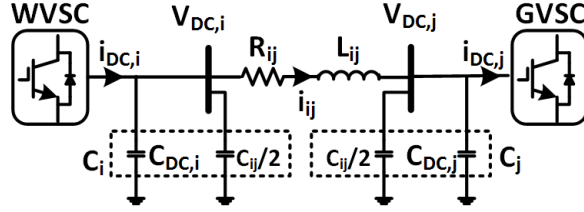
Figure 4.10: Circuit diagram of DC-link

$$
\begin{aligned}
\frac{\mathrm{d}V_{DC,i}}{\mathrm{d}t} &= \frac{i_{DC,i} - \sum i_{ij}}{C_i} \\
\frac{\mathrm{d}V_{DC,j}}{\mathrm{d}t} &= \frac{-i_{DC,j} + \sum i_{ij}}{C_j} \\
C_i &= C_{DC,i} + 0.5 \sum C_{ij} \\
C_j &= C_{DC,j} + 0.5 \sum C_{ij} \\
\frac{\mathrm{d}i_{ij}}{\mathrm{d}t} &= -\frac{R_{ij}}{L_{ij}} i_{ij} + \frac{V_{DC,i} - V_{DC,j}}{L_{ij}}
\end{aligned}
\tag{4.24}
$$

Where R_{ij}, L_{ij}, and C_{ij} are the resistance, inductance, and capacitance of the DC line between buses i and j, respectively; $V_{DC,i}$ and $i_{DC,i}$ are the DC voltage and DC current at i^{th} bus, respectively; $V_{DC,j}$ is the DC voltage at j^{th} bus; $C_{DC,i}$ and $C_{DC,j}$ are the capacitance of the VSC at i^{th} bus and j^{th} bus, respectively; and C_i and C_j are the total capacitance at i^{th} bus and j^{th} bus, respectively.

Dynamic modelling of the VSC-HVDC system is explained in following section. It elaborates the dynamic equations of the PI and SMC based controllers with block diagram and closed-loop transfer functions. The dynamic modelling of the (a) conventional controller design of the VSC-HVDC system and (b) hybrid controller design of the VSC-HVDC system are expalined in Section4.6.

4.6 Dynamic modelling of the VSC-HVDC system

The dynamic model diagram of the grid-integrated VSC-HVDC system is shown in Figure 4.11. It consists of the source model, VSC model, DC-link model and AC grid model. To simplify the process of developing the system state-space model, the step-up transformer inductance and AC filter capacitor equation are added to the AC source and AC grid models. The dynamic equations of the conventional and hybrid

controller design of the VSC-HVDC system are explained in the following sections.
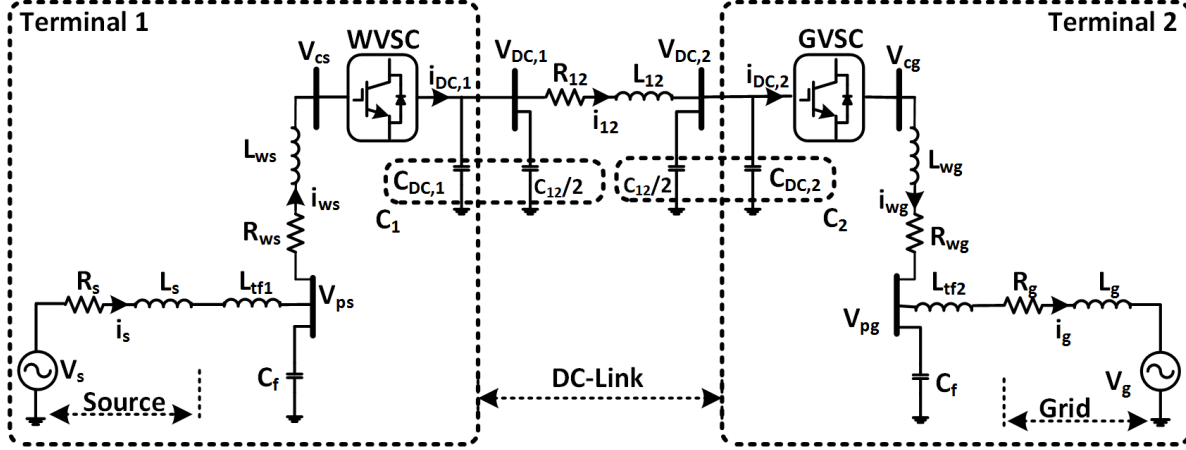
Figure 4.11: Dynamic model diagram of the grid-integrated VSC-HVDC system

4.6.1 Dynamic modelling of the conventional controller design

The conventional controller design of the VSC-HVDC system contains wind farm side VSC and grid side VSC. The dynamic equations of the WVSC and GVSC are explained in the following sections.

4.6.1.1 Inner controller of the WVSC

The inner controller of the WVSC is based on a PI controller that is responsible for controlling the decoupled AC current components $i_{ws,d}$ and $i_{ws,q}$. The inner controller of the WVSC generates the dq reference voltages $V_{cs,d}^*$ and $V_{cs,q}^*$. The equation (4.7) and PI controller are used to develop the AC current controller and the reference current components $i_{ws,d}^*$ and $i_{ws,q}^*$ are produced from the outer controller of the WVSC. The dynamic equations of the wind farm side AC current dq components $i_{ws,d}$ and $i_{ws,q}$ are formulated using equation (4.7) and it is stated as (4.25).

$$
\begin{aligned}
\frac{\mathrm{d}i_{ws,d}}{\mathrm{d}t} &= \frac{-R_{ws}}{L_{ws}}i_{ws,d} + \omega i_{ws,q} - \frac{1}{L_{ws}}V_{cs,d} + \frac{1}{L_{ws}}V_{ps,d} \\
\frac{\mathrm{d}i_{ws,q}}{\mathrm{d}t} &= \frac{-R_{ws}}{L_{ws}}i_{ws,q} - \omega i_{ws,d} - \frac{1}{L_{ws}}V_{cs,q} + \frac{1}{L_{ws}}V_{ps,q}
\end{aligned}
\tag{4.25}
$$

Where $i_{ws,d}$ and $i_{ws,q}$ are the dq components of the phase current i_{ws}; R_{ws} and L_{ws} are the phase resistance and inductance, respectively; $i^*_{ws,d}$ and $i^*_{ws,q}$ are reference values of the $i_{ws,d}$ and $i_{ws,q}$, respectively; and $V_{cs,d}$ and $V_{cs,q}$ are the dq voltage components of the V_{cs}.

The dq current components $i_{ws,d}$ and $i_{ws,q}$ are controlled by the PI controller. The output of inner controller are reference converter voltages $V^*_{cs,d}$ and $V^*_{cs,q}$, as shown in (4.26).

$$
\begin{aligned}
V^*_{cs,d} &= -K_{PCC}(i^*_{ws,d} - i_{ws,d}) - E_{dCC} + \omega L_{ws} i_{ws,q} + V_{ps,d} \\
V^*_{cs,q} &= -K_{PCC}(i^*_{ws,q} - i_{ws,q}) - E_{qCC} - \omega L_{ws} i_{ws,d} + V_{ps,q}
\end{aligned}
\tag{4.26}
$$

Where $K_{P_{CC}}$ and $K_{I_{CC}}$ are the proportional and integral gains of the AC current controller, respectively. From (4.25) and (4.26), the dynamic equations of the dq current components can be formed as given in (4.27).

$$
\begin{aligned}
\frac{di_{ws,d}}{dt} &= -\left(\frac{K_{PCC} + R_{ws}}{L_{ws}}\right) i_{ws,d} + \frac{K_{PCC}}{L_{ws}} i^*_{ws,d} + \frac{1}{L_{ws}} E_{dCC} \\
\frac{di_{ws,q}}{dt} &= -\left(\frac{K_{PCC} + R_{ws}}{L_{ws}}\right) i_{ws,q} + \frac{K_{PCC}}{L_{ws}} i^*_{ws,q} + \frac{1}{L_{ws}} E_{qCC}
\end{aligned}
\tag{4.27}
$$

Where E_{dCC} and E_{qCC} are auxiliary states of the AC current controller as stated in (4.28).

$$
\begin{aligned}
\frac{dE_{dCC}}{dt} &= K_{ICC}(i^*_{ws,d} - i_{ws,d}) \\
\frac{dE_{qCC}}{dt} &= K_{ICC}(i^*_{ws,q} - i_{ws,q})
\end{aligned}
\tag{4.28}
$$

In VSC-HVDC system, the AC side and DC side of the VSCs are interconnected and here converter switches are lossless. Hence, the DC power is equal to the AC active power with subtracting the losses in phase resistance as given in (4.29).

$$
\begin{aligned}
V_{DC} i_{DC} &= 1.5(V_{ps,d} i_{ws,d} + V_{ps,q} i_{ws,q}) - i^2_{ws,d} R_{ws} - i^2_{ws,q} R_{ws} \\
i_{DC} &= \frac{1.5(V_{ps,d} i_{ws,d} + V_{ps,q} i_{ws,q}) - i^2_{ws,d} R_{ws} - i^2_{ws,q} R_{ws}}{V_{DC}}
\end{aligned}
\tag{4.29}
$$

The block diagram of an AC current controller is shown in Figure 4.12. In Figure 4.12, $G_{PI,CC}$, G_C, G_I, G_{CC}, and H are the transfer functions of PI block for AC current
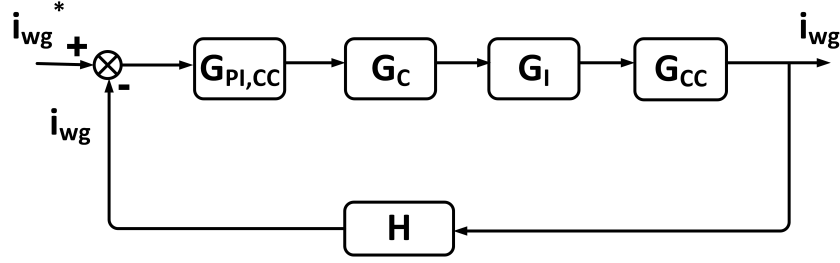
Figure 4.12: Block diagram of the AC current controller

controller, a control delay block, an inverter block, an AC current control block, and sampling block, respectively. The transfer functions are given in (4.30).

$$G_{PI,CC} = K_{P_{CC}} + \frac{K_{I_{CC}}}{s}$$
$$G_C = \frac{1}{1 + sT_s}$$
$$G_I = \frac{1}{1 + \frac{sT_{sw}}{2}}$$
$$G_{CC} = \frac{1}{sL}$$
$$H = \frac{1}{1 + \frac{sT_s}{2}}$$

(4.30)

Where $T_{sw} = 1/f_{sw}$, f_{sw} is the switching frequency, T_s is the sampling time $T_s = 1/f_s$, and f_s is the sampling frequency. The closed-loop transfer function of the AC current controller TF_{CC} can be derived from (4.30) and it is given in (4.31)

$$TF_{PI,CC} = \frac{G_{PI,CC} * G_C * G_I * G_{CC}}{1 + G_{PI,CC} * G_C * G_I * G_{CC} * H}$$

(4.31)

4.6.1.2   Outer controller of the WVSC

The outer controller of the WVSC controller is the AC voltage controller. It controls the AC voltage and generates the reference decoupled currents $i^*_{ws,d}$ and $i^*_{ws,q}$ for the inner controller of the WVSC. The dynamic equations of the PI based AC voltage controller are explained in the following section.

4.6.1.2.1   PI based AC voltage controller

The AC voltage controller is operated as an outer controller for wind farm side VSC and it is developed based on the PI control for the conventional model. Equation (4.13) and PI controller equations are used to develop the AC voltage controller. It provides the reference dq component currents to the inner controller. The dynamic equations of the PI based AC voltage controller are explained in (4.32).

$$
\begin{aligned}
i^*_{ws,d} &= K_{P_{AC}}(V^*_{ps,d} - V_{ps,d}) + E_{d_{AC}} + \omega C_f V_{ps,q} + i_{s,d} \\
i^*_{ws,q} &= K_{P_{AC}}(V^*_{ps,q} - V_{ps,q}) + E_{q_{AC}} - \omega C_f V_{ps,d} + i_{s,q}
\end{aligned}
\tag{4.32}
$$

Where $K_{P_{AC}}$ and $K_{I_{AC}}$ are the proportional and integral gains of the AC voltage controller; and $E_{d_{AC}}$ and $E_{q_{AC}}$ are auxiliary states of the PI based AC voltage controller as stated in (4.33).

$$
\begin{aligned}
\frac{dE_{d_{AC}}}{dt} &= K_{I_{AC}}(V^*_{ps,d} - V_{ps,d}) \\
\frac{dE_{q_{AC}}}{dt} &= K_{I_{AC}}(V^*_{ps,q} - V_{ps,q})
\end{aligned}
\tag{4.33}
$$

The block diagram of PI based AC voltage controller is given in Figure 4.13.

Figure 4.13: Block diagram of the PI based AC voltage controller

In Figure 4.13, G_{AC} is the transfer function of the AC voltage control block and it is given as (4.34); and $G_{PI,AC}$ is the transfer function of the PI block for AC voltage controller and it is given as (4.35);

$$
G_{AC} = \frac{1}{sC_f}
\tag{4.34}
$$

$$G_{PI,AC} = K_{P_{AC}} + \frac{K_{I_{AC}}}{s} \tag{4.35}$$

The closed-loop transfer function of the PI based AC voltage controller $TF_{PI,AC}$ can be derived from (4.51), 4.34), and (4.35). It is stated as (4.36).

$$TF_{PI,AC} = \frac{G_{PI,AC} * G_C * G_{AC}}{1 + G_{PI,AC} * G_C * G_{AC} * H} \tag{4.36}$$

4.6.1.3 Inner controller of the GVSC

The inner controller of the GVSC is based on a PI controller that is responsible for controlling the decoupled AC current components $i_{wg,d}$ and $i_{wg,q}$. The inner controller of the GVSC generates the dq reference voltages $V_{cg,d}^*$ and $V_{cg,q}^*$. The equation (4.7) and PI controller are used to develop the AC current controller and the reference current components $i_{wg,d}^*$ and $i_{wg,q}^*$ are produced from the outer controller of the GVSC. The dynamic equations of the grid side AC current dq components $i_{wg,d}$ and $i_{wg,q}$ are formulated using equation (4.7) and it is stated as (4.37).

$$\begin{aligned}
\frac{di_{wg,d}}{dt} &= \frac{-R_{wg}}{L_{wg}}i_{wg,d} + \omega i_{wg,q} - \frac{1}{L_{wg}}V_{cg,d} + \frac{1}{L_{wg}}V_{pg,d} \\
\frac{di_{wg,q}}{dt} &= \frac{-R_{wg}}{L_{wg}}i_{wg,q} - \omega i_{wg,d} - \frac{1}{L_{wg}}V_{cg,q} + \frac{1}{L_{wg}}V_{pg,q}
\end{aligned} \tag{4.37}$$

Where $i_{wg,d}$ and $i_{wg,q}$ are the dq components of the phase current i_{wg}; R_{wg} and L_{wg} are the phase resistance and inductance, respectively; $i_{wg,d}^*$ and $i_{wg,q}^*$ are reference values of the $i_{wg,d}$ and $i_{wg,q}$, respectively; and $V_{cg,d}$ and $V_{cg,q}$ are the dq voltage components of the V_{cg}.

The dq current components $i_{wg,d}$ and $i_{wg,q}$ are controlled by the PI controller. The output of inner controller are reference converter voltages $V_{cg,d}^*$ and $V_{cg,q}^*$, as shown in (4.38).

$$\begin{aligned}
V_{cg,d}^* &= -K_{P_{CC}}(i_{wg,d}^* - i_{wg,d}) - E_{dg_{CC}} + \omega L_{wg}i_{wg,q} + V_{pg,d} \\
V_{cg,q}^* &= -K_{P_{CC}}(i_{wg,q}^* - i_{wg,q}) - E_{qg_{CC}} - \omega L_{wg}i_{wg,d} + V_{pg,q}
\end{aligned} \tag{4.38}$$

From (4.37) and (4.38), the dynamic equations of the dq current components can

82

be formed as given in (4.39).

$$\frac{\mathrm{d}i_{wg,d}}{\mathrm{d}t} = -\left(\frac{K_{PCC} + R_{wg}}{L_{wg}}\right) i_{wg,d} + \frac{K_{PCC}}{L_{wg}} i^*_{wg,d} + \frac{1}{L_{wg}} E_{dgCC}$$

$$\frac{\mathrm{d}i_{wg,q}}{\mathrm{d}t} = -\left(\frac{K_{PCC} + R_{wg}}{L_{wg}}\right) i_{wg,q} + \frac{K_{PCC}}{L_{wg}} i^*_{wg,q} + \frac{1}{L_{wg}} E_{qgCC}$$

(4.39)

Where $i_{wg,d}$ and $i_{wg,q}$ are the dq components of the phase current i_{wg}; R_{wg} and L_{wg} are the phase resistance and inductance, respectively; $i^*_{wg,d}$ and $i^*_{wg,q}$ are reference values of the $i_{wg,d}$ and $i_{wg,q}$, respectively; $V_{cg,d}$ and $V_{cg,q}$ are the dq voltage components of the V_{cg}; and E_{dgCC} and E_{qgCC} are auxiliary states of the AC current controller as stated in (4.40).

$$\frac{\mathrm{d}E_{dgCC}}{\mathrm{d}t} = K_{ICC}(i^*_{wg,d} - i_{wg,d})$$

$$\frac{\mathrm{d}E_{qgCC}}{\mathrm{d}t} = K_{ICC}(i^*_{wg,q} - i_{wg,q})$$

(4.40)

In VSC-HVDC system, the AC side and DC side of the VSCs are interconnected and here converter switches are used to be lossless. Hence, the DC power is equal to the AC active power with subtracting the losses in phase resistance as given in (4.41).

$$i_{DC} = \frac{1.5(V_{pg,d}i_{wg,d} + V_{pg,q}i_{wg,q}) - i^2_{wg,d}R_{wg} - i^2_{wg,q}R_{wg}}{V_{DC}}$$

(4.41)

4.6.1.4   Outer controller of the GVSC

The DC voltage and reactive power controller are act as the outer controllers of the GVSC. The outer controller of GVSC regulates the DC voltage and reactive power. It generates the reference decoupled currents $i^*_{wg,d}$ and $i^*_{wg,q}$ for the inner controller of the GVSC. The dynamic equations of the PI based DC voltage controller and PI based reactive power controller are explained in the following sections.
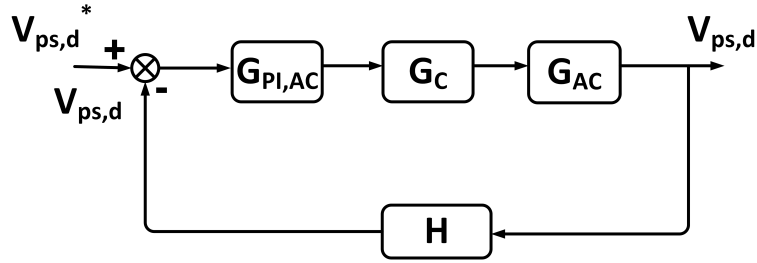
4.6.1.4.1   PI based DC voltage controller

The DC voltage controller is operated as one of the outer controllers for grid side VSC and it is developed based on the PI control for the conventional controller. It regulates the DC-link voltage. The stable DC link voltage ensures the steady power flow between the VSCs and it provides the reference $i^*_{wg,d}$ value to the inner controller.

The dynamic equations of the PI based DC voltage controller are given in (4.42).

$$i^*_{wg,d} = K_{P_{DC}}(V^*_{DC} - V_{DC}) + E_{DC}$$
$$\frac{\mathrm{d}E_{DC}}{\mathrm{dt}} = K_{I_{DC}}(V^*_{DC} - V_{DC})$$

(4.42)

Where $K_{P_{DC}}$ and $K_{I_{DC}}$ are the proportional and integral gains of the AC voltage controller; V^*_{DC} is the reference of the V_{DC}; and E_{DC} are auxiliary state of the PI based DC voltage control. The block diagram of the PI based DC voltage controller is shown in Figure 4.14.
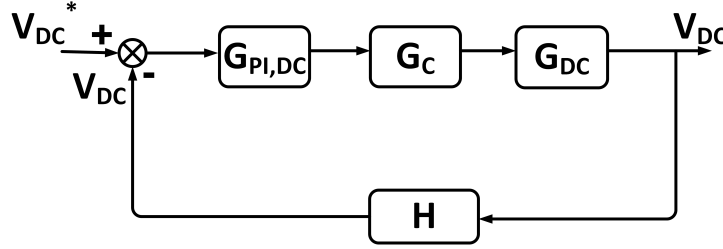
Figure 4.14: Block diagram of the PI based DC voltage controller

In Figure 4.14, G_{DC} is the transfer function of the DC voltage control block and it is given as (4.43); and $G_{PI,DC}$ is the transfer function of the PI block for DC voltage controller and it is given as (4.44)

$$G_{DC} = \frac{1}{sC_{DC}}$$

(4.43)

$$G_{PI,DC} = K_{P_{DC}} + \frac{K_{I_{DC}}}{s}$$

(4.44)

The closed-loop transfer function of the PI based DC voltage controller $TF_{PI,DC}$ can be derived from (4.30), (4.43), and (4.44). It is stated as (4.45)

$$TF_{PI,DC} = \frac{G_{PI,DC} * G_C * G_{DC}}{1 + G_{PI,DC} * G_C * G_{DC} * H}$$

(4.45)

4.6.1.4.2 PI based reactive power controller

The reactive power controller regulates the reactive power and it generates the reference $i^*_{wg,q}$ to the inner controller. The $i^*_{wg,q}$ is achieved by the instantaneous power equations as given in (4.46).

$$P = V_{pg,d}i_{g,d} + V_{pg,q}i_{g,q}$$
$$Q = V_{pg,q}i_{g,d} - V_{pg,d}i_{g,q}$$

$$(4.46)$$

Where P and Q are the active and reactive power, respectively; and $i_{g,d}$ and $i_{g,q}$ are the reference dq components of the grid current i_g. The reference quadratic current $i^*_{wg,q}$ is expressed in (4.47).

$$i^*_{wg,q} = i^*_{g,q} = \frac{PV_{pg,q} - QV_{pg,d}}{V^2_{pg,d} + V^2_{pg,q}}$$

$$(4.47)$$

The dynamic equations of the PI based reactive power controller are given in (4.48).

$$i^*_{wg,q} = -K_{P_Q} \left(Q^* - Q \right) + E_Q$$
$$\frac{\mathrm{d}E_Q}{\mathrm{d}t} = -K_{I_Q} \left(Q^* - Q \right)$$

$$(4.48)$$

Where E_Q is auxiliary state of the PI based reactive power controller.

4.6.2 Sliding mode control

V. Utkin introduced the sliding mode control technique in the early 1950s. It is a nonlinear control technique which is used to design a robust controller for complex higher order non-linear systems working at different operating situations. Sliding mode control is highly insensitive to fluctuations of parameters, has a quick response, provides robustness and disturbance elimination. The high-frequency oscillations may arise in the control process which is replicated in the actual system performance, and this is called as chattering effect. For high-frequency applications, sliding mode control may not be suitable due to the chattering effect. The continuous functions such as hyperbolic tangent, Signum, and saturation functions are considered to mitigate the chattering effect and to improve the system stability (Ramadan et al., 2012). The analytical model of sliding mode control is explained as follows (Tan et al., 2011):

The sliding surface S_s is the function of the sliding coefficient α and an error signal e as expressed in equation (4.49).

$$S_s = \alpha e + \dot{e}$$
$$e = x^* - x$$
(4.49)

The discontinuous control action τ_c is given in equation (4.50).

$$\tau_c = K \tanh \frac{S_s}{\phi}$$
(4.50)

Where K is the sliding gain constant and ϕ is the boundary layer thickness. The SMC block transfer function G_{SMC} can be expressed using equations (4.49)-(4.50) and it is given in (4.51).

$$G_{SMC} = \frac{K}{\phi}[\frac{\alpha}{s} + 1]$$
(4.51)

4.6.3 Dynamic modelling of the hybrid controller design

The hybrid controller design of the VSC-HVDC system contains wind farm side VSC and grid side VSC. The dynamic equations of the WVSC and GVSC are explained in the following sections.

4.6.3.1 Inner controller of the WVSC

The inner controller of the WVSC is based on a PI controller that is responsible for controlling the decoupled AC current components $i_{ws,d}$ and $i_{ws,q}$. It generates the dq reference voltages $V_{cs,d}^*$ and $V_{cs,q}^*$. The equation (4.7) and PI controller are used to develop the AC current controller and the reference current components $i_{ws,d}^*$ and $i_{ws,q}^*$ are produced from the outer controller of the WVSC. The dynamic equations of the WVSC inner controller model are explained in the section 4.6.1.1.

4.6.3.2 Outer controller of the WVSC

The AC voltage controller performs as the outer controller of WVSC. It controls the AC voltage and generates the reference decoupled currents $i_{ws,d}^*$ and $i_{ws,q}^*$ for the inner controller of the WVSC. The dynamic equations of the SMC based AC voltage controller are explained in the following section.

4.6.3.2.1   SMC based AC voltage controller

The AC voltage controller is developed based on the SMC method for the hybrid controller. The equation (4.13) and SMC equation (4.51) are used to develop the AC voltage controller and it provides the reference dq component currents to the inner controller. The dynamic equations of the SMC based AC voltage controller are explained in (4.52).

$$
\begin{aligned}
i_{ws,d}^* &= \frac{K_{AC}}{\phi_{AC}}(V_{ps,d}^* - V_{ps,d}) + E_{ds_{AC}} + \omega C_f V_{ps,q} + i_{s,d} \\
i_{ws,q}^* &= \frac{K_{AC}}{\phi_{AC}}(V_{ps,q}^* - V_{ps,q}) + E_{qs_{AC}} - \omega C_f V_{ps,d} + i_{s,q}
\end{aligned}
\tag{4.52}
$$

Where K_{AC}, α_{AC}, and ϕ_{AC} are the switch gain, sliding coefficient, and boundary layer thickness of the AC voltage controller, respectively; and $E_{ds_{AC}}$ and $E_{qs_{AC}}$ are auxiliary states of the SMC based AC voltage controller as stated in (4.53).

$$
\begin{aligned}
\frac{\mathrm{d}E_{ds_{AC}}}{\mathrm{d}t} &= \frac{K_{AC}}{\phi_{AC}}\alpha_{AC}(V_{ps,d}^* - V_{ps,d}) \\
\frac{\mathrm{d}E_{qs_{AC}}}{\mathrm{d}t} &= \frac{K_{AC}}{\phi_{AC}}\alpha_{AC}(V_{ps,q}^* - V_{ps,q})
\end{aligned}
\tag{4.53}
$$

The block diagram of SMC based AC voltage controller is given in Figure 4.15.
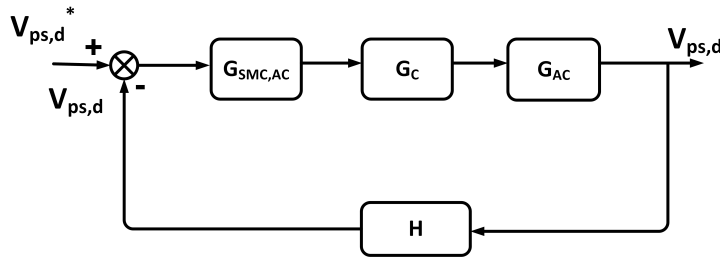
Figure 4.15: Block diagram of the SMC based AC voltage controller

In Figure 4.15, $G_{SMC,AC}$ is the transfer function of the SMC block for AC voltgae controller and it is shown in (4.54).

$$
G_{SMC,AC} = \frac{K_{AC}}{\phi_{AC}}[\frac{\alpha_{AC}}{s} + 1]
\tag{4.54}
$$

The closed-loop transfer function of the SMC based AC voltage controller $TF_{SMC,AC}$ can be derived from (4.30), (4.34), and (4.54). It is stated as (4.55).

$$TF_{SMC,AC} = \frac{G_{SMC,AC} * G_C * G_{AC}}{1 + G_{SMC,AC} * G_C * G_{AC} * H} \tag{4.55}$$

4.6.3.3 Inner controller of the GVSC

The inner controller of the GVSC is based on a PI controller that is responsible for controlling the decoupled AC current components $i_{wg,d}$ and $i_{wg,q}$. It generates the dq reference voltages $V_{cg,d}^*$ and $V_{cg,q}^*$. The equation (4.7) and PI controller are used to develop the AC current controller and the reference current components $i_{wg,d}^*$ and $i_{wg,q}^*$ are produced from the outer controller of the GVSC. The dynamic equations of the GVSC inner controller model are explained in section 4.6.1.3.

4.6.3.4 Outer controller of the GVSC

The DC voltage and reactive power controller are act as the outer controllers of the GVSC. The outer controller of GVSC regulates the DC voltage and reactive power. It generates the reference decoupled currents $i_{wg,d}^*$ and $i_{wg,q}^*$ for the inner controller of the GVSC. The SMC discontinuous control action τ_c includes the continuous function and it mitigates the chattering effect due to high-frequency oscillations of the system parameters. The dynamic equations of the SMC based DC voltage controller and SMC based reactive power controller are explained in the following sections.

4.6.3.4.1 SMC based DC voltage controller

The DC voltage control for the hybrid controller is designed based on the SMC method and it controls the DC-link voltage. The dynamic equations of the SMC based DC voltage controller are given in (4.56).

$$i_{wg,d}^* = \frac{K_{DC}}{\phi_{DC}}(V_{DC}^* - V_{DC}) + E_{s_{DC}}$$
$$\frac{dE_{s_{DC}}}{dt} = \frac{K_{DC}}{\phi_{DC}}\alpha_{DC}(V_{DC}^* - V_{DC}) \tag{4.56}$$

Where K_{DC}, α_{DC}, and ϕ_{DC} are the switch gain, sliding coefficient, and boundary layer thickness of the DC voltage controller, respectively; and $E_{s_{DC}}$ are auxiliary state of

the SMC based DC voltage controller. The block diagram of the SMC based DC voltage controller is shown in Figure 4.16. In Figure 4.16, $G_{SMC,DC}$ is the transfer
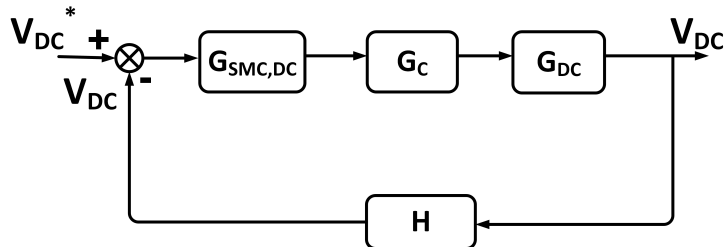
Figure 4.16: Block diagram of the SMC based DC voltage controller

function of the SMC block for DC voltage controller and it is given as (4.57).

$$G_{SMC,DC} = \frac{K_{DC}}{\phi_{DC}}[\frac{\alpha_{DC}}{s} + 1] \tag{4.57}$$

The closed-loop transfer function of the SMC based DC voltage controller $TF_{SMC,DC}$ can be derived from (4.30), (4.43), and (4.57). It is stated as (4.58)

$$TF_{SMC,DC} = \frac{G_{SMC,DC} * G_C * G_{DC}}{1 + G_{SMC,DC} * G_C * G_{DC} * H} \tag{4.58}$$

4.6.3.4.2   SMC based reactive power controller

The dynamic equations of the SMC based reactive power controller are given in (4.59).

$$i_{wg,q}^* = \frac{-K_Q\ (Q^* - Q)}{\phi_Q} + E_{s_Q}$$
$$\frac{\mathrm{d}E_{s_Q}}{\mathrm{dt}} = \frac{-K_Q\alpha_Q(Q^* - Q)}{\phi_Q} \tag{4.59}$$

Where E_{s_Q} is auxiliary state of the SMC based reactive power controller.

4.6.4   Dynamic model of the AC grid

The dynamic equations of the AC grid model are formulated using (4.21). To simply the process of developing the system state-space model, the grid side transformer inductance L_{tf2} is added to AC grid model. So, total inductance is equal to $L_g + L_{tf2}$.

The dynamic equations of the $i_{g,d}$ and $i_{g,q}$ are given in (4.60).

$$\frac{\mathrm{d}i_{g,d}}{\mathrm{d}t} = \left(\frac{-R_g \ i_{g,d}}{L_g + L_{tf2}}\right) + \omega i_{g,q} - \left(\frac{V_{g,d} - V_{pg,d}}{L_g + L_{tf2}}\right)$$

$$\frac{\mathrm{d}i_{g,q}}{\mathrm{d}t} = \left(\frac{-R_g \ i_{g,q}}{L_g + L_{tf2}}\right) - \omega i_{g,d} - \left(\frac{V_{g,q} - V_{pg,q}}{L_g + L_{tf2}}\right)$$

(4.60)

Where the dq voltage components $V_{pg,d}$ and $V_{pg,q}$ are formulated using (4.23)) and it stated as in (4.61).

$$\frac{\mathrm{d}V_{pg,d}}{\mathrm{d}t} = \frac{(i_{wg,d} - i_{g,d})}{C_f} + \omega V_{pg,q}$$

$$\frac{\mathrm{d}V_{pg,q}}{\mathrm{d}t} = \frac{(i_{wg,q} - i_{g,q})}{C_f} - \omega V_{pg,d}$$

(4.61)

4.6.5 Dynamic model of the AC source

The dynamic equations of the AC source model are formulated using (4.16). To simply the process of developing the system state-space model, the source side transformer inductance L_{tf1} is added to AC source model. So, total inductance is equal to $L_s + L_{tf1}$. The dynamic equations of the $i_{s,d}$ and $i_{s,q}$ are given in (4.62).

$$\frac{\mathrm{d}i_{s,d}}{\mathrm{d}t} = \left(\frac{-R_s \ i_{s,d}}{L_s + L_{tf1}}\right) + \omega i_{s,q} + \left(\frac{V_{s,d} - V_{ps,d}}{L_s + L_{tf1}}\right)$$

$$\frac{\mathrm{d}i_{s,q}}{\mathrm{d}t} = \left(\frac{-R_s \ i_{s,q}}{L_s + L_{tf1}}\right) - \omega i_{s,d} + \left(\frac{V_{s,q} - V_{ps,q}}{L_s + L_{tf1}}\right)$$

(4.62)

Where the dq voltage components $V_{ps,d}$ and $V_{ps,q}$ are formulated using (4.18)) and it stated as in (4.63).

$$\frac{\mathrm{d}V_{ps,d}}{\mathrm{d}t} = \frac{(i_{s,d} - i_{ws,d})}{C_f} + \omega V_{ps,q}$$

$$\frac{\mathrm{d}V_{ps,q}}{\mathrm{d}t} = \frac{(i_{s,q} - i_{ws,q})}{C_f} - \omega V_{ps,d}$$

(4.63)

4.6.6 Dynamic model of the DC-link

The dynamic equations of the DC-link model for two terminal VSC-HVDC system can be expressed from (4.24) and as given in (4.64).

$$
\begin{aligned}
\frac{\mathrm{d}V_{DC,1}}{\mathrm{dt}} &= \frac{i_{DC,1} - i_{12}}{C_1} \\
\frac{\mathrm{d}V_{DC,2}}{\mathrm{dt}} &= \frac{i_{12} - i_{DC,2}}{C_2} \\
\frac{\mathrm{d}i_{12}}{\mathrm{dt}} &= -\frac{R_{12}}{L_{12}}i_{12} + \frac{V_{DC,1} - V_{DC,2}}{L_{12}}
\end{aligned}
\tag{4.64}
$$

Where $V_{DC,1}$ and $V_{DC,2}$ are the DC voltage at buses 1 and 2, respectively; $i_{DC,1}$ and $i_{DC,2}$ are the DC currents at buses 1 and 2, respectively; $C_{DC,1}$ and $C_{DC,2}$ are the capacitance of the VSC at buses 1 and 2, respectively; and R_{12}, L_{12}, and C_{12} are the resistance, inductance, and capacitance of the DC line between buses 1 and 2, respectively. The total capacitances of each bus side C_1 and C_2 are given as (4.65).

$$
\begin{aligned}
C_1 &= C_{DC,1} + 0.5C_{12} \\
C_2 &= C_{DC,2} + 0.5C_{12}
\end{aligned}
\tag{4.65}
$$

4.7 Linearized state-space modelling

The grid-integrated OSWF through VSC-HVDC systems are complex and it has multiple inputs and outputs. The system representation with differential equations or transfer functions turns to be complex. So, the state-space modeling is applied to reduce the complexity of system representation. The linearized system can be designed by the state-space model. The state space representation of a system replaces an nth order differential equation with a single first order matrix differential equation. The genarlized state-space model equations are mentioned as in (4.66). The state equation is expressed in terms of the state vector x, system matrix A, input vector u, and system input matrix B. The output equation is stated in terms of the output vector y, output matrix C, and the transmission or feed-forward matrix D.

$$
\begin{aligned}
\dot{x} &= Ax + Bu \\
y &= Cx + Du
\end{aligned}
\tag{4.66}
$$

The eigenvalues of the system matrix signify the poles of the system which decide the system stability. The eigenvalues can be calculated from the characteristic equation as shown in (4.67).

$$|\lambda I - A| = 0 \tag{4.67}$$

Where I is the identity matrix and λ is the eigenmatrix of A.

4.7.1 Linearized state-space model of the VSC-HVDC system with conventional controller

The linearized state-space model of the VSC-HVDC transmission system with conventional controller is formulated from the dynamic equations of the PI based VSC-HVDC system. To make the state-space system model simple and easy, the PI based VSC-HVDC system model is divided into wind farm side VSC model, grid side VSC model and DC-link model.

4.7.1.1 State-space model of the conventional controller based wind farm side VSC model

The conventional controller based wind farm side VSC model is the combination of the inner and outer controllers. Here, the inner controller and outer controller are designed based on PI control technique. The linearized state-space model of the current controller and AC voltage controller models are explained in the following sections.

4.7.1.1.1 State-space model of PI based WVSC inner controller

The current controller is operated as an inner controller for wind farm side VSC. The linearized state-space model of PI based WVSC inner controller can be developed from the equations (4.25)-(4.29) and it is given in (4.68).

$$\dot{x}_i = A_i x_i + B_{ia} u_{ca} + B_{id} u_{cd} + B_{ir} u_{ir}$$
$$y_{ia} = C_{ia} x_i + D_{ia1} u_{ca} + D_{id1} u_{cd} + D_{ir1} u_{ir} \tag{4.68}$$
$$y_{id} = C_{id} x_i + D_{ia2} u_{ca} + D_{id2} u_{cd} + D_{ir2} u_{ir}$$

Where $x_i = \begin{bmatrix} i_{ws,d} & i_{ws,q} & E_{d_{CC}} & E_{q_{CC}} \end{bmatrix}^T$; $u_{ca} = \begin{bmatrix} i_{s,d} & i_{s,q} & V_{ps,d} & V_{ps,q} \end{bmatrix}^T$; $u_{cd} = V_{DC}$; $u_{ir} = \begin{bmatrix} i^*_{ws,d} & i^*_{ws,q} \end{bmatrix}^T$; $y_{ia} = \begin{bmatrix} i_{ws,d} & i_{ws,q} \end{bmatrix}^T$; $y_{id} = i_{DC}$; and the state matrices of the PI based WVSC inner controller are given as below,

$$A_i = \begin{bmatrix} \frac{-(R_{ws}+K_{P_{CC}})}{L_{ws}} & 0 & \frac{1}{L_{ws}} & 0 \\ 0 & \frac{-(R_{ws}+K_{P_{CC}})}{L_{ws}} & 0 & \frac{1}{L_{ws}} \\ K_{I_{CC}} & 0 & 0 & 0 \\ 0 & K_{I_{CC}} & 0 & 0 \end{bmatrix}; \quad B_{ia} = 0_{4,4}; \quad B_{id} = 0_{4,1};$$

$$C_{ia} = \begin{bmatrix} 1 & 0 & 0 & 0 \\ 0 & 1 & 0 & 0 \end{bmatrix}; \quad B_{ir} = \begin{bmatrix} \frac{K_{P_{CC}}}{L_{ws}} & 0 \\ 0 & \frac{K_{P_{CC}}}{L_{ws}} \\ -K_{I_{CC}} & 0 \\ 0 & -K_{I_{CC}} \end{bmatrix}; \quad C_{id} = \begin{bmatrix} \frac{1.5\ V_{ps,d}}{V_{DC}} & \frac{1.5\ V_{ps,q}}{V_{DC}} & 0 & 0 \end{bmatrix};$$

$$D_{ia1} = 0_{2,4}; D_{ia2} = 0_{1,4}; D_{ir1} = 0_{2,2}; D_{ir1} = 0_{1,2}; D_{id1} = 0_{2,1}; D_{id2} = \begin{bmatrix} \frac{-(i^2_{ws,d}+i^2_{ws,q})R_{ws}}{V_{DC}^2} \end{bmatrix}$$

4.7.1.1.2   State-space model of PI based WVSC outer controller

The AC voltage controller based on PI control is operated as outer controller for wind farm side VSC. The linearized state-space model of PI based WVSC outer controller can be developed from the equations (4.32) and (4.33). It is given in (4.69).

$$\dot{x}_o = A_o x_o + B_{oa} u_{ca} + B_{od} u_{cd} + B_{or} u_{ir}$$
$$y_o = C_o x_o + D_{oa} u_{ca} + D_{od} u_{cd} + D_{or} u_{ir} \tag{4.69}$$

Where $x_o = \begin{bmatrix} E_{d_{AC}} & E_{q_{AC}} \end{bmatrix}^T$; $u_{ir} = \begin{bmatrix} V_{ps,d} & V_{ps,q} \end{bmatrix}^T$; $y_o = \begin{bmatrix} i^*_{ws,d} & i^*_{ws,q} \end{bmatrix}^T$; and the state matrices of the PI based WVSC outer controller are given as below,

$$A_o = 0_{2,2}; \quad B_{oa} = \begin{bmatrix} 0 & 0 & K_{I_{AC}} & 0 \\ 0 & 0 & 0 & K_{I_{AC}} \end{bmatrix}; \quad B_{od} = D_{od} = 0_{2,1}; \quad C_o = I_2;$$

$$B_{or} = \begin{bmatrix} -K_{I_{AC}} & 0 \\ 0 & -K_{I_{AC}} \end{bmatrix}; \quad D_{oa} = \begin{bmatrix} 1 & 0 & K_{P_{AC}} & \omega C_f \\ 0 & 1 & -\omega C_f & K_{P_{AC}} \end{bmatrix}; \quad D_{or} = \begin{bmatrix} -K_{P_{AC}} & 0 \\ 0 & -K_{P_{AC}} \end{bmatrix}$$

4.7.1.1.3 Complete converter model of the conventional WVSC

The complete converter model of the conventional WVSC is the cascaded model of the PI based WVSC inner controller and PI based WVSC outer controller. To derive the complete converter model, replace $u_{ir} = y_o$ in (4.68). The resultant state-space equations of the WVSC complete converter model are stated as (4.70).

$$
\begin{aligned}
\dot{x}_c &= A_c x_c + B_{ca} u_{ca} + B_{cd} u_{cd} + B_{cr} u_{cr} \\
y_{ca} &= C_{ca} x_c + D_{ca1} u_{ca} + D_{cd1} u_{cd} + D_{cr1} u_{cr} \\
y_{cd} &= C_{cd} x_c + D_{ca2} u_{ca} + D_{cd2} u_{cd} + D_{cr2} u_{cr}
\end{aligned}
\tag{4.70}
$$

Where $x_c = \begin{bmatrix} x_i & x_o \end{bmatrix}^T$ and the complete converter model of the conventional WVSC state matrices are given as below,

$$
A_c = \begin{bmatrix} A_i & B_{ir} C_o \\ 0_{2,4} & A_o \end{bmatrix} ; \ B_{ca} = \begin{bmatrix} B_{ia} + B_{ir} D_{oa} \\ B_{oa} \end{bmatrix} ; \ B_{cd} = \begin{bmatrix} B_{id} + B_{ir} D_{od} \\ B_{od} \end{bmatrix} ;
$$

$$
B_{cr} = \begin{bmatrix} B_{ir} D_{or} \\ B_{or} \end{bmatrix} ; \ C_{ca} = \begin{bmatrix} C_{ia} & D_{ir1} C_o \end{bmatrix} ; \ C_{cd} = \begin{bmatrix} C_{id} & D_{ir2} C_o \end{bmatrix} ;
$$

$$
D_{ca1} = \begin{bmatrix} D_{ia1} + D_{ir1} D_{oa} \end{bmatrix} ; D_{cd1} = \begin{bmatrix} D_{id1} + D_{ir1} D_{od} \end{bmatrix} ; \ D_{cr1} = \begin{bmatrix} D_{ir1} D_{or} \end{bmatrix} ;
$$

$$
D_{ca2} = \begin{bmatrix} D_{ia2} + D_{ir2} D_{oa} \end{bmatrix} ; D_{cd2} = \begin{bmatrix} D_{id2} + D_{ir2} D_{od} \end{bmatrix} ; \ D_{cr2} = \begin{bmatrix} D_{ir2} D_{or} \end{bmatrix}
$$

Where A_i, B_{ia}, B_{id}, B_{ir}, C_{ia}, C_{id}, D_{ia1}, D_{id1}, D_{ir1}, D_{ia2}, D_{id2}, and D_{ir2} are state matrices of the equation (4.68). A_o, B_{oa}, B_{od}, B_{or}, C_o, D_{oa}, D_{od}, and D_{or} are state matrices of the equation (4.69).

4.7.1.1.4 AC source model

The linearized state-space model of the AC source can be developed from the equations (4.62) and (4.63). It is given in (4.71).

$$
\begin{aligned}
\dot{x}_s &= A_s x_s + B_s u_s \\
y_s &= C_s x_s
\end{aligned}
\tag{4.71}
$$

Where $x_s = \begin{bmatrix} i_{s,d} & i_{s,q} & V_{ps,d} & V_{ps,q} \end{bmatrix}^T$; $y_s = \begin{bmatrix} i_{s,d} & i_{s,q} & V_{ps,d} & V_{ps,q} \end{bmatrix}^T$;
$u_s = \begin{bmatrix} i_{ws,d} & i_{ws,q} & V_{s,d} & V_{s,q} \end{bmatrix}^T$; and the AC source state matrices are given as below,

$$
A_s = \begin{bmatrix}
\frac{-R_s}{L_s+L_{tf1}} & \omega & \frac{-1}{L_s+L_{tf1}} & 0 \\
-\omega & \frac{-R_s}{L_s+L_{tf1}} & 0 & \frac{-1}{L_s+L_{tf1}} \\
\frac{1}{C_f} & 0 & 0 & \omega \\
0 & \frac{1}{C_f} & -\omega & 0
\end{bmatrix} ; \;
B_s = \begin{bmatrix}
0 & 0 & \frac{1}{L_s+L_{tf1}} & 0 \\
0 & 0 & 0 & \frac{1}{L_s+L_{tf1}} \\
\frac{-1}{C_f} & 0 & 0 & 0 \\
0 & \frac{-1}{C_f} & 0 & 0
\end{bmatrix} ; \; Cs = I_4
$$

4.7.1.1.5 Total WVSC system model with conventional controller

The total WVSC system model with conventional controller is the cascaded model of the AC source model and complete converter model of the WVSC. To derive the total WVSC system model with conventional controller, replace $u_s = y_{ca}$ in (4.71) and substitute $u_{ca} = C_s\, x_s$ in the resulting expression and in (4.70). The resultant state-space equations of the total WVSC system model with conventional controller are stated as (4.72).

$$
\begin{aligned}
\dot{x}_{sc} &= A_{sc}x_{sc} + B_{sc_d}u_{cd} + B_{sc_r}u_{sc_r} \\
y_{sc_d} &= C_{sc_d}x_{sc} + D_{sc_d}u_{cd} + D_{sc_r}u_{sc_r}
\end{aligned}
\tag{4.72}
$$

Where $x_{sc} = \begin{bmatrix} x_c & x_s \end{bmatrix}^T$; $y_{sc_d} = \begin{bmatrix} i_{DC} \end{bmatrix}$; $u_{sc_r} = \begin{bmatrix} V_{ps,d} & V_{ps,q} \end{bmatrix}^T$; and the state matrices of the total WVSC system model with conventional controller are given as below,

$$
A_{sc} = \begin{bmatrix}
A_c & B_{ca}C_s \\
B_sC_{ca} & A_s + B_sD_{ca1}C_s
\end{bmatrix} ; \;
B_{sc_d} = \begin{bmatrix}
B_{cd} \\
B_sD_{cd1}
\end{bmatrix} ;
$$

$$
B_{sc_r} = \begin{bmatrix}
B_{cr} \\
B_sD_{cr1}
\end{bmatrix} ; \;
C_{sc_d} = \begin{bmatrix} C_{cd} & 0_{1,4} \end{bmatrix} ; \;
D_{sc_d} = D_{cd2}; \; D_{sc_r} = D_{cr2}
$$

Where A_c, B_{ca}, B_{cd}, B_{cr}, C_{ca}, C_{cd}, D_{ca1}, D_{cd1}, D_{cr1}, D_{ca2}, D_{cd2}, and D_{cr2} are state matrices of the equation (4.70). A_s, B_s, and C_s are state matrices of the equation (4.71).

4.7.1.2 State-space model of the conventional controller based grid side VSC model

The conventional controller based grid side VSC model is the combination of the inner and outer controllers. Here, the inner and outer controllers are designed based on PI control technique. The linearized state-space model of the inner and outer controller models are explained in the following sections.

4.7.1.2.1 State-space model of PI based GVSC inner controller

The current controller is operated as an inner controller for grid side VSC. The linearized state-space model of PI based GVSC inner controller can be developed from the equations (4.39)-(4.41) and it is given in (4.73).

$$\dot{x}_{i_g} = A_{i_g} x_{i_g} + B_{ia_g} u_{ca_g} + B_{id_g} u_{cd_g} + B_{ir_g} u_{ir_g}$$
$$y_{ia_g} = C_{ia_g} x_{i_g} + D_{ia_{g1}} u_{ca_g} + D_{id_{g1}} u_{cd_g} + D_{ir_{g1}} u_{ir_g} \qquad (4.73)$$
$$y_{id_g} = C_{id_g} x_{i_g} + D_{ia_{g2}} u_{ca_g} + D_{id_{g2}} u_{cd_g} + D_{ir_{g2}} u_{ir_g}$$

Where $x_{i_g} = \begin{bmatrix} i_{wg,d} & i_{wg,q} & E_{dg_{CC}} & E_{qg_{CC}} \end{bmatrix}^T$; $u_{ca_g} = \begin{bmatrix} i_{g,d} & i_{g,q} & V_{pg,d} & V_{pg,q} \end{bmatrix}^T$; $u_{cd_g} = V_{DC}$; $u_{ir_g} = \begin{bmatrix} i^*_{wg,d} & i^*_{wg,q} \end{bmatrix}^T$; $y_{ia_g} = \begin{bmatrix} i_{wg,d} & i_{wg,q} \end{bmatrix}^T$; $y_{id_g} = i_{DC}$; and the state matrices of the PI based GVSC inner controller are given as below,

$$A_{i_g} = \begin{bmatrix} \frac{-(R_{wg}+K_{P_{CC}})}{L_{wg}} & 0 & \frac{1}{L_{wg}} & 0 \\ 0 & \frac{-(R_{wg}+K_{P_{CC}})}{L_{wg}} & 0 & \frac{1}{L_{wg}} \\ K_{I_{CC}} & 0 & 0 & 0 \\ 0 & K_{I_{CC}} & 0 & 0 \end{bmatrix}; \; B_{ia_g} = 0_{4,4}; \; B_{id} = 0_{4,1};$$

$$C_{ia_g} = \begin{bmatrix} 1 & 0 & 0 & 0 \\ 0 & 1 & 0 & 0 \end{bmatrix}; B_{ir_g} = \begin{bmatrix} \frac{K_{P_{CC}}}{L_{wg}} & 0 \\ 0 & \frac{K_{P_{CC}}}{L_{wg}} \\ -K_{I_{CC}} & 0 \\ 0 & -K_{I_{CC}} \end{bmatrix}; \; C_{id_g} = \begin{bmatrix} \frac{1.5\, V_{pg,d}}{V_{DC}} & \frac{1.5\, V_{pg,q}}{V_{DC}} & 0 & 0 \end{bmatrix};$$

$$D_{ia_{g1}} = 0_{2,4}; D_{ia_{g2}} = 0_{1,4}; D_{ir_{g1}} = 0_{2,2}; D_{ir_{g2}} = 0_{1,2}; D_{id_{g1}} = 0_{2,1}; D_{id_{g2}} = \begin{bmatrix} \frac{-(i^2_{wg,d}+i^2_{wg,q})R_{wg}}{V^2_{DC}} \end{bmatrix}$$

4.7.1.2.2 State-space model of PI based GVSC outer controller

The PI based DC voltage controller and PI based reactive power controller are operated as outer controller for grid side VSC. The linearized state-space model of PI based GVSC outer controller can be developed from the equations (4.42) and (4.48). It is given in (4.74).

$$
\begin{aligned}
\dot{x}_{og} &= A_{o_g} x_{o_g} + B_{oa_g} u_{ca} + B_{od_g} u_{cd} + B_{or_g} u_{ir} \\
y_{o_g} &= C_{o_g} x_{o_g} + D_{oa_g} u_{ca} + D_{od_g} u_{cd} + D_{or_g} u_{or}
\end{aligned}
\tag{4.74}
$$

Where $x_{o_g} = \begin{bmatrix} E_{DC} & E_Q \end{bmatrix}^T$; $u_{ca} = \begin{bmatrix} V_{DC}^* & Q^* \end{bmatrix}^T$; $u_{ir} = \begin{bmatrix} V_{DC} & Q \end{bmatrix}^T$; $y_{o_g} = \begin{bmatrix} i_{wg,d} & i_{wg,q} \end{bmatrix}^T$; and matrices of the PI based GVSC outer controller are given as below,

$$
A_{o_g} = 0_{2,2}; \; B_{oa_g} = \begin{bmatrix} K_{I_{DC}} & 0 \\ 0 & -K_{I_Q} \end{bmatrix}; \; B_{od_g} = D_{od_g} = 0_{2,1}; \; C_{o_g} = I_2;
$$

$$
B_{or_g} = \begin{bmatrix} -K_{I_{DC}} & 0 \\ 0 & K_{I_Q} \end{bmatrix}; \; D_{oa_g} = \begin{bmatrix} K_{P_{DC}} & 0 \\ 0 & -K_{P_Q} \end{bmatrix}; \; D_{or_g} = \begin{bmatrix} -K_{P_{DC}} & 0 \\ 0 & K_{P_Q} \end{bmatrix}
$$

4.7.1.2.3 Complete converter model of the conventional GVSC

The complete converter of the conventional GVSC model is the cascaded model of the PI based GVSC inner controller and PI based GVSC outer controller. To derive the complete converter model, replace $u_{ir_g} = y_{o_g}$ in (4.73). The resultant state-space equations of the GVSC complete converter model are stated as (4.75).

$$
\begin{aligned}
\dot{x}_{c_g} &= A_{c_g} x_{c_g} + B_{ca_g} u_{ca} + B_{cd_g} u_{cd} + B_{cr_g} u_{cr} \\
y_{ca_g} &= C_{ca_g} x_{c_g} + D_{ca_{g1}} u_{ca} + D_{cd_{g1}} u_{cd} + D_{cr_{g1}} u_{cr} \\
y_{cd_g} &= C_{cd_g} x_{c_g} + D_{ca_{g2}} u_{ca} + D_{cd_{g2}} u_{cd} + D_{cr_{g2}} u_{cr}
\end{aligned}
\tag{4.75}
$$

Where $x_{c_g} = \begin{bmatrix} x_{i_g} & x_{o_g} \end{bmatrix}^T$ and the complete converter of the conventional GVSC model state matrices are given as below,

$$
A_{c_g} = \begin{bmatrix} A_{i_g} & B_{ir_g}C_{o_g} \\ 0_{2,4} & A_{o_g} \end{bmatrix} ; \; B_{ca_g} = \begin{bmatrix} B_{ia_g} + B_{ir_g}D_{oa_g} \\ B_{oa_g} \end{bmatrix} ; \; B_{cd_g} = \begin{bmatrix} B_{id_g} + B_{ir_g}D_{od_g} \\ B_{od_g} \end{bmatrix} ;
$$

$$
B_{cr_g} = \begin{bmatrix} B_{ir_g}D_{or_g} \\ B_{or_g} \end{bmatrix} ; \; C_{ca_g} = \begin{bmatrix} C_{ia_g} & D_{ir_{g1}}C_{o_g} \end{bmatrix} ; \; C_{cd_g} = \begin{bmatrix} C_{id_g} & D_{ir_{g2}}C_{o_g} \end{bmatrix} ;
$$

$$
D_{ca_{g1}} = \begin{bmatrix} D_{ia_{g1}} + D_{ir_{g1}}D_{oa_g} \end{bmatrix} ; D_{cd_{g1}} = \begin{bmatrix} D_{id_{g1}} + D_{ir_{g1}}D_{od_g} \end{bmatrix} ; \; D_{cr_{g1}} = \begin{bmatrix} D_{ir_{g1}}D_{or_g} \end{bmatrix} ;
$$

$$
D_{ca_{g2}} = \begin{bmatrix} D_{ia_{g2}} + D_{ir_{g2}}D_{oa_g} \end{bmatrix} ; D_{cd_{g2}} = \begin{bmatrix} D_{id_{g2}} + D_{ir_{g2}}D_{od_g} \end{bmatrix} ; \; D_{cr_{g2}} = \begin{bmatrix} D_{ir_{g2}}D_{or_g} \end{bmatrix}
$$

Where A_{i_g}, B_{ia_g}, B_{id_g}, B_{ir_g}, C_{ia_g}, C_{id_g}, $D_{ia_{g1}}$, $D_{id_{g1}}$, $D_{ir_{g1}}$, $D_{ia_{g2}}$, $D_{id_{g2}}$, and $D_{ir_{g2}}$ are state matrices of the equation (4.73). A_{o_g}, B_{oa_g}, B_{od_g}, B_{or_g}, C_{o_g}, D_{oa_g}, D_{od_g}, and D_{or_g} are state matrices of the equation (4.74).

4.7.1.2.4 AC grid model

The linearized state-space model of the AC grid can be developed from the equations (4.60) and (4.61). It is given in (4.76).

$$
\begin{aligned}
\dot{x}_g &= A_g x_g + B_g u_g \\
y_g &= C_g x_g
\end{aligned}
\tag{4.76}
$$

Where $x_g = \begin{bmatrix} i_{g,d} & i_{g,q} & V_{pg,d} & V_{pg,q} \end{bmatrix}^T$; $y_g = \begin{bmatrix} i_{g,d} & i_{g,q} & V_{pg,d} & V_{pg,q} \end{bmatrix}^T$; $u_s = \begin{bmatrix} i_{wg,d} & i_{wg,q} & V_{g,d} & V_{g,q} \end{bmatrix}^T$; and the AC grid state matrices are given as below,

$$
A_g = \begin{bmatrix} \frac{-R_g}{L_g+L_{tf2}} & \omega & \frac{1}{L_g+L_{tf2}} & 0 \\ -\omega & \frac{-R_g}{L_g+L_{tf2}} & 0 & \frac{1}{L_g+L_{tf2}} \\ \frac{-1}{C_f} & 0 & 0 & \omega \\ 0 & \frac{-1}{C_f} & -\omega & 0 \end{bmatrix} ; \; B_g = \begin{bmatrix} 0 & 0 & \frac{-1}{L_g+L_{tf2}} & 0 \\ 0 & 0 & 0 & \frac{-1}{L_g+L_{tf2}} \\ \frac{1}{C_f} & 0 & 0 & 0 \\ 0 & \frac{1}{C_f} & 0 & 0 \end{bmatrix} ; \; C_g = I_4
$$

4.7.1.2.5 Total GVSC system model with conventional controller

The total GVSC system model with conventional controller is the cascaded model of the AC grid model and complete converter model of the GVSC. To derive the total GVSC system model with conventional controller, replace $u_g = y_{ca_g}$ in (4.76)

and substitute $u_{ca} = C_g\, x_g$ in the resulting expression and in (4.75). The resultant state-space equations of the total GVSC system model with conventional controller are stated as (4.77).

$$
\dot{x}_{gc} = A_{gc}x_{gc} + B_{gc_d}u_{cd} + B_{gc_r}u_{gc_r}
$$
$$
y_{gc_d} = C_{gc_d}x_{gc} + D_{gc_d}u_{cd} + D_{gc_r}u_{gc_r}
$$
(4.77)

Where $x_{gc} = \begin{bmatrix} x_{c_g} & x_g \end{bmatrix}^T$; $y_{gc_d} = \begin{bmatrix} i_{DC} \end{bmatrix}$; $u_{gc_r} = \begin{bmatrix} V_{DC} & Q \end{bmatrix}^T$; and the state matrices of the total GVSC system model with conventional controller are given as below,

$$
A_{gc} = \begin{bmatrix} A_{c_g} & B_{ca_g}C_g \\ B_g C_{ca_g} & A_g + B_g D_{ca_{g1}} C_g \end{bmatrix} ; \; B_{gc_d} = \begin{bmatrix} B_{cd_g} \\ B_g D_{cd_{g1}} \end{bmatrix} ;
$$

$$
B_{gc_r} = \begin{bmatrix} B_{cr_g} \\ B_g D_{cr_{g1}} \end{bmatrix} ; \; C_{gc_d} = \begin{bmatrix} C_{cd_g} & 0_{1,4} \end{bmatrix} ;
$$

$$
D_{gc_d} = D_{cd_{g2}}; \; D_{gc_r} = D_{cr_{g2}}
$$

Where A_{c_g}, B_{ca_g}, B_{cd_g}, B_{cr_g}, C_{ca_g}, C_{cd_g}, $D_{ca_{g1}}$, $D_{cd_{g1}}$, $D_{cr_{g1}}$, $D_{ca_{g2}}$, $D_{cd_{g2}}$, and $D_{cr_{g2}}$ are state matrices of the equation 4.75. A_g, B_g, and C_g are state matrices of the equation 4.76.

4.7.1.3 DC-link model

The linearized state-space model of the DC-link can be developed from the equations (4.64) and (4.65). It is given in (4.78).

$$
\dot{x}_{dc} = A_{dc}x_{dc} + B_{dc_1}u_{dc_1} + B_{dc_2}u_{dc_2}
$$
$$
y_{dc_1} = C_{dc_1}x_{dc}
$$
$$
y_{dc_2} = C_{dc_2}x_{dc}
$$
(4.78)

Where $x_{dc} = \begin{bmatrix} i_{12} & V_{DC,1} & V_{DC,2} \end{bmatrix}^T$; $u_{dc_1} = i_{DC,1}$; $u_{dc_2} = i_{DC,2}$; $y_{dc_1} = V_{DC,1}$; and $y_{dc_2} = V_{DC,2}$ and the DC-link model state matrices are given as below,

$$
A_{dc} = \begin{bmatrix} \frac{-R_{12}}{L_{12}} & \frac{1}{L_{12}} & \frac{-1}{L_{12}} \\ \frac{-1}{C_1} & 0 & 0 \\ \frac{1}{C_2} & 0 & 0 \end{bmatrix} ; \ B_{dc_1} = \begin{bmatrix} 0 \\ \frac{1}{C_1} \\ 0 \end{bmatrix} ; \ B_{dc_2} = \begin{bmatrix} 0 \\ 0 \\ \frac{-1}{C_2} \end{bmatrix} ; \ C_{dc_1} = \begin{bmatrix} 0 & 1 & 0 \end{bmatrix} ; \ C_{dc_2} = \begin{bmatrix} 0 & 0 & 1 \end{bmatrix}
$$

4.7.1.4 Total VSC-HVDC system with conventional controller

The total VSC-HVDC system with conventional controller model is the cascaded model of the total WVSC system model with conventional controller, total GVSC system model with conventional controller and DC-link model. To derive the total VSC-HVDC system model, replace $u_{dc_1} = y_{gc_d}$ and $u_{dc_2} = y_{sc_d}$ in (4.78). The resultant state-space equations of the VSC-HVDC system with conventional controller model are stated as (4.79).

$$
\begin{aligned}
\dot{x}_{sys} &= A_{sys} x_{sys} + B_{sys} u_{sys} \\
y_{sys} &= C_{sys} x_{sys}
\end{aligned}
\tag{4.79}
$$

Where $x_{sys} = \begin{bmatrix} x_{gc} & x_{sc} & x_{dc} \end{bmatrix}^T$; $u_{sys} = \begin{bmatrix} u_{gc_r} & u_{sc_r} \end{bmatrix}^T$; $y_{sys} = \begin{bmatrix} x_{gc} & x_{sc} & x_{dc} \end{bmatrix}^T$; and the state matrices of the total VSC-HVDC system with conventional controller model are given as below,

$$
A_{sys} = \begin{bmatrix} A_{gc} & 0_{10,10} & B_{gc_d} C_{dc_1} \\ 0_{10,10} & A_{sc} & B_{sc_d} C_{dc,2} \\ B_{dc_1} C_{gc_d} & B_{dc_2} C_{sc_d} & (A_{dc} + B_{dc_1} D_{gc_d} C_{dc_1} + B_{dc_2} D_{sc_d} C_{dc_2}) \end{bmatrix} ;
$$

$$
B_{sys} = \begin{bmatrix} B_{gc_r} & 0_{10,2} \\ 0_{10,2} & B_{sc_r} \\ B_{dc_1} D_{gc_r} & B_{dc_2} D_{sc_r} \end{bmatrix} ; \ C_{sys} = I_3
$$

Where A_{sc}, B_{sc_d}, B_{sc_r}, C_{sc_d}, D_{sc_r}, and D_{sc_d} are the system matrices of the equation 4.72. A_{gc}, B_{gc_d}, B_{gc_r}, C_{gc_d}, D_{gc_r}, and D_{gc_d} are the system matrices of the equation (4.77). A_{dc}, B_{dc_1}, B_{dc_2}, C_{dc_1}, and C_{dc_2} are the system matrices of the equation (4.78).

4.7.2 Linearized state-space model of the VSC-HVDC system with hybrid controller

The linearized state-space model of the VSC-HVDC transmission system with hybrid controller is formulated from the dynamic equations of the VSC-HVDC system with hybrid controller. To make the state-space system model simple and easy, the VSC-HVDC system with hybrid controller model is divided into wind farm side VSC model, grid side VSC model, and DC-link model.

4.7.2.1 State-space model of the hybrid controller based wind farm side VSC model

The hybrid controller based wind farm side VSC model is the combination of the inner and outer controllers. Here, the inner and outer controllers are designed based on PI control and SMC techniques, respectively. The linearized state-space model of the PI based WVSC inner controller model is explained in section 4.7.1.1.1 and the outer controller model will be discussed in the following section.

4.7.2.1.1 State-space model of SMC based WVSC outer controller

The AC voltage controller based on SMC is operated as outer controller for wind farm side VSC. The linearized state-space model of SMC based WVSC outer controller can be developed from the equations (4.52) and (4.53). It is given in (4.80).

$$
\begin{aligned}
\dot{x}_{o_h} &= A_{o_h} x_{o_h} + B_{oa_h} u_{ca} + B_{od_h} u_{cd} + B_{or_h} u_{ir} \\
y_{o_h} &= C_{o_h} x_{o_h} + D_{oa_h} u_{ca} + D_{od_h} u_{cd} + D_{or_h} u_{or}
\end{aligned}
\tag{4.80}
$$

Where $x_{o_h} = \begin{bmatrix} E_{ds_{AC}} & E_{qs_{AC}} \end{bmatrix}^T$ and $y_{o_h} = y_o$ and the state matrices of the SMC based WVSC outer controller are given as below,

$$
A_{o_h} = 0_{2,2}; \ B_{oa_h} = \begin{bmatrix} 0 & 0 & \frac{K_{AC}\alpha_{AC}}{\phi_{AC}} & 0 \\ 0 & 0 & 0 & \frac{K_{AC}\alpha_{AC}}{\phi_{AC}} \end{bmatrix}; \ B_{od_h} = D_{od_h} = 0_{2,1}; \ C_{o_h} = I_2;
$$

$$
B_{or_h} = \begin{bmatrix} -\frac{K_{AC}\alpha_{AC}}{\phi_{AC}} & 0 \\ 0 & -\frac{K_{AC}\alpha_{AC}}{\phi_{AC}} \end{bmatrix}; \ D_{oa_h} = \begin{bmatrix} 1 & 0 & \frac{K_{AC}}{\phi_{AC}} & \omega C_f \\ 0 & 1 & -\omega C_f & \frac{K_{AC}}{\phi_{AC}} \end{bmatrix}; \ D_{or_h} = \begin{bmatrix} -\frac{K_{AC}}{\phi_{AC}} & 0 \\ 0 & -\frac{K_{AC}}{\phi_{AC}} \end{bmatrix}
$$

4.7.2.1.2 Complete converter model of the hybrid WVSC

The complete converter model of the hybrid WVSC is the cascaded model of the PI based WVSC inner controller and SMC based WVSC outer controller. To derive the complete converter model, replace $u_{ir} = y_{o_h}$ in (4.68). The resultant state-space equations of the WVSC complete converter model are stated as (4.81).

$$
\begin{aligned}
\dot{x}_{c_h} &= A_{c_h} x_{c_h} + B_{ca_h} u_{ca} + B_{cd_h} u_{cd} + B_{cr_h} u_{cr} \\
y_{ca_h} &= C_{ca_h} x_{c_h} + D_{ca_{h1}} u_{ca} + D_{cd_{h1}} u_{cd} + D_{cr_{h1}} u_{cr} \\
y_{cd} &= C_{cd} x_{c_h} + D_{ca_{h2}} u_{ca} + D_{cd_{h2}} u_{cd} + D_{cr_{h2}} u_{cr}
\end{aligned}
\tag{4.81}
$$

Where $x_{c_h} = \begin{bmatrix} x_i & x_{o_h} \end{bmatrix}$ and the complete converter model of the hybrid WVSC state matrices are given as below,

$$
A_{c_h} = \begin{bmatrix} A_i & B_{ir} C_{o_h} \\ 0_{2,4} & A_{o_h} \end{bmatrix} ; \;
B_{ca_h} = \begin{bmatrix} B_{ia} + B_{ir} D_{oa_h} \\ B_{oa_h} \end{bmatrix} ; \;
B_{cd_h} = \begin{bmatrix} B_{id} + B_{ir} D_{od_h} \\ B_{od_h} \end{bmatrix} ;
$$

$$
B_{cr_h} = \begin{bmatrix} B_{ir} D_{or_h} \\ B_{or_h} \end{bmatrix} ; \;
C_{ca_h} = \begin{bmatrix} C_{ia} & D_{ir1} C_{o_h} \end{bmatrix} ; \;
C_{cd_h} = \begin{bmatrix} C_{id} & D_{ir2} C_{o_h} \end{bmatrix} ;
$$

$$
D_{ca_{h1}} = \begin{bmatrix} D_{ia1} + D_{ir1} D_{oa_h} \end{bmatrix} ; D_{cd_{h1}} = \begin{bmatrix} D_{id1} + D_{ir1} D_{od_h} \end{bmatrix} ; \;
D_{cr_{h1}} = \begin{bmatrix} D_{ir1} D_{or_h} \end{bmatrix} ;
$$

$$
D_{ca_{h2}} = \begin{bmatrix} D_{ia2} + D_{ir2} D_{oa_h} \end{bmatrix} ; D_{cd_{h2}} = \begin{bmatrix} D_{id2} + D_{ir2} D_{od_h} \end{bmatrix} ; \;
D_{cr_{h2}} = \begin{bmatrix} D_{ir2} D_{or_h} \end{bmatrix}
$$

Where A_i, B_{ia}, B_{id}, B_{ir}, C_{ia}, C_{id}, D_{ia1}, D_{id1}, D_{ir1}, D_{ia2}, D_{id2}, and D_{ir2} are state matrices of the equation (4.68). A_{o_h}, B_{oa_h}, B_{od_h}, B_{or_h}, C_{o_h}, D_{oa_h}, D_{od_h}, and D_{or_h} are state matrices of the equation (4.80).

4.7.2.1.3 Total WVSC system model with hybrid controller

The total WVSC system model with hybrid controller is the cascaded model of the AC source model and complete converter model of the WVSC. To derive the total WVSC system model with hybrid controller, replace $u_s = y_{ca_h}$ in (4.71) and substitute $u_{ca} = C_s \, x_s$ in the resulting expression and in (4.81). The resultant state-space

equations of the total WVSC system model are stated as (4.82).

$$\dot{x}_{sc_h} = A_{sc_h} x_{sc_h} + B_{sc_{dh}} u_{cd} + B_{sc_{rh}} u_{scr}$$
$$y_{sc_{dh}} = C_{sc_{dh}} x_{sc_h} + D_{sc_{dh}} u_{sc_d} + D_{sc_{rh}} u_{scr}$$

(4.82)

Where $x_{sc_h} = \begin{bmatrix} x_{c_h} & x_s \end{bmatrix}^T$; $y_{sc_{dh}} = \begin{bmatrix} i_{DC} \end{bmatrix}$; and the state matrices of the total WVSC system model with hybrid controller are given as below,

$$A_{sc_h} = \begin{bmatrix} A_{c_h} & B_{ca_h} C_s \\ B_s C_{ca_h} & A_s + B_s D_{ca_{h1}} C_s \end{bmatrix} ; \; B_{sc_{dh}} = \begin{bmatrix} B_{cd_h} \\ B_s D_{cd_{h1}} \end{bmatrix} ;$$

$$B_{sc_{rh}} = \begin{bmatrix} B_{cr_h} \\ B_s D_{cr_{h1}} \end{bmatrix} ; \; C_{sc_{dh}} = \begin{bmatrix} C_{cd_h} & 0_{1,4} \end{bmatrix} ; \; D_{sc_{dh}} = D_{cd_{h2}}; \; D_{sc_{rh}} = D_{cr_{h2}}$$

Where A_{c_h}, B_{ca_h}, B_{cd_h}, B_{cr_h}, C_{ca_h}, C_{cd_h}, $D_{ca_{h1}}$, $D_{cd_{h1}}$, $D_{cr_{h1}}$, $D_{ca_{h2}}$, $D_{cd_{h2}}$, and $D_{cr_{h2}}$ are state matrices of the equation 4.81. A_s, B_s, and C_s are state matrices of the equation 4.71.

4.7.2.2 State-space model of the hybrid controller based grid side VSC model

The hybrid controller based grid side VSC model is the combination of the inner and outer controllers. Here, the inner and outer controllers are designed based on PI control and SMC technique, respectively. The linearized state-space model of PI based GVSC inner controller model is explained in section 4.7.1.2.1 and SMC based GVSC outer controller model will be discussed in the succeeding section.

4.7.2.2.1 State-space model of SMC based GVSC outer controller

The SMC based DC voltage controller and SMC based reactive power controller are operated as outer controller for grid side VSC. The linearized state-space model of SMC based GVSC outer controller can be developed from the equations (4.56) and

(4.59). It is given in (4.83).

$$\dot{x}_{o_{gh}} = A_{o_{gh}} x_{o_{gh}} + B_{oa_{gh}} u_{ca} + B_{od_{gh}} u_{cd} + B_{or_{gh}} u_{ir}$$

$$y_{o_{gh}} = C_{o_{gh}} x_{o_g} + D_{oa_{gh}} u_{ca} + D_{od_{gh}} u_{cd} + D_{or_{gh}} u_{ir}$$

(4.83)

Where $x_{o_{gh}} = \begin{bmatrix} E_{s_{DC}} & E_{s_Q} \end{bmatrix}^T$ and $y_{o_{gh}} = y_o$ and the state matrices of the SMC based GVSC outer controller are given as below,

$$A_{o_{gh}} = 0_{2,2}; \ B_{oa_{gh}} = \begin{bmatrix} \frac{K_{DC}\alpha_{DC}}{\phi_{DC}} & 0 \\ 0 & -\frac{K_Q\alpha_Q}{\phi_Q} \end{bmatrix}; \ B_{od_{gh}} = D_{od_{gh}} = 0_{2,1};$$

$$C_{o_{gh}} = I_2; \ B_{or_{gh}} = \begin{bmatrix} -\frac{K_{DC}\alpha_{DC}}{\phi_{DC}} & 0 \\ 0 & \frac{K_Q\alpha_Q}{\phi_Q} \end{bmatrix};$$

$$D_{oa_{gh}} = \begin{bmatrix} \frac{K_{DC}}{\phi_{DC}} & 0 \\ 0 & -\frac{K_Q}{\phi_Q} \end{bmatrix}; \ D_{or_{gh}} = \begin{bmatrix} -\frac{K_{DC}}{\phi_{DC}} & 0 \\ 0 & \frac{K_Q}{\phi_Q} \end{bmatrix}$$

4.7.2.2.2 Complete converter model of the hybrid GVSC

The complete converter model of the hybrid GVSC is the cascaded model of the PI based GVSC inner controller and SMC based GVSC outer controller. To derive the complete converter model, replace $u_{ir_g} = y_{o_{gh}}$ in (4.73). The resultant state-space equations of the GVSC complete converter model are stated as (4.84).

$$\dot{x}_{c_{gh}} = A_{c_{gh}} x_{c_{gh}} + B_{ca_{gh}} u_{ca} + B_{cd_{gh}} u_{cd} + B_{cr_{gh}} u_{cr}$$

$$y_{ca_{gh}} = C_{ca_{gh}} x_{c_g} + D_{ca_{gh1}} u_{ca} + D_{cd_{gh1}} u_{cd} + D_{cr_{gh1}} u_{cr}$$

(4.84)

$$y_{cd_{gh}} = C_{cd_{gh}} x_{c_g} + D_{ca_{gh2}} u_{ca} + D_{cd_{gh2}} u_{cd} + D_{cr_{gh2}} u_{cr}$$

Where $x_{c_{gh}} = \begin{bmatrix} x_i & x_{o_{gh}} \end{bmatrix}^T$ and the complete converter model of the hybrid GVSC state matrices are given as below,

104

$$A_{c_{gh}} = \begin{bmatrix} A_{i_g} & B_{ir_g} C_{o_{gh}} \\ 0_{2,4} & A_{o_{gh}} \end{bmatrix} ; \ B_{ca_{gh}} = \begin{bmatrix} B_{ia_g} + B_{ir_g} D_{oa_{gh}} \\ B_{oa_{gh}} \end{bmatrix} ; \ B_{cd_{gh}} = \begin{bmatrix} B_{id_g} + B_{ir_g} D_{od_{gh}} \\ B_{od_{gh}} \end{bmatrix} ;$$

$$B_{cr_{gh}} = \begin{bmatrix} B_{ir_g} D_{or_{gh}} \\ B_{or_{gh}} \end{bmatrix} ; \ C_{ca_{gh}} = \begin{bmatrix} C_{ia_g} & D_{ir_{g1}} C_{o_{gh}} \end{bmatrix} ; \ C_{cd_{gh}} = \begin{bmatrix} C_{id_g} & D_{ir_{g2}} C_{o_{gh}} \end{bmatrix} ;$$

$$D_{ca_{gh1}} = \begin{bmatrix} D_{ia_{g1}} + D_{ir_{g1}} D_{oa_{gh}} \end{bmatrix} ; D_{cd_{gh1}} = \begin{bmatrix} D_{id_{g1}} + D_{ir_{g1}} D_{od_{gh}} \end{bmatrix} ; \ D_{cr_{gh1}} = \begin{bmatrix} D_{ir_{g1}} D_{or_{gh}} \end{bmatrix} ;$$

$$D_{ca_{gh2}} = \begin{bmatrix} D_{ia_{g2}} + D_{ir_{g2}} D_{oa_{gh}} \end{bmatrix} ; D_{cd_{gh2}} = \begin{bmatrix} D_{id_{g2}} + D_{ir_{g2}} D_{od_{gh}} \end{bmatrix} ; \ D_{cr_{gh2}} = \begin{bmatrix} D_{ir_{g2}} D_{or_{gh}} \end{bmatrix}$$

Where A_{i_g}, B_{ia_g}, B_{id_g}, B_{ir_g}, C_{ia_g}, C_{id_g}, $D_{ia_{g1}}$, $D_{id_{g1}}$, $D_{ir_{g1}}$, $D_{ia_{g2}}$, $D_{id_{g2}}$, and $D_{ir_{g2}}$ are state matrices of the equation (4.73). $A_{o_{gh}}$, $B_{oa_{gh}}$, $B_{od_{gh}}$, $B_{or_{gh}}$, $C_{o_{gh}}$, $D_{oa_{gh}}$, $D_{od_{gh}}$, and $D_{or_{gh}}$ are state matrices of the equation (4.83).

4.7.2.2.3   Total GVSC system model with hybrid controller

The total GVSC system model with hybrid controller is the cascaded model of the AC grid model and complete converter model of the GVSC. To derive the total GVSC system model with hybrid controller, replace $u_g = y_{ca_{gh}}$ in (4.76) and substitute $u_{ca} = C_g\, x_g$ in the resulting expression and in (4.84). The resultant state-space equations of the total GVSC system model are stated as (4.85).

$$
\begin{aligned}
\dot{x}_{gc_h} &= A_{gc_h} x_{gc_h} + B_{gc_{dh}} u_{cd} + B_{gc_{rh}} u_{gc_r} \\
y_{gc_{dh}} &= C_{gc_{dh}} x_{gc_h} + D_{gc_{dh}} u_{cd} + D_{gc_{rh}} u_{gc_r}
\end{aligned}
\tag{4.85}
$$

Where $x_{gc_h} = \begin{bmatrix} x_{c_{gh}} & x_g \end{bmatrix}^T$; $y_{gc_{dh}} = \begin{bmatrix} i_{DC} \end{bmatrix}$; and the state matrices of the total GVSC system model with hybrid controller are given as below,

$$A_{gc_h} = \begin{bmatrix} A_{c_{gh}} & B_{ca_{gh}} C_g \\ B_g C_{ca_{gh}} & A_g + B_g D_{ca_{gh1}} C_g \end{bmatrix} ; \ B_{gc_{dh}} = \begin{bmatrix} B_{cd_{gh}} \\ B_g D_{cd_{gh1}} \end{bmatrix} ;$$

$$B_{gc_{rh}} = \begin{bmatrix} B_{cr_{gh}} \\ B_g D_{cr_{gh1}} \end{bmatrix} ; \ C_{gc_{dh}} = \begin{bmatrix} C_{cd_{gh}} & 0_{1,4} \end{bmatrix} ;$$

$$D_{gc_{dh}} = D_{cd_{gh2}}; \ D_{gc_{rh}} = D_{cr_{gh2}}$$

Where $A_{c_{gh}}$, $B_{ca_{gh}}$, $B_{cd_{gh}}$, $B_{cr_{gh}}$, $C_{ca_{gh}}$, $C_{cd_{gh}}$, $D_{ca_{gh1}}$, $D_{cd_{gh1}}$, $D_{cr_{gh1}}$, $D_{ca_{gh2}}$, $D_{cd_{gh2}}$, and $D_{cr_{gh2}}$ are state matrices of the equation 4.84. A_g, B_g, and C_g are state matrices of the equation 4.76.

4.7.2.3 Total VSC-HVDC system with hybrid controller

The total VSC-HVDC system model with hybrid controller is the cascaded model of the total WVSC system model with hybrid controller, total GVSC system model with hybrid controller and DC-link model. To derive the total VSC-HVDC system model, replace $u_{dc_1} = y_{gc_{dh}}$ and $u_{dc_2} = y_{sc_{dh}}$ in (4.78). The resultant state-space equations of the VSC-HVDC system with hybrid controller model are stated as (4.86).

$$\dot{x}_{sys_h} = A_{sys_h} x_{sys_h} + B_{sys_h} u_{sys_h}$$
$$y_{sys_h} = C_{sys_h} x_{sys_h}$$

(4.86)

Where $x_{sys_h} = \begin{bmatrix} x_{gc_h} & x_{sc_h} & x_{dc} \end{bmatrix}^T$; $u_{sys_h} = \begin{bmatrix} u_{gc_r} & u_{sc_r} \end{bmatrix}^T$; $y_{sys_h} = \begin{bmatrix} x_{gc_h} & x_{sc_h} & x_{dc} \end{bmatrix}^T$ and state matrices of the total VSC-HVDC system model with hybrid controller are given as below,

$$A_{sys_h} = \begin{bmatrix} A_{gc_h} & 0_{10,10} & B_{gc_{dh}}C_{dc_1} \\ 0_{10,10} & A_{sc_h} & B_{gc_{dh}}C_{dc_2} \\ B_{dc_1}C_{gc_{dh}} & B_{dc_2}C_{sc_{dh}} & (A_{dc} + B_{dc_1}D_{gc_{dh}}C_{dc_1} + B_{dc_2}D_{sc_{dh}}C_{dc_2}) \end{bmatrix};$$

$$B_{sys_h} = \begin{bmatrix} B_{gc_{rh}} & 0_{10,2} \\ 0_{10,2} & B_{sc_{rh}} \\ B_{dc_1}D_{gc_{rh}} & B_{dc_2}D_{sc_{rh}} \end{bmatrix}; \ C_{sys_h} = I_3$$

Where A_{sc_h}, $B_{sc_{dh}}$, $B_{sc_{rh}}$, $C_{sc_{dh}}$, $D_{sc_{rh}}$, and $D_{sc_{dh}}$ are the system matrices of the equation (4.82). A_{gc_h}, $B_{gc_{dh}}$, $B_{gc_{rh}}$, $C_{gc_{dh}}$, $D_{gc_{rh}}$, and $D_{gc_{dh}}$ are the system matrices of the equation (4.85). A_{dc}, B_{dc_1}, B_{dc_2}, C_{dc_1}, and C_{dc_2} are the system matrices of the equation (4.78).

4.8   Stability analysis of the VSC-HVDC system

Stability analysis of the VSC-HVDC system includes the stability study on the PI and SMC based controllers; and small signal analysis of the VSC-HVDC system with conventional controllers and hybrid controllers.

4.8.1   Stability study on the controllers

The stability of the controllers is studied using Nyquist plot responses and eigenvalues of the controllers, where eigenvalues are calculated based on the system matrices of the respective controllers. The system matrix can be formed from the closed loop transfer function and state equations of the controllers. The system matrix of the current controller $A_{PI,CC}$ can be derived from closed-loop transfer function of the current controller (4.31) and (B.8) and it is expressed below,

$$A_{PI,CC} = \begin{bmatrix} 0 & 1 & 0 & 0 & 0 \\ 0 & 0 & 1 & 0 & 0 \\ 0 & 0 & 0 & 1 & 0 \\ 0 & 0 & 0 & 0 & 1 \\ \frac{-4K_{I_{CC}}}{T_s{}^3 L} & \frac{-4K_{P_{CC}}}{T_s{}^3 L} & \frac{-4}{T_s{}^3} & \frac{-8}{T_s{}^2} & \frac{-5}{T_s} \end{bmatrix}$$

The system matrix of the PI based AC voltage controller $A_{PI,AC}$ can be derived from closed-loop transfer function of the PI based AC voltage controller (4.36) and (B.8) and it is given below,

$$A_{PI,AC} = \begin{bmatrix} 0 & 1 & 0 & 0 \\ 0 & 0 & 1 & 0 \\ 0 & 0 & 0 & 1 \\ \frac{-2K_{I_{AC}}}{T_s{}^2 C_f} & \frac{-2K_{P_{AC}}}{T_s{}^2 C_f} & \frac{-2}{T_s{}^2} & \frac{-3}{T_s} \end{bmatrix}$$

The system matrix of the PI based DC voltage controller $A_{PI,DC}$ can be derived from closed-loop transfer function of the PI based DC voltage controller (4.45) and (B.8)

and it is shown below,

$$
A_{PI,DC} = \begin{bmatrix} 0 & 1 & 0 & 0 \\ 0 & 0 & 1 & 0 \\ 0 & 0 & 0 & 1 \\ \frac{-2K_{I_{DC}}}{T_s{}^2 C_{DC}} & \frac{-2K_{P_{DC}}}{T_s{}^2 C_{DC}} & \frac{-2}{T_s{}^2} & \frac{-3}{T_s} \end{bmatrix}
$$

The system matrix of the SMC based AC voltage controller $A_{SMC,AC}$ can be derived from closed-loop transfer function of the SMC based AC voltage controller (4.55) and (B.8) and it is given below,

$$
A_{SMC,AC} = \begin{bmatrix} 0 & 1 & 0 & 0 \\ 0 & 0 & 1 & 0 \\ 0 & 0 & 0 & 1 \\ \frac{-2K_{AC}\alpha_{AC}}{T_s{}^2 C_f \phi_{AC}} & \frac{-2K_{AC}}{T_s{}^2 C_f \phi_{AC}} & \frac{-2}{T_s{}^2} & \frac{-3}{T_s} \end{bmatrix}
$$

The system matrix of the SMC based DC voltage controller $A_{SMC,DC}$ can be derived from closed-loop transfer function of the SMC based DC voltage controller (4.57) and (B.8) and it is shown below,

$$
A_{SMC,DC} = \begin{bmatrix} 0 & 1 & 0 & 0 \\ 0 & 0 & 1 & 0 \\ 0 & 0 & 0 & 1 \\ \frac{-2K_{DC}\alpha_{DC}}{T_s{}^2 C_{DC} \phi_{DC}} & \frac{-2K_{DC}}{T_s{}^2 C_{DC} \phi_{DC}} & \frac{-2}{T_s{}^2} & \frac{-3}{T_s} \end{bmatrix}
$$

Nyquist plot responses of the PI based AC voltage controller, PI based current controller, PI based DC voltage controller, SMC based AC voltage controller, and SMC based DC voltage controller are illustrated in Figure 4.17. The Nyquist stability condition states that if the Nyquist contour in s-plane encircles the point (-1+0j) in the anti-clockwise direction as many times as the number of the right half s-plane poles of open-loop transfer function then, the closed-loop system is stable (Kani, 2014). Tables 4.2 and 4.3 detail the eigenvalues of the PI based controllers and eigenvalues of the SMC based controllers, respectively.
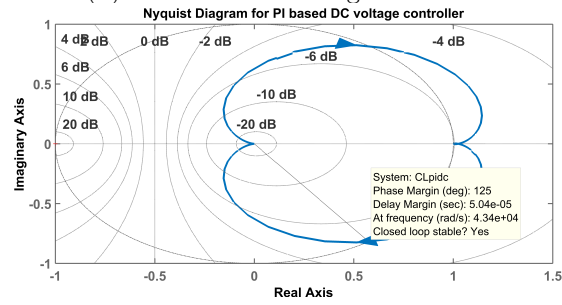
The stability condition states that if the system poles are placed on the left side of the s-plane, then the system is stable. The eigenvalues of the PI and SMC based controllers satisfy the stability condition. The PI based and SMC based controllers
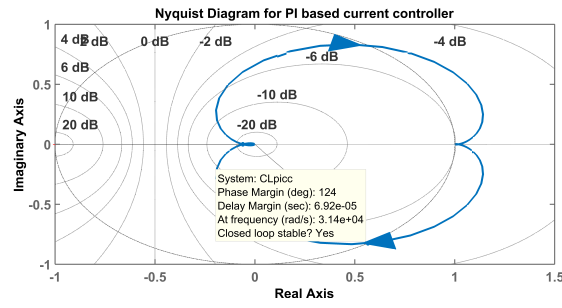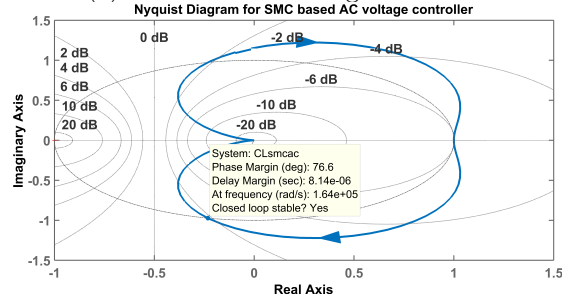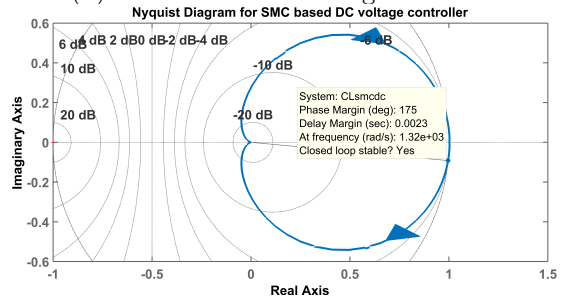
(a) Current controller
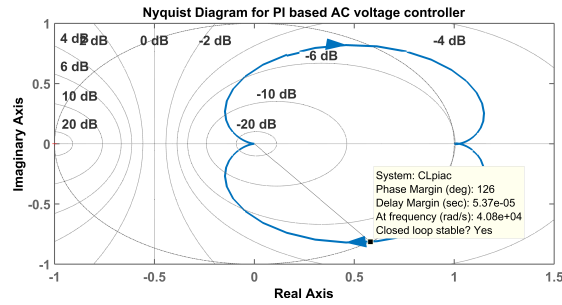
(b) PI based AC voltage controller

(c) PI based DC voltage controller

(d) SMC based AC voltage controller

(e) SMC based DC voltage controller

Figure 4.17: Nyquist plot responses of the controllers

have fulfilled the Nyquist stability condition. Therefore, it can be concluded that the PI and SMC based controllers are stable. From Table 4.2, the dominant pole of the PI based AC voltage controller λ_4 and dominant pole of the PI based DC voltage controller λ_{13} are located far away from the origin point on the left side of the s-plane. From Table 4.2, the dominant pole of the SMC based AC voltage controller λ_4 and dominant pole of the SMC based DC voltage controller λ_8 are located closer to the origin point on the left side of the s-plane. If the dominant pole position far away in the negative direction, then system is stable , but the system response become too slow. From dominant pole positions of the SMC based controllers, the system response faster compared to PI based controllers. The PI based controller ploes are located far away from the origin point in negative direction as compared to SMC based controller ploes. So, the PI based controllers are relatively more stable as compared to SMC based controllers. Table 4.4 details the time domain specifications of the controllers concerning the settling time and rise time. From Table 4.4, it is observed that the SMC based controllers have acquired less settling time as compared to PI-based controllers.

Table 4.2: Eigenvalues of the PI based controllers

Controller	Eigenvalues
AC voltage controller (λ_{1-4})	-4.3176e5
	-1.0353e5
	-5.2023e5
	-1.2690e4
Current controller (λ_{5-9})	-4.2782e5+9.1586e4i
	-4.2782e5-9.1586e4i
	-9.4808e4
	-4.0475e4
	-9.0687e3
DC voltage controller (λ_{10-13})	-4.3326e5
	-8.7392e4
	-6.7052e4
	-1.2295e4

Table 4.3: Eigenvalues of the SMC based controllers

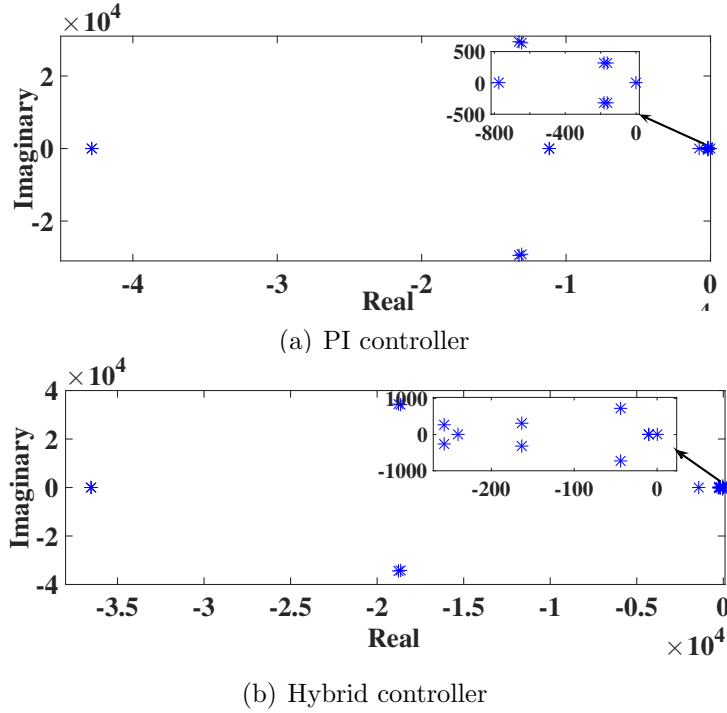| Controller	Eigenvalues
AC voltage controller (λ_{1-4})	-4.7569e5 -6.2151e4 +1.3010e5i -6.2151e4 -1.3010e5i -3.9001
DC voltage controller (λ_{5-8})	-4.1266e5 -1.7166e5 -1.5629e4 -50.1812

Table 4.4: Time domain specifications of the designed controllers

Controller	Settling time (ms)	Rise time (ms)
PI based AC voltage controller	0.267	0.027
SMC based AC voltage controller	0.058	0.010
PI based DC voltage controller	0.262	0.026
SMC based DC voltage controller	0.246	0.140

4.8.2 Small signal analysis on the VSC-HVDC system

The small-signal analysis has been done on the linearized model of the grid-integrated VSC-HVDC system. The eigenmatrix of total VSC-HVDC system with conventional controller system matrix A_{sys} and total VSC-HVDC system with hybrid controller sysem matrix A_{sys_h} has the 23 eigenvalues. Equations (4.79) and (4.86), include the dynamics of the total system with conventional controller and hybrid controller; and the system stability can be decided by analyzing the location of the eigenvalues. Figures 4.18(a) and 4.18(b) show the eigenvalues of the total VSC-HVDC system. The effect of parameter uncertainty on stability of the total system is explained through the variation of the C_f and ω. Hence, the values of the C_f and ω are subjected to small variations and it is reflected on the system performance and stability. Small variations in C_f can be due to reactive power compensation and AC filter harmonics; whereas small changes in frequency ω can be associated to grid transients. The locations of the system eigenvalues vary with respect to the variations of the C_f and ω values.

Figure 4.19(a) shows the eigenvalues plot for total system with conventional con-

(a) PI controller

(b) Hybrid controller

Figure 4.18: Eigenvalue plot of the total VSC-HVDC system

troller when C_f values vary from $12.59\mu F$ to $100.73\mu F$. Also, the zoomed view of the region closer to the instability area is shown in Figure 4.19(b). Figure 4.20(a) shows the eigenvalues plot for total system with hybrid controller when C_f values vary from $12.59\mu F$ to $100.73\mu F$. Also, the zoomed view of the region closer to the instability area is shown in Figure 4.20(b). From Figures 4.19 and 4.20, it can be observed that the location of eigenvalues is shifting to the stability region with respect to variation of C_f values.

Figure 4.21(a) shows the eigenvalues plot for total system with conventional controller when ω values varies from 280 rad/sec to 346 rad/sec. In addition, the zoomed view of the region closer to the instability area is shown in Figure 4.21(b). Figure 4.22(a) shows the eigenvalues plot for total system with hybrid controller when ω values varies from 280 rad/sec to 346 rad/sec. In addition, the zoomed view of the region closer to the instability area is shown in Figure 4.22(b). Figure 4.21 and 4.22, show how the variation in ω value influence the system stability.

112
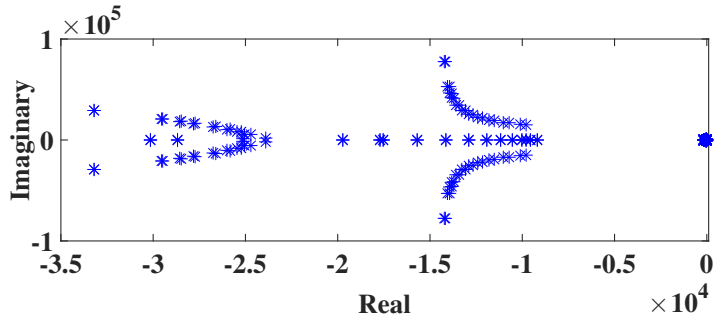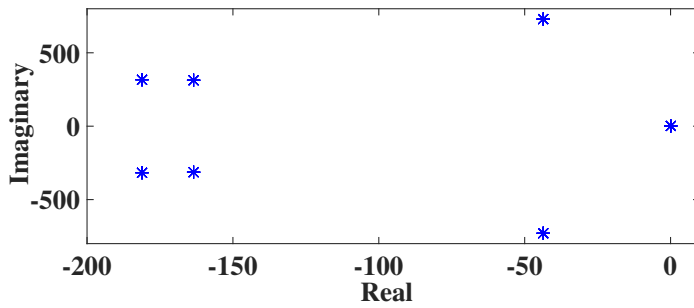
(a) Total Plot

(b) Zoomed view of the region closer to the instability area

Figure 4.19: Eigenvalue plot of VSC-HVDC system with PI controller for variable C_f values from $12.59\mu F$ to $100.73\mu F$
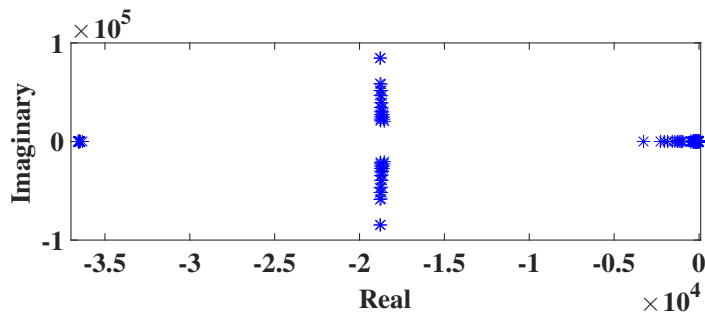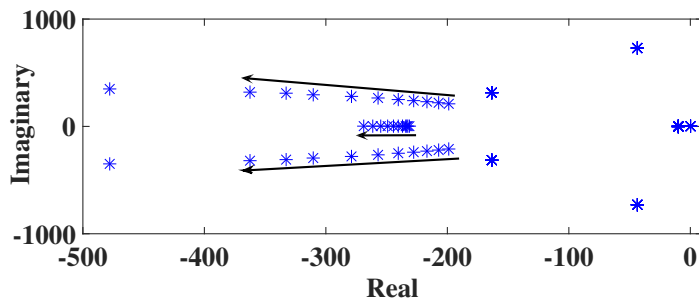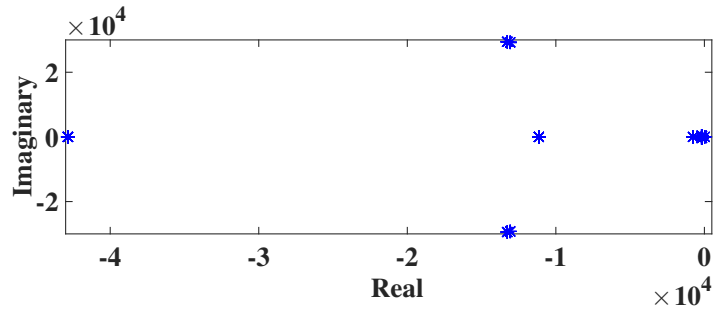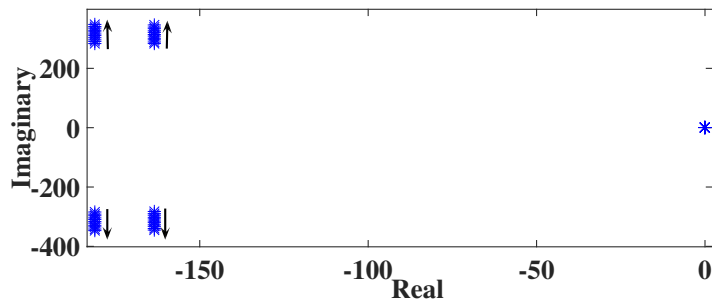

(a) Total Plot

(b) Zoomed view of the region closer to the instability area

Figure 4.20: Eigenvalue plot of VSC-HVDC system with hybrid controller for variable C_f values from $12.59\mu F$ to $100.73\mu F$
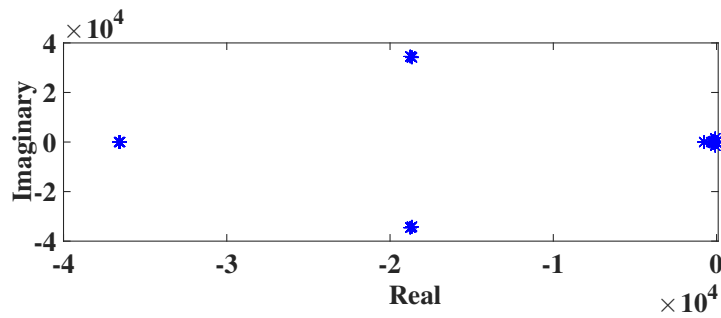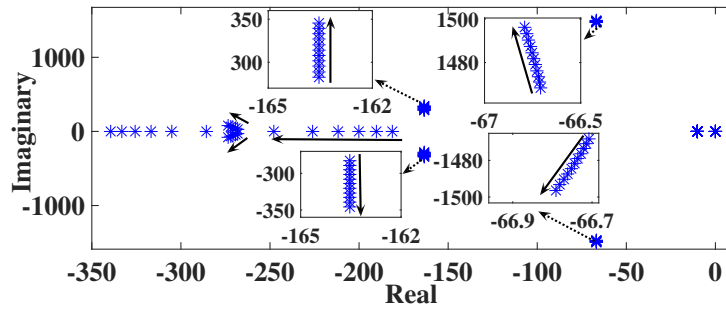
(a) Total Plot

(b) Zoomed view of the region closer to the instability area

Figure 4.21: Eigenvalue plot VSC-HVDC system with PI controller for variable ω from 280 rad/sec to 346 rad/sec

(a) Total Plot

(b) Zoomed view of the region closer to the instability area

Figure 4.22: Eigenvalue plot VSC-HVDC system with hybrid controller for variable ω from 280 rad/sec to 346 rad/sec

114

4.9   Simulation results and analysis

The performance of a 400MW OSWF integrated to onshore AC grid with VSC-HVDC transmission system is investigated using the MATLAB/Simulink software, where proposed hybrid control and conventional control schemes are implemented. The specifications and tuned gain values of controllers for the VSC-HVDC system are detailed in Tables 4.1 and 4.5, respectively. The gain values of PI-based and SMC-based controllers are computed through the PID tuner tool and GA method, respectively. The performance of the VSC-HVDC system under different cases is presented in this section. Cases considered are (i) 3-phase to ground (LLLG) fault near to grid, (ii) phase to ground (LG) fault near to grid (iii) step change of the wind speed from 12m/s to 13m/s, and (iv) step change of the wind speed from 13m/s to 12m/s.

**Table 4.5:** Tuned gain values of the controllers

System	Parameters	Values
WVSC gain values	$K_{P_{AC}}$	2.1
	$K_{I_{AC}}$	18579.0
	$K_{P_{CC}}$	838.6
	$K_{I_{CC}}$	5590900.0
	K_{AC}	3.9
	α_{AC}	10.0
	ϕ_{AC}	1.6
GVSC gain values	$K_{P_{DC}}$	19.3
	$K_{I_{DC}}$	175500.0
	K_{P_Q}	1.8
	K_{I_Q}	300000.0
	K_{DC}	3.9
	α_{DC}	10.0
	ϕ_{DC}	1.6
	K_Q	3.9
	α_Q	5.0
	ϕ_Q	0.5

In case 1, to study the FRT performance of the VSC-HVDC system during the abnormal situation by applying the LLLG fault near to AC grid. The fault is created

at 3s with duration of 0.1s and it is cleared at 3.1s as given in Figures 4.23 and 4.24. In faulty condition, the responses of grid-integrated VSC-HVDC system for PI and hybrid controllers are displayed in Figures 4.23 and 4.24, respectively. In fault duration, the grid voltage is decreased to a minimum level and it can be seen in the grid side voltage waveform as shown in Figure 4.24(a). When the LLLG fault occurs, the DC-link voltage V_{DC} drops as shown in Figures 4.23(d) and 4.24(d). It affects the active power transmitted to the AC grid. Response of grid active power with hybrid controller is seen in Figure 4.24(b) and it takes 0.7s to reach the pre-fault value where as PI controller takes 1.4s as seen in Figure 4.23(b). Due to the rapid drop of V_{DC}, the grid reactive power fluctuates and it can be seen in Figure 4.23(c) and Figure 4.24(c). The grid reactive power is stablized at -0.01pu value within 0.2s for both PI and hybrid controllers. From the observation of Figures 4.23(d) and 4.24(d), the V_{DC} response of hybrid controller stabilized at 1pu value within 0.92s and PI controller takes 1.15s.

In case 2, to study the FRT performance of the VSC-HVDC system during the abnormal situation by applying the LG fault near to AC grid. The fault is created at 3s with duration of 0.1s and it is cleared at 3.1s as given in Figures 4.25 and 4.26. In faulty condition, the responses of grid-integrated VSC-HVDC system for PI and hybrid controllers are displayed in Figures 4.25 and 4.26, respectively. Dufing the fault duration, the grid voltage is decreased to a minimum level and it can be seen in the grid side voltage waveform as shown in Figure 4.26(a). When the LG fault occurs, the DC-link voltage V_{DC} drops as shown in Figures 4.25(d) and 4.26(d). It affects the active power transmitted to the AC grid. Response of grid active power with hybrid controller is seen in Figure 4.26(b) and it takes 0.65s to reach the pre-fault value where as PI controller takes 1s as seen in Figure 4.25(b). Due to the rapid drop of V_{DC}, the grid reactive power is fluctuated and it can be seen in Figures 4.25(c) and 4.26(c). The grid reactive power is stablized at -0.01pu value within 0.2s for both PI and hybrid controllers. From the observation of Figures 4.25(d) and 4.26(d), the V_{DC} response of hybrid controller stabilized at 1pu value within 0.93s and PI controller takes 1.15s. The time taken to restore the pre-fault values of grid active power, grid reactive power and DC-link voltage for VSC-HVDC system with LLLG fault and LG fault conditions are given in Table 4.6.
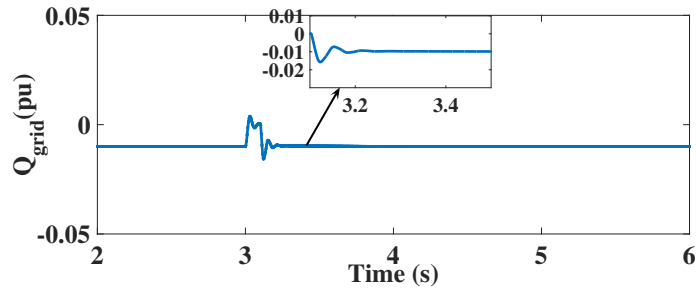
In case 3, the wind speed experienced by wind turbines in OSWF is raised at time 3.5s from 12 m/s to rated value (13m/s). It means the 12m/s is 0.923 pu of rated wind
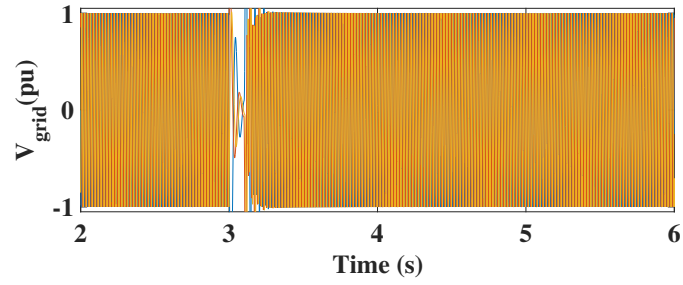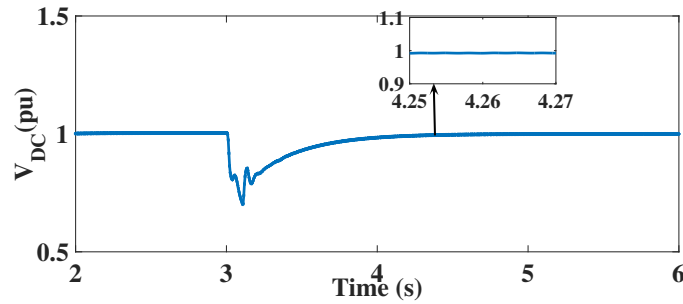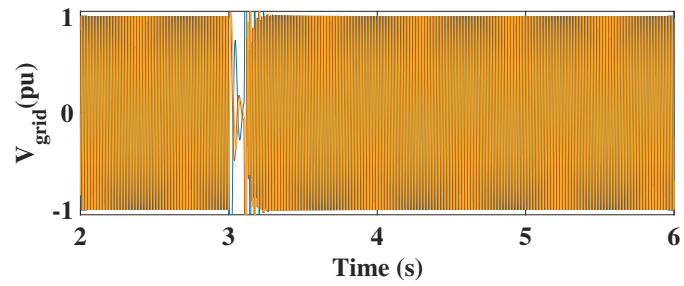
(a) Grid voltage
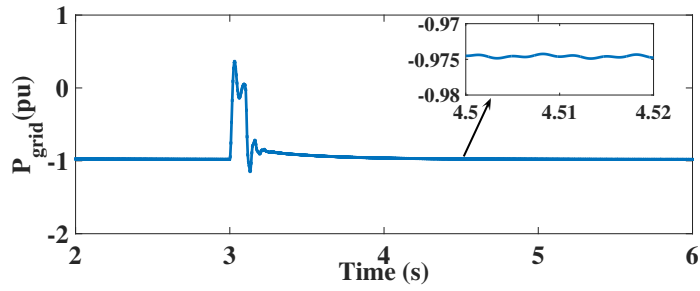
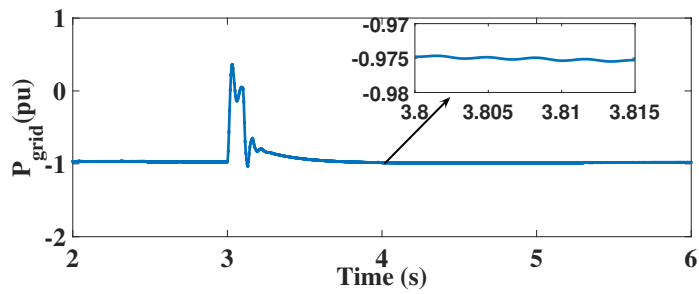(b) Grid active power

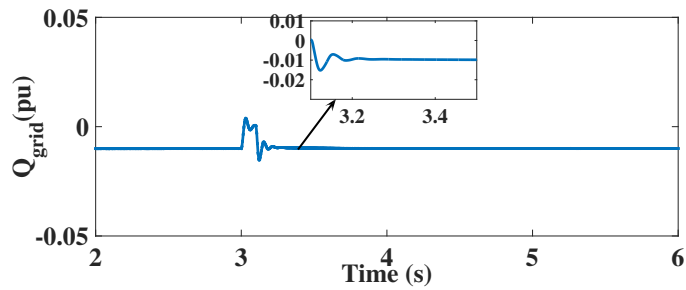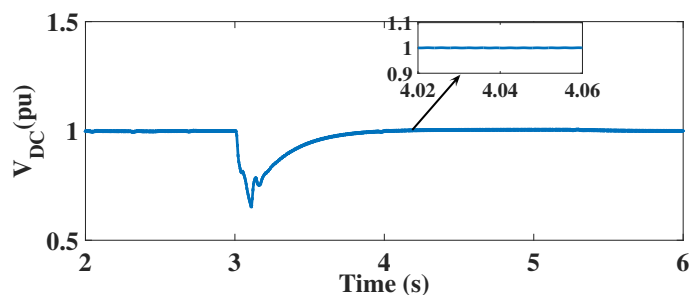(c) Grid reactive power

(d) DC-link voltage

Figure 4.23: Responses of the VSC-HVDC system with PI controller for LLLG fault
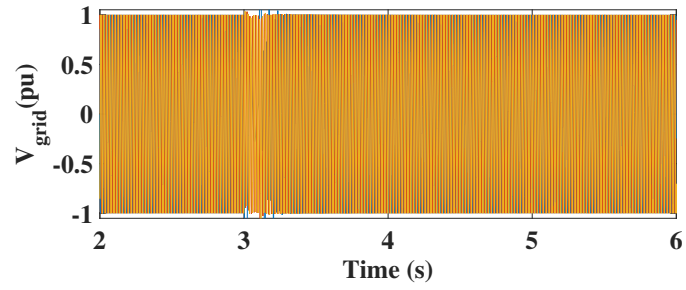
117

(a) Grid voltage

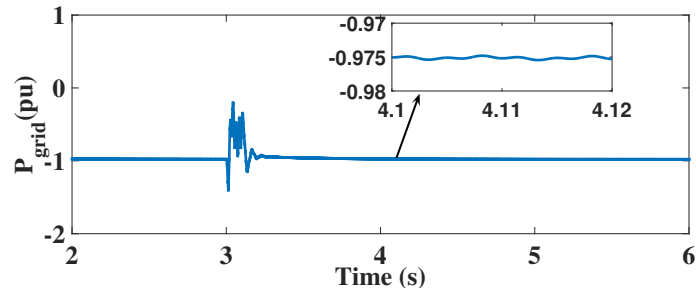

(b) Grid active power

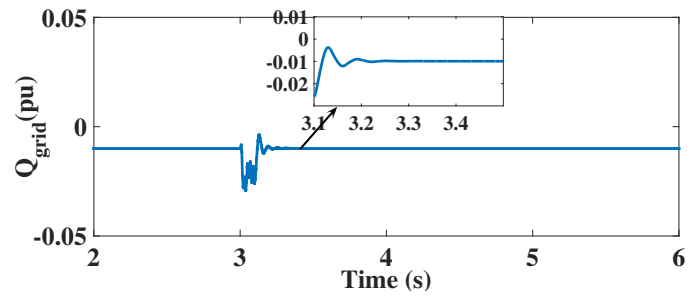(c) Grid reactive power

(d) DC-link voltage

Figure 4.24: Responses of the VSC-HVDC system with hybrid controller for LLLG fault

(a) Grid voltage

(b) Grid active power

(c) Grid reactive power

(d) DC-link voltage

Figure 4.25: Responses of the VSC-HVDC system with PI controller for LG fault
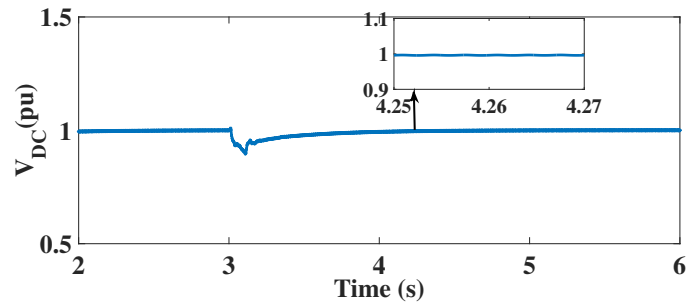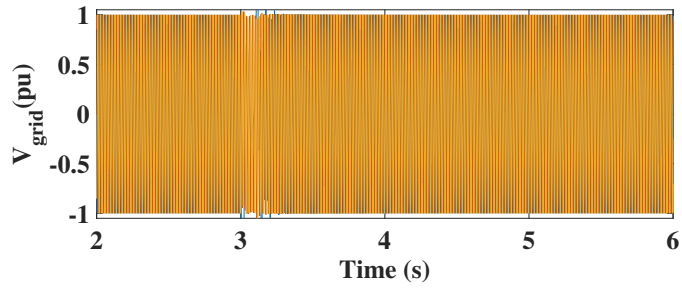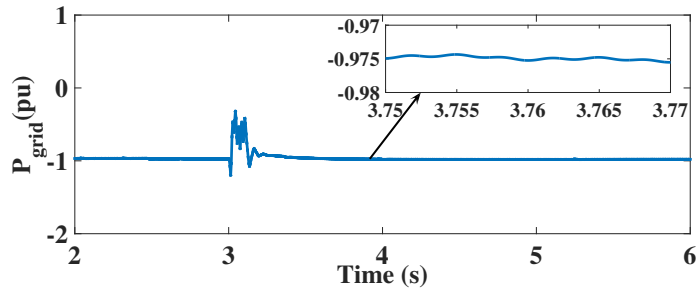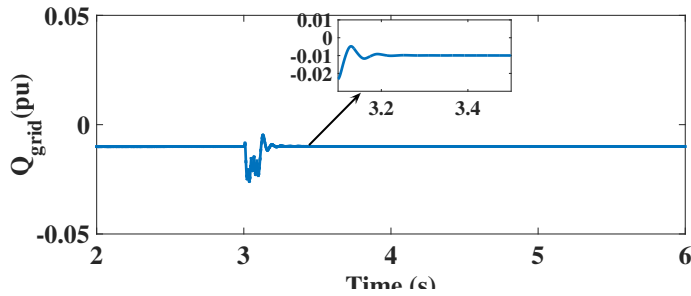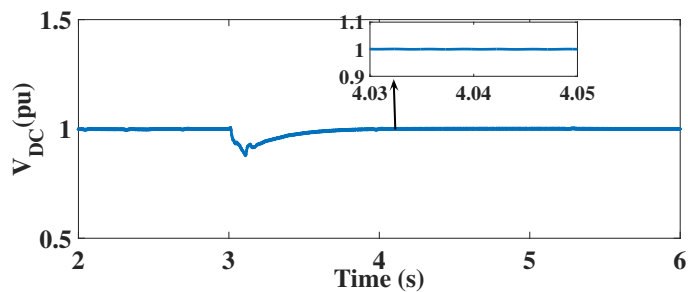
(a) Grid voltage

(b) Grid active power

(c) Grid reactive power

(d) DC-link voltage

Figure 4.26: Responses of the VSC-HVDC system with hybrid controller for LG fault

**Table 4.6:** Time taken to restore the pre-fault values for VSC-HVDC system

| Specification | Time taken to restore the pre-fault values (s) | | | |
| | LLLG fault | | LG fault | |
	PI controller	Hybrid controller	PI controller	Hybrid controller
Grid active power	1.40	0.70	1.00	0.65
Grid reactive power	0.20	0.20	0.20	0.20
DC-link voltage	1.15	0.92	1.15	0.93

speed and the power generated by OSWF is 0.8 pu. For 13m/s, the power generated by OSWF is 0.975 pu. Figures 4.27 and 4.28 show the responses of the VSC-HVDC system with PI controller and hybrid controller, respectively. From Figures 4.27(c) and 4.28(c) it is observed that, the hybrid controller takes 0.64s to reach the 0.975pu after a step change of wind speed at 3.5s and the PI controller takes 0.9s to reach 0.975pu value. Source reactive power is maintained at 0.01pu value and it can be observed from Figures 4.27(b) and 4.28(b). Grid reactive power is maintained at -0.01pu value and it can be observed from Figures 4.27(d) and 4.28(d). DC-link voltage is stabilized at 1 pu and it can be seen from Figures 4.27(e) and 4.28(e).

In case 4, the wind speed experienced by wind turbines in OSWF is stepped down at time 3.5s from the rated value (13m/s) to 12m/s. It means the active power step down from 1pu to 0.8pu at time 3.5s. Figures 4.29 and 4.30 show the responses of the VSC-HVDC system with PI controller and hybrid controller, respectively. From Figures 4.29(c) and 4.30(c) it is observed that, the hybrid controller takes 0.504s to reach the 0.8pu after a step change of wind speed at 3.5s and the PI controller takes 1.5s to reach 0.8pu. Source reactive power is maintained at 0.01pu value and it can be observed from Figures 4.29(b) and 4.30(b). Grid reactive power is maintained at -0.01pu value and it can be observed from Figures 4.29(d) and 4.30(d). DC-link voltage is stabilized at 0.9 pu and it can be seen from Figures 4.29(e) and 4.30(e).

4.10   Summary

In this chapter, a hybrid control scheme is proposed for an onshore AC grid integrated to an offshore wind farm with VSC-HVDC transmission link. A SMC and conventional PI control techniques are adopted to design the proposed hybrid controller for wind farm side and grid side VSCs, where outer and inner controllers are based on
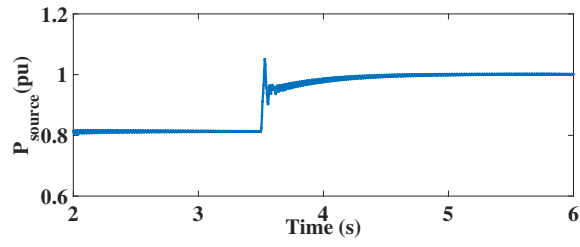
(a) Source active power
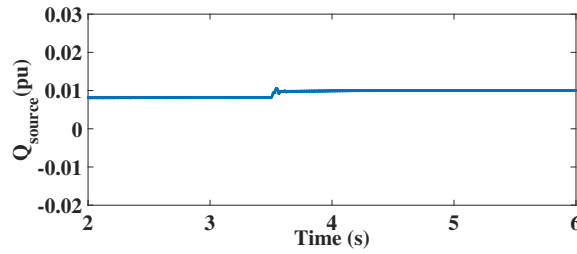
(b) Source reactive power
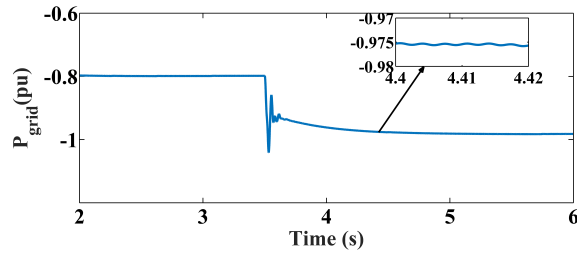
(c) Grid active power

(d) Grid reactive power

(e) DC-link voltage

Figure 4.27: Responses of the VSC-HVDC system with PI controller for step change wind speed from 12 m/s to 13 m/s

(a) Source active powere

(b) Source reactive power

(c) Grid active power

(d) Grid reactive power

(e) DC-link voltage

Figure 4.28: Responses of the VSC-HVDC system with hybrid controller for step change wind speed from 12 m/s to 13 m/s

123

(a) Source active power

(b) Source reactive power

(c) Grid active power

(d) Grid reactive power

(e) DC-link voltage

Figure 4.29: Responses of the VSC-HVDC system with PI controller for step change wind speed from 13 m/s to 12 m/s
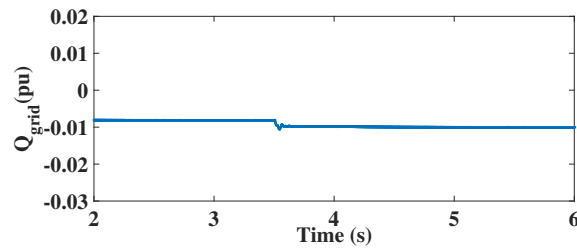
(a) Source active power
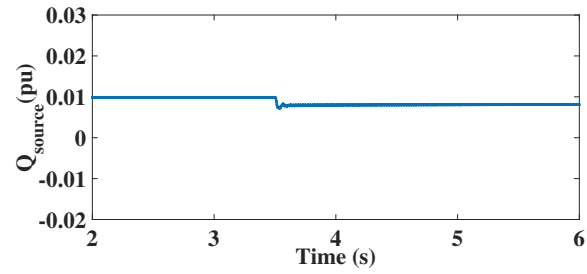
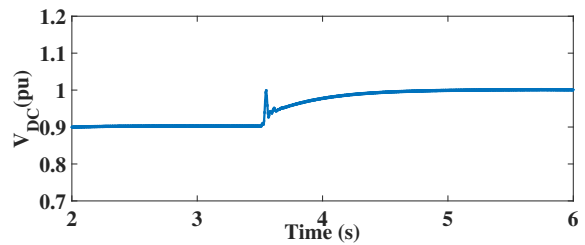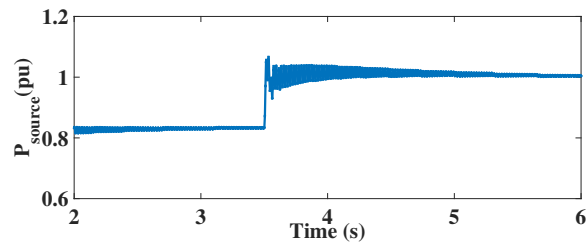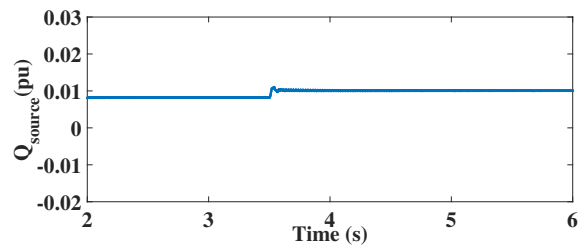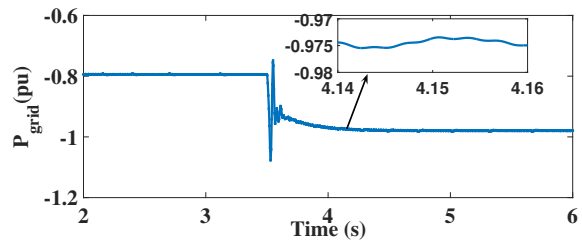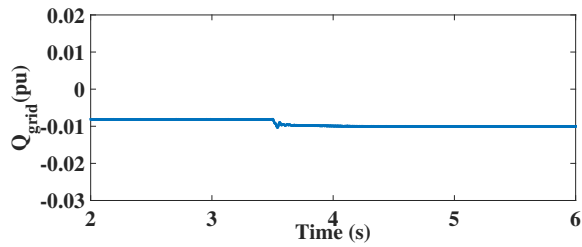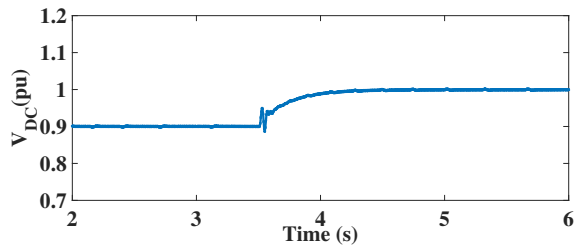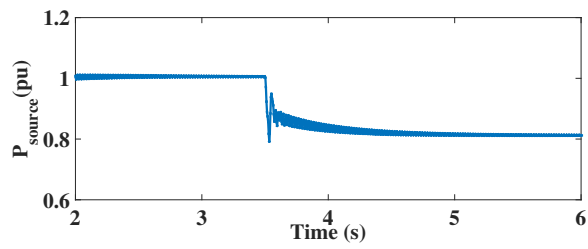(b) Source reactive power

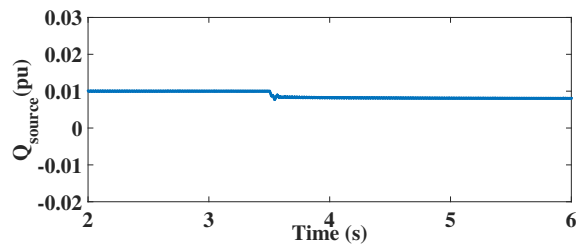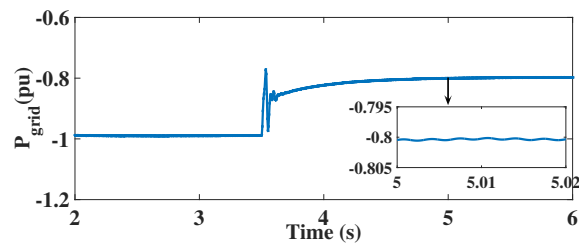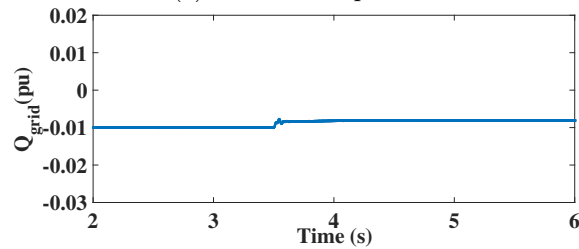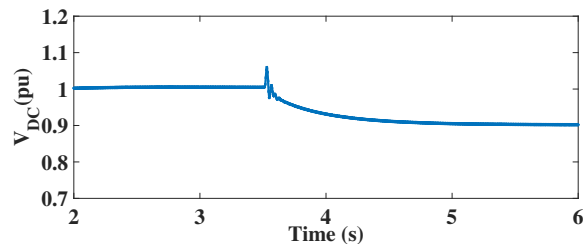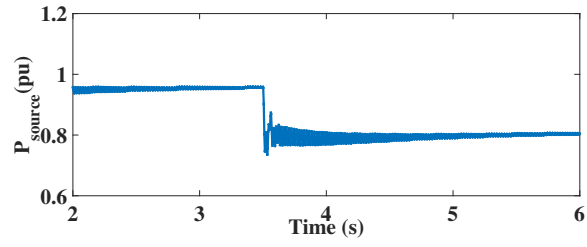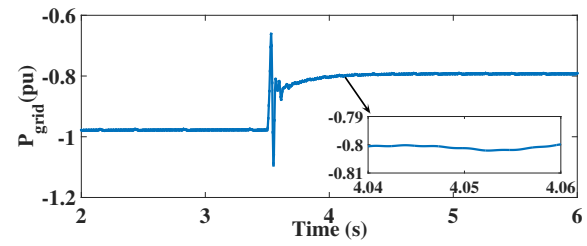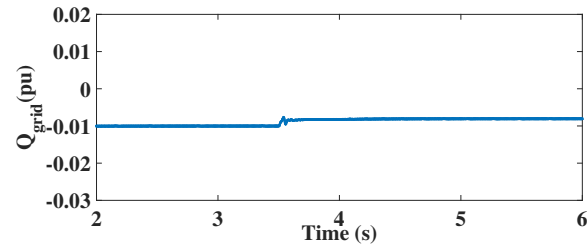(c) Grid active power

(d) Grid reactive power
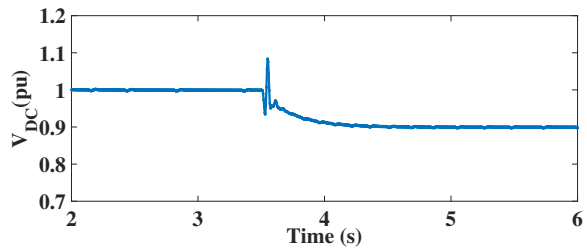
(e) DC-link voltage

Figure 4.30: Responses of the VSC-HVDC system with hybrid controller for step change wind speed from 13 m/s to 12 m/s

SMC and PI, respectively. It is designed for obtaining the effective power transfer between the source and grid. The mathematical modelling, dynamic modelling and state-space model of the VSC-HVDC system are discussed. The performance of the VSC-HVDC system with hybrid and conventional controller for various cases (LLLG, LG, wind speed stepped up, and wind speed stepped down) are analyzed and compared. Furthermore, the FRT capability is examined by applying the symmetrical and unsymmetrical faults at grid end. The WVSC side controller is operated to maintain the AC voltage. The GVSC side controller is operated to maintain the stable DC-link voltage and to control grid reactive power to minimum value.The proposed controller is operated to reach the pre-fault value of grid active power and DC-link voltage within less time as related to the conventional controller. The system stability is analyzed with the help of the eigenvalue plots for the parameter uncertainty which includes a variation of the AC filter capacitance and system frequency values. Additionally, the Nyquist plot and eigenvalue analysis are used to observe the controller stability. The time domain specifications of the designed controller in terms of settling time and rise time are evaluated based on the ste response of the controllers. It is found that the SMC baased controller has less settling time compared to PI and rise time is comparable with PI. With regard to settling and rise time, where the SMC based controllers have taken less settling time compared to conventional controllers. Finally, it is concluded that the VSC-HVDC system with the proposed hybrid controller is stable and gives better performance with regard to the FRT capability under a fault condition compared to conventional PI controller.

Chapter 5 deals with the new controller approach for grid integration of the OS-WFs with multi-terminal VSC-HVDC transmission system. The controller is designed to regulate the DC-link voltage, AC voltage, active, and reactive power. The proposed hybrid controller approach is developed by adopting the sliding mode control and conventional PI control techniques. The dynamic modelling and linearized state space modelling of the conventional controller based multi-terminal VSC-HVDC system and hybrid controller based multi-terminal VSC-HVDC system are discussed.

Chapter 5

CONTROLLER DESIGN FOR GRID-INTEGRATED OFFSHORE WIND FARMS WITH MULTI-TERMINAL VSC-HVDC SYSTEM

5.1 Introduction

In this chapter, the hybrid controller design for grid-integrated OSWFs with multi-terminal VSC-HVDC transmission system is explained and the performance of the multi-terminal VSC-HVDC system is analyzed based on FRT capability and small signal analysis of the system. To do the FRT capability analysis of the multi-terminal VSC-HVDC system, the symmetrical and unsymmetrical faults are applied near to the grid. The multi-terminal VSC-HVDC system controller deals with the effective power transmission between the OSWFs and grid. However, the effective power transmission between the VSC's depends on the stable DC-link voltage. Hence, the controller must be designed to regulate the DC-link voltage, AC voltage, active, and reactive power. The proposed hybrid controller approach is developed by adopting the sliding mode control and conventional PI control techniques.

This chapter is documented as follows: Firstly, the configuration and analytical

model of the multi-terminal VSC-HVDC system is explained, followed by the proposed controller design for a wind farm side VSC and grid side VSC are discussed. Secondly, dynamic modelling of the multi-terminal VSC-HVDC system is discussed. Detailed explanation on Linearized state-space model of the multi-terminal VSC-HVDC system is discussed in next section, followed by small signal analysis on the multi-terminal VSC-HVDC system are explained. Lastly, the simulation results and analysis of the multi-terminal VSC-HVDC system followed by summary is detailed

5.2   Configuration of the multi-terminal VSC-HVDC system

The outline of the multi-terminal VSC-HVDC system, where two OSWFs are interconnected to an AC grid through a three-terminal VSC-HVDC transmission system is shown in Figure 5.1. The wind turbines in the 400 MW OSWF1 are interconnected to 33 kV AC collector bus and it is coupled to WVSC1 through the step-up transformer 1 which is rated as 33/150 kV. The 400MW OSWF2 is interconnected to 33 kV AC collector bus and it is coupled to WVSC2 through the step-up transformer 2 which is rated as 33/150 kV. The WVSC1, WVSC2, and grid side VSC are connected by the 100 km length of the DC cable. The GVSC and WVSC are operated based on the proposed hybrid controller with PWM technique. The AC filters are placed next to the transformer 1, 2 and preceding the transformer 3. The GVSC and 400 kV onshore AC grid are connected through the step-up transformer3 which is rated as 150/400 kV. Table 5.1 details the multi-terminal VSC-HVDC system specifications.

5.3   Conventional controller design for VSC-HVDC system

The design of the conventional controller is based on the PI control technique. The grid-integrated OSWF with VSC-HVDC link involves the WVSC and GVSC, where each VSC controller consists of an inner controller and outer controller. The inner and outer controllers are designed by adopting the PI technique. The inner controller has to control the AC current while it tracks the reference output provided by the outer controller. The outer controller of WVSC produces the output signals as dq

128
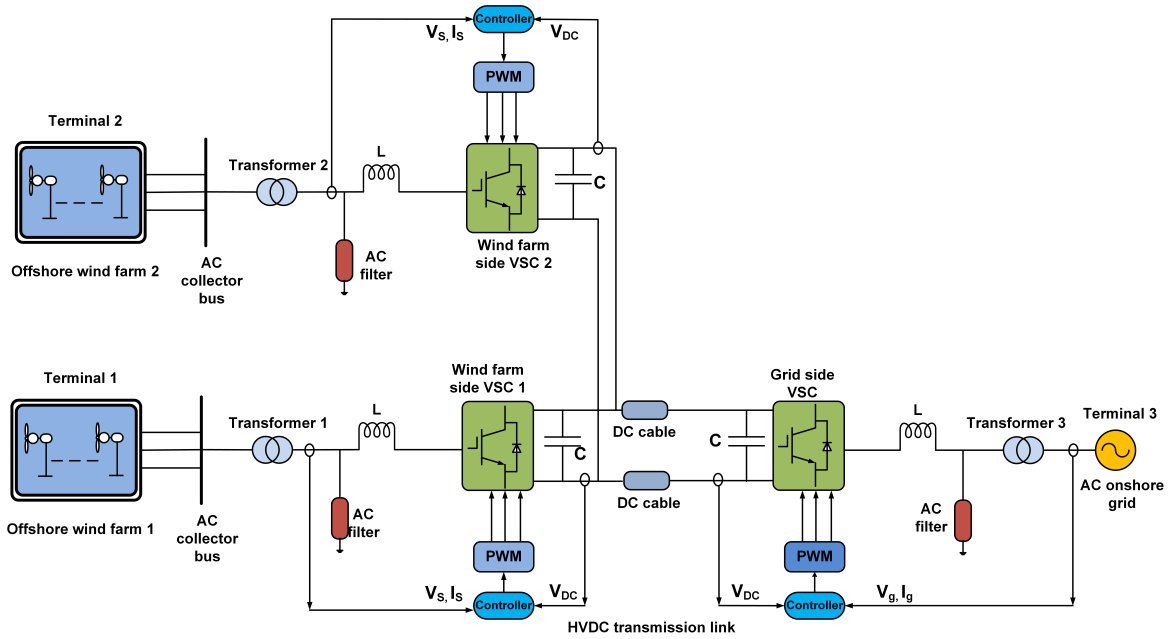
Figure 5.1: Single line diagram of the grid-integrated OSWFs with multi-terminal VSC-HVDC transmission system

Table 5.1: Specifications of multi-terminal VSC-HVDC system

System	Specifications	Values
OSWF side	Rated power of OSWF 1	400 MW (0.5 pu)
	Rated power of OSWF 2	400 MW (0.5 pu)
	Transformer 1	33/150 $kV_{ph-ph,rms}$
	Transformer 2	33/150 $kV_{ph-ph,rms}$
DC link	Length	100 km
	Capacitor	225 μ F
Grid side	Transformer 3	150/400 $kV_{ph-ph,rms}$
	Grid voltage	400 $kV_{ph-ph,rms}$
AC filter	Inductance	16.700 μ H
	Capacitance	50.368 μ F
	Resistance	0.579 ohms

component currents $i^*_{ws,d}$ and $i^*_{ws,q}$. The inner controller of WVSC produces the output signals as dq component voltages $V^*_{cs,d}$ and $V^*_{cs,q}$. The outputs of the inner controller is coupled to PWM generator through the dq to abc converter. The AC voltage controller performs as an outer controller of WVSC and it regulates the AC voltage. The conventional controller design of the WVSC is shown in Figure 4.2.

The outer controller of GVSC produces the output signals as dq component currents $i^*_{wg,d}$, and $i^*_{wg,q}$. The inner controller of GVSC produces the output signals as dq component voltages $V^*_{cg,d}$ and $V^*_{cg,q}$. The output of the inner controller is coupled to PWM generator through the dq to abc converter. The DC voltage and reactive power controllers act as an outer controller of the GVSC and it governs the DC-link voltage and grid reactive power. The conventional controller design of the GVSC is shown in Figure 4.3.

5.4 Hybrid controller design for VSC-HVDC system

The design of the hybrid controller is based on the combination of the conventional PI and SMC control techniques. It can give effective control to the system by controlling the parameters such as active power, reactive power, DC-link voltage, AC current, and AC voltage. The grid-integrated OSWF with VSC-HVDC link involves the WVSC and GVSC, where each VSC controller consists of an inner and outer controller. The inner and outer controllers are designed by adopting the PI and SMC techniques, respectively. The inner controller has to control the AC current while it tracks the reference output provided by the outer controller. The outer controller of WVSC produces the output signals as dq component currents $i^*_{ws,d}$ and $i^*_{ws,q}$. The inner controller of WVSC produces the output signals as dq component voltages $V^*_{cs,d}$ and $V^*_{cs,q}$. The outputs of the inner controller is coupled to PWM generator through the dq to abc converter. The AC voltage controller performs as an outer controller of WVSC and it regulates the AC voltage. The hybrid controller design of the WVSC is shown in Figure 4.4.

The outer controller of GVSC produces the output signals as dq component currents $i^*_{wg,d}$, and $i^*_{wg,q}$. The inner controller of GVSC produces the output signals as dq component voltages $V^*_{cg,d}$ and $V^*_{cg,q}$. The output of the inner controller is coupled

to PWM generator through the dq to abc converter. The DC voltage and reactive power controllers act as an outer controller of the GVSC and it regulates the DC-link voltage and grid reactive power. The hybrid controller design of the GVSC is shown in Figure 4.5.

Dynamic modelling of the multi-terminal VSC-HVDC system is explained in following section. It elaborates the dynamic equations of the PI and SMC based controllers with block diagram and closed-loop transfer functions. It contains the dynamic modelling of the (a) conventional controller design of the multi-terminal VSC-HVDC system and (b) hybrid controller design of the multi-terminal VSC-HVDC system.

5.5 Dynamic modelling of the multi-terminal VSC-HVDC system

The dynamic model diagram of the grid-integrated multi-terminal VSC-HVDC system is shown in Figure 5.2. It consists of the source model, WVSC1 model, WVSC2 model, GVSC model, DC-link model, and AC grid model. To simplify the process of developing the system state-space model, the step-up transformer inductance and AC filter capacitor equation are added to the AC source and AC grid models. The dynamic equations of the conventional and hybrid controller design of the VSC-HVDC system are explained in the following sections.

5.5.1 Dynamic modelling of the conventional controller design

The conventional controller design of the multi-terminal VSC-HVDC system contains wind farm side VSC and grid side VSC. The dynamic equations of the WVSC and GVSC are explained in the following sections.

5.5.1.1 Inner controller of the WVSC

The inner controller of the WVSC is based on a PI controller that is responsible for controlling the decoupled AC current components $i_{ws,d}$ and $i_{ws,q}$. The inner controller of the WVSC generates the dq reference voltages $V_{cs,d}^*$ and $V_{cs,q}^*$. The equation (4.7)

131
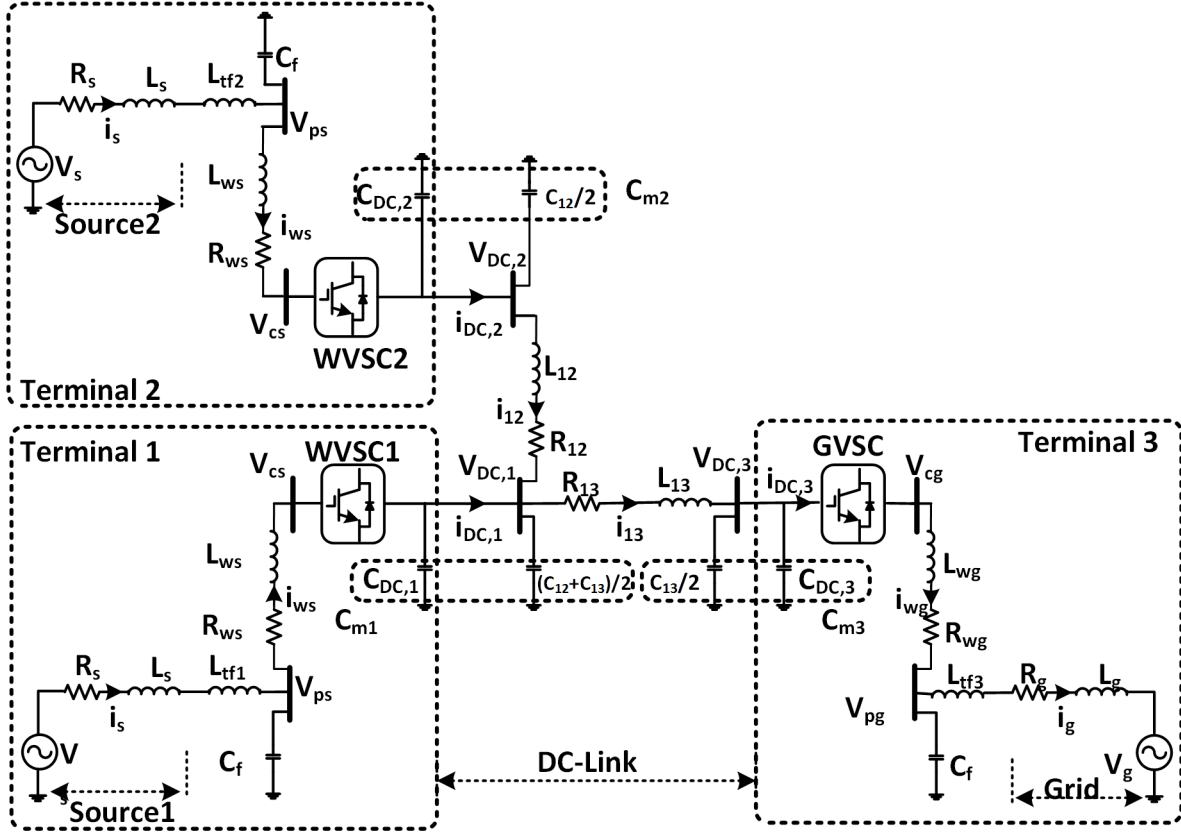
Figure 5.2: Dynamic model diagram of the grid-integrated multi-terminal VSC-HVDC system

and PI controller are used to develop the AC current controller and the reference current components $i_{ws,d}^*$ and $i_{ws,q}^*$ are produced from the outer controller of the WVSC. The dynamic modelling of the inner controller of the WVSC is explained in section4.6.1.1.

5.5.1.2 Outer controller of the WVSC

The AC voltage controller performs as the outer controller of WVSC. It controls the AC voltage and generates the reference decoupled currents $i_{ws,d}^*$ and $i_{ws,q}^*$ for the inner controller of the WVSC. The dynamic equations of the PI based AC voltage controller are explained in the following section.

5.5.1.2.1   PI based AC voltage controller

The AC voltage controller is operated as an outer controller for wind farm side VSC and it is developed based on the PI control for the conventional model. It controls the AC voltage by the AC filter capacitor. Equation (4.13) and PI controller are used to develop the AC voltage controller and it provides the reference dq component currents to the inner controller. The dynamic modelling of the PI based AC voltage controller is explained in section 4.6.1.2.1.

5.5.1.3   Inner controller of the GVSC

The inner controller of the GVSC is based on a PI controller that is responsible for controlling the decoupled AC current components $i_{wg,d}$ and $i_{wg,q}$. The inner controller of the GVSC generates the dq reference voltages $V_{cg,d}^*$ and $V_{cg,q}^*$. The equation (4.7) and PI controller are used to develop the AC current controller and the reference current components $i_{wg,d}^*$ and $i_{wg,q}^*$ are produced from the outer controller of the GVSC. The dynamic modelling of the inner controller of the GVSC is explained in section4.6.1.3.

5.5.1.4   Outer controller of the GVSC

The outer controller is the part of the GVSC controller. The DC voltage and reactive power controller are act as the outer controllers of the GVSC. The outer controller of GVSC regulates the DC voltage and reactive power. It generates the reference decoupled currents $i_{wg,d}^*$ and $i_{wg,q}^*$ for the inner controller of the GVSC. The dynamic equations of the PI based DC voltage controller and PI based reactive power controller are explained in the following sections.

5.5.1.4.1   PI based DC voltage controller

The DC voltage controller is operated as one of the outer controllers for grid side VSC and it is developed based on the PI control for the conventional controller. It regulates the DC-link voltage. The stable DC link voltage ensures the steady power flow between the VSCs and it provides the reference $i_{wg,d}^*$ value to the inner controller. The dynamic modelling of the PI based DC voltage controller is explained in section 4.6.1.4.1.

5.5.1.4.2 PI based reactive power controller

The reactive power controller is operated as one of the outer controllers for grid side VSC and it is developed based on the PI control for the conventional controller. The reactive power controller regulates the reactive power and it generates the reference $i^*_{wg,q}$ to the inner controller. The $i^*_{wg,q}$ is achieved by the instantaneous power equations as given in (4.46). The dynamic modelling of the PI based reactive power controller is explained in section 4.6.1.4.2.

5.5.2 Dynamic modelling of the hybrid controller design

The hybrid controller design of the multi-terminal VSC-HVDC system contains wind farm side VSC and grid side VSC. The dynamic equations of the WVSC and GVSC are explained in the following sections.

5.5.2.1 Inner controller of the WVSC

The inner controller of the WVSC is based on a PI controller that is responsible for controlling the decoupled AC current components $i_{ws,d}$ and $i_{ws,q}$. It generates the dq reference voltages $V^*_{cs,d}$ and $V^*_{cs,q}$. The equation (4.7) and PI controller are used to develop the AC current controller and the reference current components $i^*_{ws,d}$ and $i^*_{ws,q}$ are produced from the outer controller of the WVSC. The dynamic equations of the WVSC inner controller model are explained in the section 4.6.1.1.

5.5.2.2 Outer controller of the WVSC

The AC voltage controller performs as the outer controller of WVSC. It controls the AC voltage and generates the reference decoupled currents $i^*_{ws,d}$ and $i^*_{ws,q}$ for the inner controller of the WVSC. The dynamic equations of the SMC based AC voltage controller are explained in the following section.

5.5.2.2.1 SMC based AC voltage controller

The AC voltage controller is developed based on the SMC method for the hybrid controller. The equation (4.13) and SMC equation (4.51) are used to develop the AC voltage controller and The dynamic modelling of the SMC based AC voltage controller is explained in section 4.6.3.2.1.

5.5.2.3 Inner controller of the GVSC

The inner controller of the GVSC is based on a PI controller that is responsible for controlling the decoupled AC current components $i_{wg,d}$ and $i_{wg,q}$. It generates the dq reference voltages $V^*_{cg,d}$ and $V^*_{cg,q}$. The equation (4.7) and PI controller are used to develop the AC current controller and the reference current components $i^*_{wg,d}$ and $i^*_{wg,q}$ are produced from the outer controller of the GVSC. The dynamic equations of the GVSC inner controller model are explained in section 4.6.1.3.

5.5.2.4 Outer controller of the GVSC

The DC voltage and reactive power controller are act as the outer controllers of the GVSC. The outer controller of GVSC regulates the DC voltage and reactive power. It generates the reference decoupled currents $i^*_{wg,d}$ and $i^*_{wg,q}$ for the inner controller of the GVSC. The SMC discontinuous control action τ_c includes the continuous function and it mitigates the chattering effect due to high-frequency oscillations of the system parameters. The dynamic equations of the SMC based DC voltage controller and SMC based reactive power controller are explained in the following sections.

5.5.2.4.1 SMC based DC voltage controller

The DC voltage control for the hybrid controller is designed based on the SMC method and it controls the DC-link voltage. The dynamic modelling of the SMC based DC voltage controller is explained in section 4.6.3.4.1.

5.5.2.4.2 SMC based reactive power controller

The reactive power controller is operated as one of the outer controllers for grid side VSC and it is developed based on the SMC technique for the hybrid controller. The dynamic modelling of the SMC based reactive power controller is explained in section 4.6.3.4.2.

5.5.3 Dynamic model of the DC-link

The dynamic equations of the DC-link for multi-terminal VSC-HVDC system can be derived from (4.24) and it is specified in (4.64).

$$
\begin{aligned}
\frac{\mathrm{d}V_{DC,1}}{\mathrm{d}t} &= \frac{i_{DC,1} + i_{12} - i_{13}}{C_{m1}} \\
\frac{\mathrm{d}V_{DC,2}}{\mathrm{d}t} &= \frac{i_{DC,2} - i_{12}}{C_{m2}} \\
\frac{\mathrm{d}V_{DC,3}}{\mathrm{d}t} &= \frac{-i_{DC,3} + i_{13}}{C_{m3}} \\
\frac{\mathrm{d}i_{12}}{\mathrm{d}t} &= -\frac{R_{12}}{L_{12}}i_{12} + \frac{V_{DC,1} - V_{DC,2}}{L_{12}} \\
\frac{\mathrm{d}i_{13}}{\mathrm{d}t} &= -\frac{R_{13}}{L_{13}}i_{13} + \frac{V_{DC,1} - V_{DC,3}}{L_{13}}
\end{aligned}
\tag{5.1}
$$

Where $V_{DC,1}$, $V_{DC,2}$, and $V_{DC,3}$ are the DC voltage at buses 1, 2 and 3, respectively; $i_{DC,1}$, $i_{DC,2}$, and $i_{DC,3}$ are the DC currents at buses 1, 2, and 3, respectively; $C_{DC,1}$, $C_{DC,2}$, and $C_{DC,3}$ are the capacitance of the VSC at buses 1, 2, and 3, respectively; R_{12}, L_{12}, and C_{12} are the resistance, inductance, and capacitance of the DC line between buses 1 and 2, respectively; and R_{13}, L_{13}, and C_{13} are the resistance, inductance, and capacitance of the DC line between buses 1 and 3, respectively. The total capacitances of each bus side C_{m1}, C_{m2}, and C_{m3} are given as (5.2).

$$
\begin{aligned}
C_{m1} &= C_{DC,1} + 0.5(C_{12} + C_{13}) \\
C_{m2} &= C_{DC,2} + 0.5C_{12} \\
C_{m3} &= C_{DC,3} + 0.5C_{13}
\end{aligned}
\tag{5.2}
$$

5.6 Linearized state-space model of the multi-terminal VSC-HVDC system

The linearized state-space model of the multi-terminal VSC-HVDC system based on conventional controller and hybrid controller are explained in following sections.

5.6.1 Linearized state-space modelling of the multi-terminal VSC-HVDC system with conventional controller

The linearized state-space modelling of the multi-terminal VSC-HVDC transmission system with conventional controller is formulated from the dynamic equations of the multi-terminal VSC-HVDC system. To make the state-space system model simple and easy, the multi-terminal VSC-HVDC system model is divided into wind farm side VSC1 model, wind farm side VSC2 model, grid side VSC model, and DC-link model.

5.6.1.1 State-space model of the conventional controller based wind farm side VSC model

The conventional controller based wind farm side VSC model is the combination of the inner and outer controllers. Here, the inner and outer controllers are designed based on PI control technique. The linearized state-space model of the PI based WVSC inner controller and PI based WVSC outer controller models are explained in the section 4.7.1.1.1 and 4.7.1.1.2, respectively.

5.6.1.1.1 Total WVSC system model with conventional controller

The total WVSC system model with conventional controller is the cascaded model of the AC source model and complete converter model of the WVSC. To derive the total conventional WVSC system model, replace $u_s = y_{ca}$ in (4.71) and substitute $u_{ca} = C_s\ x_s$ in the resulting expression and in (4.70). The resultant state-space equations of the total WVSC1 system model with conventional controller are stated as (5.3).

$$\dot{x}_{sc_1} = A_{sc_1}x_{sc_1} + B_{sc_{d1}}u_{cd} + B_{sc_{r1}}u_{sc_{r1}}$$
$$y_{sc_{d1}} = C_{sc_{d1}}x_{sc_1} + D_{sc_{d1}}u_{cd} + D_{sc_{r1}}u_{sc_{r1}}$$

(5.3)

Where $x_{sc_1} = \begin{bmatrix} x_c & x_s \end{bmatrix}^T$; $y_{sc_{d1}} = \begin{bmatrix} i_{DC} \end{bmatrix}$; $u_{sc_{r1}} = \begin{bmatrix} V_{ps,d} & V_{ps,q} \end{bmatrix}^T$; and the state matrices of the total WVSC1 system model with conventional controller are given as below,

$$A_{sc_1} = \begin{bmatrix} A_c & B_{ca}C_s \\ B_sC_{ca} & A_s + B_sD_{ca1}C_s \end{bmatrix}; \; B_{sc_{d1}} = \begin{bmatrix} B_{cd} \\ B_sD_{cd1} \end{bmatrix};$$

$$B_{sc_{r1}} = \begin{bmatrix} B_{cr} \\ B_sD_{cr1} \end{bmatrix}; \; C_{sc_{d1}} = \begin{bmatrix} C_{cd} & 0_{1,4} \end{bmatrix}; \; D_{sc_{d1}} = D_{cd2}; \; D_{sc_{r1}} = D_{cr2};$$

The resultant state-space equations of the total WVSC2 system model with conventional controller are stated as (5.4).

$$\dot{x}_{sc_2} = A_{sc_2}x_{sc_2} + B_{sc_{d2}}u_{cd} + B_{sc_{r2}}u_{sc_{r2}}$$
$$y_{sc_{d1}} = C_{sc_{d2}}x_{sc} + D_{sc_{d2}}u_{cd} + D_{sc_{r2}}u_{sc_{r2}}$$

(5.4)

Where $x_{sc_2} = \begin{bmatrix} x_c & x_s \end{bmatrix}^T$; $y_{sc_{d2}} = \begin{bmatrix} i_{DC} \end{bmatrix}$; $u_{sc_{r2}} = \begin{bmatrix} V_{ps,d} & V_{ps,q} \end{bmatrix}^T$; and the state matrices of the total WVSC2 system model with conventional controller are given as below,

$$A_{sc_2} = \begin{bmatrix} A_c & B_{ca}C_s \\ B_sC_{ca} & A_s + B_sD_{ca1}C_s \end{bmatrix}; \; B_{sc_{d2}} = \begin{bmatrix} B_{cd} \\ B_sD_{cd1} \end{bmatrix};$$

$$B_{sc_{r2}} = \begin{bmatrix} B_{cr} \\ B_sD_{cr1} \end{bmatrix}; \; C_{sc_{d2}} = \begin{bmatrix} C_{cd} & 0_{1,4} \end{bmatrix}; \; D_{sc_{d2}} = D_{cd2}; \; D_{sc_{r2}} = D_{cr2};$$

Where A_c, B_{ca}, B_{cd}, B_{cr}, C_{ca}, C_{cd}, D_{ca1}, D_{cd1}, D_{cr1}, D_{ca2}, D_{cd2}, and D_{cr2} are state matrices of the equation (4.70). A_s, B_s, and C_s are state matrices of the equation (4.71).

5.6.1.2 State-space model of the conventional controller based grid side VSC model

The conventional controller based grid side VSC model is the combination of the inner and outer controllers. Here, the inner and outer controllers are designed based on PI control technique. The linearized state-space model of PI based GVSC inner controller and PI based GVSC outer controller models are explained in the section 4.7.1.2.1 and 4.7.1.2.2.

5.6.1.2.1 Total GVSC system model with conventional controller

The total GVSC system model with conventional controller is the cascaded model of the AC grid model and complete converter model of the GVSC. To derive the total GVSC system model with conventional controller , replace $u_g = y_{ca_g}$ in (4.76) and substitute $u_{ca} = C_g\, x_g$ in the resulting expression and in (4.75). The resultant state-space equations of the total GVSC system model with conventional controller are stated in section 4.7.1.2.5.

5.6.1.3 DC-link model

The linearized state-space model of the DC-link can be developed from the equations (4.64) and (4.65). It is given in (5.5).

$$
\begin{aligned}
\dot{x}_{dc_m} &= A_{dc_m} x_{dc_m} + B_{dc_{m1}} u_{dc_1} + B_{dc_{m2}} u_{dc_2} + B_{dc_{m3}} u_{dc_3} \\
y_{dc_1} &= C_{dc_1} x_{dc_m} \\
y_{dc_2} &= C_{dc_2} x_{dc_m} \\
y_{dc_3} &= C_{dc_3} x_{dc_m}
\end{aligned}
\tag{5.5}
$$

Where $x_{dc_m} = \begin{bmatrix} i_{12} & i_{13} & V_{DC,1} & V_{DC,2} & V_{DC,3} \end{bmatrix}^T$; $u_{dc_1} = i_{DC,1}$; $u_{dc_2} = i_{DC,2}$; $u_{dc_3} = i_{DC,3}$; $y_{dc_1} = V_{DC,1}$; $y_{dc_2} = V_{DC,2}$; $y_{dc_3} = V_{DC,3}$ and the DC-link model state matrices are given as below,

$$
A_{dc_m} = \begin{bmatrix}
\frac{-R_{12}}{L_{12}} & 0 & \frac{1}{L_{12}} & \frac{-1}{L_{12}} & 0 \\
0 & \frac{-R_{13}}{L_{13}} & \frac{1}{L_{13}} & 0 & \frac{-1}{L_{13}} \\
\frac{1}{C_{m1}} & \frac{-1}{C_{m1}} & 0 & 0 & 0 \\
\frac{-1}{C_{m2}} & 0 & 0 & 0 & 0 \\
0 & \frac{1}{C_{m3}} & 0 & 0 & 0
\end{bmatrix} ; \;
B_{dc_{m1}} = \begin{bmatrix} 0 \\ 0 \\ \frac{1}{C_{m1}} \\ 0 \\ 0 \end{bmatrix} ; \;
B_{dc_{m2}} = \begin{bmatrix} 0 \\ 0 \\ 0 \\ \frac{1}{C_{m2}} \\ 0 \end{bmatrix} ; \;
B_{dc_{m3}} = \begin{bmatrix} 0 \\ 0 \\ 0 \\ 0 \\ \frac{-1}{C_{m3}} \end{bmatrix} ;
$$

$$
C_{dc_{m1}} = \begin{bmatrix} 0 & 0 & 1 & 0 & 0 \end{bmatrix} ; \;
C_{dc_{m2}} = \begin{bmatrix} 0 & 0 & 0 & 1 & 0 \end{bmatrix} ; \;
C_{dc_{m3}} = \begin{bmatrix} 0 & 0 & 0 & 0 & 1 \end{bmatrix} ;
$$

5.6.1.4 Total multi-terminal VSC-HVDC system with conventional controller

The total multi-teminal VSC-HVDC system with conventional controller model is the cascaded model of the total WVSC1 system model with conventional controller , total

WVSC2 system model with conventional controller , total GVSC system model with conventional controller and DC-link model. To derive the total VSC-HVDC system model, replace $u_{dc_1} = y_{gc_d}$, $u_{dc_2} = y_{sc_{d1}}$, and $u_{dc_3} = y_{sc_{d2}}$ in (5.5). The resultant state-space equations of the total multi-terminal VSC-HVDC system with conventional controller model are stated as (5.6).

$$\dot{x}_{sys_m} = A_{sys_m} x_{sys_m} + B_{sys_m} u_{sys_m}$$
$$y_{sys_m} = C_{sys_m} x_{sys_m}$$

(5.6)

Where $x_{sys_m} = \begin{bmatrix} x_{gc} & x_{sc_1} & x_{sc_2} & x_{dc_m} \end{bmatrix}^T$; $u_{sys_m} = \begin{bmatrix} u_{gc_r} & u_{sc_{r1}} & u_{sc_{r2}} \end{bmatrix}^T$;

$y_{sys_m} = \begin{bmatrix} x_{gc} & x_{sc_1} & x_{sc_2} & x_{dc_m} \end{bmatrix}^T$; and the state matrices of the total multi-terminal VSC-HVDC system model are given as below,

$$A_{sys_m} = \begin{bmatrix} A_{gc} & 0_{10,10} & 0_{10,10} & B_{gc_d}C_{dc_{m1}} \\ 0_{10,10} & A_{sc_1} & 0_{10,10} & B_{sc_{d1}}C_{dc_{m2}} \\ 0_{10,10} & 0_{10,10} & A_{sc_2} & B_{sc_{d2}}C_{dc_{m3}} \\ B_{dc_{m1}}C_{gc_d} & B_{dc_{m2}}C_{sc_{d1}} & B_{dc_{m3}}C_{sc_{d2}} & \begin{matrix}(A_{dc_m} + B_{dc_{m1}}D_{gc_d}C_{dc_{m1}} \\ +B_{dc_{m2}}D_{sc_{d1}}C_{dc_{m2}} \\ +B_{dc_{m3}}D_{sc_{d2}}C_{dc_{m3}})\end{matrix} \end{bmatrix} ;$$

$$B_{sys_m} = \begin{bmatrix} B_{gc_r} & 0_{10,2} & 0_{10,2} \\ 0_{10,2} & B_{sc_{r1}} & 0_{10,2} \\ 0_{10,2} & 0_{10,2} & B_{sc_{r2}} \\ B_{dc_{m1}}D_{gc_r} & B_{dc_{m2}}D_{sc_{r1}} & B_{dc_{m3}}D_{sc_{r2}} \end{bmatrix} ; \quad C_{sys_m} = I_4$$

Where A_{sc_1}, $B_{sc_{d1}}$, $B_{sc_{r1}}$, $C_{sc_{d1}}$, $D_{sc_{r1}}$, and $D_{sc_{d1}}$ are the system matrices of the equation (5.3). A_{sc_2}, $B_{sc_{d2}}$, $B_{sc_{r2}}$, $C_{sc_{d2}}$, $D_{sc_{r2}}$, and $D_{sc_{d2}}$ are the system matrices of the equation (5.4). A_{gc}, B_{gc_d}, B_{gc_r}, C_{gc_d}, D_{gc_r}, and D_{gc_d} are the system matrices of the equation (4.77). A_{dc_m}, $B_{dc_{m1}}$, $B_{dc_{m2}}$, $B_{dc_{m3}}$, $C_{dc_{m1}}$, $C_{dc_{m2}}$, and $C_{dc_{m3}}$ are the system matrices of the equation (5.5).

5.6.2 Linearized state-space model of the multi-terminal VSC-HVDC system with hybrid controller

The linearized state-space model of the multi-terminal VSC-HVDC transmission system with hybrid controller is formulated from the dynamic equations of the multi-terminal VSC-HVDC system. To make the state-space system model simple and easy, the multi-terminal VSC-HVDC system model is divided into wind farm side VSC1 model, wind farm side VSC2 model, grid side VSC model and DC-link model.

5.6.2.1 State-space model of the hybrid controller based wind farm side VSC model

The hybrid controller based wind farm side VSC model is the combination of the inner and outer controllers. Here, the inner and outer controllers are designed based on PI control and SMC techniques, respectively. The linearized state-space model of the PI based WVSC inner controller model is explained in section 4.7.1.1.1 and SMC based WVSC outer controller model will be discussed in the section 4.7.2.1.1.

5.6.2.1.1 Total WVSC system model with hybrid controller

The total WVSC system model with hybrid controller is the cascaded model of the AC source model and complete converter model of the WVSC. To derive the total WVSC system model with hybrid controller, replace $u_s = y_{ca_h}$ in (4.71) and substitute $u_{ca} = C_s\, x_s$ in the resulting expression and in (4.81). The resultant state-space equations of the total WVSC1 system model with hybrid controller are stated as (5.7).

$$
\begin{aligned}
\dot{x}_{sc_{h1}} &= A_{sc_{h1}} x_{sc_{h1}} + B_{sc_{dh1}} u_{cd} + B_{sc_{rh1}} u_{sc_{r1}} \\
y_{sc_{dh1}} &= C_{sc_{dh1}} x_{sc_{h1}} + D_{sc_{dh1}} u_{sc_d} + D_{sc_{rh1}} u_{sc_{r1}}
\end{aligned}
\tag{5.7}
$$

Where $x_{sc_{h1}} = \begin{bmatrix} x_{c_h} & x_s \end{bmatrix}^T$; $y_{sc_{dh1}} = \begin{bmatrix} i_{DC} \end{bmatrix}$; and the state matrices of the total WVSC1 system model are given as below,

$$A_{sc_{h1}} = \begin{bmatrix} A_{c_h} & B_{ca_h}C_s \\ B_sC_{ca_h} & A_s + B_sD_{ca_{h1}}C_s \end{bmatrix}; \ B_{sc_{dh1}} = \begin{bmatrix} B_{cd_h} \\ B_sD_{cd_{h1}} \end{bmatrix};$$

$$B_{sc_{rh1}} = \begin{bmatrix} B_{cr_h} \\ B_sD_{cr_{h1}} \end{bmatrix}; \ C_{sc_{dh1}} = \begin{bmatrix} C_{cd_h} & 0_{1,4} \end{bmatrix};$$

$$D_{sc_{dh1}} = D_{cd_{h2}}; \ D_{sc_{rh1}} = D_{cr_{h2}};$$

The resultant state-space equations of the total WVSC2 system model with hybrid controller are stated as (5.8).

$$\dot{x}_{sc_{h2}} = A_{sc_{h2}}x_{sc_{h2}} + B_{sc_{dh2}}u_{cd} + B_{sc_{rh2}}u_{sc_{r2}}$$
$$y_{sc_{dh2}} = C_{sc_{dh2}}x_{sc_{h2}} + D_{sc_{dh2}}u_{sc_d} + D_{sc_{rh2}}u_{sc_{r2}}$$

(5.8)

Where $x_{sc_{h2}} = \begin{bmatrix} x_{c_h} & x_s \end{bmatrix}^T$; $y_{sc_{dh2}} = \begin{bmatrix} i_{DC} \end{bmatrix}$; and the state matrices of the total WVSC2 system model with hybrid controller are given as below,

$$A_{sc_{h2}} = \begin{bmatrix} A_{c_h} & B_{ca_h}C_s \\ B_sC_{ca_h} & A_s + B_sD_{ca_{h1}}C_s \end{bmatrix}; \ B_{sc_{dh2}} = \begin{bmatrix} B_{cd_h} \\ B_sD_{cd_{h1}} \end{bmatrix};$$

$$B_{sc_{rh2}} = \begin{bmatrix} B_{cr_h} \\ B_sD_{cr_{h1}} \end{bmatrix}; \ C_{sc_{dh2}} = \begin{bmatrix} C_{cd_h} & 0_{1,4} \end{bmatrix};$$

$$D_{sc_{dh2}} = D_{cd_{h2}}; \ D_{sc_{rh2}} = D_{cr_{h2}};$$

Where A_{c_h}, B_{ca_h}, B_{cd_h}, B_{cr_h}, C_{ca_h}, C_{cd_h}, $D_{ca_{h1}}$, $D_{cd_{h1}}$, $D_{cr_{h1}}$, $D_{ca_{h2}}$, $D_{cd_{h2}}$, and $D_{cr_{h2}}$ are state matrices of the equation (4.81). A_s, B_s, and C_s are state matrices of the equation (4.71).

5.6.2.2 State-space model of the hybrid controller based grid side VSC model

The hybrid controller based grid side VSC model is the combination of the inner and outer controllers. Here, the inner and outer controllers are designed based on PI control and SMC technique, respectively. The linearized state-space model of PI

based GVSC inner controller model is explained in section 4.7.1.2.1 and the SMC based GVSC outer controller model will be discussed in section 4.7.2.2.1.

5.6.2.2.1 Total GVSC system model with hybrid controller

The total GVSC system model with hybrid controller is the cascaded model of the AC grid model and complete converter model of the GVSC. To derive the total GVSC system model with hybrid controller, replace $u_g = y_{ca_{gh}}$ in (4.76) and substitute $u_{ca} = C_g\, x_g$ in the resulting expression and in (4.84). The resultant state-space equations of the total GVSC system model with hybrid controller are stated in section 4.7.2.2.3.

5.6.2.3 Total multi-terminal VSC-HVDC system with hybrid controller

The total multi-terminal VSC-HVDC system with hybrid controller model is the cascaded model of the total WVSC1 system model with hybrid controller, total WVSC2 system model with hybrid controller, total GVSC system model with hybrid controller, and DC-link model. To derive the total VSC-HVDC system model, by making $u_{dc_1} = y_{gc_{dh}}$, $u_{dc_2} = y_{sc_{dh}}$, and $u_{dc_3} = y_{sc_{dh}}$ in (5.5). The resultant state-space equations of the total multi-terminal VSC-HVDC system with hybrid controller model are stated as (5.9).

$$\dot{x}_{sys_{mh}} = A_{sys_{mh}} x_{sys_{mh}} + B_{sys_{mh}} u_{sys_{mh}}$$

$$(5.9)$$

$$y_{sys_{mh}} = C_{sys_{mh}} x_{sys_{mh}}$$

Where $x_{sys_{mh}} = \begin{bmatrix} x_{gc_h} & x_{sc_{h1}} & x_{sc_{h2}} & x_{dc_m} \end{bmatrix}^T$; $u_{sys_{mh}} = \begin{bmatrix} u_{gc_r} & u_{sc_{r1}} & u_{sc_{r2}} \end{bmatrix}^T$; $y_{sys_m} = \begin{bmatrix} x_{gc_h} & x_{sc_{h1}} & x_{sc_{h2}} & x_{dc_m} \end{bmatrix}^T$; and the state matrices of the total multi-terminal VSC-HVDC system with hybrid controller model are given as below,

$$
A_{sys_{mh}} = \begin{bmatrix}
A_{gc_h} & 0_{10,10} & 0_{10,10} & B_{gc_{dh}}C_{dc_{m1}} \\
0_{10,10} & A_{sc_{h1}} & 0_{10,10} & B_{sc_{dh1}}C_{dc_{m2}} \\
0_{10,10} & 0_{10,10} & A_{sc_{h2}} & B_{sc_{dh2}}C_{dc_{m3}} \\
B_{dc_{m1}}C_{gc_{dh}} & B_{dc_{m2}}C_{sc_{dh1}} & B_{dc_{m3}}C_{sc_{dh2}} & \begin{array}{c}(A_{dc_m} + B_{dc_{m1}}D_{gc_{dh}}C_{dc_{m1}} \\ +B_{dc_{m2}}D_{sc_{dh1}}C_{dc_{m2}} \\ +B_{dc_{m3}}D_{sc_{dh2}}C_{dc_{m3}})\end{array}
\end{bmatrix} ;
$$

$$
B_{sys_{mh}} = \begin{bmatrix}
B_{gc_{rh}} & 0_{10,2} & 0_{10,2} \\
0_{10,2} & B_{sc_{rh1}} & 0_{10,2} \\
0_{10,2} & 0_{10,2} & B_{sc_{rh2}} \\
B_{dc_{m1}}D_{gc_{rh}} & B_{dc_{m2}}D_{sc_{rh1}} & B_{dc_{m3}}D_{sc_{rh2}}
\end{bmatrix} ; \quad C_{sys_m} = I_4
$$

Where $A_{sc_{h1}}$, $B_{sc_{dh1}}$, $B_{sc_{rh1}}$, $C_{sc_{dh1}}$, $D_{sc_{rh1}}$, and $D_{sc_{dh1}}$ are the system matrices of the equation (5.7). $A_{sc_{h2}}$, $B_{sc_{dh2}}$, $B_{sc_{rh2}}$, $C_{sc_{dh2}}$, $D_{sc_{rh2}}$, and $D_{sc_{dh2}}$ are the system matrices of the equation (5.8). A_{gc_h}, $B_{gc_{dh}}$, $B_{gc_{rh}}$, $C_{gc_{dh}}$, $D_{gc_{rh}}$, and $D_{gc_{dh}}$ are the system matrices of the equation (4.85). A_{dc_m}, $B_{dc_{m1}}$, $B_{dc_{m2}}$, $B_{dc_{m3}}$, $C_{dc_{m1}}$, $C_{dc_{m2}}$, and $C_{dc_{m3}}$ are the system matrices of the equation (5.5).

5.7 Small signal analysis on the multi-terminal VSC-HVDC system

The small-signal analysis has been done on the linearized model of the grid-integrated multi-terminal VSC-HVDC system. The eigenmatrix of total multi-terminal VSC-HVDC system with conventional controller system matrix A_{sys_m} and total multi-terminal VSC-HVDC system with hybrid controller sysem matrix $A_{sys_{mh}}$ has the 35 eigenvalues. Equations (5.6) and (5.9), include the dynamics of the total multi-terminal VSC-HVDC system with conventional controller and hybrid controller; and the system stability can be decided by analyze the location of the eigenvalues. Figures 5.3(a) and 5.3(b) show the eigenvalues of the total multi-terminal VSC-HVDC system. The effect of parameter uncertainty on stability of the total system is explained through the variation of the C_f and ω. Hence, the values of the C_f and ω are subjected to small variations and it is reflected on the system performance and stability. Small variations in C_f can be due to reactive power compensation and AC

144

filter harmonics; whereas small changes in frequency ω can be associated to grid transients. The locations of the system eigenvalues vary with respect to the variations of the C_f and ω values.
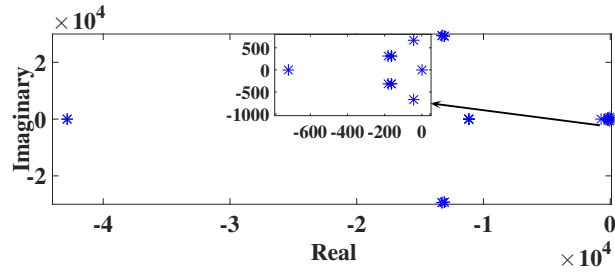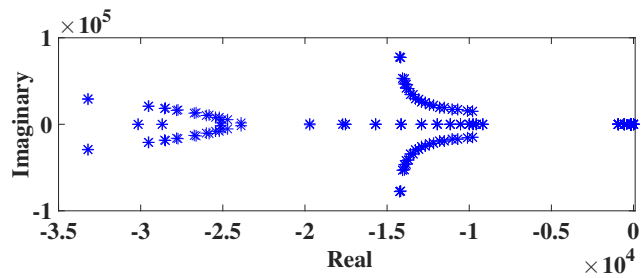

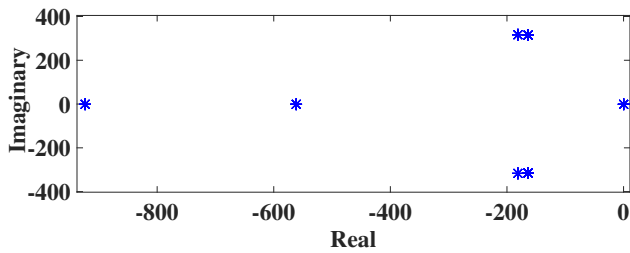(a) PI controller
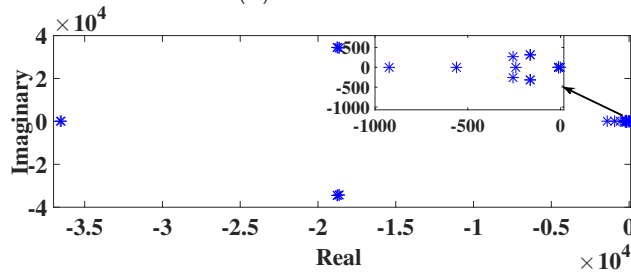
(b) Hybrid controller

Figure 5.3: Eigenvalue plot of total multi-terminal VSC-HVDC system

Figure 5.4(a) shows the eigenvalues plot for total system with conventional controller when C_f values vary from $12.59\mu F$ to $100.73\mu F$. Also, the zoomed view of the region closer to the instability area is shown in Figure 5.4(b). Figure 5.5(a) shows the eigenvalues plot for total system with hybrid controller when C_f values vary from $12.59\mu F$ to $100.73\mu F$. Also, the zoomed view of the region closer to the instability area is shown in Figure 5.5(b). From Figures 5.4 and 5.5, it can be observed that the location of eigenvalues is shifting to the stability region with respect to variation of C_f values.

Figure 5.6(a) shows the eigenvalues plot for total system with conventional controller when ω values varies from 280 rad/sec to 346 rad/sec. In addition, the zoomed view of the region closer to the instability area is shown in Figure 5.6(b). Figure 5.7(a) shows the eigenvalues plot for total system with hybrid controller when ω values varies from 280 rad/sec to 346 rad/sec. In addition, the zoomed view of the region closer to the instability area is shown in Figure 5.7(b). Figures 5.6 and 5.7, show how the variation in ω value influence the system stability.
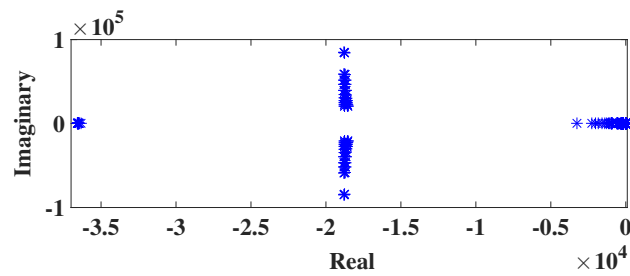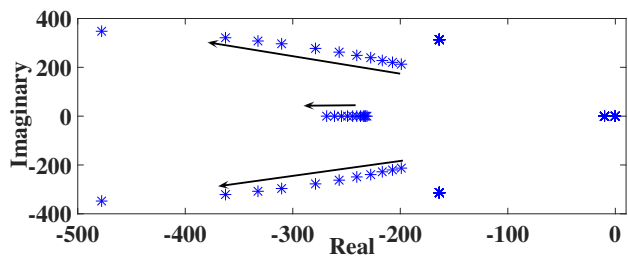
145

(a) Total Plot

(b) Zoomed view of the region closer to the instability area

Figure 5.4: Eigenvalue plot of multi-terminal VSC-HVDC system with PI controller for variable C_f values from $12.59\mu F$ to $100.73\mu F$
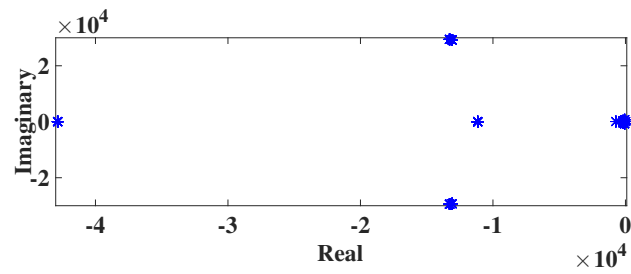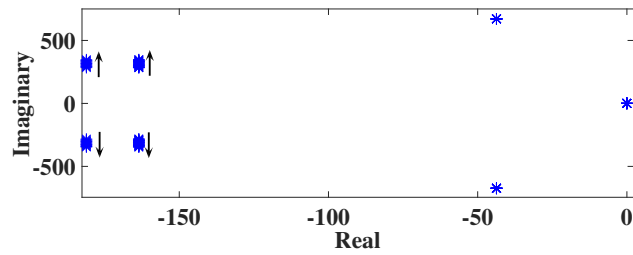

(a) Total Plot

(b) Zoomed view of the region closer to the instability area

Figure 5.5: Eigenvalue plot of multi-terminal VSC-HVDC system with hybrid controller for variable C_f values from $12.59\mu F$ to $100.73\mu F$
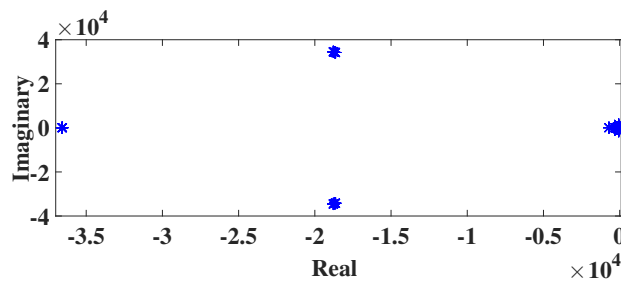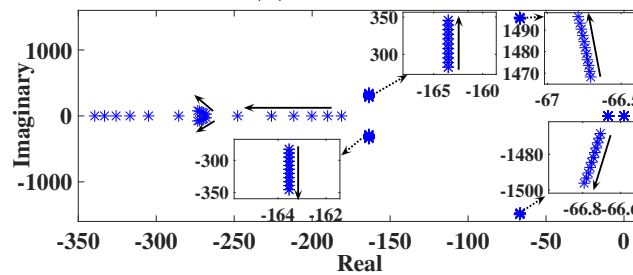
146

(a) Total Plot

(b) Zoomed view of the region closer to the instability
area

Figure 5.6: Eigenvalue plot multi-terminal VSC-HVDC system with PI controller for variable ω from 280 rad/sec to 346 rad/sec

(a) Total Plot

(b) Zoomed view of the region closer to the instability
area

Figure 5.7: Eigenvalue plot multi-terminal VSC-HVDC system with hybrid controller for variable ω from 280 rad/sec to 346 rad/sec

5.8 Simulation results

The performance of two 400MW OSWF connected to onshore AC grid with multi-terminal VSC-HVDC transmission system is investigated using the MATLAB/Simulink software, where proposed hybrid control and conventional control schemes are implemented. The specifications and tuned gain values of controllers for the multi-terminal VSC-HVDC system are detailed in Tables 5.1 and 5.2, respectively. The gain values of PI-based and SMC-based controllers are computed through the PID tuner tool and GA method, respectively. The performance of the multi-terminal VSC-HVDC system under different cases is presented in this section. Cases considered are (i) 3-phase to ground (LLLG) fault near to grid, (ii) phase to ground (LG) fault near to grid (iii) step change of the wind speed from 12m/s to 13m/s, and (iv) step change of the wind speed from 13m/s to 12m/s.

**Table 5.2:** Tuned gain values of the controllers

System	Parameters	Values
WVSC1 and WVSC2 gain values	$K_{P_{AC}}$	2.1
	$K_{I_{AC}}$	18579.0
	$K_{P_{CC}}$	828.6
	$K_{I_{CC}}$	5590900.0
	K_{AC}	3.9
	α_{AC}	10.0
	ϕ_{AC}	1.6
GVSC gain values	$K_{P_{DC}}$	19.3
	$K_{I_{DC}}$	175500.0
	K_{P_Q}	1.8
	K_{I_Q}	300000.0
	K_{DC}	3.9
	α_{DC}	10.0
	ϕ_{DC}	1.6
	K_Q	3.9
	α_Q	5.0
	ϕ_Q	0.5

In case 1, to study the FRT performance of the multi-terminal VSC-HVDC system during the abnormal situation by applying the LLLG fault near to AC grid. The fault is created at 3s with duration of 0.1s and it is cleared at 3.1s as given in Figures 5.8 and 5.9. In faulty condition, the responses of grid-integrated multi-terminal VSC-HVDC system for PI and hybrid controllers are displayed in Figures 5.8 and 5.9, respectively. In fault duration, the grid voltage is decreased to a minimum level and

it can be seen in the grid side voltage waveform as shown in Figure 5.9(a). When the LLLG fault occurs, the DC-link voltage V_{DC} drops as shown in Figures 5.8(d) and 5.9(d). It affects the active power transmitted to the AC grid. Response of grid active power with hybrid controller is seen in Figure 5.9(b) and it takes 0.64s to reach the pre-fault value where as PI controller takes 1.11s as seen in Figure 5.8(b). Due to the rapid drop of V_{DC}, grid reactive power is fluctuated and it can be seen in Figure 5.8(c) and Figure 5.9(c). The grid reactive power is stablized at -0.01pu value within 0.15s for both PI and hybrid controllers. From the observation of Figures 5.8(d) and 5.9(d), the V_{DC} response of hybrid controller stabilized at 1pu value within 0.9s and PI controller takes 1.15s.

In case 2, to study the FRT performance of the multi-terminal VSC-HVDC system during the abnormal situation by applying the LG fault near to AC grid. The fault is created at 3s with duration of 0.1s and it is cleared at 3.1s as given in Figures 5.10 and 5.11. In faulty condition, the responses of grid-integrated multi-terminal VSC-HVDC system for PI and hybrid controllers are displayed in Figures 5.10 and 5.11, respectively. In fault duration, the grid voltage is decreased to a minimum level and it can be seen in the grid side voltage waveform as shown in Figure 5.11(a). When the LG fault occurs, the DC-link voltage V_{DC} drops as shown in Figures 5.10(d) and 5.11(d). It affects the active power transmitted to the AC grid. Response of grid active power with hybrid controller is seen in Figure 5.11(b) and it takes 0.64s to reach the pre-fault value where as PI controller takes 1.11s as seen in Figure 5.10(b). Due to the rapid drop of V_{DC}, grid reactive power is fluctuated and it can be seen in Figures 5.10(c) and 5.11(c). The grid reactive power is stablized at -0.01pu value within 0.15s for both PI and hybrid controllers. From the observation of Figures 5.10(d)and 5.11(d), the V_{DC} response of hybrid controller stabilized at 1pu value within 0.75s and PI controller takes 1.15s.The time taken to restore the pre-fault values of grid active power, grid reactive power and DC-link voltage for multi-terminal VSC-HVDC system with LLLG fault and LG fault conditions are given in Table 5.3.

In case 3, the wind speed experienced by wind turbines in OSWF is raised at time 3.5s from 12 m/s to rated value (13m/s). Figures 5.12 and 5.13 show the responses of the multi-terminal VSC-HVDC system with PI controller and hybrid controller, respectively. From Figures 5.12(c) and 5.13(c) it is observed that, the hybrid controller takes 1.2s to reach the 0.96pu after a step change of wind speed at 3.5s and the PI controller takes 1.3s to reach 0.96pu. Source reactive power is maintained at 0.01pu
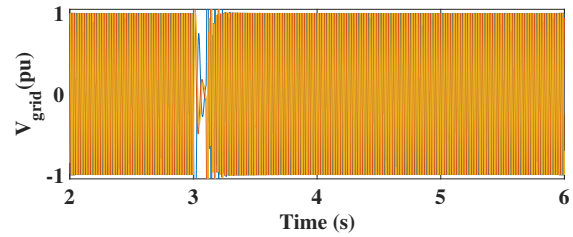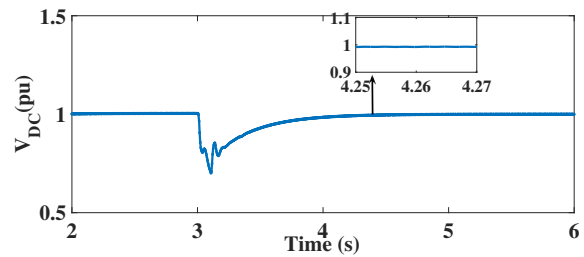
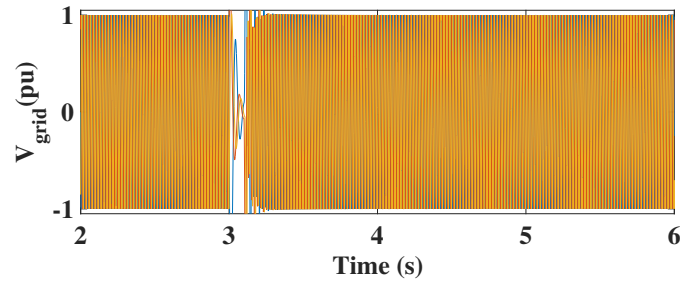(a) Grid voltage
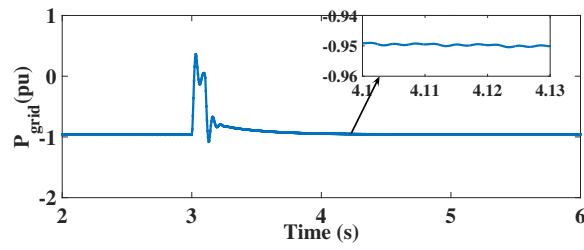
(b) Grid active power
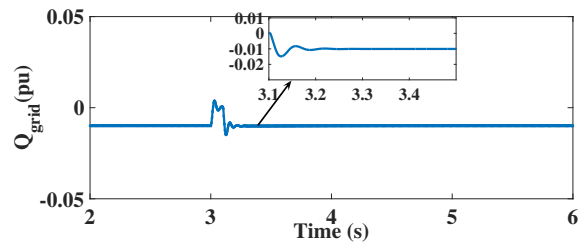
(c) Grid reactive power

(d) DC-link voltage

Figure 5.8: Responses of the multi-terminal VSC-HVDC system with PI controller for LLLG fault

(a) Grid voltage

(b) Grid active power

(c) Grid reactive power

(d) DC-link voltage

Figure 5.9: Responses of the multi-terminal VSC-HVDC system with hybrid controller for LLLG fault

(a) Grid voltage
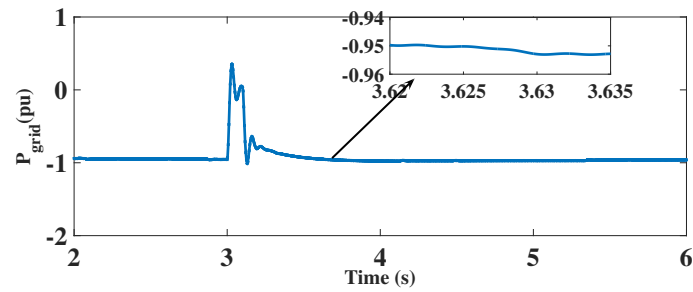

(b) Grid active power

(c) Grid reactive power

(d) DC-link voltage

Figure 5.10: Responses of the multi-terminal VSC-HVDC system with PI controller for LG fault

(a) Grid voltage

(b) Grid active power

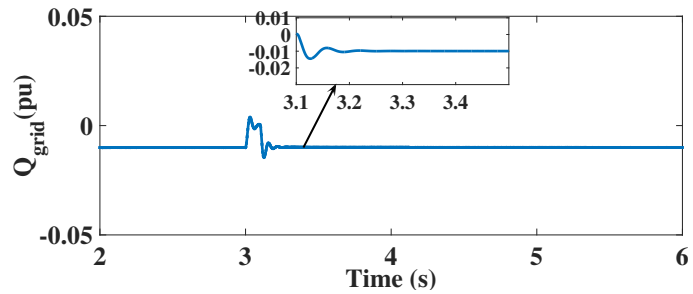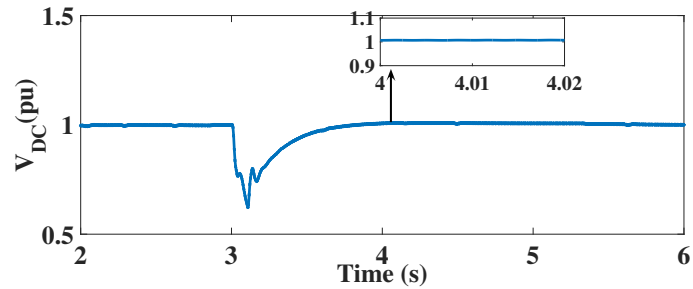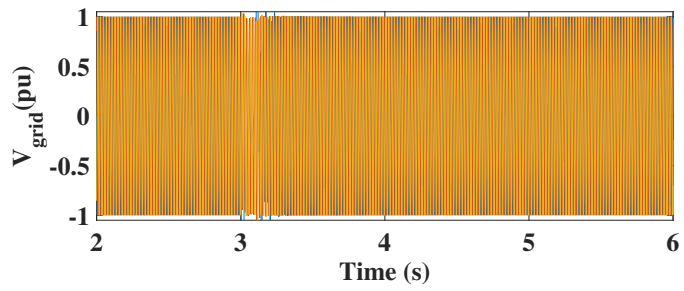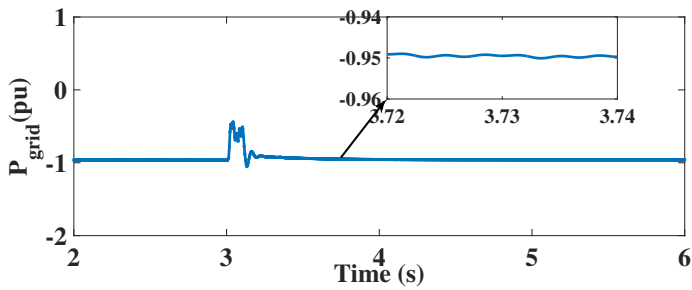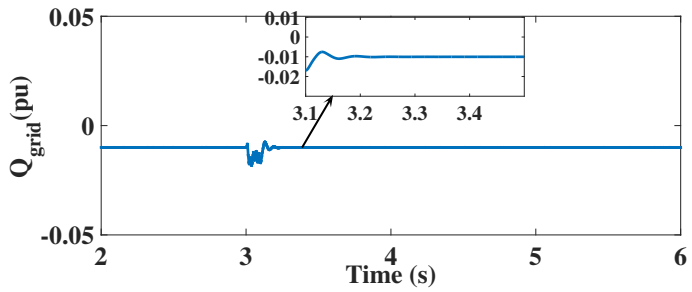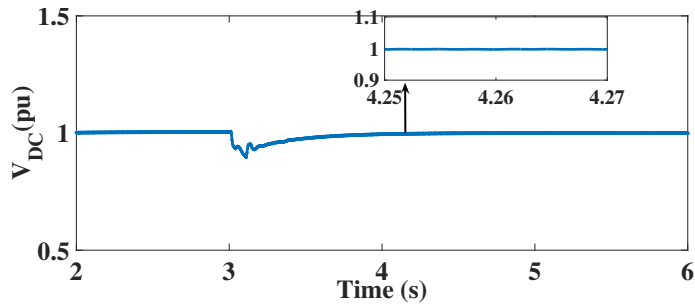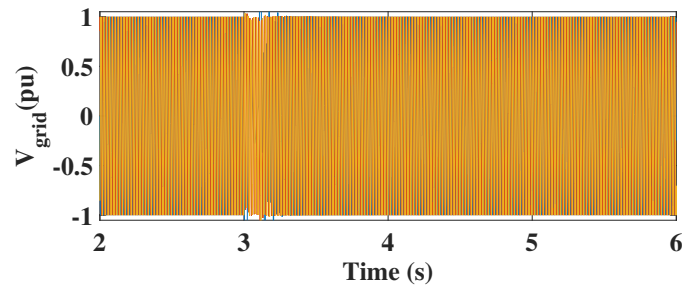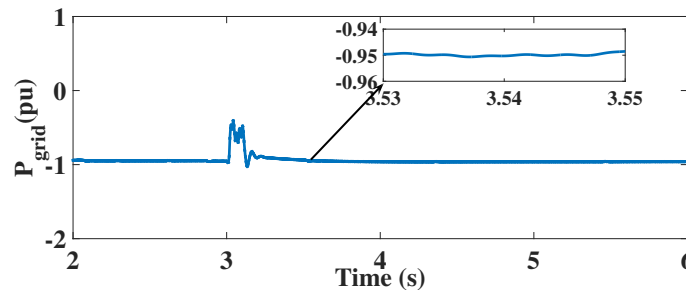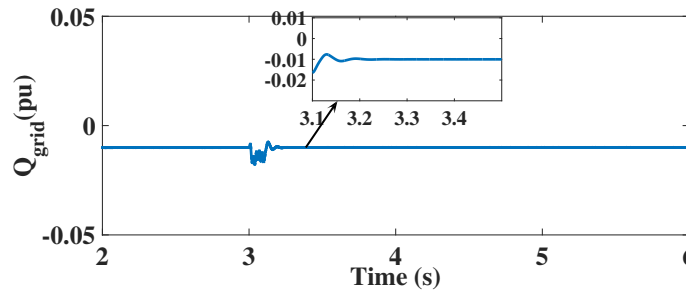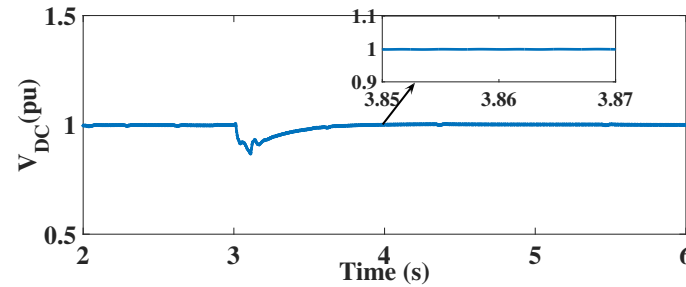

(c) Grid reactive power

(d) DC-link voltage

Figure 5.11: Responses of the multi-terminal VSC-HVDC system with hybrid controller for LG fault

153

Table 5.3: Time taken to restore the pre-fault values for multi-terminal VSC-HVDC system

| Specification | Time taken to restore the pre-fault values (s) | | | |
| | LLLG fault | | LG fault | |
	PI controller	Hybrid controller	PI controller	Hybrid controller
Grid active power	1.00	0.52	0.62	0.43
Grid reactive power	0.15	0.15	0.15	0.15
DC-link voltage	1.15	0.90	1.15	0.75

value and it can be observed from Figures 5.12(b) and 5.13(b). Grid reactive power is maintained at a -0.01pu value and it can be observed from Figures 5.12(d) and 5.13(d). DC-link voltage is stabilized at 1 pu and it can be seen from Figures 5.12(e) and 5.13(e).

In case 4, the wind speed experienced by wind turbines in OSWF is step down at time 3.5s from the rated value (13m/s) to 12m/s. It means the active power step down from 1pu to 0.8pu at time 3.5s. Figures 5.14 and 5.15 show the responses of the multi-terminal VSC-HVDC system with PI controller and hybrid controller, respectively. From Figures 5.14(c) and 5.15(c) it is observed that, the hybrid controller takes 0.42s to reach the 0.79pu after a step change of wind speed at 3.5s and the PI controller takes 1s t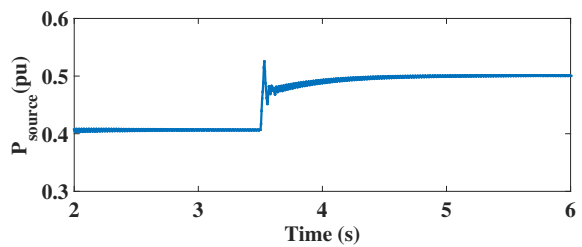o reach 0.79pu. Source reactive power is maintained at 0.01pu value and it can be observed from Figures 5.14(b) and 5.15(b). Grid reactive power is maintained at -0.01pu value and it can be observed from Figures 5.14(d) and 5.15(d). DC-link voltage is stabilized at 0.9 pu and it can be seen from Figures 5.14(e) and 5.15(e).

5.9 Summary

In this chapter, a hybrid control scheme is proposed for an onshore AC grid-integrated to an offshore wind farms with multi-terminal VSC-HVDC transmission link. A SMC and PI control techniques are adopted to design the proposed hybrid controller for wind farm side and grid side VSCs, where outer and inner controllers are based on SMC and PI, respectively. It is designed for obtaining the effective power transfer between the source and grid. The mathematical modelling, dynamic modelling and state-space model of the multi-terminal VSC-HVDC system are discussed. The performance of the multi-terminal VSC-HVDC system with hybrid and conventional controller for various cases are analyzed and compared. Furthermore, the FRT ca-

(a) Source active power of OSWF 1 & 2
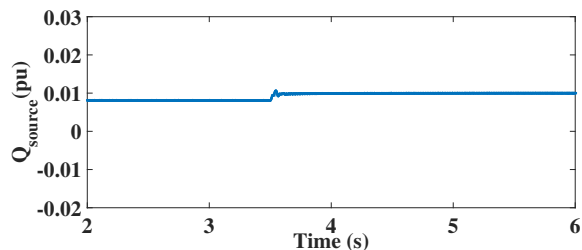
(b) Source reactive power of OSWF 1 & 2

(c) Grid active power

(d) Grid reactive power
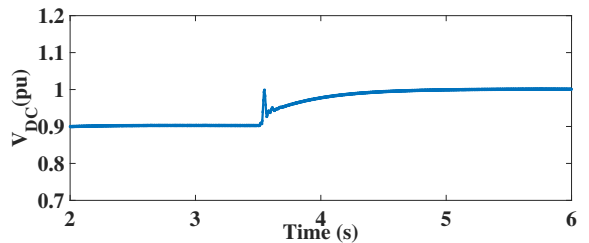
(e) DC-link voltage

Figure 5.12: Responses of the multi-terminal VSC-HVDC system with PI controller for step change wind speed from 12 m/s to 13 m/s
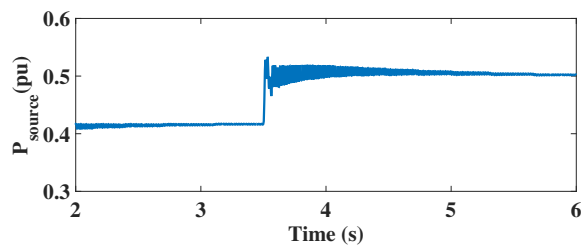
(a) Source active power of OSWF 1 & 2
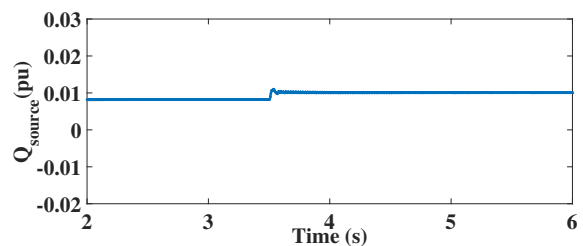
(b) Source reactive power of OSWF 1 & 2
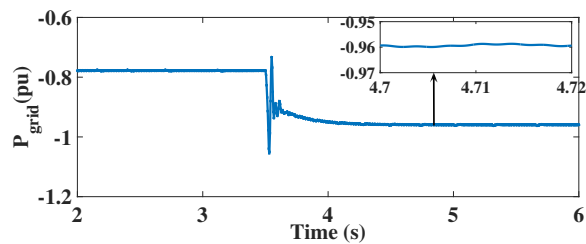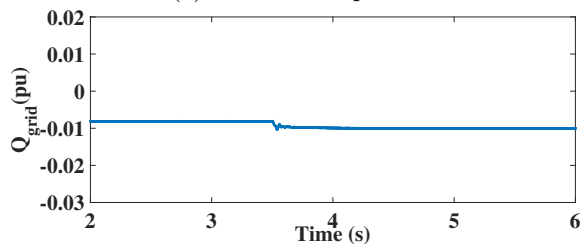
(c) Grid active power

(d) Grid reactive power
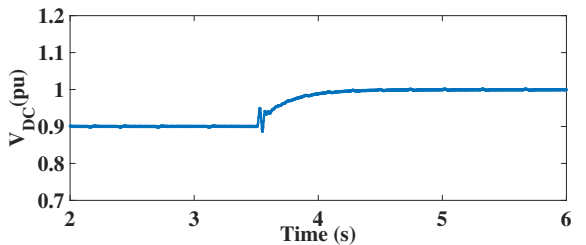
(e) DC-link voltage

Figure 5.13: Responses of the multi-terminal VSC-HVDC system with hybrid controller for step change wind speed from 12 m/s to 13 m/s
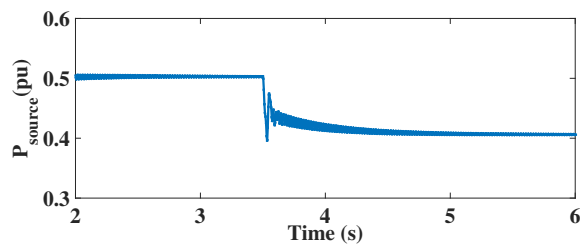
(a) Source active power of OSWF 1 & 2
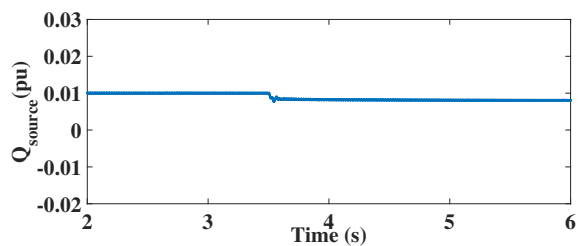
(b) Source reactive power of OSWF 1 & 2
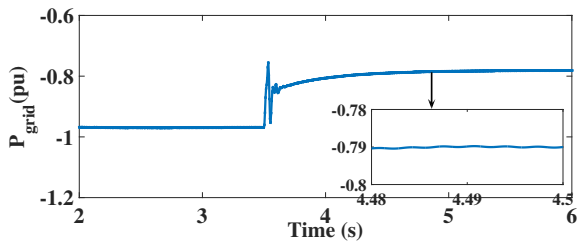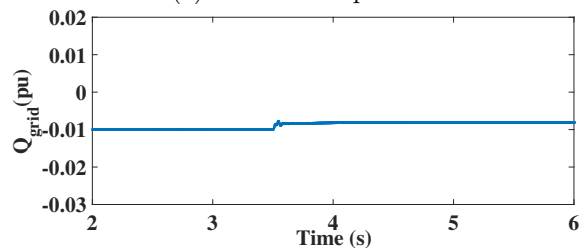
(c) Grid active power

(d) Grid reactive power
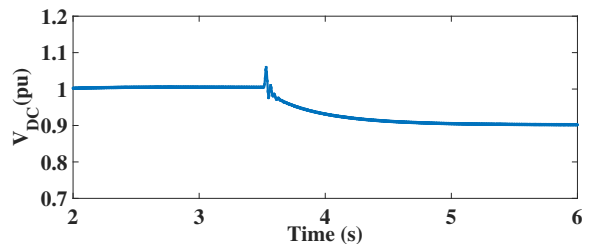
(e) DC-link voltage

Figure 5.14: Responses of the multi-terminal VSC-HVDC system with PI controller for step change wind speed from 13 m/s to 12 m/s
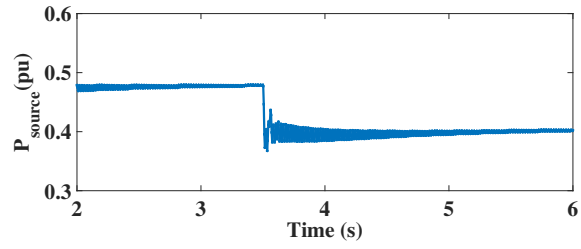
(a) Source active power of OSWF 1 & 2
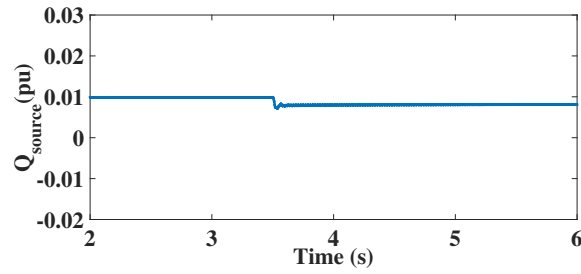
(b) Source reactive power of OSWF 1 & 2
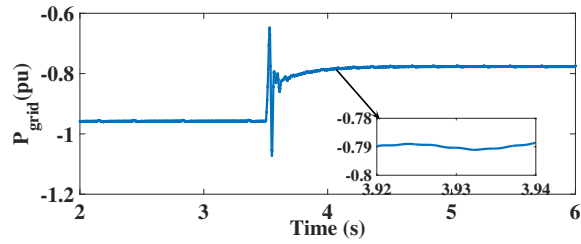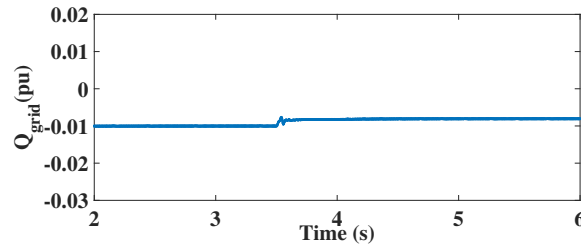
(c) Grid active power

(d) Grid reactive power
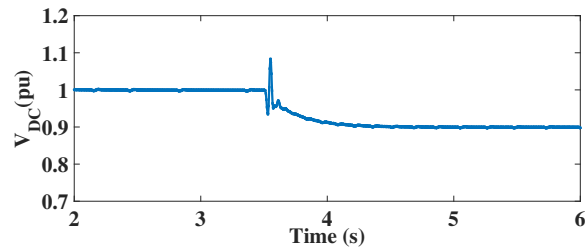
(e) DC-link voltage
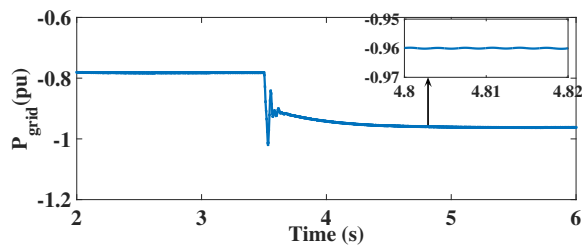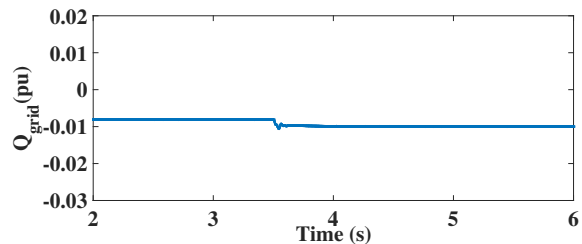
Figure 5.15: Responses of the multi-terminal VSC-HVDC system with hybrid controller for step change wind speed from 13 m/s to 12 m/s

pability is examined by applying the symmetrical and unsymmetrical faults at grid end. The WVSC side controller is operated to maintain the AC voltage. The GVSC side controller is operated to maintain the stable DC-link voltage and to control grid reactive power to minimum value. The proposed controller is operated to reach the pre-fault values of grid active power and DC-link voltage within less time as related to the conventional controller. The system stability is analyzed with the help of the eigenvalue plots for the parameter uncertainty which includes a variation of the AC filter capacitance and system frequency values. Finally, it is concluded that the multi-terminal VSC-HVDC system with the proposed hybrid controller is stable and capably handled the FRT capability under a fault condition compared to conventional PI controller.

Chapter 6

CONCLUSION

6.1   Conclusion

In recent times, the world energy scenario is purely dependent on sustainable power sources among which offshore wind farms are the main contributing factors in the form of wind energy. The offshore wind farms are experiencing quite a few challenges such as the electrical collector system design problem, wake effect, and effective power transmission from an offshore site to the onshore grid. Firstly, new optimization approaches are proposed to address the design of the electrical collector system. Next, the hybrid controller scheme is proposed to design a robust controller for grid-integrated offshore wind farm through the VSC-HVDC transmission system and grid-integrated multiple OSWFs through the multi-terminal VSC-HVDC transmission system. The conclusions of each of the above chapters is given below:

In chapter 1, an introduction consisting of the overview of the thesis and the reasons for its motivation are elaborated followed by the research objectives and a brief flow of the organization of the thesis discoursed at the end.

In chapter 2, the literature survey related to the objectives is discussed. Firstly, the various electrical collector topologies for offshore wind farms are explained in detail, namely AC collector systems, DC collector systems, and Redundant path topologies. Secondly, the different approaches applied for the design of optimal electrical collector system are reviewed, followed by a description of the various control schemes for grid-integrated offshore wind farm through the VSC-HVDC transmission system. Lastly, the different control schemes for grid-integrated multiple offshore wind farms through the multi-terminal VSC-HVDC transmission system are elucidated.

In chapter 3, new optimization approaches are proposed to design optimal electrical collector system for OSWF. In large OSWF, WTs are affected by the wake and it leads to the reduction of power production. The optimal placement of WTs resolves the wake issue. Wind rose of OSWF will give an indication of the direction in which WTs have to be placed. Larsen and Jensen wake model-based wake analysis are explained and the analytical wake model is implemented to study the wake effect, wake loss and to obtain optimal placement of WTs. Also, ACO-TSP, ACO-MTSP, FA-TSP and FA-MTSP are proposed and applied to achieve an optimal electrical collector system design of OSWFs. The mathematical model is discussed to estimate the levelized production cost, and annual energy yields. The results obtained from the optimized model are compared with the reference OSWF. From the results obtained from the OSWF designs, the length of inter-array cable, cable cost, and wake loss of optimal designs are observed to be minimized compared to reference OSWF. The average wind velocity, approximate power production, and annual energy yields of optimal designs are improved. The levelized production cost of optimal designs is reduced. The optimal designs of the NH OSWF based on ACO-MTSP and FA-MTSP are found to be better models compared to reference NH OSWF. The optimal designs of the HR OSWF based on ACO-MTSP and FA-MTSP are found to be better models compared to reference HR OSWF. As per the computation time and cable length, the ACO-based OSWF is observed to be better optimal design as compared to FA and GA-based designs. In the case of the optimal design for ring collector system, the FA based optimal design is found to be better design as compared to ACO based optimal design. The ring collector system improves the reliability of the OSWF. From the optimal design outcomes, it is concluded that ACO and FA are a better methods to solve the large OSWF collector layout problems in comparison with GA.

In chapter 4, a hybrid control scheme is proposed for an onshore AC grid integrated to an offshore wind farm with VSC-HVDC transmission link. A SMC and conventional PI control techniques are adopted for outer and inner controller respectively in the proposed hybrid controller for wind farm side and grid side VSCs. It is designed for obtaining the effective power transfer between the source and grid. The mathematical modelling, dynamic modelling and state-space model of the VSC-HVDC system are discussed. The performance of the VSC-HVDC system with hybrid and conventional controller for various cases are analyzed and compared. Furthermore, the FRT capability is examined by applying the symmetrical and unsymmetrical

faults at grid end. The WVSC side controller is operated to maintain the AC voltage. The GVSC side controller is operated to maintain the stable DC-link voltage and control grid reactive power to minimum value. For LLLG fault case, (a) the grid active power of the hybrid controlller is restored to a pre-fault value within 0.7s and PI controller took 1.4s, (b) the grid reactive power is stablized at -0.01pu value within 0.2s for both PI and hybrid controllers, and (c) the DC-link voltage response of hybrid controller stabilized at 1pu value within 0.92s and PI controller took 1.15s. For LG fault case, (a) the grid active power of the hybrid controlller is restored to a pre-fault value within 0.65s and PI controller took 1s, (b) the grid reactive power is stablized at -0.01pu value within 0.2s for both PI and hybrid controllers, and (c) the DC-link voltage response of hybrid controller stabilized at 1pu value within 0.93s and PI controller took 1.15s. The proposed controller is takes less time to reach the pre-fault value of grid active power and DC-link voltage compared to the conventional controller. The system stability is analyzed with the help of the eigenvalue plots for the parameter uncertainty which includes a variation of the AC filter capacitance and system frequency values. Additionally, the Nyquist plot and eigenvalue analysis are used to observe the controller stability. With reference to time domain specifications of the designed controller in terms of settling and rise time, SMC based controllers have taken less settling time compared to conventional controller this is verified by analyzing the step response of the controllers. Finally, it is concluded that the VSC-HVDC system with the proposed hybrid controller is stable and shown better the FRT capability compared to conventional PI controller under a fault condition.

In chapter 5, a hybrid controller approach based on a PI-SMC approach for the multi-terminal VSC-HVDC system is proposed. The hybrid controller is modelled for WVSC to control the AC voltage and GVSC to regulate the DC voltage and reactive power. The responses of the conventional controller approach (outer and inner are based on PI) and hybrid controller approach (outer is SMC-based and inner is PI-based) are observed and compared. The mathematical modelling, dynamic modelling and state-space model of the multi-terminal VSC-HVDC system are discussed. Further, the FRT capability of the multi-terminal VSC-HVDC system is examined under the symmetrical fault and unsymmetrical fault conditions. For LLLG fault case, (a) the grid active power of the hybrid controlller is restored to a pre-fault value within 0.52s and PI controller took 1s, (b) the grid reactive power is stablized at -0.01pu value within 0.15s for both PI and hybrid controllers, and (c) the DC-link voltage

response of hybrid controller stabilized at 1pu value within 0.9s and PI controller took 1.15s. For LG fault case, (a) the grid active power of the hybrid controlller is restored to a pre-fault value within 0.43s and PI controller took 0.62s, (b) the grid reactive power is stablized at -0.01pu value within 0.15s for both PI and hybrid controllers, and (c) the DC-link voltage response of hybrid controller stabilized at 1pu value within 0.75s and PI controller took 1.15s. The hybrid controller has shown better responses such as AC voltage maintained at unity, DC-link voltage is regulated to 1 pu, and grid reactive power is controlled to a minimum value. The hybrid controller responses took less time compared to a conventional controller. With regard to time domain specifications of the designed controller in terms of settling and rise time, SMC based controllers took less settling time compared to a conventional controller. The proposed controller is operated to reach the pre-fault values of grid active power and DC-link voltage within less time as related to the conventional controller. The system stability is analyzed with the help of the eigenvalue plots for the parameter uncertainty which includes a variation of the AC filter capacitance and system frequency values. Finally, it is concluded that the multi-terminal VSC-HVDC system with the proposed hybrid controller is stable and capable of handling the FRT capability better compared to conventional PI controller under a fault condition.

6.2 Contributions

The main contributions of the thesis is as follows,

- ACO-TSP and FA-TSP approaches are proposed to design an optimal electrical collector system for small offshore wind farms.

- ACO-MTSP and FA-MTSP approaches are proposed to design an optimal electrical collector system for small and large offshore wind farms.

- Combination of sliding mode control and PI control based hybrid controller is proposed for a grid-integrated offshore wind farm with VSC-HVDC transmission system. Dynamic model, linearized state-space model are developed. Small signal stability analysis for the VSC-HVDC system is carried out.

- Combination of sliding mode control and PI control based hybrid controller is proposed for grid-integrated multiple offshore wind farms with the multi-

164

terminal VSC-HVDC transmission system. Dynamic model, linearized state-space model are developed. Small signal stability analysis for the VSC-HVDC system is carried out.

6.3   Future scope

The future scope of the thesis is as follows,

- The proposed optimization approach can be applied to design the optimal electrical collector system for (a) irregular shaped OSWF with consideration of the restricted area, (b) irregular shaped OSWF without consideration of the restricted area, and (c) regular shaped OSWF with consideration of the restricted area.

- The proposed hybrid control scheme can be used to design the robust controller for (a) grid-integrated OSWF with the CSC-HVDC transmission system and (b) grid-integrated multiple OSWFs with the multi-terminal CSC-HVDC transmission system.

- A robust controller can be designed based on the SMC technique for grid-integrated OSWF with VSC-HVDC and CSC-HVDC transmission system.

Appendix A

MATLAB CODE FOR PROPOSED OPTIMIZATION APPROACHES

A.1   ACO-MTSP

```
%%%%%%% Radial model optimal design of wind farm %%%%%%%%%%
clc
clear all
tic
Nwt=11;
ABwt=importdata('AB.txt')
Awt=ABwt(1:Nwt,1)';
Bwt=ABwt(1:Nwt,2)';
Nat=Nwt;
% wind turbines are located at point (Awt,Bwt) distance between wind turbines
T=zeros(Nwt,Nwt);
NEwt=0;
dd=[0 0];
OPTDf=zeros(3,Nwt+1);
OPTD=RADIALnew(Nwt,Nat,Awt,Bwt,T,NEwt,dd);
OPTDf(1,:)=OPTD;
```

```
%%%%%%%%%%%%%%%%%%%%%%%%%%%%%%%%%%%%%%%%%%
Awt=ABwt(Nwt+1:2*Nwt,1)';
Bwt=ABwt(Nwt+1:2*Nwt,2)';
T=zeros(Nwt,Nwt);
NEwt=0;
dd=[0 0];
OPTD=RADIALnew(Nwt,Nat,Awt,Bwt,T,NEwt,dd);
OPTDf(2,:)=OPTD;
%%%%%%%%%%%%%%%%%%%%%%%%%%%%%%%%%%%%%%%%%%%%
Awt=ABwt(2*Nwt+1:3*Nwt,1)';
Bwt=ABwt(2*Nwt+1:3*Nwt,2)';
T=zeros(Nwt,Nwt);
NEwt=0;
dd=[0 0];
OPTD=RADIALnew(Nwt,Nat,Awt,Bwt,T,NEwt,dd);
OPTDf(3,:)=OPTD
t1=toc
```

A.1.1   Function-RADIALnew

```
function [ OPTD ] = RADIALnew(Nwt,Nat,T,Awt,Bwt,NEwt,dd)
y=zeros(3,Nwt+1);
for ii=1:3 %%%%%% to get optimal
dwt=zeros(Nwt,Nwt)
for ic=1:Nwt
for id=1:Nwt
dwt(ic,id)=sqrt((Awt(ic)-Awt(id))^2+(Bwt(ic)-Bwt(id))^2);
end % id
end % ic
V=1./dwt;                % visibility(V) equals inverse of distance
PHro=1*ones(Nwt,Nwt);  % initialized pheromones between wind turbines
ITmax=100;               % max number of iterations
a=2;
b=6;
rr=0.5;
```

168

```
Q=sum(1./(1:8));
dbt=9999999;
e=5;
err=0.1; %%  intial error
D1=500; %% intial value
Di=ones(1,10000)*500;
t=0;
while err>1e-2 %%%%error condition
for ic=1:Nat
T(ic,:)=randperm(Nwt);
end % ic
k=1
for IT=1:ITmax
% find the wind turbine tour for each ant
% Swt is the current wind turbine
% Tour next contains the remaining wind turbines to be visited
for ia=1:Nat
for iq=2:Nwt-1[iq T(ia,:)]
Swt=T(ia,iq-1);
Tnext=T(ia,iq:Nwt);
P=((PHro(Swt,Tnext).^a).*(V(Swt,Tnext).^b))
    ./sum((PHro(Swt,Tnext).^a).*(V(Swt,Tnext).^b)));  % P probability
Rwt=rand; % Rwt random wind turbines
for iz=1:length(P)
if Rwt<sum(P(1:iz))
NEwt=iq-1+iz; % NEWwt next wind turbine to be visited
break
end % if
end % iz
Ttemp=T(ia,NEwt); %Temporary  tours puts the new wind turbine
% selected next in line
T(ia,NEwt)=T(ia,iq);
T(ia,iq)=Ttemp;
end % iq
```

```
end % ia
% calculate the length of each tour and pheromone distribution
PHtp=zeros(Nwt,Nwt);
for ic=1:Nat
d(ic,1)=0;
for id=1:Nwt-1
d(ic,1)=d(ic)+dwt(T(ic,id),T(ic,id+1));
PHtp(T(ic,id),T(ic,id+1))=Q/d(ic,1);
end % id
end % ic
[dmin,ind]=min(d);
if dmin<dbt
dbt=dmin;
end % if
% pheromone for elite path
PH=zeros(Nwt,Nwt);
for id=1:Nwt-1
PH(T(ind,id),T(ind,id+1))=Q/dbt;
end % id
% update pheromone trails
PHro=(1-rr)*PHro+PHtp+e*PH;
dd(IT,:)=[dbt dmin];
[IT dmin dbt];
[dm ind1]=min(d);
x(k,1:(Nwt+1))=[T(ind1,:) d(ind1)];
k=k+1;
end %it
D=min(x(:,(Nwt+1)));
t=t+1;
Di(1,t)=D;
err=abs(D1-D)
D1=min(Di);
end
[dmf ind2]=(min(x(:,(Nwt+1))));% dmf final minimum distance of tour
```

```
 disp('optimal Tour and Distance')
 y(ii,:)=x(ind2,:);
 end
 [dmfi ind3]=(min(y(:,(Nwt+1))));
 OPTD=y(ind3,:)
 end
```

A.2 FA-MTSP

```
clear all
clc
tic
Nwt=11; % number of wind turbines
ABwt=importdata('AB.txt')
Awt=ABwt(1:Nwt,1)';
Bwt=ABwt(1:Nwt,2)';
Nat=Nwt;
N=Nwt;
T=zeros(Nwt,Nwt);
NEwt=0;
dd=[0 0];
OPTDf=zeros(3,Nwt+1);
OPTD=RADIALfanew(N,Awt,Bwt,NEwt,dd);
OPTDf(1,:)=OPTD;
%%%%%%%%%%%%%%%%%%%%%%%%%%%%%%%%%%%%%%%%%%%
Awt=ABwt(Nwt+1:2*Nwt,1)';
Bwt=ABwt(Nwt+1:2*Nwt,2)';
T=zeros(Nwt,Nwt);
NEwt=0;
dd=[0 0];
OPTD=RADIALfanew(N,Awt,Bwt,NEwt,dd);
OPTDf(2,:)=OPTD;
%%%%%%%%%%%%%%%%%%%%%%%%%%%%%%%%%%%%%%%%%%%
Awt=ABwt(2*Nwt+1:3*Nwt,1)';
```

```
Bwt=ABwt(2*Nwt+1:3*Nwt,2)';
T=zeros(Nwt,Nwt);
NEwt=0;
dd=[0 0];
OPTD=RADIALfanew(N,Awt,Bwt,NEwt,dd);
OPTDf(3,:)=OPTD
t1=toc
```

A.2.1 Function-RADIALfanew

```
function [ OPTD ] = RADIALfanew(N,Awt,Bwt,NEwt,dd)
y=zeros(10,N+1);
for ii=1:10 %%%%%% to get optimal
f=vectorize('sqrt(Awt^2 + Bwt^2)');
alpha=0.2;      % Randomness 0--1 (highly random)
gamma=1.0;     % Absorption coefficient
delta=0.97;     % Randomness reduction (similar to an annealing schedule)
dbt=100000;
z=zeros(size(Awt));
for i=1:N
z(i)=sqrt(Awt(i)^2 + Bwt(i)^2);
end
% Ranking the fireflies by their light intensity
[lightn,Ind]=sort(z);
for ic=1:N
for id=1:N
dwt(ic,id)=sqrt((Awt(ic)-Awt(id))^2+(Bwt(ic)-Bwt(id))^2);
end % id
end % ic
err=0.1; %%  intial error
D1=500; %% intial value
Di=ones(1,10000)*500;
t=0;
while err>1e-5 %%%%error condition
% tours(T) Initialization
```

```
T= zeros(N);
for ic=1:N
T(ic,:)=randperm(N);
end
%%%%%%%%%%%%%change for ring to radial%%%%%%%%%%%%%%%%%%%%%%%%%
%T(:,N+1)=T(:,1); % tour ends on wind turbine it starts with
ITmax=100;
k=1;
for IT=1:ITmax
for ia=1:N
Ts=T(ia,:);
for iq=2:N-1
Swt=T(ia,iq-1);
Tnext=T(ia,iq:N);
%%%%%%%%%%%%%%%%%
% The attractiveness parameter beta=exp(-gamma*r)
r=dwt(Swt,Tnext);
beta0=1;
beta=beta0*exp(-gamma*r.^2);
[r1 ind]=sort(r);
[b1 ind2]=sort(beta,'descend');
Tt=Tnext(ind(1));
if Tnext(ind(1))== Tnext(ind2(1)) % Brighter and more attractive
[row,col]=find(Ts==Tt);
NEwt=col;
end
Ttemp=T(ia,NEwt);
%Temporary  tours puts the new wind turbine selected next in line
T(ia,NEwt)=T(ia,iq);
T(ia,iq)=Ttemp;
end % iq
end % ia
% calculate the length of each tour and pheromone distribution
for ic=1:N
```

```
d(ic,1)=0;
%%%%%%%%%%%%%change for ring (N)to radial (N-1)%%%%%%%%%%%%%%%%%%%%%%%%%%%%
for id=1:N-1
d(ic,1)=d(ic)+dwt(T(ic,id),T(ic,id+1));
end % id
end % ic
[dmin,ind]=min(d);
%%%%%%%%%%%%%%%%%%%%%%%%%
if dmin<dbt
dbt=dmin;
end
%%%%%%%%%%%%%%%%%%%%%%%%%%%
dd(IT,:)=[dbt dmin];
[IT dmin dbt];
[dm ind1]=min(d);
%%%%%%%%%%%%%change for ring (N+2)to radial (N+1)%%%%%%%%%%%%%%%%%%%%%%%%%%%%
x1(k,1:(N+1))=[T(ind1,:) d(ind1)];
k=k+1;
end %it
%%%%%%%%%%%%%change for ring (N+2)to radial (N+1)%%%%%%%%%%%%%%%%%%%%%%%%%%%%
D=min(x1(:,(N+1)));
t=t+1;
Di(1,t)=D;
err=abs(D1-D);
D1=min(Di);
end
%%%%%%%%%%%%%change for ring (N+2)to radial (N+1)%%%%%%%%%%%%%%%%%%%%%%%%%%%%
[dmf ind3]=(min(x1(:,(N+1))));% dmf final minimum distance of tour
disp('optimal Tour and Distance')
y(ii,:)=x1(ind3,:);
end
[dmfi ind4]=(min(y(:,(N+1))));
OPTD=y(ind4,:)
end
```

Appendix B

B.1 Clarke and Park transformation

The Clarke and park transformation convert the three-phase ac quantities to two-phase dq quantities. The system control with two-phase quantities is easier than the three-phase ac quantities. So, the dq frame equations reduce the complexity of system control. The phase transformation from abc frame to $\alpha\beta$ frame of reference is by Clarke transformation as given in (B.1). Clarke transformation matrix is given in (B.2).

$$Y_{\alpha\beta} = Y_\alpha + jY_\beta = k[Y_a + Y_b e^{-j\frac{2\pi}{3}} + Y_c e^{-j\frac{4\pi}{3}}] \tag{B.1}$$

$$\begin{bmatrix} Y_\alpha \\ Y_\beta \end{bmatrix} = k \begin{bmatrix} 1 & \frac{-1}{2} & \frac{-1}{2} \\ 0 & \frac{\sqrt{3}}{2} & \frac{-\sqrt{3}}{2} \end{bmatrix} \begin{bmatrix} Y_a \\ Y_b \\ Y_c \end{bmatrix} \tag{B.2}$$

Where constant k value is 2/3. The Park transformation is used to convert $\alpha\beta$ frame to dq frame with a phase shift of angle θ and Park transformation matrix is shown in (B.3).

$$\begin{bmatrix} Y_d \\ Y_q \end{bmatrix} = \begin{bmatrix} \cos\theta & \sin\theta \\ -\sin\theta & \cos\theta \end{bmatrix} \begin{bmatrix} Y_\alpha \\ Y_\beta \end{bmatrix} \tag{B.3}$$

B.2 State-space equations for the generalized system transfer function

The generalized transfer function of the system is given in (B.4).

$$\frac{y(s)}{u(s)} = \frac{(b_0 s^n + b_1 s^{n-1} + ... + b_{n-1}s + b_n)}{(a_0 s^n + a_1 s^{n-1} + ... + a_{n-1}s + a_n)} \tag{B.4}$$

Multiply the nominator and denominator terms of (B.6) with s^{-n}, to ensure that all differential operators have been eliminated and it is stated in (B.5)

$$\frac{y(s)}{u(s)} = \frac{(b_0 + b_1 s^{-1} + ... + b_{n-1} s^{-(n-1)} + b_n s^{-n})}{(a_0 + a_1 s^{-1} + ... + a_{n-1} s^{-(n-1)} + a_n s^{-n})} \tag{B.5}$$

Adjust the (B.5) to get state vector equation $x(s)$ with respect to input vector $u(s)$ and it is shown in (B.6).

$$\frac{y(s)}{x(s)} * \frac{x(s)}{u(s)} = \frac{(b_0 + b_1 s^{-1} + ... + b_{n-1} s^{-(n-1)} + b_n s^{-n})}{1} * \frac{1}{(a_0 + a_1 s^{-1} + ... + a_{n-1} s^{-(n-1)} + a_n s^{-n})} \tag{B.6}$$

The $\frac{x(s)}{u(s)}$ equation formed from (B.6) and it is given in(B.7).

$$\frac{x(s)}{u(s)} = \frac{1}{(a_0 + a_1 s^{-1} + ... + a_{n-1} s^{-(n-1)} + a_n s^{-n})} \tag{B.7}$$

$$\frac{1}{a_0} * u(s) = x(s) * (1 + \frac{a_1}{a_0} s^{-1} + ... + \frac{a_{n-1}}{a_0} s^{-(n-1)} + \frac{a_n}{a_0} s^{-n})$$

The inverse Laplace transformation is applied to (B.7) and convert s-term function to t-term function. The state-space equations in matrix form is shown in (B.8) and system matrix A and input matrix B are shown in (B.8).

$$
\overbrace{\begin{bmatrix} \dot{x}_1 \\ \dot{x}_2 \\ . \\ . \\ . \\ . \\ \dot{x}_n \end{bmatrix}}^{\dot{x}(t)} = \overbrace{\begin{bmatrix} 0 & 1 & ..... & 0 \\ 0 & 0 & ..... & 0 \\ . & . & ..... & . \\ . & . & ..... & . \\ . & . & ..... & . \\ 0 & 0 & ..... & 1 \\ \frac{-a_n}{a_0} & \frac{-a_{n-1}}{a_0} & ..... & \frac{-a_1}{a_0} \end{bmatrix}}^{A} \overbrace{\begin{bmatrix} x_1 \\ x_2 \\ . \\ . \\ . \\ . \\ x_n \end{bmatrix}}^{x(t)} + \overbrace{\begin{bmatrix} 0 \\ 0 \\ . \\ . \\ . \\ . \\ \frac{1}{a_0} \end{bmatrix}}^{B} u(t) \tag{B.8}
$$

176

Bibliography

Abdelsalam, A. M. and El-Shorbagy, M. (2018). Optimization of wind turbines siting in a wind farm using genetic algorithm based local search. *Renewable Energy*, 123:748–755.

Adeuyi, O. D., Cheah-Mane, M., Liang, J., Livermore, L., and Mu, Q. (2015). Preventing dc over-voltage in multi-terminal hvdc transmission. *CSEE Journal of Power and Energy Systems*, 1(1):86–94.

Ahmed, M., Ebrahim, M., Ramadan, H., and Becherif, M. (2015). Optimal genetic-sliding mode control of vsc-hvdc transmission systems. *Energy Procedia*, 74:1048–1060.

Ali, M., Matevosyan, J., and Milanović, J. (2012). Probabilistic assessment of wind farm annual energy production. *Electric Power Systems Research*, 89:70–79.

Amaral, L. and Castro, R. (2017). Offshore wind farm layout optimization regarding wake effects and electrical losses. *Engineering Applications of Artificial Intelligence*, 60:26–34.

Aragüés-Peñalba, M., Egea-Àlvarez, A., Gomis-Bellmunt, O., and Sumper, A. (2012). Optimum voltage control for loss minimization in hvdc multi-terminal transmission systems for large offshore wind farms. *Electric Power Systems Research*, 89:54–63.

Bala, J. P. S. and Sandeberg, M. C. P. (2014). Dc connection of offshore wind power plants without platform. In *Paper presented at the 13th Wind Integration Workshop*, volume 11, page 13.

Bansal, J. C. and Farswan, P. (2017). Wind farm layout using biogeography based optimization. *Renewable Energy*, 107:386–402.

Bauer, J. and Lysgaard, J. (2015). The offshore wind farm array cable layout problem: a planar open vehicle routing problem. *Journal of the Operational Research Society*, 66(3):360–368.

Benadja, M. and Chandra, A. (2015). Adaptive sensorless control of pmsgs-based offshore wind farm and vsc-hvdc stations. *IEEE Journal of Emerging and Selected Topics in Power Electronics*, 3(4):918–931.

Beşkirli, M., Koç, İ., Haklı, H., and Kodaz, H. (2018). A new optimization algorithm for solving wind turbine placement problem: Binary artificial algae algorithm. *Renewable Energy*, 121:301–308.

Blasco-Gimenez, R., Ano-Villalba, S., Rodríguez-D'Derlée, J., Morant, F., and Bernal-Perez, S. (2010). Distributed voltage and frequency control of offshore wind farms connected with a diode-based hvdc link. *IEEE Transactions on Power Electronics*, 25(12):3095–3105.

Chaudhuri, N. R. and Yazdani, A. (2011). An aggregation scheme for offshore wind farms with vsc-based hvdc collection system. In *Power and Energy Society General Meeting, 2011 IEEE*, pages 1–8. IEEE.

Chen, Y., Dong, Z., Meng, K., Luo, F., Yao, W., and Qiu, J. (2013). A novel technique for the optimal design of offshore wind farm electrical layout. *Journal of Modern Power Systems and Clean Energy*, 1(3):258–263.

Chen, Y., Dong, Z. Y., Meng, K., Luo, F., Xu, Z., and Wong, K. P. (2016). Collector system layout optimization framework for large-scale offshore wind farms. *IEEE Transactions on Sustainable Energy*, 7(4):1398–1407.

Choi, J. and Shan, M. (2013). Advancement of jensen (park) wake model. In *Proceedings of the European Wind Energy Conference and Exhibition*, pages 1–8.

Chowdhury, S., Zhang, J., Messac, A., and Castillo, L. (2013). Optimizing the arrangement and the selection of turbines for wind farms subject to varying wind conditions. *Renewable Energy*, 52:273–282.

Chuangpishet, S. and Tabesh, A. (2011). Matrix interconnected topology for dc collector systems of offshore wind farms. In *Renewable Power Generation (RPG 2011), IET Conference on*, pages 1–4. IET.

Chuangpishit, S., Tabesh, A., Moradi-Sharbabk, Z., and Saeedifard, M. (2014). Topology design for collector systems of offshore wind farms with pure dc power systems. *Industrial Electronics, IEEE Transactions on*, 61(1):320–328.

Colbia-Vega, A., de Leon-Morales, J., Fridman, L., Salas-Pena, O., and Mata-Jiménez, M. (2008). Robust excitation control design using sliding-mode technique for multimachine power systems. *Electric Power Systems Research*, 78(9):1627–1634.

Council(GWEC), G. W. E. (2017). Global wind statistics 2017. `https://gwec.net/wp-content/uploads/vip/GWEC_PRstats2017_EN-003_FINAL.pdf`.

Dahmani, O., Bourguet, S., Machmoum, M., Guérin, P., Rhein, P., and Jossé, L. (2015). Optimization of the connection topology of an offshore wind farm network. *IEEE Systems Journal*, 9(4):1519–1528.

De Prada, M., Corchero, C., Gomis-Bellmunt, O., Sumper, A., et al. (2015). Hybrid ac-dc offshore wind power plant topology: Optimal design. *IEEE Transactions on Power Systems*, 30(4):1868–1876.

Dierckxsens, C., Srivastava, K., Reza, M., Cole, S., Beerten, J., and Belmans, R. (2012). A distributed dc voltage control method for vsc mtdc systems. *Electric Power Systems Research*, 82(1):54–58.

Dorigo, M. and Thomas, S. (2004). *Ant Colony Optimization*. The MIT press, Cambridge, Massachusetts.

Du, C. (2007). *VSC-HVDC for industrial power systems*. Chalmers University of Technology.

Dutta, S. and Overbye, T. J. (2012). Optimal wind farm collector system topology design considering total trenching length. *IEEE Transactions on Sustainable Energy*, 3(3):339–348.

Edrah, M., Lo, K. L., Anaya-Lara, O., and Elansari, A. (2015). Impact of dfig based offshore wind farms connected through vsc-hvdc link on power system stability. pages 1–7.

Egea-Àlvarez, A., Aragüés-Peñalba, M., Prieto-Araujo, E., and Gomis-Bellmunt, O. (2017). Power reduction coordinated scheme for wind power plants connected with vsc-hvdc. *Renewable energy*, 107:1–13.

Erlich, I., Feltes, C., and Shewarega, F. (2014). Enhanced voltage drop control by vsc–hvdc systems for improving wind farm fault ridethrough capability. *IEEE Transactions on Power Delivery*, 29(1):378–385.

Feltes, C., Wrede, H., Koch, F. W., and Erlich, I. (2009). Enhanced fault ride-through method for wind farms connected to the grid through vsc-based hvdc transmission. *IEEE Transactions on Power Systems*, 24(3):1537–1546.

Feng, J. and Shen, W. Z. (2015). Solving the wind farm layout optimization problem using random search algorithm. *Renewable Energy*, 78:182–192.

Gavriluta, C., Candela, I., Citro, C., Luna, A., and Rodriguez, P. (2015). Design considerations for primary control in multi-terminal vsc-hvdc grids. *Electric Power Systems Research*, 122:33–41.

Giddani, O., Abbas, A. Y., Adam, G. P., Anaya-Lara, O., and Lo, K. L. (2013). Multi-task control for vsc–hvdc power and frequency control. *International Journal of Electrical Power & Energy Systems*, 53:684–690.

Gil, M. D. P., Domínguez-García, J., Díaz-González, F., Aragüés-Peñalba, M., and Gomis-Bellmunt, O. (2015). Feasibility analysis of offshore wind power plants with dc collection grid. *Renewable Energy*, 78:467–477.

González, J. S., García, Á. L. T., Payán, M. B., Santos, J. R., and Rodríguez, Á. G. G. (2017). Optimal wind-turbine micro-siting of offshore wind farms: A grid-like layout approach. *Applied energy*, 200:28–38.

González, J. S., Payán, M. B., and Santos, J. R. (2013). A new and efficient method for optimal design of large offshore wind power plants. *IEEE Transactions on Power Systems*, 28(3):3075–3084.

Gonzalez-Longatt, F. M. (2013). Optimal offshore wind farms' collector design based on the multiple travelling salesman problem and genetic algorithm. In *PowerTech (POWERTECH), 2013 IEEE Grenoble*, pages 1–6. IEEE.

Gonzalez-Longatt, F. M., Wall, P., Regulski, P., and Terzija, V. (2012). Optimal electric network design for a large offshore wind farm based on a modified genetic algorithm approach. *IEEE Systems Journal*, 6(1):164–172.

Hansen, K. S., Barthelmie, R. J., Jensen, L. E., and Sommer, A. (2012). The impact of turbulence intensity and atmospheric stability on power deficits due to wind turbine wakes at horns rev wind farm. *Wind Energy*, 15(1):183–196.

Haupt, R. L. and Haupt, S. E. (2004). *Practical genetic algorithms*. John Wiley & Sons.

Hou, P., Hu, W., Chen, C., and Chen, Z. (2016a). Optimisation of offshore wind farm cable connection layout considering levelised production cost using dynamic minimum spanning tree algorithm. *IET Renewable Power Generation*, 10(2):175–183.

Hou, P., Hu, W., Chen, C., Soltani, M., and Chen, Z. (2016b). Optimization of offshore wind farm layout in restricted zones. *Energy*, 113:487–496.

Hou, P., Hu, W., and Chen, Z. (2015a). Offshore substation locating in wind farms based on prim algorithm. In *2015 IEEE Power & Energy Society General Meeting*, pages 1–5. IEEE.

Hou, P., Hu, W., and Chen, Z. (2016c). Optimisation for offshore wind farm cable connection layout using adaptive particle swarm optimisation minimum spanning tree method. *IET Renewable Power Generation*, 10(5):694–702.

Hou, P., Hu, W., Soltani, M., Chen, C., and Chen, Z. (2017a). Combined optimization for offshore wind turbine micro siting. *Applied energy*, 189:271–282.

Hou, P., Hu, W., Soltani, M., Chen, C., Zhang, B., and Chen, Z. (2017b). Offshore wind farm layout design considering optimized power dispatch strategy. *IEEE Transactions on Sustainable Energy*, 8(2):638–647.

Hou, P., Hu, W., Soltani, M., and Chen, Z. (2015b). Optimized placement of wind turbines in large-scale offshore wind farm using particle swarm optimization algorithm. *IEEE Transactions on Sustainable Energy*, 6(4):1272–1282.

181

Hou, P., Hu, W., Zhang, B., Soltani, M., Chen, C., and Chen, Z. (2016d). Optimised power dispatch strategy for offshore wind farms. *IET Renewable Power Generation*, 10(3):399–409.

Hoyle, N. (2004). North hoyle offshore wind farm. `https://www.4coffshore.com/windfarms/north-hoyle-united-kingdom-uk16.html`.

Jovcic, D., Taherbaneh, M., Taisne, J.-P., and Nguefeu, S. (2015). Offshore dc grids as an interconnection of radial systems: Protection and control aspects. *Smart Grid, IEEE Transactions on*, 6(2):903–910.

Kalcon, G. O., Adam, G. P., Anaya-Lara, O., Lo, S., and Uhlen, K. (2012). Small-signal stability analysis of multi-terminal vsc-based dc transmission systems. *IEEE Transactions on Power Systems*, 27(4):1818–1830.

Kani, A. N. (2014). *Control systems*. RBA publications.

Khenar, M., Adabi, J., Pouresmaeil, E., Gholamian, A., and Catalão, J. P. (2017). A control strategy for a multi-terminal hvdc network integrating wind farms to the ac grid. *International Journal of Electrical Power & Energy Systems*, 89:146–155.

Kirakosyan, A., El Moursi, M. S., and Khadkikar, V. (2017). Fault ride through and grid support topology for the vsc-hvdc connected offshore wind farms. *IEEE Transactions on Power Delivery*, 32(3):1592–1604.

Korompili, A., Wu, Q., and Zhao, H. (2016). Review of vsc hvdc connection for offshore wind power integration. *Renewable and Sustainable Energy Reviews*, 59:1405–1414.

Kunjumuhammed, L. P., Pal, B. C., Gupta, R., and Dyke, K. J. (2017). Stability analysis of a pmsg-based large offshore wind farm connected to a vsc-hvdc. *IEEE Transactions on Energy Conversion*, 32(3):1166–1176.

Li, W., Özcan, E., and John, R. (2017). Multi-objective evolutionary algorithms and hyper-heuristics for wind farm layout optimisation. *Renewable Energy*, 105:473–482.

Liu, H. and Chen, Z. (2015). Contribution of vsc-hvdc to frequency regulation of power systems with offshore wind generation. *IEEE Transactions on Energy Conversion*, 30(3):918–926.

Liu, H. and Sun, J. (2014). Voltage stability and control of offshore wind farms with ac collection and hvdc transmission. *IEEE Journal of Emerging and selected topics in Power Electronics*, 2(4):1181–1189.

Lumbreras, S. and Ramos, A. (2013). Optimal design of the electrical layout of an offshore wind farm applying decomposition strategies. *IEEE Transactions on Power Systems*, 28(2):1434–1441.

Mahapatra, K. and Dash, P. (2015). Inertia emulation based sliding mode control of vsc hvdc system for transmission of power from onshore wind farms to ac grids. In *Power, Communication and Information Technology Conference (PCITC), 2015 IEEE*, pages 522–528. IEEE.

Mallick, R. (2011). Adaptive sliding mode control of vsc-hvdc transmission links. In *Energy, Automation, and Signal (ICEAS), 2011 International Conference on*, pages 1–6. IEEE.

Maniezzo, A. (1992). Distributed optimization by ant colonies. In *Toward a practice of autonomous systems: proceedings of the First European Conference on Artificial Life*, page 134. Mit Press.

Mitra, P., Zhang, L., and Harnefors, L. (2014). Offshore wind integration to a weak grid by vsc-hvdc links using power-synchronization control: A case study. *IEEE Transactions on Power Delivery*, 29(1):453–461.

Muyeen, S., Takahashi, R., and Tamura, J. (2010). Operation and control of hvdc-connected offshore wind farm. *IEEE Transactions on Sustainable Energy*, 1(1):30–37.

Nanou, S. and Papathanassiou, S. (2015). Evaluation of a communication-based fault ride-through scheme for offshore wind farms connected through high-voltage dc links based on voltage source converter. *IET Renewable Power Generation*, 9(8):882–891.

Nanou, S. I., Patsakis, G. N., and Papathanassiou, S. A. (2015). Assessment of communication-independent grid code compatibility solutions for vsc–hvdc connected offshore wind farms. *Electric Power Systems Research*, 121:38–51.

Nguyen, T. H., Le, Q. A., and Lee, D.-C. (2015). A novel hvdc-link based on hybrid voltage-source converters. In *Energy Conversion Congress and Exposition (ECCE), 2015 IEEE*, pages 3338–3343. IEEE.

Nguyen, T. H. and Lee, D.-C. (2012). Control of offshore wind farms based on hvdc. In *Energy Conversion Congress and Exposition (ECCE), 2012 IEEE*, pages 3113–3118. IEEE.

npower Renewables Limited (2007). Capital grant scheme for the north hoyle offshore wind farm annual report: July 2006 –june 2007. `https://webarchive.nationalarchives.gov.uk/+/http:/www.berr.gov.uk/files/file41542.pdf`.

Park, J. and Law, K. H. (2015). Layout optimization for maximizing wind farm power production using sequential convex programming. *Applied Energy*, 151:320–334.

Pérez, B., Mínguez, R., and Guanche, R. (2013). Offshore wind farm layout optimization using mathematical programming techniques. *Renewable Energy*, 53:389–399.

Pillai, A., Chick, J., Johanning, L., Khorasanchi, M., and de Laleu, V. (2015). Offshore wind farm electrical cable layout optimization. *Engineering Optimization*, 47(12):1689–1708.

Pillai, A. C., Chick, J., Khorasanchi, M., Barbouchi, S., and Johanning, L. (2017). Application of an offshore wind farm layout optimization methodology at middelgrunden wind farm. *Ocean Engineering*, 139:287–297.

Pookpunt, S. and Ongsakul, W. (2016). Design of optimal wind farm configuration using a binary particle swarm optimization at huasai district, southern thailand. *Energy conversion and management*, 108:160–180.

Prabhu, N. P., Yadav, P., Prasad, B., and Panda, S. K. (2013). Optimal placement of off-shore wind turbines and subsequent micro-siting using intelligently tuned harmony search algorithm. In *2013 IEEE Power & Energy Society General Meeting*, pages 1–7. IEEE.

Pradhan, J. K., Ghosh, A., and Bhende, C. (2017). Small-signal modeling and multivariable pi control design of vsc-hvdc transmission link. *Electric Power Systems Research*, 144:115–126.

Prieto-Araujo, E., Bianchi, F. D., Junyent-Ferre, A., and Gomis-Bellmunt, O. (2011). Methodology for droop control dynamic analysis of multiterminal vsc-hvdc grids for offshore wind farms. *IEEE Transactions on power delivery*, 26(4):2476–2485.

Quinonez-Varela, G., Ault, G., Anaya-Lara, O., and McDonald, J. (2007). Electrical collector system options for large offshore wind farms. *Renewable Power Generation, IET*, 1(2):107–114.

Ramadan, H. S., Siguerdidjane, H., Petit, M., and Kaczmarek, R. (2012). Performance enhancement and robustness assessment of vsc–hvdc transmission systems controllers under uncertainties. *International Journal of Electrical Power & Energy Systems*, 35(1):34–46.

Raza, A., Dianguo, X., Yuchao, L., Xunwen, S., Williams, B., and Cecati, C. (2016). Coordinated operation and control of vsc based multiterminal high voltage dc transmission systems. *IEEE Transactions on Sustainable Energy*, 7(1):364–373.

Renkema, D. J. (2007). Validation of wind turbine wake models. *Master of Science Thesis, Delft University of Technology*.

Rev, H. (2002). Horns rev offshore wind farm. `https://www.4coffshore.com/windfarms/horns-rev-1-denmark-dk03.html`.

Samorani, M. (2013). The wind farm layout optimization problem. In *Handbook of wind power systems*, pages 21–38. Springer.

Sandano, R., Farrell, M., and Basu, M. (2017). Enhanced master/slave control strategy enabling grid support services and offshore wind power dispatch in a multiterminal vsc hvdc transmission system. *Renewable Energy*, 113:1580–1588.

Shakoor, R., Hassan, M. Y., Raheem, A., and Wu, Y.-K. (2016). Wake effect modeling: A review of wind farm layout optimization using jensen's model. *Renewable and Sustainable Energy Reviews*, 58:1048–1059.

Sun, J. (2015). Autonomous local control and stability analysis of multiterminal dc systems. *IEEE Journal of Emerging and Selected Topics in Power Electronics*, 3(4):1078–1089.

Tan, S.-C., Lai, Y.-M., and Tse, C.-K. (2011). *Sliding mode control of switching power converters: techniques and implementation.* CRC press.

Tang, G., Xu, Z., Dong, H., and Xu, Q. (2016). Sliding mode robust control based active-power modulation of multi-terminal hvdc transmissions. *IEEE Transactions on Power Systems*, 31(2):1614–1623.

Wagan, A. I., Shaikh, M. M., Abro, R., et al. (2015). Wind turbine micrositing by using the firefly algorithm. *Applied Soft Computing*, 27:450–456.

Wang, L. and Thi, M. S. N. (2013a). Comparative stability analysis of offshore wind and marine-current farms feeding into a power grid using hvdc links and hvac line. *IEEE Transactions on Power Delivery*, 28(4):2162–2171.

Wang, L. and Thi, M. S.-N. (2013b). Comparisons of damping controllers for stability enhancement of an offshore wind farm fed to an omib system through an lcc-hvdc link. *IEEE Transactions on Power Systems*, 28(2):1870–1878.

Wdzik, A., Siewierski, T., and Szypowski, M. (2016). A new method for simultaneous optimizing of wind farm's network layout and cable cross-sections by milp optimization. *Applied Energy*, 182:525–538.

Wei, S., Zhang, L., Xu, Y., Fu, Y., and Li, F. (2017). Hierarchical optimization for the double-sided ring structure of the collector system planning of large offshore wind farms. *IEEE Transactions on Sustainable Energy*, 8(3):1029–1039.

Xu, L. and Yao, L. (2011). Dc voltage control and power dispatch of a multi-terminal hvdc system for integrating large offshore wind farms. *IET renewable power generation*, 5(3):223–233.

Yang, B., Sang, Y., Shi, K., Yao, W., Jiang, L., and Yu, T. (2016). Design and real-time implementation of perturbation observer based sliding-mode control for vsc-hvdc systems. *Control Engineering Practice*, 56:13–26.

Yang, X.-S. and Press, L. (2010). *Nature-Inspired Metaheuristic Algorithms Second Edition.* Luniver Press United Kingdom.

Zhang, L., Liu, L., Yang, X.-S., and Dai, Y. (2016). A novel hybrid firefly algorithm for global optimization. *PloS one*, 11(9):e0163230.

Zhao, X. and Li, K. (2013). Control of vsc-hvdc for wind farm integration based on adaptive backstepping method. In *Intelligent Energy Systems (IWIES), 2013 IEEE International Workshop on*, pages 64–69. IEEE.

Zhao, X. and Li, K. (2015). Adaptive backstepping droop controller design for multi-terminal high-voltage direct current systems. *IET Generation, Transmission & Distribution*, 9(10):975–983.

PUBLICATIONS BASED ON THE THESIS

Papers published in refereed journals

1. Ramu Srikakulapu and Vinatha U., "Stability Analysis and A Hybrid Controller Design of Grid-Connected Offshore Wind Farm Through A VSC-HVDC Transmission Link ", *Asian journal of control, Wiley.* 21(4), pp. 2017-2026, 2019 (SCIE indexed).

2. Ramu Srikakulapu and Vinatha U., "Optimized design of collector topology for offshore wind farm based on ant colony optimization with multiple travelling salesman problem.", *Journal of Modern Power Systems and Clean Energy, Springer.*, pp. 1-12, 2018 (SCI indexed).

3. Ramu Srikakulapu and Vinatha U., "New Optimization Approach Based on Ant Colony Optimization with Travelling Salesmen Problem for Optimal Design of Offshore Wind Farm.", *International Journal of Control Theory and Applications , IJCTA.*, 10(5), pp. 691-700, 2017 (Scopus indexed).

Papers published in peer-reviewed conference proceedings

1. Ramu Srikakulapu and Vinatha U., "Design of a hybrid controller based on GA-SMC for the Multi-terminal VSC-HVDC transmission system. ", *In 2nd IEEE International Conference on Power Electronics, Intelligent Control and Energy Systems (ICPEICES)*, pp. 1-6. IEEE, 2018.

2. Ramu Srikakulapu and Vinatha U., "Combined approach based on ACO with MTSP for optimal internal electrical system design of large offshore wind farm.", *In 2018 International Conference on Power, Instrumentation, Control and Computing (PICC)*, pp. 1-6. IEEE, 2018.

3. Ramu Srikakulapu and Vinatha U., "A hybrid controller design for VSC-HVDC transmission system for PMSG based offshore wind farm.", *In Asia-Pacific Power and Energy Engineering Conference (APPEEC)*, 2017 IEEE PES, pp. 1-5. IEEE, 2017.

4. Ramu Srikakulapu and Vinatha U., "Combined approach of firefly algorithm with travelling salesmen problem for optimal design of offshore wind farm.", *In Power & Energy Society General Meeting, 2017 IEEE*, pp. 1-5. IEEE, 2017.

5. Ramu Srikakulapu and Vinatha U., "New Optimization Approach Based on Ant Colony Optimization with Travelling Salesmen Problem for Optimal Design of Offshore Wind Farm.", *In 2nd International Conference on Smart Electric Grid (IC-SEG)*, 2016.

6. Ramu Srikakulapu and Vinatha U., "Optimal design of collector topology for offshore wind farm based on ant colony optimization approach.", *In Power Electronics, Drives and Energy Systems (PEDES), 2016 IEEE International Conference on*, pp. 1-6. IEEE, 2016.

7. Ramu Srikakulapu and Vinatha U., "Electrical collector topologies for offshore wind power plants: A survey.", *In Industrial and Information Systems (ICIIS), 2015 IEEE 10th International Conference on*, pp. 338-343. IEEE, 2015.

Bio-data

Name : Ramu Srikakulapu

Date of birth: 14-08-1987

Marital status: married

E-mail: ram2314u@gmail.com

Mobile: +91-9494670711

Address

Research Scholar

Department of Electrical & Electronics Engineering

National Institute of Technology Karnataka

Surathkal, Mangaluru, India-575025, India.

Education

- **M.Tech.**, Control Systems, National Institute of Technology (NIT), Kurukshetra, CGPA-7.92, 2012.

- **B.Tech.**, Electrical & Electronics Engineering, Vignan Institute Information Technology, Visakhapatnam, Percentage-63.65, 2008.